Stray Fields and The Electron's Electric Dipole Moment

by

T. H. Wright

B.A., Amherst College, 2018

M.S., Yale University, 2020

A thesis submitted to the

Faculty of the Graduate School of the

University of Colorado in partial fulfillment

of the requirements for the degree of

Doctor of Philosophy

Department of Physics

2024

Committee Members:

Eric Cornell, Chair

Jun Ye

John Bohn

Adam Kaufman

J. Mathias Weber

Wright, T. H. (Ph.D., Physics)

Stray Fields and The Electron's Electric Dipole Moment

Thesis directed by Prof. Eric Cornell

The universe is full of matter, and we cannot explain how it got there. According to our most accurate theory of particle physics, the Standard Model, the big bang created equal parts matter and antimatter. In the billions of years since, matter and antimatter should have collided and annihilated, leaving (almost) nothing behind. This obviously is not what happened; we live inside of an entire universe made of matter. Despite this serious shortcoming, the Standard Model is outrageously successful in predicting how particles will behave in experiments here on Earth. To salvage the Standard Model, new theories tack on as-of-yet undiscovered particles and interactions that violate the symmetry between matter and antimatter. A side effect of breaking this symmetry is that electrons should have a non-zero electric dipole moment (EDM). In this thesis, I present the world's most precise measurement of the electron EDM to date using electrons confined inside hafnium fluoride molecular ions (HfF^+). We trap HfF^+ in corotating electric and magnetic fields and measure the electron EDM signal by performing Ramsey spectroscopy with coherence times up to 3 seconds. Our result is consistent with an electron EDM of zero and improves on the previous best upper limit by a factor of ~ 2.4, further constraining proposed theories of particle physics. I also worked towards a future measurement, hopefully $10\times$ more precise, of the electron EDM using thorium fluoride molecular ions. I discuss the systematic errors we uncovered in our HfF^+ measurement that require our future experiment to be magnetically shielded.

Dedication

To everyone who reads my dissertation.

"As far as I'm concerned, if something is so complicated that you can't explain it in ten seconds, then it's probably not worth knowing anyway."

- Bill Watterson, The Indispensable Calvin and Hobbes

Acknowledgements

Thank you to my teachers, from those who taught me how to tie my shoes to the people still teaching me how to work in a lab. Connie Isbell, Jeanne Jewell, Arthur Crumm and Mark Adams are just a few of the incredible teachers I had growing up.

Thank you to the administrators who pushed me through hoops I did my best to stumble through, particularly Krista Beck.

Thank you to anyone who spent time cleaning up after me.

Thank you to everyone who worked with me, particularly those who still think I know what I am doing. Nate Clayburn, Claire Carlin, Olivier Grasdijk, Oskari Timgren, Jakob Kastelic, Andy White, Guanchen Peng, Luke Caldwell, Tanya Roussy, Kia Boon Ng, Noah Schlossberger, Sun Yool Park, Anzhou Wang, Addison Hartman and Patricia Hernandez have all been a joy to work with.

Thank you to Larry Hunter, Dave DeMille, Dave Kawall, Tanya Zelevinsky, Steve Lamoreaux, Ben Sauer, Mike Tarbutt, Eric Cornell and Jun Ye. I learned an incredible amount working in their labs, from how to use a level to precision molecular spectroscopy.

Thank you to all of my friends and family who helped me find my way through two graduate programs. My parents have been a wellspring of support my entire life, and I could not have made it this far without them. My cousin Kate Berrigan gets a special mention because she adopted a dog, letting me have a pet in graduate school without the responsibility.

Contents

Chapter

Tables

Table

Figures

Figure

Chapter 1

Introduction

"The universe is a big place, perhaps the biggest."

- Kilgore Trout, Venus on the Half-Shell

A survey of recent JILA electric dipole moment (EDM) theses shows that their introductions focus on a few common subjects. These include the usual story about matter and antimatter [1,2,3], an overview of how our measurement works [1, 3, 4], a history of past EDM measurements [2, 4] and a survey of contemporary experiments [1, 2, 4].[1] I will leave the latter three topics to the other recent theses, and dive into why even null results of the electron EDM (eEDM) are so interesting.

1.1 Crash Course in Quantum Field Theory

Nathaniel Craig, a professor at University of California Santa Barbara, is an expert in quantum field theory (QFT). He gave a virtual department colloquium at Boulder, titled "The Return of the LHC" in April 2022, which began with the most succinct and understandable overview of QFT that I have heard [5]. I will draw heavily from his talk to give a non-rigorous explanation of QFT which will help to explain the motivation for the JILA EDM experiment. This is a notoriously

[1] I particularly recommend the introduction of Tanya Roussy's thesis [2] for those who would like to read more detail about how the JILA eEDM experiment came to be. She's a comedian.

difficult subject, but I hope future EDM graduate students will be able to understand this section even if they have never taken a QFT course.

1.1.1 Feynman Diagrams

Even though QFT is an abstract and mathematically dense subject, physical interactions are represented pictorially in Feynman diagrams like the ones shown in Figure 1.1. The first Feynman diagram, Figure 1.1a, depicts electron scattering. We know from classical physics that the electrons moving towards one another will feel a repulsive force that grows as they get closer. In QFT, the electromagnetic interaction is mediated by the "exchange of virtual photons." This interaction is depicted in Figure 1.1a by a squiggly red line between the two blue lines which represent electrons. The photon is "virtual" because it is a particle that only exists during the interaction - it does not exist at the initial or final time depicted in the Feynman diagram. Particles that enter or leave Feynman diagrams are called "real." This interaction modifies the electrons' momenta, indicated by the electron lines going off in new directions.

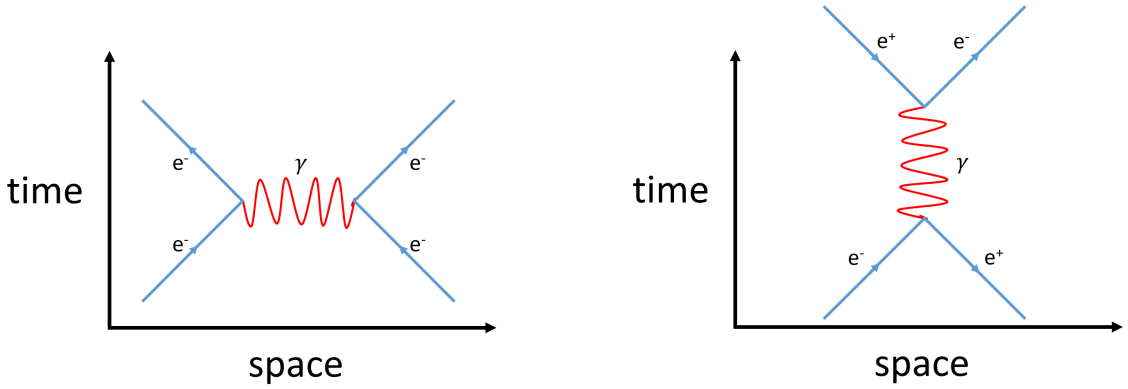

(a) Electron scattering

(b) Electron-positron annihilation and creation

Figure 1.1: A Feynman diagram (a) depicting electron scattering. Quantum field theories respect the symmetries of special relativity so we can exchange the time and space axes of our Feynman diagram, equivalent to rotating the diagram 90 degrees. This rotated diagram (b) shows electron and positron annihilation followed by pair production.

There are a few more things worth pointing out about Figure 1.1a. The first is that the electrons, like all fermions, are depicted by solid lines with an arrow. Lines with an arrow pointing

in the direction the fermion is traveling represent matter particles, while lines with an arrow pointing in the opposite direction depict antimatter particles. The arrows in Figure 1.1a all point in the same direction the particles are moving, so they all represent electrons instead of positrons. The other thing to know is that Feynman diagrams come with a set of mathematical rules to calculate the depicted event's probability amplitude [6]. I will not try to explain all of the math behind these Feynman diagrams, but it is good to know that the usual rules of momentum, energy and charge conservation apply to these calculations and can help guide our intuition.

Moving on to Figure 1.1b, it is clear that this is the same diagram as Figure 1.1a rotated 90 degrees. This is not a coincidence. QFT is a quantum theory that is consistent with and respects the symmetries of special relativity, which include Lorentz transformations that convert space into time and vice versa. This means Feynman diagrams which have been rotated describe real, physical processes. In the case of electron scattering, the 90 degree rotated Feynman diagram describes electron-positron annihilation which creates a virtual photon that then turns into a new electron-positron pair.

It's worth pausing to let this sink in – we can take a simple Feynman diagram like electron scattering, rotate it on its side because QFT follows the rules of special relativity, and determine that pair production and annihilation are really things that happen. This alone predicts the existence of antimatter and that particle number is not a conserved quantity, both of which are observed experimentally! Half of why I chose to write about QFT in more than the usual detail is to share this point, I think this is so cool.

It is interesting to see what happens when we replace one of the electrons in Figure 1.1a with another charged particle like a muon μ^-, the 207 times heavier "cousin" of the electron, as shown in Figure 1.2a. This diagram still represents particles scattering via the electromagnetic force, where one particle is much heavier than the other. The interesting part comes when we rotate the diagram by 90 degrees, as shown in Figures 1.2b and 1.2c. In Figure 1.2b we have a muon and antimuon

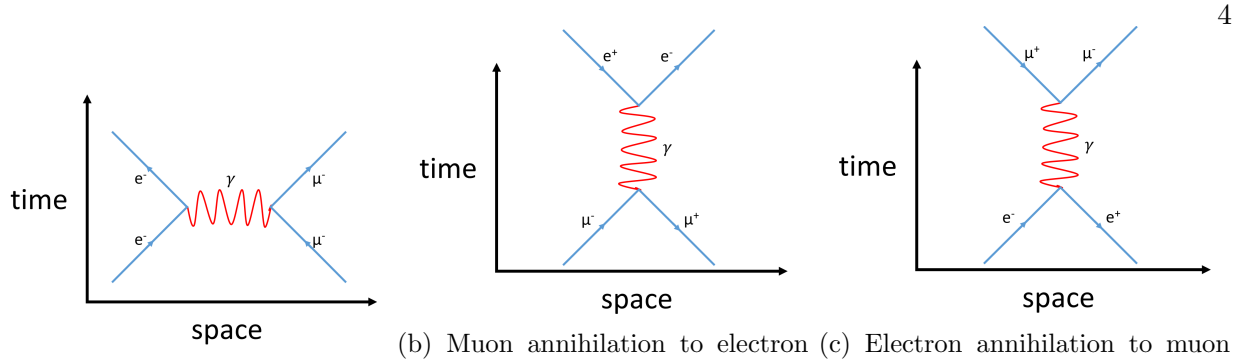

(a) Electron-muon scattering

(b) Muon annihilation to electron pair production

(c) Electron annihilation to muon pair production

Figure 1.2: A Feynman diagram of (a) electron-muon scattering which has been rotated (b) clockwise and (c) counter clockwise by 90 degrees. The second two diagrams depict annihilation and pair production interactions where the initial and final particles are different species.

annihilating which leads to electron-positron pair production. This means that we can start with one pair of particles and end up with a completely new pair!

It is important to think about energy conservation in Feynman diagrams like Figure 1.2b. Here the initial energy is given by the sum of the rest mass $E_{\text{rest}} = \sum_i m_i c^2$ and kinetic energy. Since muons are 207 times heavier than electrons, most of the muon's and antimuon's rest mass energy will be carried away as kinetic energy of the electron positron pair. Figure 1.2c shows the same interaction happening in reverse. While this is a valid Feynman diagram, it can only take place if the incoming electron and positron have enough kinetic energy produce a muon and antimuon.

There is a final point worth mentioning about Figure 1.1b that concerns momentum and energy conservation. These conservation laws apply at every vertex. This means that the energy and momentum of the initial electron/positron, the virtual photon and the final electron/positron pair must be the same. We can consider the Feynman diagram from the center of mass frame, where $p_{\text{tot,initial}} = 0$ and $E_{\text{tot,initial}} \geq 2m_e c^2$. This means the photon will have momentum $p_\gamma = \dfrac{\hbar\omega}{c} = 0$ and energy $E_\gamma = \hbar\omega \geq 2m_e c^2$ – which seems to be a contradiction! The resolution is that virtual particles can be "off-shell," meaning they have unusual values of energy and momentum which is

allowed since they only exist for a short amount of time and do not exit the Feynman diagram. All particles that enter or exit the diagram must be "on-shell" and behave normally.[2] In this case, the virtual photon is off-shell and then produces two on-shell particles, an electron and a positron.

Annihilation and pair production can occur independently of one another, as shown in Figure 1.3. In order for energy and momentum to be conserved at the end of these processes they each involve two real photons. Figure 1.3a shows an electron emitting a real photon and becoming an off-shell particle, which can annihilate with a positron to produce a second real photon. Rotating this Feynman diagram 180 degrees would depict two photons coming together to produce an electron and a positron, an allowed but relatively rare two body process. The more common Feynman diagram depicting pair production is shown in Figure 1.3b, where one energetic photon turns into the particle and antiparticle pair directly.

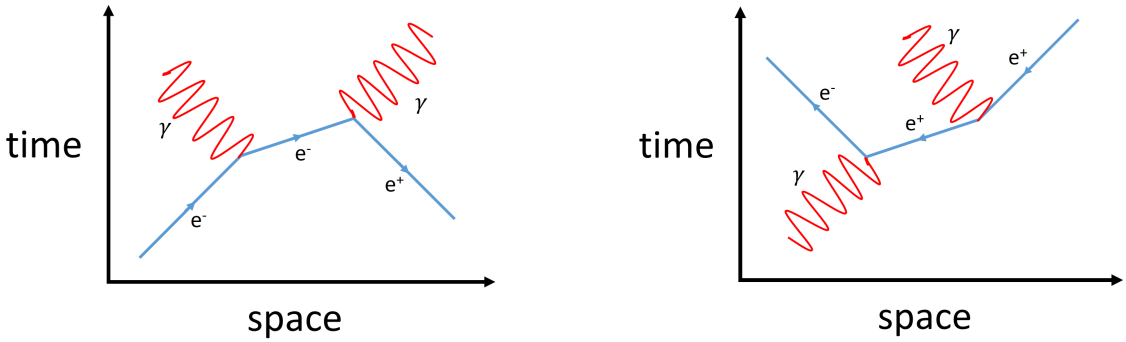

(a) Electron-positron annihilation

(b) Electron-positron pair production

Figure 1.3: Feynman diagrams of (a) annihilation and (b) pair production. Note that there is no preference for the electron or positron to be the particle in the middle of each diagram.

1.1.2 The Vacuum

Every particle-antiparticle pair is associated with a multicomponent quantum field, which has values at every point in spacetime.[3] Electrons, for example, have a four component quantum

[2] Particles that are on-shell have the usual dispersion relation $E^2 = m^2c^4 + p^2c^2$. Particles which are off-shell have energies and momenta which do not follow this relationship.

[3] This is quite similar to electric fields, which three components $\mathcal{E}_x$, $\mathcal{E}_y$ and $\mathcal{E}_z$ defined at each point in spacetime.

field for the spin up/down components of electrons/positrons. When the electron quantum field is in its ground state, there are no electrons or positrons at all. Excitations of the quantum field correspond to particles that exist at certain points in spacetime.

That means in QFT there are no truly empty regions of space. Regions of space where all of the quantum fields are in their ground state are considered the "vacuum," but those fields can fluctuate. In quantum mechanics there is an uncertainty relationship between energy and time which can be written as:

$$\Delta E \Delta t \geq \frac{\hbar}{2} \tag{1.1}$$

We can interpret this equation as saying that for short times Δt, the energy of the quantum fields can have fluctuations on the order of $\frac{\hbar}{2\Delta t}$. If this energy is large compared to $2mc^2$ there is enough energy to produce a short lived particle antiparticle pair. For example, an electron positron pair can be created for $\Delta t \leq \frac{\hbar}{4m_e c^2} = 3 \times 10^{-22}$ seconds. So what we normally consider to be the "vacuum" includes these short lived particle pairs as shown in Figure 1.4.

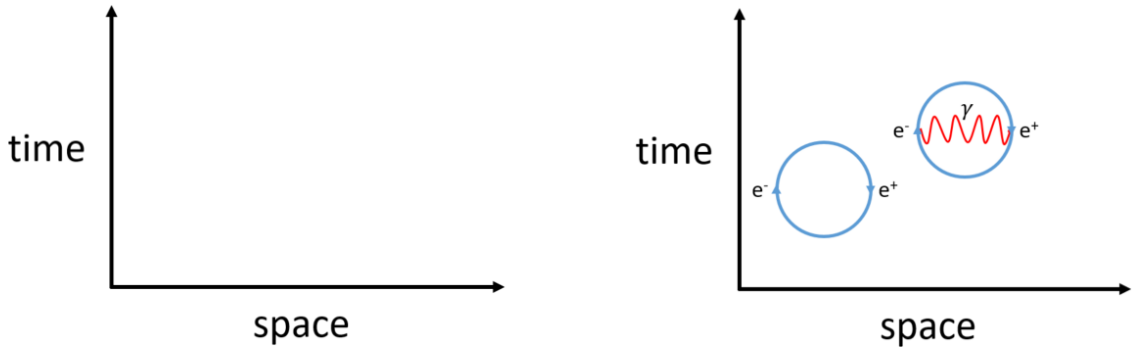

(a) Classical vacuum, $\hbar = 0$ (b) QFT vacuum, $\hbar \neq 0$

Figure 1.4: Vacuum in (a) classical and (b) quantum field theories. In QFT, pair production and annihilation can occur due to energy fluctuations. Those virtual particles can interact with one another, as shown in the upper right of (b).

The important point is that we never measure bare particles, we always measure particles

that are interacting with the vacuum. Take the example of an electron with no orbital angular momentum in a uniform external magnetic field.[4] We know that the magnetic moment of the electron's spin $\vec{\mu}_s = g_s \mu_B \frac{\vec{S}}{\hbar}$ will interact with the magnetic field $\vec{\mathcal{B}}$ causing an energy shift:

$$H_{\text{Zeeman}} = -\vec{\mu}_s \cdot \vec{\mathcal{B}} = -g_s \mu_B \frac{\vec{S}}{\hbar} \cdot \vec{\mathcal{B}} = -g_s \mu_B M_s \mathcal{B} \tag{1.2}$$

Here g_s is the electron's g-factor, which encodes how strongly the electron's states split in energy due to the external magnetic field. If we were able to measure the bare electron, Paul Dirac predicted that we would measure $g_s = -2$. Dirac's calculation was equivalent to evaluating the Feynman diagram in Figure 1.5a, where the electron interacts with an external magnetic field represented by a real photon[5] without any virtual particles popping in.

When we compare Dirac's prediction of $g_s = -2$ to the current state of the art measurement $g_s = -2.00231930436(26)$, we see that he was only off by about 0.1 % [7]. This gap starts to close when we calculate how virtual particles modify the size of the electron's magnetic moment. The simplest virtual particle we can consider is shown in Figure 1.5b where the electron emits and reabsorbs a virtual photon. This process changes the prediction of the electron's g-factor from -2 to $-(2+\frac{\alpha}{\pi}) = -2.0023228...$, which is just two parts in a million different from the measured value.

We can keep drawing Feynman diagrams with more and more virtual particles, like the one in Figure 1.5c, which will all contribute to the predicted value of g_s. We fortunately do not need

[4]Since I spend the entirety of Chapter 4 on the sign of the g-factor in HfF^+, I will make sure the signs of the quantities are clear here. The electron's spin magnetic moment $\vec{\mu}_s$ has a positive magnitude $\mu_s = g_s \mu_B$ if the magnetic moment is parallel to the electron's spin $\vec{S}$. The Bohr magneton μ_B is defined to be a positive quantity, so the sign of the magnetic moment's magnitude is determined by the sign of g_s. Since we know that the electron's magnetic moment is antiparallel to its spin, $g_s \approx -2.002$ is a negative quantity.

[5]In QFT, bosons (particles with integer spin) like photons are "force carriers". Photons are the force carriers of the electromagnetic force. Whenever a particle is interacting with an external electric or magnetic field, that shows up in Feynman diagrams as a real photon.

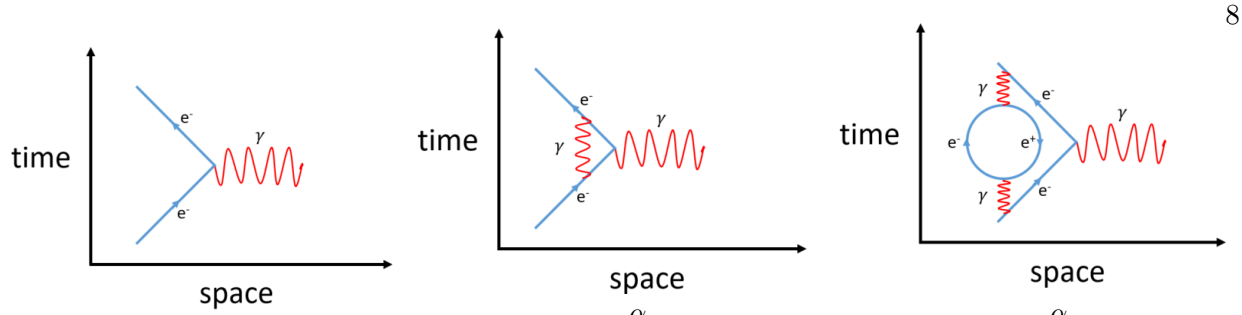

(a) $g = -2$ (b) $g = -(2 + \frac{\alpha}{2\pi}) \approx$ -2.002 (c) $g = -(2 + \frac{\alpha}{2\pi} + \mathcal{O}(\alpha^2))$

Figure 1.5: Feynman diagrams that describe the electron's g-factor. The dominant term effect is given by (a), the electron interacting with an external magnetic field represented by a photon. The next largest term is from (b), where a virtual photon emitted and then later absorbed by the electron modifies the g-factor from -2 to -2.002. This is a one-loop Feynman diagram as the only closed path we can draw is between the three electron-photon vertices. Higher order effects which include more or heavier particles, like (c), contribute smaller perturbations to the g-factor. This is a two-loop Feynman diagram.

to calculate all of these Feynman diagrams to get a reasonably accurate result. As a general rule, the more complicated the Feynman diagram the smaller the effect it will have on a prediction.[6] In fact, we can sort Feynman diagrams by the number of non-overlapping closed loops that they contain. For example, Figure 1.5a has no closed loops and therefore is the zeroth order effect. This makes sense because it is the only Feynman diagram with an incoming and outgoing electron that interacts with the external electromagnetic field and no virtual particles. Figure 1.5b has one closed loop – the triangle between the virtual photon and electron – so it provides the first order perturbation.[7] There are many Feynman diagrams we can draw with two loops, one of which is Figure 1.5c. All Feynman diagrams with an incoming and outgoing electron interacting with a real photon that have two loops are summed together to make up the second order perturbation to g_s.

In order to match today's experimental precision, theorists need to include all of the more

[6]This is true for interactions of the electromagnetic and weak forces, but is not true for the strong force. This makes strong force calculations very difficult.

[7]There is another Feynman diagram we can draw with just one loop, where we replace the virtual photon with a virtual Z boson, see Subsection 1.1.3. Z bosons are massive and chargeless carriers of the weak force, and this Feynman diagram causes a $\left(\frac{m_e}{m_Z}\right)^2 \approx 3 \times 10^{-10}$ times smaller change to g_s than Figure 1.5b [8].

than 10,000 unique Feynman diagrams out to five loops [7]. Amazingly, the predicted value agrees with the experimental result even with its tiny uncertainty at the 0.1 part per trillion level. While this level of agreement is a triumph of theoretical and experimental physics, people are working hard to reduce the error bars on both sides. One motivation for this further work is to try and discover new particles and/or interactions which slightly modify the electron's g-factor from the expected theoretical value.

The important takeaway is this: particles interact with the vacuum which contains particles popping into and out of existence. That interaction modifies the properties of all particles, such as the electron's magnetic dipole moment. If undiscovered particles exist that even indirectly interact with electrons, the strength of the electron's magnetic moment will be different than is predicted by our most accurate quantum field theory, the Standard Model (SM). So increasingly precise measurements of quantities like the electron's magnetic moment can signal the existence of new particles and interactions if those measurements do not agree with what is predicted by the SM. Alternatively, if more precise measurements continue to agree with the SM, the measurements can rule out proposed new theories which make different predictions than the SM.

1.1.3 The Standard Model, Particles and Interactions

Before jumping into the story about the electron's electric dipole moment, it will help to have some background on the Standard Model. The SM is the current state of the art quantum field theory that best describes particle physics. It contains the 17 known particles, shown in Figure 1.6, and how they interact via the electromagnetic, weak and strong forces. Notably, the only force it does not include is gravity, which is best explained by Einstein's theory of General Relativity.

The blue and green particles in Figure 1.6 are fermions, paticles with half-integer spins which make up matter. All of these particles have associated antiparticles which have the same properties but have the opposite signed charge.[8] Fermions interact with one another via the three forces

[8] Neutrinos have no charge, so their associated antimater particles are chargeless as well.

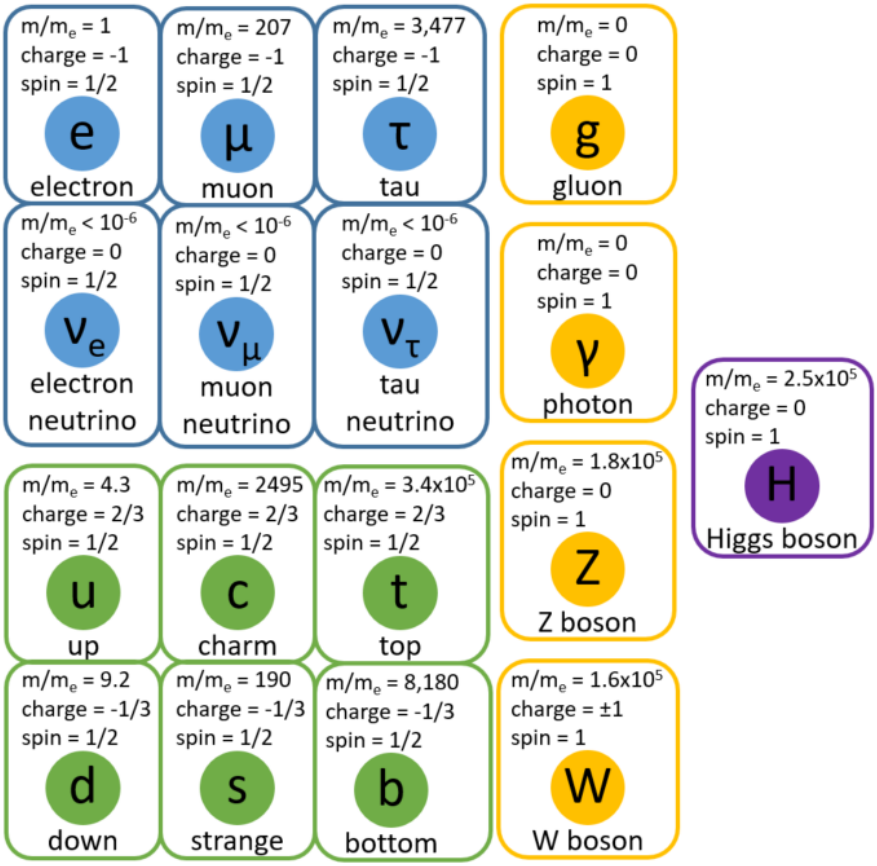

Figure 1.6: Particles in the Standard Model. Each particle's mass relative to the electron's mass $m_e = 0.511$ MeV/c^2, charge and spin are listed. Blue and green particles are fermions which each have an associated antimatter particle with all the same properties except for the opposite signed charge. Blue particles are leptons, green particles are quarks and yellow particles are force carrying bosons. Interactions with the Higgs boson give particles their mass.

included in the Standard Model, which are mediated by the yellow bosons in Figure 1.6. The electromagnetic force acts on all fermions with nonzero charge, and is mediated by photons as shown in Figure 1.1a. It attracts oppositely charged fermions together and repels fermions with the same charge, as we would expect.

The strong force is mediated by gluons and only acts on quarks, which are the fermions shown in green in Figure 1.6. In addition to their mass, charge and spin, quarks also have a "color" which can be red, green or blue. The strong force is a powerful attractive force which is mediated by gluons and binds quarks together to make "color-neutral" composite particles. A composite

particle is color-neutral if it is made of a red, green and blue quark bound together, or if it is made of a quark and antiquark of the same color. For example, a red up quark, a blue up quark and a green down quark can be bound together by the strong force. A composite particle made of two up quarks and a down quark, regardless which quark is which color, is called a proton. One up quark can combine with two differently colored down quarks to make a neutron. Both protons and neutrons are examples of baryons, composite particles made of an odd number of quarks. Baryons and antibaryons, particles made of an odd number of antiquarks, will play an important role in the story about the eEDM. The strong force is notoriously difficult to calculate, so it is fortunate that we do not need to dive into those details.

The weak force requires the longest explanation. It is mediated by the Z and $W^{\pm}$ bosons, and is the only force that interacts with all twelve fermions of the Standard Model. When fermions interact via the Z boson they exchange energy and momentum, which is similar to electromagnetic interactions like the one shown in Figure 1.1a. As hinted at by its name, the forces mediated by the Z boson are weak compared to electromagnetic ones. The more interesting weak interactions are those mediated by the W^{+} and W^{-} bosons, which cause fermions of one type to change to another. These "flavor" or identity changing interactions are subject to many restrictions beyond energy, momentum and charge conservation, which we will explore now.

One restriction comes from the "helicity" or "handedness" of particles. Particles are either "right-handed" or "left-handed" if their spin angular momentum is in the same or opposite direction as their motion, as shown in Figure 1.7. Most particles and antiparticles can be either left- or right-handed, occurring in nature with equal frequency. However, all neutrinos are left-handed and antineutrinos are right-handed. Additionally, the $W^{\pm}$ bosons only interact with left-handed fermions and right-handed antifermions. These facts together mean that the weak force acts differently on left- and right-handed particles, a peculiarity not shared by the electromagnetic or strong forces.

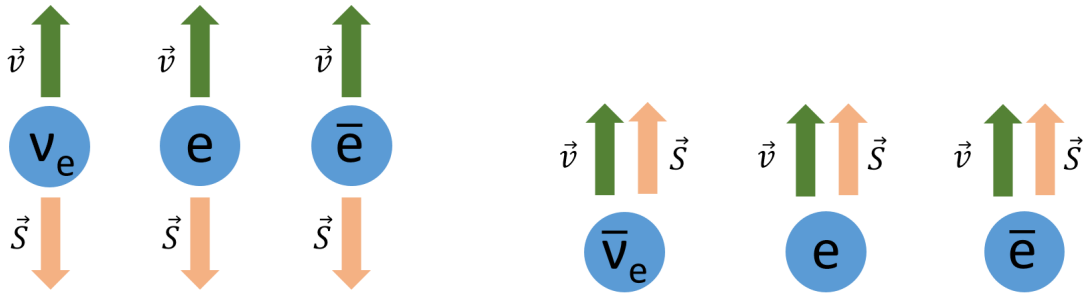

(a) Left-handed particles

(b) Right-handed particles

Figure 1.7: Examples of (a) left-handed and (b) right-handed particles. Most particles and their antiparticles, like electrons and positrons, can be left- or right-handed. However, all neutrinos are left-handed and antineutrinos are right-handed.

Another important constraint on flavor changing weak interactions are that they cannot turn quarks into leptons or leptons into quarks. For interactions with leptons, $W^{\pm}$ bosons conserve a property called "lepton number". Lepton number is the total number of leptons minus the number of antileptons, so this restriction means that the weak interaction cannot change a lepton into an antilepton or vice versa. The final constraint for leptons is that $W^{\pm}$ bosons must interact with leptons of the same "generation". Looking back at Figure 1.6, we see that each row contains three fermions which have similar properties but vary in mass.[9] For example, electrons are more or less light versions of muons which in turn are light versions of taus. We call the leftmost and lightest column of particles the first generation, the middle column the second generation and the right column the third generation. Exactly why there are three generations of each fermion is open question [9]. The restriction that the weak force cannot change lepton generation means that electrons and electron neutrinos can turn into one another, but they cannot turn into a muon.[10]

With these rules for lepton flavor changing in place, we can finally see an example of the $W^{\pm}$ boson changing the identity of a particle. In Figure 1.8a we see an incoming muon turn into a muon neutrino by emitting a W^{-} boson. We know the muon must be left-handed since it interacts with

[9] Only upper limits have been measured for the neutrino masses, but they are expected to have different masses as well.

[10] Muons cannot directly turn into an electron, but they can indirectly as shown in Figure 1.8a

a W^- boson, and it produces a left-handed muon neutrino. This interaction follows the rules of charge and lepton number conservation and it preserves lepton generation. However, this explains only the first half of the Feynman diagram in Figure 1.8a. Muon neutrinos are stable particles that can leave the Feynman diagram, but the W^- boson is not. $W^{\pm}$ and Z bosons are massive, unstable particles with multiple decay channels and lifetimes of about 3×10^{-25} seconds [10]. The decay mode shown in Figure 1.8a is the W^- boson turning into an electron and antielectron neutrino. These particles are both stable and the interaction complies with all of the rules listed above.

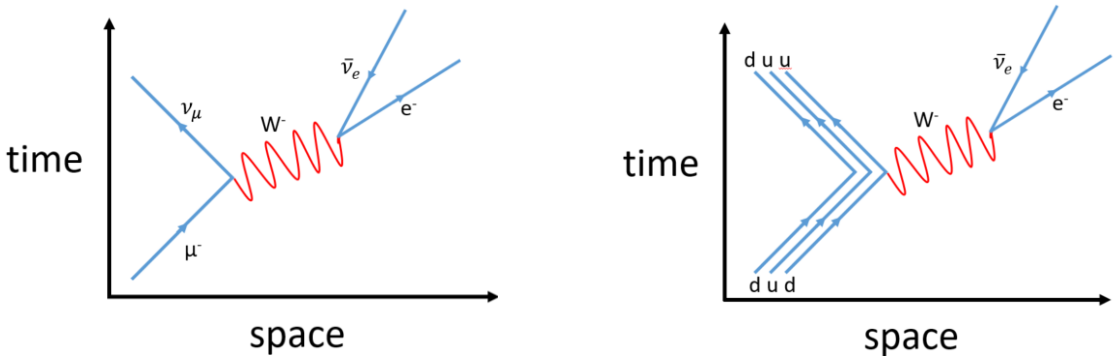

(a) Muon Decay

(b) Beta Decay

Figure 1.8: Two Feynman diagrams showing decay due to the weak force. (a) A muon transforms into a muon neutrino, emitting a W^- boson. The unstable W^- boson then decays into an electron and antielectron neutrino. (b) A down quark inside of a neutron emits a W^- boson and turns into an up quark. This changes the composite baryon into a proton. The unstable W^- boson then decays into an electron and antielectron neutrino. The entire process is known as beta decay.

We can now turn to the weak interactions mediated by $W^{\pm}$ bosons between quarks. As was the case for leptons, weak interactions cannot change quarks to antiquarks or vice versa. This rule is normally expressed by stating that baryon number, the number of baryons minus the number of antibaryons, must be conserved. However, this is where the similarities for weak interactions between leptons and quarks ends. The weak force is allowed to transform quarks from one generation into another, which it cannot do to leptons. The only additional restriction on quark flavor transformations is that the weak force always turns "up-type" quarks (the up, charm and top quarks with charge $+\frac{2}{3}$) into a "down-type" quarks (the down, strange and bottom quarks

with charge $-\frac{1}{3}$) or vice versa. This can be understood as a consequence of charge conservation, since the $W^{\pm}$ bosons which mediate flavor change are themselves charged particles.

In total, there are nine weak interactions that turn one of the three down-type quarks into one of the three up-type quarks. These nine interaction strengths are characterized by the 3x3 unitary CKM matrix:

$$V_{\mathrm{CKM}} = \begin{pmatrix} V_{\mathrm{ud}} & V_{\mathrm{us}} & V_{\mathrm{ub}} \\ V_{\mathrm{cd}} & V_{\mathrm{cs}} & V_{\mathrm{cb}} \\ V_{\mathrm{td}} & V_{\mathrm{ts}} & V_{\mathrm{tb}} \end{pmatrix} \tag{1.3}$$

The entries in the top row of this matrix characterize the relative probability amplitudes of the down, strange and bottom quarks transforming into the up quark. The next two rows parameterize the relative probability amplitudes of down-type quark transitions into the charm and top quarks. The relative probability amplitude of an up-type quark transforming into a down-type quark is given by the complex conjugate of the relevant matrix element. This means that the CKM matrix completely parameterizes all weak interactions that change quark flavor.

In general, all nine complex parameters of a 3x3 unitary matrix like the CKM matrix can be described by just four real numbers, three rotation angles and one complex phase [11]. The three rotation angles are the three "mixing angles" which parameterize the likelihood of each of the nine quark transformations. The complex phase is a parameter which describes how much each of these interactions violates time-reversal symmetry, which will be explained further in the next subsection [6].[11]

A common example of quarks turning into one another is shown in Figure 1.8b, where a

[11] Weak interactions that change lepton flavor cannot change generation, so these relative probability amplitudes are described by the 3x3 identity matrix. This matrix obviously does not have any imaginary components, so weak interactions that change lepton flavor do not violate time-reversal symmetry.

down quark inside a neutron turns into an up quark making the composite particle a proton. This interaction is characterized by the V_{ud} term in the CKM matrix.

1.1.4 The Standard Model, Discrete Symmetries

The last prerequisite we need to cover is discrete symmetry in the Standard Model. There are three particularly important discrete symmetries – charge conjugation (C), parity (P) and time-reversal (T). These three symmetries are defined by a particular transformation, and we say that a system respects a given symmetry if the physical laws are the same before and after the transformation.

It is easiest to see what that means with an example. The charge conjugation transformation is to swap all of the matter particles in a system for their antiparticles, and vice versa.[12] Consider once again electron scattering, as shown in Figure 1.1a. The negatively charged electrons exchange a photon resulting in a repulsive force. If we replace the electrons with positrons, the exact same thing will happen – the two particles will approach one another, exchange a photon and feel a repulsive force. Because the particles behave the same way whether or not the particles are swapped for antiparticles, this interaction respects charge conjugation symmetry. In fact, all electromagnetic and strong interactions are C-symmetric, though it is not the case for weak interactions. The example of muon decay, shown in Figure 1.8a, involves a left-handed muon turning into a left-handed muon neutrino while emitting a W^- boson. This interaction is impossible if we swap the particles for antiparticles because there are no left-handed antineutrinos, so it violates C-symmetry. Note that weak interactions mediated by Z bosons do not necessarily involve neutrinos, so some weak interactions violate C-symmetry while others do not.

Parity's transformation inverts spatial coordinates, $(x, y, z) \to (-x, -y, -z)$. This is equivalent to a mirror inversion $(x, y, z) \to (x, y, -z)$ followed by a 180 degree rotation $(x, y, -z) \to (-x, -y, -z)$ about the same axis. An 180 degree rotation is a standard Lorentz transformation

[12] The C transformation also involves swapping the charge of $\mathrm{W}^{\pm}$ bosons.

and is common fare, which is why parity symmetry is sometimes referred to as mirror symmetry. Just as is the case for charge conjugation, the electromagnetic and strong forces respect parity while the weak force does not. This is because the parity transformation flips the handedness of particles. Consider again the left-handed muon decaying into a left-handed muon neutrino and emitting a W^- boson. The parity inverted version of this decay would involve a right-handed muon, which cannot interact with a W^- boson, decaying into a right-handed muon neutrino, which does not exist. So weak interactions violate P as well as C symmetries.

The third symmetry is time-reversal symmetry, whose associated transformation is to reverse the direction of time $t \to -t$. While we can test various systems with matter and antimatter (C) and in different spatial orientations (P), it is a bit harder to set time running backwards in our experiments. However, if we can infer that an interaction would behave differently if we reversed time's arrow, we say that it violates T-symmetry. The way time-reversal symmetry breaking is described mathematically is by a Hamiltonian with imaginary components, like the CKM matrix that describes quark flavor changing weak interactions [6]. This means the probability amplitude of quark a turning into quark b is different than the probability amplitude of quark b turning into quark a. These two processes are the same except the arrow of time has been reversed, so they violate T-symmetry [12].

In addition to considering the three discrete symmetries on their own, they combine to form composite symmetries. The most important combined symmetry for the eEDM story is CP-symmetry, the symmetry whose operation is to 1) swap matter with anitmatter and 2) invert space. If a process respects both of the joined symmetries, it is straightforward to see that it will respect the combined symmetry. Electromagnetic interactions behave the same way under C and P symmetries separately, so they will still behave the same way when both symmetry operations are applied. A process will also conserve a combined symmetry if it violates both of the merged symmetries. In Figure 1.8a we started with a left-handed muon that decays to a left-handed muon neutrino while emitting a W^- boson. Applying the C and P transformations, we get a right-handed antimuon that

decays to a right-handed antimuon neutrino while emitting a W^+ boson. All of these particles exist and the interaction has the same probability amplitude as the the original interaction, so muon decay respects CP-symmetry.

In addition to CP, CT and PT symmetries, all three symmetries can be combined to make CPT-symmetry. If an interaction violates zero or two of the three individual symmetries it respects the overall CPT symmetry, and if the interaction violates an odd number of the symmetries it breaks CPT-symmetry. When QFT was first being developed in the early to mid 20th century it was widely believed that all three of the symmetries are strictly conserved by nature [13]. This was until the 1950s when it was found that beta decay, as shown in Figure 1.8b, violates parity [14]. Now it is believed that while the individual symmetries can be violated, the joint CPT-symmetry will always be conserved. This is largely based on the CPT theorem, a mathematical proof that shows that any QFT which is Lorentz invariant (plays nicely with special relativity) will conserve CPT-symmetry [15].

If we assume on this basis that CPT-symmetry really is a good symmetry of nature, we conclude that T-symmetry violation found in quark mixing implies that quark mixing also violates CP-symmetry. While it is possible that CPT-symmetry is broken in nature, I will assume that it is preserved and that CP- and T-symmetries are equivalent. Quark mixing is the only interaction in the Standard Model that has been measured to violate CP-symmetry. Theorists have been puzzled that the strong force is seemingly allowed to violate CP-symmetry [16], but every measurement of the strong force so far indicates that it is CP-even [17].[13]

That covers the preliminaries we need to know about QFT and the Standard Model, so we can begin the story that motivates our measurement of the eEDM.

[13] A few recent papers claim that a more nuanced understanding of the Standard Model implies that the strong force inherently respects CP-symmetry [18,19,20], though I believe that this viewpoint has not been widely accepted.

1.2 The Baryon Asymmetry of the Universe

14 billion years ago the universe began as we know it with the big bang. A particularly colorful description of the big bang that I enjoy is that "at an early time in the standard cosmological model, the Universe began as a fireball, filling all space, with extremely high temperature and energy density" [21]. The source of this quotation together with [22] provide a detailed and understandable history of that fireball, which I will summarize parts of here.

Immediately after the fireball initially exploded, there was plenty of energy for all the fermions and their antiparticles to pop into existence, depicted by Feynman diagrams like Figure 1.3b. The particles that were produced had so much energy that the quarks, usually bound together by the strong force, could roam freely. The big bang caused space itself to rapidly expand, spreading the fireball out and decreasing the energy density and temperature of the universe. After the first 20 microseconds or so of fun the temperature fell below the hadronization temperature $T_h \approx 1.7 \times 10^{12}$ K $= 150$ MeV/k_B, and the strong force was able to overcome the quarks' kinetic energy to wrangle the individual quarks into stable composite particles. At this point there was no longer enough energy to form new protons and antiprotons or neutrons and antineutrons as $2m_pc^2 \approx 2m_nc^2 \approx 1.8$ GeV, so the number of baryons and antibaryons in the universe had hit its maximum.

Shortly after the universe cooled to the hadronization temperature, the baryons and antibaryons found one another and annihilated in similar processes to the one shown in Figure 1.3a. Since all of the interactions described in the Standard Model in Subsection 1.1.3 conserve baryon number, we might expect that the mass annihilation event destroyed all of the baryons and antibaryons. But this is not what happened – while all the antibaryons disappeared, there were baryons left over.[14] That means there must be a process that can occur at energies large compared to the hadronization temperature which can increase the baryon number, so that after annihilation

[14] There is the possibility that matter and antimatter spread out in different directions, and we find ourselves in a matter dominated domain of the universe [21, 22]. This idea will be addressed later in this section.

a portion of the baryons can survive.

The asymmetry in the number of baryons and antibaryons just after baryon pair production froze out is known as the baryon asymmetry of the universe (BAU).[15] The BAU is defined as:

$$\text{BAU} = \left.\frac{N_B - N_{\overline{B}}}{N_B + N_{\overline{B}}}\right|_{\text{T}\gtrsim 1\text{GeV/k}_\text{B}} \tag{1.4}$$

Quantifying this asymmetry is an important step to solving the mystery of how we ended up in a universe full of matter after the big bang. However, as almost all of the baryons and antibaryons that existed immediately after the big bang were annihilated, we cannot measure the quantities in this expression. Fortunately, we can relate the sum of baryons and antibaryons in the early universe to the number of photons that exist currently. As shown in Figure 1.3a, when two particles annihilate there will typically be two photons produced. Bravely ignoring the fact that leptons annihilate and produce photons as well, we can say that the sum of baryons and antibaryons in the early universe is something like the total number of photons in the universe now, which has a temperature of 3 Kelvin:

$$\text{BAU} = \left.\frac{N_B - N_{\overline{B}}}{N_B + N_{\overline{B}}}\right|_{\text{T}\gtrsim 1\text{GeV/k}_\text{B}} \sim \left.\frac{N_B - N_{\overline{B}}}{N_\gamma}\right|_{\text{T=3K}} = \left.\frac{N_B}{N_\gamma}\right|_{\text{T=3K}} = \eta \tag{1.5}$$

We can use the observation[16] that there is no antimatter currently in the universe to simplify the numerator, and we find that the BAU can be estimated by the baryon to photon ratio η [22].

[15] There is a similar story about leptons and the LAU [21]. Leptons on the whole are lighter than baryons, so lepton pair production froze out when the universe was cooler, about a second after the big bang. The BAU gets more attention because it can be measured quite precisely, especially compared to the LAU since it is challenging to measure the background neutrino level of the universe.

[16] Again, the possibility of an inhomogeneous universe of matter and antimatter domains will be addressed later on

Astronomers have two methods of of determining the baryon to photon ratio. The first is by measuring the relative abundance of light nuclei (^{2}H, ^{3}He, ^{4}He and ^{7}Li) created a few minutes after the big bang, when the baryon to photon ratio was stable but there was still enough latent energy ($\gtrsim 2$ MeV) in the universe to trigger thermonuclear reactions [21,22]. This process is known as the big bang nucleosynthesis (BBN). Contemporary research in plasma physics shows that the relative abundances depend heavily on η, and astronomers find that $\eta = 6.10 \times 10^{-10}$ [22,23].

The second method to determine η is by measuring the power fluctuations of the cosmic microwave background (CMB). It took much longer, around 380,000 years, for most electron-positron pairs to annihilate [21]. At this point the energy of the universe was approximately 0.3 eV, and the remaining electrons bound with the nuclei to form atoms, primarily hydrogen. For the first time the universe was no longer a plasma, so the photons emitted when the atoms were formed could freely propagate. These photons were emitted nearly 14 billion years ago so they have been substantially red-shifted and now appear as microwaves that approach Earth from every direction in the universe, hence the name cosmic microwave background. It turns out that the baryon to photon ratio η, which has not varied since just seconds after the big bang, significantly affects the power spectrum of the CMB [22]. This method gives $\eta = 6.1 \times 10^{-10}$, in good agreement with the BBN method.

Both of these results tell us that before the universe hit the hadronization temperature at 150 MeV just tens of microseconds after the big bang, the universe had approximately one billion plus one baryons for every billion antibaryons. But where did the extra baryons come from? If matter can only be created in ways that preserve baryon number, as described in Subsection 1.1.3, this would be impossible.

In 1967 Andrei Sakhorov[17] studied this problem and realized that there are three criteria that

[17]Not only did Sakhorov divine the three necessary conditions for a matter dominated universe, he came up with the idea of a tokamak, the main experimental apparatus of modern nuclear physics. He did not win the Nobel prize in physics for either of these achievements, but he did win the Nobel peace prize in 1975 for his activisim against

a theory of particle physics must meet in order to have a positive baryon to photon ratio η [24]:

(1) Baryon number violation. Since at the big bang the universe began with a baryon number $B = N_B - N_{\overline{B}} = 0 - 0 = 0$ and there is a positive baryon number now, there must be a process that changes baryon number.

(2) C- and CP-symmetry violation. If C is a good symmetry of nature, then baryon number increasing interactions would be just as likely as baryon number decreasing interactions and the total baryon number would remain zero. If C-symmetry was violated but CP-symmetry was conserved, then interaction which produces right (left) handed baryons and left (right) handed antibaryons would be preferred, but the total baryon number would still remain zero [22].[18]

(3) Deviation from thermal equilibrium. If the universe was in thermal equilibrium when the baryon number violating interactions took place, then by definition the average baryon number of the universe would not change.

So we live in a universe dominated by matter and Sakhorov has listed requirements of particle physics for that to be the case. We have a theory of particle physics called the Standard Model, which was loosely explained in Subsection 1.1.3. Does the Standard Model meet those requirements?

The Standard Model includes the non-perturbative[19] sphaleron processes that violate baryon and lepton number simultaneously, so it checks off the first box [22].[20] As we saw before, the weak force violates C-symmetry because all neutrinos are left-handed while all antineutrinos are right-

nuclear proliferation and advocacy for human rights more broadly. Check out his wikipedia page, it's a good read.

[18] Note that there is no analogous requirement for CT or CPT-symmetry violation since the universe only runs forwards in time and therefore whether or not these interactions are T-odd is irrelevant.

[19] "Non-perturbative" interactions cannot be explained via Feynman diagrams, and they are far too complicated for me to explain in Subsection 1.1.3.

[20] One of the recent papers which claim that the strong force cannot violate CP-symmetry also claims that sphaleron processes do not occur [19], so it is possible that the Standard Model does not satisfy the first criterion.

handed. It also violates CP-symmetry when talking specifically about quark mixing (assuming the CPT theorem holds), so the Standard Model meets the second criterion. The third requirement is met as the universe was not in thermal equilibrium during its first few microseconds as it was rapidly cooling and expanding [22].

So can the Standard Model explain the baryon to photon ratio $\eta = 6.1 \times 10^{-10}$? Despite including processes that meet Sakhorov's three requirements, the answer is a resounding no. The SM can only generate η on the order of 10^{-20}, falling a full 10 orders of magnitude short of what astronomers observe [22]. There are different ways the SM could be modified in order to bridge this gap, but doing so requires much more CP-violation than is included in the SM [22].

The fact that the Standard Model cannot explain the BAU is just one of its most glaring problems. Others include that it cannot explain gravity, it seems to omit most of the matter holding together galaxies (dark matter) and it cannot account for the accelerating expansion of the universe (dark energy) [5]. But we should stay on topic. Because the Standard Model does not contain enough CP-symmetry violation in order to explain the observed baryon asymmetry, we should be able to find evidence of more CP-violating interactions than the Standard Model predicts [17]. There are many new theories which predict the existence of more particles and/or interactions in order to account for the deficiencies of the Standard Model, called Beyond the Standard Model (BSM) theories [17]. The goal of our experiment at JILA is to search for CP-violation that is not predicted by the SM in order to test these proposed BSM theories which can explain why there is matter left over after the universe-scale particle annihilation which shortly followed the big bang.

As a two paragraph aside, I will now address the possibility that the universe produced an equal number of baryons and antibaryons in the first tens of microseconds after the big bang. This hypothetically could have happened if the big bang separated the universe into different spatial

domains, some filled with matter and others filled with antimatter.[21] If this were the case, the domain of matter we live in would have to be at least the size of the observable universe. If our domain was smaller than the observable universe astronomers would be able to see the domain walls, the two dimensional planes where matter and antimatter meet. These domain walls would be the location of many annihilation events which produce gamma rays (high energy photons) that would be easy for astronomers to spot.

So if there are domains of matter and antimatter in the universe, the observable universe must exist entirely inside a matter dominated domain. The hypothesis that the universe is split into domains is therefore untestable, we cannot rule it out. In this case Sakhorov's conditions would be relaxed – we no longer need baryon number violation (since there is as much matter as antimatter). But we would still need plenty of CP-violation [19], so additional CP-violation beyond what is predicted in the Standard Model is well motivated even if this untestable theory is correct.

1.3 The Electron's Electric Dipole Moment

Our experiment searches for BSM CP-violating interactions by measuring the electron's electric dipole moment. We think this is a sensible observable to measure for a few reasons. 1) A nonzero eEDM would violate T-symmetry (and therefore CP-symmetry by the CPT theorem). 2) The Standard Model predicts that the eEDM is almost negligibly small, so any nonzero measurement can be attributed to BSM physics. And 3) BSM theories which predict new instances of CP-violation in order to explain the BAU generally induce an eEDM. In the next three subsections I will explain each of these points in turn.

[21] Another possibility, which can be relegated to a footnote, is that matter and antimatter were homogeneously spread throughout the universe but did not annihilate. This is all but ruled out by galaxy collisions, which would cause the regions of matter and antimatter in each galaxy to overlap and annihilate producing crazy amounts of high energy photons that astronomers simply do not observe [22].

1.3.1 The eEDM Violates CP-Symmetry

Strictly speaking, the electric dipole moment of the electron is a T- and P-symmetry violating effect.[22] If we accept the CPT theorem as true, then T-symmetry violation is just as good as CP-symmetry violation as far as resolving the BAU goes. For a depiction showing that a nonzero value of the eEDM would violate P- and T-symmetries, see Figure 1.9.

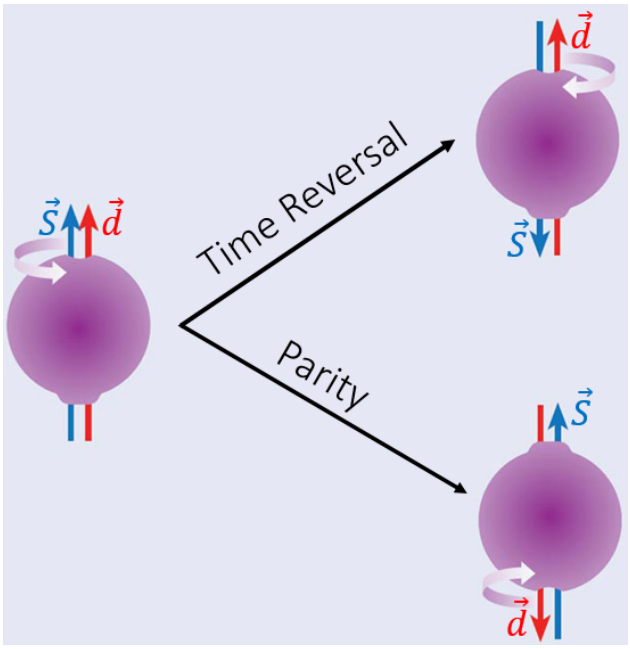

Figure 1.9: As electrons are spin-half particles, the Wigner-Eckart theorem implies that if electrons have a nonzero EDM $\vec{d}$ it must be parallel or antiparallel to its spin $\vec{S}$. Suppose that the eEDM is nonzero and $\vec{d} \parallel \vec{S}$, as shown on the left side of the figure. Its spin is indicated by the light purple arrow indicating the rotation direction, and its electric dipole moment is depicted by the lump of extra negative charge at the bottom of the electron and the cavity of charge at the top. Reversing the direction of time (top right) would cause the electron to spin in the opposite direction ($\vec{S} \xrightarrow{\mathrm{T}} -\vec{S}$) but would not change the orientation of the charge ($\vec{d} \xrightarrow{\mathrm{T}} \vec{d}$). A parity inversion (bottom right) would cause the cavity and lump of charge to swap places ($\vec{d} \xrightarrow{\mathrm{P}} -\vec{d}$) but would not change the direction of the electron's spin ($\vec{S} \xrightarrow{\mathrm{P}} \vec{S}$). In both cases, we start with parallel and end with antiparallel vectors. Because we assumed that $\vec{d} \parallel \vec{S}$ and we know that all electrons are identical, the electrons on the right side of the above image do not exist in nature. Therefore the eEDM violates T- and P-symmetries.

[22] This is true of any fundamental fermion with an EDM, not just electrons. Electrons are a convenient choice since they are stable, readily available and exist as free particles unlike quarks.

1.3.2 The eEDM is Background Free

A nonzero measurement of the eEDM would be a signal of CP-violating physics, but how do we know if it comes from the Standard Model or from something more exciting? Fortunately, the SM predicts a value for the eEDM which can be calculated precisely via Feynman diagrams.

We saw before that the electron's magnetic dipole moment is represented in Feynman diagrams where an electron interacts with a real photon as shown in Figure 1.5. Feynman diagrams where an electron interacts with a real photon that also contain interactions that violate P- and T-symmetries instead generate the electron's electric dipole moment, as the eEDM also violates these symmetries [25].

The only T- and P-violating interactions in the Standard Model are weak interactions that change quark flavor. The simplest way to include those interactions in a Feynman diagram that starts and ends with an electron is to draw the two-loop diagram shown in Figure 1.10a. Here an electron is first converted into an electron neutrino and W^- boson by the weak force. That W^- boson converts into a down-type and an antiup-type quark, which is described by a complex entry of the CKM matrix that violates T-symmetry. The quarks then recombine into a W^- boson, parameterized by the complex conjugate of the same CKM matrix element, and then the W^- boson and electron neutrino turn back into an electron. While this two-loop diagram contains interactions that violate T-symmetry, in the math of calculating the probability amplitude of this Feynman diagram we multiply the CKM matrix element by its complex conjugate, making the total amplitude real and T-symmetry conserving. So this Feynman diagram does not induce an eEDM. Note that the external photon in Figure 1.10a is detached because it can interact with any of the virtual charged particles in the Feynman diagram.

In order to find the Standard Model's prediction of the eEDM, we must include more interactions. We can go to three-loop Feynman Diagrams, like the one shown in Figure 1.10b. Note that this one diagram represents many diagrams with every permutation of up- and down-type quarks

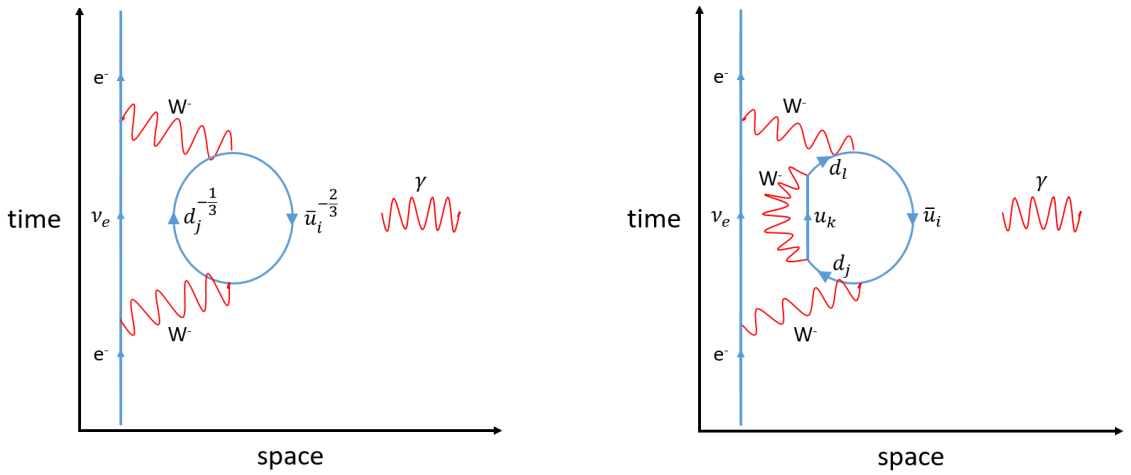

(a) Two-Loop SM Contribution to eEDM

(b) Three-Loop SM Contribution to eEDM

Figure 1.10: (a) A two-loop Feynman diagram which connects a real electron to CP violating physics in the Standard Model. $\overline{u}_i$ and d_j are any antiup-type and down-type quarks, and the external photon can couple to any of the charged virtual particles. While this Feynman diagram contains CP-violating interactions at the vertices between the W^- bosons, down- and antiup-type quarks, the overall probability amplitude is CP-symmetric as it is proportional to $V_{ij}V_{ij}^* = |V_{ij}|^2$, which is completely real. (b) A three-loop Feynman diagram that violates CP-symmetry and can induce an eEDM. However, the sum of all of the probability amplitudes from three-loop diagrams of this type is real, meaning that even at three loops the eEDM predicted by the SM is zero.

included at the four quark lines, and the external photon interacting with any of the charged particles. These diagrams now include four vertices where quarks transform into one another via the weak force, so the probability amplitude is proportional to the product of four entries of the CKM matrix. The probability amplitudes are in general complex numbers which violate T-symmetry and therefore induce an eEDM. However, it turns out when you add together all of the possible three-loop Feynman diagrams, the SM predicts an eEDM equal to zero [25].[23]

The Standard Model does predict a finite value of the eEDM at the four loop level. It turns out that the four-loop diagrams which contain even more weak interactions contribute to the eEDM (Figure 1.11a), and so do four-loop diagrams that contain a strong interaction mediated by a gluon (Figure 1.11b). These fourth order diagrams add together in a way that their probability

[23] A satisfactory explanation that the three-loop diagrams add up to zero eEDM requires a deeper dive into the math, as explained in [25].

amplitudes have an imaginary component, which results in an eEDM of 5.8×10^{-40} e cm [26].

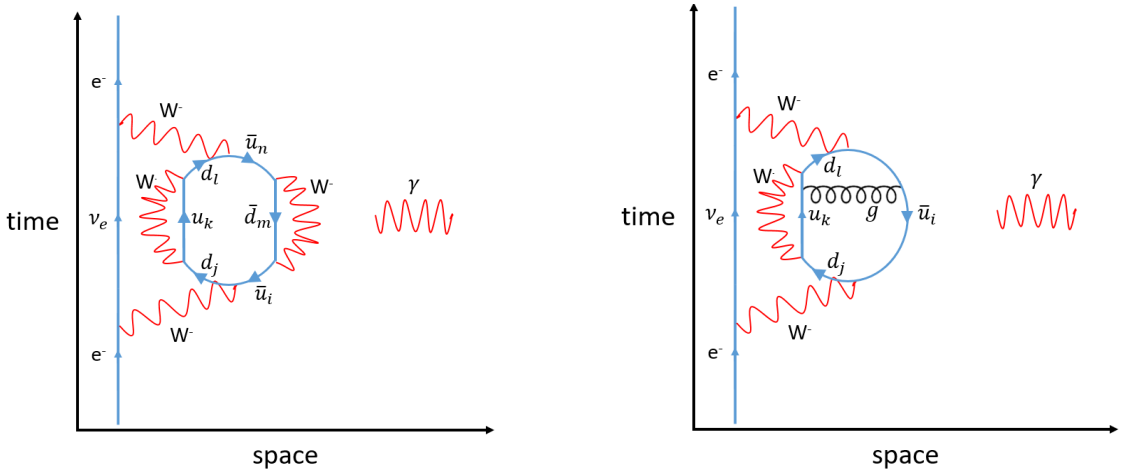

(a) SM eEDM, all weak interactions

(b) SM eEDM, one strong interaction

Figure 1.11: Four-loop Feynman diagrams that give the electron an EDM. These diagrams are the same as the one shown in Figure 1.10b with the addition of (a) a weak interaction that changes quark flavor or (b) a strong interaction between quarks.

The Standard Model predicts a nonzero value of the eEDM, but it is orders of magnitude smaller than the sensitivity of leading eEDM experiments [27, 28]. This means that if we can measure the eEDM with a smaller error bar than anyone before and we find that our measurement does not agree with zero, it can only be explained by CP-violating physics beyond the Standard Model (or, of course, a measurement error). This helps make the eEDM an appealing place to look for new CP-violating physics, but why should new CP-violating physics show up as eEDM at all?

1.3.3 The eEDM is Sensitive to BSM Physics

We saw in Subsection 1.1.3 that the strong force couples to quarks (half of the fermions), the electromagnetic force couples to charged particles (75% of the fermions) and the weak force couples to all fermions. How do we know which fermions will couple to Beyond the Standard Model interactions and therefore be the best probes of new physics? The answer is that we cannot know in advance, we can only make an intelligent guess. Many of the most popular BSM theories have CP-violating interactions that couple to the electron directly (via one-loop Feynman diagrams),

so the eEDM is a sensible place to look [17]. Supersymmetric theories are one example of a BSM theory that has CP-violating interactions which couple to the electron inducing an eEDM, shown in Figure 1.12.

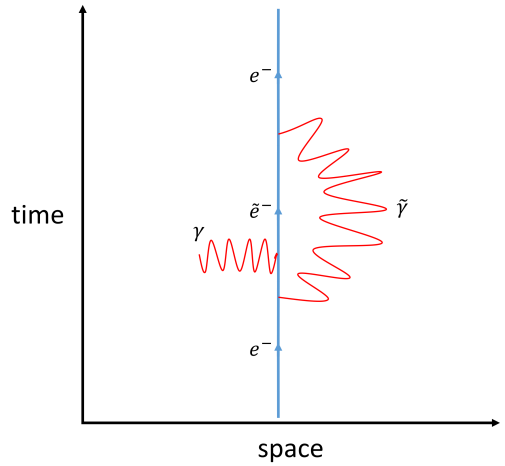

Figure 1.12: In supersymmetric BSM theories, every particle has a heavier supersymmetric partner. The electron can turn into its supersymmetric parter, the selectron $\tilde{e}^-$, by emitting a photino $\tilde{\gamma}$, the supersymmetric partner of the photon. The selectron interacts with the external electromagnetic field, giving the electron an EDM. This interaction is CP-symmetry violating.

The magnitude of the eEDM from one-loop BSM theories, like the one shown in Figure 1.12, is straightforward to calculate [29]:

$$d_e \sim \frac{ea_0\alpha}{2}\frac{g^2}{2\pi}\sin\phi_{\mathrm{CP}}\frac{m_e^2}{M^2} \tag{1.6}$$

The first fraction in the above equation gives the proper dimensions for the eEDM as ea_0 is the charge of the electron multiplied by the bohr radius. α is the fine structure constant, which is approximately $\frac{1}{137}$. This is then multiplied by $\frac{g^2}{2\pi}$, where g is the interaction strength of each electron-selectron vertex in Figure 1.12. As there are two such vertices, g^2 shows up in the magnitude of the eEDM. This is then multiplied by $\sin\phi_{\mathrm{CP}}$, a number whose magnitude is between 0 and 1, which encodes how much this interaction violates CP-symmetry. If the interaction is completely CP-symmetry violating $\sin\phi_{\mathrm{CP}} = 1$. Naively, we expect $\sin\phi_{\mathrm{CP}} \sim 1$ since the new interactions

need to be CP-symmetry violating to explain the BAU. Finally, the eEDM is multiplied by $\frac{m_e^2}{M^2}$, the ratio of the electron's mass divided by the characteristic mass of the new particles squared. The heavier the BSM particles are the smaller the eEDM will be, which makes sense as according to the Heisenburg uncertainty principle the heavier virtual particles will exist for a shorter time and have a smaller effect on the electron.

It's worth pointing out that Equation 1.6 tells us that we are at a particularly exciting time to make precise measurements of the eEDM. If we assume that $\sin\phi_{\mathrm{CP}} = 1$ and the BSM interactions are as strong as electromagnetic interactions, i.e. $g^2 = \alpha \approx \frac{1}{137}$, then we can directly relate limits of the eEDM magnitude to searches for new particles of a certain mass. The result of the experiment I describe in my thesis is that, at the 90% confidence interval, $|d_e| < 4.1 \times 10^{-30}$ e cm [27]. Plugging this relation into Equation 1.6 gives $M \gtrsim 40$ TeV/c^2.

This means that our experiment, which measured the eEDM and found a result consistent with zero, was able to rule out the existence of particles which 1) have CP-symmetry violating interactions with the electron that 2) are as strong as the electromagnetic force and 3) have a mass smaller than 40 TeV/c^2. We can compare this to the large hadron collider (LHC), the home of the world's leading high energy physics experiments, which can rule out BSM particles with masses less than about 3 TeV/c^2 [30]. This means that our eEDM measurement, which is the combined effort of orders of magnitude fewer people than work at the LHC with a much smaller budget, was able to search for a broad class of particles that are too massive to detect at the world's best particle collider. That's pretty cool.

1.4 Thesis Outline

In this introductory chapter I have explained why we expect there to exist CP-symmetry violation that is not predicted by the Standard Model and why measuring the eEDM is a good way to search for these interactions. In chapter two, I will give a succinct description of the second generation HfF^+ eEDM measurement, which has already been described in these sources [2, 27, 31].

In chapter three I will fill in the gaps of what has not been written about the second generation measurement, mostly discussing the systematic effects that I worked on. Chapter four discusses how we determined the sign of the g-factor in the $^3\Delta_1$ state of HfF^+, and chapter five is about the magnetic shielding we will need for our third generation experiment to keep known systematic effects small. I conclude my thesis in chapter six.

Chapter 2

Generation 2 Overview

"We all could have been killed - or worse, expelled. Now if you don't mind, I'm going to bed."

- J. K. Rowling, Harry Potter and the Sorcerer's Stone

The main accomplishment of my time in graduate school was my role in the second generation measurement of the eEDM at JILA [27]. In addition to writing a paper on the result, we published a lengthy document that gives a complete description of the measurement and its uncertainty [31]. Tanya Roussy, who was the senior graduate student on the project when we took the data, wrote an excellent thesis going into even more detail about the experiment [2]. As the only other graduate student who worked full time on the experiment during the years leading up to the measurement, my thesis will likely be the last document we write about the project.[1] I do not see a great value in rewriting how the experiment works in detail, so the bulk of this chapter will be a reproduction of the first half of our "Systematics" paper [31]. In Chapter 3 I will give an overview of the systematic errors in our measurement, focusing on the ones I worked on. But first, I will give my own description of how we measured the eEDM.

[1] Eric Cornell and Jun Ye presumably have better things to do at this point.

2.1 JILA eEDM Experimental Overview

A free electron with no orbital angular momentum in external electric and magnetic fields will have an energy:

$$H_e = -\vec{\mu}_s \cdot \vec{\mathcal{B}} - \vec{d}_e \cdot \vec{\mathcal{E}} = -g_s \mu_B \frac{\vec{S}}{\hbar} \cdot \vec{\mathcal{B}} - d_e \frac{\vec{S}}{\hbar} \cdot \vec{\mathcal{E}} \tag{2.1}$$

We know the electron has a magnetic dipole moment $\vec{\mu}_s$ that is antiparallel to its spin $\vec{S}$ (i.e. $g_s \approx -2 < 0$) which interacts with the magnetic field $\vec{\mathcal{B}}$ causing an energy shift. While it has not been measured, the electron may have a nonzero electric dipole moment $\vec{d}_e$, which must be parallel ($d_e > 0$) or antiparallel ($d_e < 0$) to its spin $\vec{S}$ by the Wigner-Eckart theorem [32]. In an electric field $\vec{\mathcal{E}}$ this would cause an additional, small energy shift $-\vec{d}_e \cdot \vec{\mathcal{E}}$.

A naively appealing way to measure d_e is to set $\vec{\mathcal{B}} = 0$. In this case the only energy shift is from the eEDM and we find:

$$H_e = -d_e \frac{\vec{S}}{\hbar} \cdot \vec{\mathcal{E}} = -d_e M_s \mathcal{E} \tag{2.2}$$

Here the only energy shift is caused by the eEDM interacting with $\vec{\mathcal{E}}$, so $\vec{\mathcal{E}}$ defines the quantization axis. The two states $M_s = \pm\frac{1}{2}$ are split by an energy $d_e\mathcal{E}$ which can be measured via a standard spin-flip experiment.

While this approach is straightforward, it quickly runs into a few problems. The first is that d_e is tiny; our current limit says that it would take an unreasonably large electric field of 10^{15} V/cm or more to split a free electron's spin up and down states just 1 Hz [27]. The most ambitious experiments I know of have electric fields on the order of 10^6 V/cm made from closely spaced and highly charged electrodes [33]. Even in these fields the eEDM shift would be at the nHz scale or smaller, which means the eEDM measurement needs to be quite precise. Additionally,

the large electric field poses a new problem; the field will quickly accelerate the electron out of the experimental apparatus.

Another problem is that there is no way of eliminating the magnetic field entirely. Earth's magnetic field is typically 0.5 Gauss, which would interact with the electron's magnetic moment $\mu_s = 2\mu_B/h = 2.8$ MHz/G to cause a ~ 1 MHz shift between the electron's spin up and down states. While a few orders of magnitude of magnetic shielding is achievable, the 15 orders of magnitude of shielding required to make the Zeeman effect as small as the eEDM signal are far beyond what is possible. In addition to drowning out the eEDM signal, the background field will define the quantization axis.[2] This would cause a host of problems, from reducing the magnitude of the eEDM shift to making the spin-flip experiment nearly impossible.

We can solve some of these problems by intentionally applying a small magnetic field, as shown in Figure 2.1. Per Equation 2.1, the magnetic field would define the quantization axis and cause the spin up and down states to split by 2.8 MHz/G. We could then apply an electric field parallel to the magnetic field. This would cause the energy splitting to slightly grow or shrink, depending on the sign of d_e. After measuring this energy difference in a spin-flip experiment, we could reverse the direction of the electric field and repeat the measurement. As long as the Zeeman shift is constant its magnitude will not matter – the difference between the two measurements will be $2d_e\mathcal{E}$.

This new approach solves the problem of defining the quantization axis and allows us to measure the eEDM even though its shift is small compared to the magnetic effect. However, it does not solve the problem of the electric field kicking the electron out of our apparatus. It also introduces the requirement that the noise in the magnetic field $\delta\mathcal{B}$ is small enough such that $g_s\mu_B\delta\mathcal{B} < \delta d_e\mathcal{E}$, where δd_e is the desired precision of the eEDM measurement.

[2]When one field causes a much larger energy shift than the other, the quantization axis is defined by the field which causes the larger energy shift.

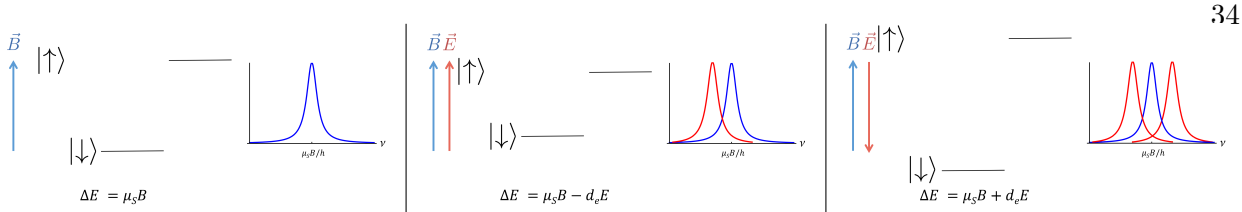

(a) Spin up and down states in a magnetic field

(b) Parallel magnetic and electric fields

(c) Antiparallel magnetic and electric fields

Figure 2.1: A simplified eEDM measurement protocol. In each subfigure the spin up $|\uparrow\rangle$ and down $|\downarrow\rangle$ states are split in a magnetic field, where the vertical axis represents energy. (a) The states are split in energy by a magnetic field. To the right there is an inset that shows the frequency $\nu = \Delta E/h$ which drives the spin flip. (b) The states are split by parallel electric and magnetic fields. For this figure we assume that d_e is positive, meaning the splitting between the spin up and down states decreases. This is shown by the red frequency trace in the inset while the blue trace shows the frequency from (a). (c) The states are split by antiparallel electric and magnetic fields causing the energy difference to increase. The value of $d_e\mathcal{E}$ can be found by taking the difference of energies measured in (b) and (c). Image adapted from [2].

Our experiment at JILA solves these problems with a method first suggested by Dave DeMille [34]; we measure the electron's EDM by experimenting on electrons trapped inside of a heavy polar molecule in the $^3\Delta_1$ electronic state. These molecules have two valence electrons, one of which is subject to a massive effective electric field $\mathcal{E}_{\text{eff}}$ on the order of 10 GV/cm [35] that is at least four orders of magnitude larger than fields we can generate in labs. Our molecule of choice is HfF^+ which has an effective electric field of + 23 GV/cm [36]. Even though one of the valence electrons is subject to a substantial effective electric field it is trapped inside the molecule and does not fly out of our experiment. Additionally, the magnetic sensitivity of HfF^+ in the $^3\Delta_1$ electronic state is about three orders of magnitude smaller than a free electron [31]. This is because in a $^3\Delta_1$ electronic state, the two valence electrons' spins are oriented in the opposite direction of two units of orbital angular momentum, largely cancelling out the molecule's magnetic dipole moment.[3]

The upshot of using a heavy polar molecule in a $^3\Delta_1$ electronic state is that the eEDM signal might be as large as 10 μHz (four orders of magnitude larger than it can be from a lab electric field) while the magnetic sensitivity is on the order of 1 kHz/G (three orders of magnitude smaller

[3]See Chapter 4 for a further discussion of this point.

than that of a free electron). This still implies that we need to control the magnetic field noise to 10 nG, a daunting task but one that is seven orders of magnitude less challenging than if we did our experiment with a bare electron.

Fortunately, $^3\Delta_1$ molecules have another trick up their sleeve. Their more complicated structure, which is explained fully in Chapter 2 of Will Cairncross's thesis [1], contains two pairs of states called omega doublets, shown in Figure 2.2. These states have nearly the same g-factors, different by only a part in 465(1) in HfF^+, but the opposite sign shift due to the eEDM [31]. Glossing over a few important details that will be addressed in Chapter 3, this means we can read out the eEDM shift by subtracting the energy difference within the upper doublet from the energy difference in the lower doublet. The crucial benefit this provides is that by measuring the upper and lower energy differences simultaneously the magnetic field noise applies to both doublets and is naturally cancelled.

This point about noise cancellation is important, so it is worth explaining how we implemented it in our experiment. We prepared a population of HfF^+ molecules, half of which were in the upper doublet of the $^3\Delta_1$ electronic state and half in the lower doublet. These molecules were held in an ion trap and overlapped spatially and temporally. They therefore experienced the same magnetic field which caused Zeeman shifts in both doublets as shown in Figure 2.2.[4] Any noise in the magnetic field would change the magnitude of the Zeeman shifts in both the upper and lower doublets simultaneously. Except for the slight difference in g-factors which we account for in [31], this noise cancels when we find $d_e\mathcal{E}_{\text{eff}} \propto \Delta E_{\text{upper}} - \Delta E_{\text{lower}}$. Simultaneously measuring the energy differences of both doublets to eliminate magnetic field noise has been incredibly useful.

We have one final scheme to reduce our sensitivity to magnetic fields. In addition to doing our experiment in a $^3\Delta_1$ state that has reduced magnetic sensitivity and doublets with similar g-factors

[4]This is true if we assume the molecules are in the exact same time and place. This is true to a very good approximation, though we have a systematic error associated with this discussed in [31].

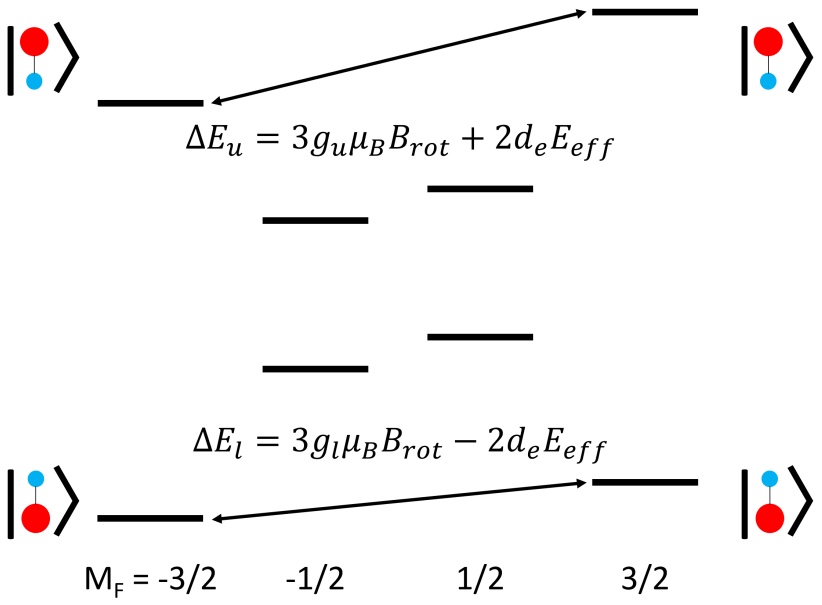

Figure 2.2: Energy levels in the $^3\Delta_1 v = 0, J = 1, F = \frac{3}{2}$ state of HfF^+ where we perform the eEDM measurement. The eight states indicated by the black horizontal lines are in the presence of an electric field ~ 60 V/cm and magnetic field ~ 10 mG. The vertical axis denotes energy and is not to scale. We call the top two states the upper doublet and the lower two states the lower doublet. The doublets are oriented the opposite direction and are split by a Stark splitting of approximately 100 MHz. Each doublet is split in energy by the Zeeman shift, about 100 Hz, and the eEDM, $\lesssim 40\mu$Hz. The Zeeman shifts of the upper and lower doublet are not identical, indicated by their different g-factors g_u and g_l, though as discussed in [31] and later in this thesis they are only different by a part in 465(1). The shift due to the eEDM has the opposite sign between the two doublets. If we ignore for a moment that the Zeeman shifts are different, we can measure the eEDM by taking the difference of the energy shifts of the upper and lower doublets. Because we measure molecules in the upper and lower doublets simultaneously, magnetic field noise will affect both doublets and (to first order) not change our measurement of the eEDM. This is a good general description of our measurement, though it contains a few loopholes which are addressed in Chapter 3 of this thesis and [31].

but opposite shifts due to the eEDM, we perform our experiment in a way that is to first-order immune to uniform magnetic fields. We hold the HfF^+ molecules in a Paul trap and polarize them with a rotating electric field, as shown in Figure 2.3a. The rotating electric field $\vec{\mathcal{E}}_{\text{rot}}$ has magnitude $\mathcal{E}_{\text{rot}} = 58$ V/cm and rotates with a frequency $f_{\text{rot}} = 375$ kHz. This causes the molecules to quickly rotate in circles with radius $r_{\text{rot}} = 0.5$ mm while the molecules slowly oscillate around the center of the trap with a secular frequency $f_{\text{sec}} \sim 1$ kHz.

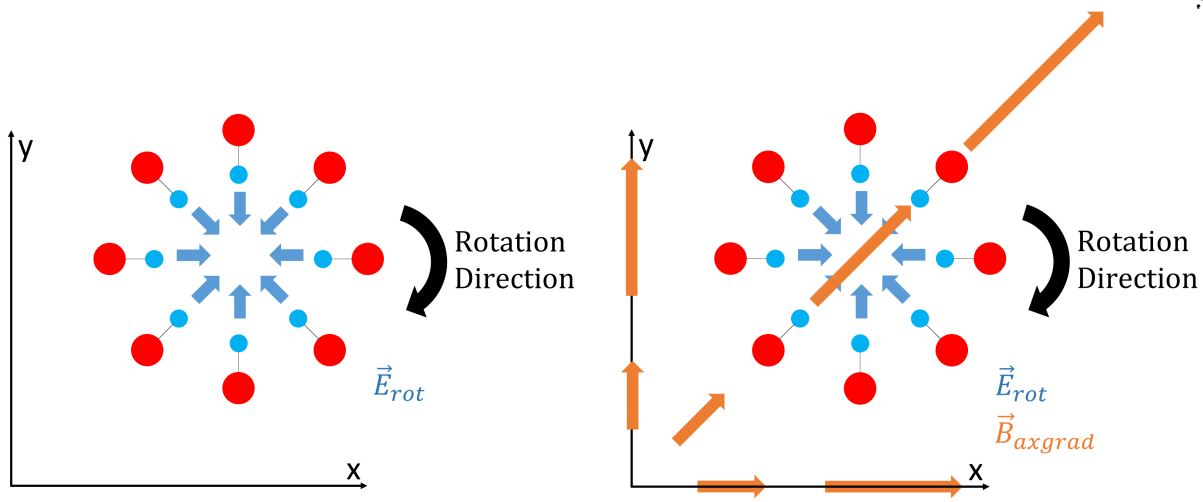

(a) HfF^+ rotating due to $\vec{\mathcal{E}}_{\text{rot}}$

(b) HfF^+ rotating due to $\vec{\mathcal{E}}_{\text{rot}}$ inside $\vec{\mathcal{B}}_{\text{axgrad}}$

Figure 2.3: (a) A HfF^+ molecule, with a red Hf nucleus and blue F nucleus, rotates in a circle with $r_{\text{rot}} = 0.5$ mm due to $\vec{\mathcal{E}}_{\text{rot}}$. We alternately take data with the molecules rotating clockwise and counterclockwise. The molecule and instantaneous direction of $\vec{\mathcal{E}}_{\text{rot}}$ is shown at eight distinct times. The molecule undergoes many such rotations while it slowly oscillates around the origin of the ion trap. (b) The molecule undergoes the same rotation in the ion trap our usual applied magnetic field $\vec{\mathcal{B}}_{\text{axgrad}} = \mathcal{B}_{\text{axgrad}}(2\vec{z} - \vec{x} - \vec{y})$. This figure is drawn with $\mathcal{B}_{\text{axgrad}} < 0$, though note that we alternately take data with $\mathcal{B}_{\text{axgrad}} < 0$ and $\mathcal{B}_{\text{axgrad}} > 0$.

The quantization axis of our experiment is defined by $\vec{\mathcal{E}}_{\text{rot}}$ as it causes the largest energy shift to our $^3\Delta_1$ state of ~ 100 MHz. This rotating quantization axis, as shown in Figure 2.3a, points in every direction in the xy-plane over a period $T_{rot} = 1/f_{\text{rot}}$. Therefore any uniform magnetic fields in the xy-plane average to zero in the direction of the quantization axis and do not cause any Zeeman shifts.[5] Uniform magnetic fields along the z-axis never point along $\vec{\mathcal{E}}_{\text{rot}}$ so they cannot cause any diagonal shifts, though they can cause off-diagonal couplings. These off-diagonal effects are considered in Section 3.1, and the systematic effects they cause are manageably small.

In order to intentionally apply the small Zeeman shift necessary for our experiment, we apply a magnetic field gradient $\vec{\mathcal{B}}_{\text{axgrad}} = \mathcal{B}_{\text{axgrad}}(2\vec{z} - \vec{x} - \vec{y})$. Figure 2.3b shows a molecule rotating through this magnetic field. This results in an average magnetic field $\vec{\mathcal{B}}_{\text{rot}}$ along the quantization

[5] Systematic effects due to static magnetic fields will be discussed in Chapter 3 and are examined in [31]. These effects will be important for our third generation experiment, which will be discussed in Chapter 5.

axis, as described in Figure 2.4. How this works is, in my opinion, one of the more clever aspects of the JILA EDM experiment.

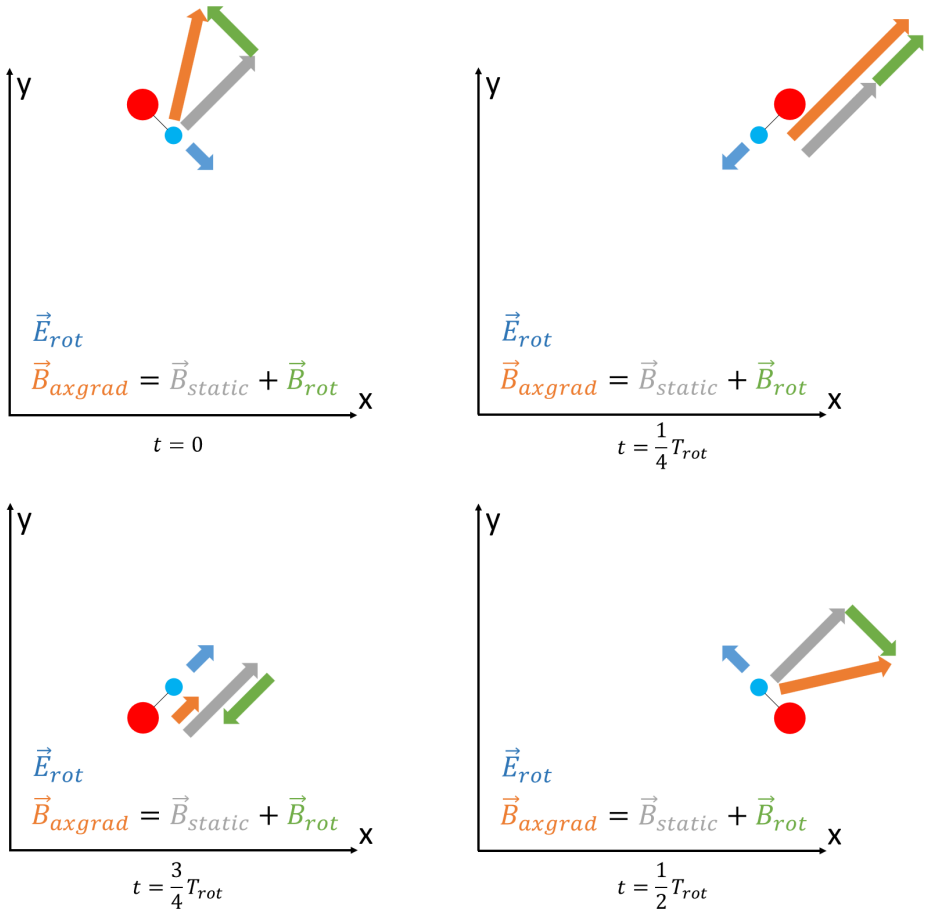

Figure 2.4: A molecule rotating due to $\vec{\mathcal{E}}_{\mathrm{rot}}$ in a magnetic field $\vec{\mathcal{B}}_{\mathrm{axgrad}}$ at four different time steps of the rotation period $T_{\mathrm{rot}} = 1/f_{\mathrm{rot}}$. Just as is shown in Figure 2.3b, the magnetic field at the location of the ion varies in direction and magnitude as the ion rotates. The total magnetic field $\vec{\mathcal{B}}_{\mathrm{axgrad}}$ can always be expressed as a sum of $\vec{\mathcal{B}}_{\mathrm{static}}$, which does not change in magnitude or direction, and $\vec{\mathcal{B}}_{\mathrm{rot}}$, which is constant in magnitude but always antiparallel to $\vec{\mathcal{E}}_{\mathrm{rot}}$. For the opposite sign of $\mathcal{B}_{\mathrm{axgrad}}$, $\vec{\mathcal{B}}_{\mathrm{rot}}$ is always parallel to $\vec{\mathcal{E}}_{\mathrm{rot}}$. The magnetic fields cause a Zeeman shift if they have a nonzero average projection along the quantization axis defined by $\vec{\mathcal{E}}_{\mathrm{rot}}$. $\vec{\mathcal{B}}_{\mathrm{static}}$ does not cause a Zeeman shift as it is parallel as often as antiparallel to $\vec{\mathcal{E}}_{\mathrm{rot}}$, but $\vec{\mathcal{B}}_{\mathrm{rot}}$ does cause a Zeeman shift.

So far I have discussed why the naturally large Zeeman shift makes it very difficult to measure a nonzero eEDM. We employ three main strategies at JILA to make our experiment possible: 1) the use of a $^3\Delta_1$ molecule with a large $\mathcal{E}_{\mathrm{eff}}$ and small g-factor, 2) the simultaneous measurement of the upper and lower doublets which have very similar g-factors but opposite sensitivities to the eEDM,

and 3) the use of a rotating quantization axis that averages out uniform magnetic fields. The first strategy is not unique to our experiment, the ACME collaboration has a comparable limit on the eEDM and uses the $^3\Delta_1$ state of the ThO molecule [28]. While ACME does not measure their doublets simultaneously, they rapidly switch back and forth between the two doublets. However, we are the only eEDM experiment that currently takes advantage of the rotating quantization axis. It is not a coincidence that we are the only recently published result without any magnetic shielding.[6] Systematic shifts due to magnetic effects are a leading error for EDM measurements and are a serious candidate for what could limit progress in the field. All three of these advantages may be key in advancing the precision of EDM measurements.

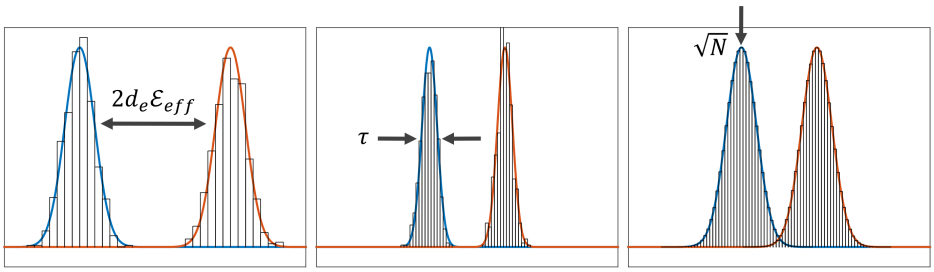

Figure 2.5: The x-axis is energy and the y-axis is number of measurements in an EDM experiment. The orange and blue curves represent data from two datasets where Energy = Zeeman shift $\pm$ EDM shift. The three graphs represent the key ingredients to statistical sensitivity of an EDM experiment. Left: the splitting between the two datasets increases with a larger $\mathcal{E}_{\text{eff}}$. Center: the width of each dataset shrinks with the coherence time τ. Right: The center of each dataset can be found more reliably with more data points and increases with $\sqrt{N}$. An ideal EDM experiment has large $\mathcal{E}_{\text{eff}}$, τ and $\sqrt{N}$.

In addition to making sure that the Zeeman shift or other systematic effects do not overwhelm the eEDM shift, we want the measurement to be as precise as possible. As discussed above, we find the eEDM by measuring the energy difference of the upper and lower doublets and then taking the difference of those measurements. As we see in Figure 2.5, the central values of those doublet measurements will be farther apart in the presence of a larger $\mathcal{E}_{\text{eff}}$. The distributions of our measurements will be narrower for data taken with a longer coherence time τ, and we will be

[6] We will need shielding for our next generation measurement, see Chapter 5. However, our shielding requirements will still be quite relaxed compared to competing experiments.

able to find the center of each distribution as we take more data points $\sqrt{N}$ [17]. All together, we find that the statistical uncertainty of the measurement is given by:

$$\delta d_e \sim \frac{\hbar}{|\mathcal{E}_{\text{eff}}|\tau\sqrt{N}} \tag{2.3}$$

As discussed earlier, we have chosen a $^3\Delta_1$ molecule with a large $\mathcal{E}_{\text{eff}} = 23$ GV/cm. A key advantage of our experiment is that we can hold our HfF^+ molecules in an ion trap for arbitrarily long times. Unfortunately the $^3\Delta_1$ electronic state of HfF^+ is metastable with a finite lifetime of about two seconds, limiting our coherence time $\tau \approx 3$ seconds at most.[7] This is still orders of magnitude longer coherence time than competing experiments like ACME which can only make their measurements over a few milliseconds [28]. We perform our experiment on as many HfF^+ molecules at a time as we can, which is typically a few hundred ions in each omega doublet. All together this gave us a good enough statistical sensitivity to make the most precise measurement of the eEDM to date [27].

2.2 How the JILA Generation Two eEDM Experiment Works

Hopefully the previous section sufficiently introduced how to measure the eEDM in general and our approach at JILA. Now I will give an explanation of how the experiment works in detail. Because this was already written up in Tanya Roussy's thesis and our "Systematics" paper, which was written by Luke Caldwell, Tanya Roussy and myself, there's not a great need for a third independent write up [2, 31]. Below is the explanation of our experiment from the Systematics paper, edited just a bit to fit smoothly into this thesis.

Table 2.1: Spectroscopic constants for $^3\Delta_1$ state of HfF^+ used throughout this document.

Constant	Value	Description	Reference
B_e/h	8.983(1) GHz	Rotational constant	[37]
$A_\parallel/h$	−62.0(2) MHz	Hyperfine constant	[38]
d_{mf}/h	1.97(1) MHz V^{-1} cm	Molecule-frame electric dipole moment	[39, 40]
$\omega_{ef}/(2\pi)$	0.74(4) MHz	Ω-doubling constant	[37]
g_N	5.257 74(2)	Nuclear magnetic g-factor of ^{19}F	[41]
$G_\parallel$	−0.0122(3)	Effective electronic g-factor	[39]
g_F	−0.0031(1)	$F = 3/2$ state g-factor	[39]
$\lvert\mathcal{E}_{\mathrm{eff}}\rvert/h$	5.5×10^{24} Hz e^{-1} cm^{-1}	Effective electric field	[42, 43]

The effective electronic g-factor given here is inferred from the measured g_F, $G_\parallel \equiv 3g_F - g_N\mu_N/\mu_{\mathrm{B}}$, and suited to calculations including only states in $^3\Delta_1$. A slightly smaller $G_\parallel$ must be used when considering the effects of interactions with other electronic states [40, 44].

Table 2.2: Example experimental parameters and associated derived parameters from our 2022 data.

Parameter	Value	Description
$\mathcal{E}_{\mathrm{rot}}$	58 V cm^{-1}	Magnitude of rotating electric field during free evolution
$\mathcal{E}_{\mathrm{rot}}^{\pi/2}$	7 V cm^{-1}	Magnitude of rotating electric field during $\pi/2$ pulses
ω_{rot}	$2\pi \times 375$ kHz	Angular frequency of $\mathcal{E}_{\mathrm{rot}}$
$\mathcal{B}_{\mathrm{rot}}$	10 mG (typ.)	Effective rotating magnetic field
$\mathcal{B}_{2,0}^{\mathrm{rev}}$	200 mG cm^{-1} (typ.)	Applied magnetic quadrupole gradient
r_{rot}	0.5 mm	Radius of ion circular motion
$\frac{\delta g_F}{g_F}$	−0.002 146(2)	Stark doublet-odd magnetic g-factor ratio (see Figure 3.2)
Δ^0	~ 0.6 Hz	Rotation induced m_F coupling
Δ^D	~ -0.9 Hz	Doublet-odd correction to Δ
V_{RF}	23.5 V	RF radial confinement voltage during free evolution
$\mathcal{E}_{\mathrm{RF}}$	0.5 V cm^{-1}	RF electric field amplitude at typical ion during free evolution
ω_{RF}	$2\pi \times 50$ kHz	Radial-confinement RF frequency
V_{DC}	3.7 V	DC axial confinement voltage during free evolution
$\mathcal{E}_{\mathrm{DC}}$	10 mV cm^{-1}	DC axial confinement electric field at typical ion
ω_x	$2\pi \times 0.95$ kHz	x secular frequency during free evolution
ω_y	$2\pi \times 1.51$ kHz	y secular frequency during free evolution
ω_z	$2\pi \times 1.60$ kHz	z secular frequency during free evolution

In the Systematics paper we report $\Delta \sim 1.0$ Hz and $\Delta^D \sim -0.6$ Hz. Recent numerical simulations by Anzhou Wang indicate that we incorrectly swapped the magnitudes of these two values. Fortunately, as each term has a magnitude of ~ 1 Hz, this does not effect the analysis of our experiment.

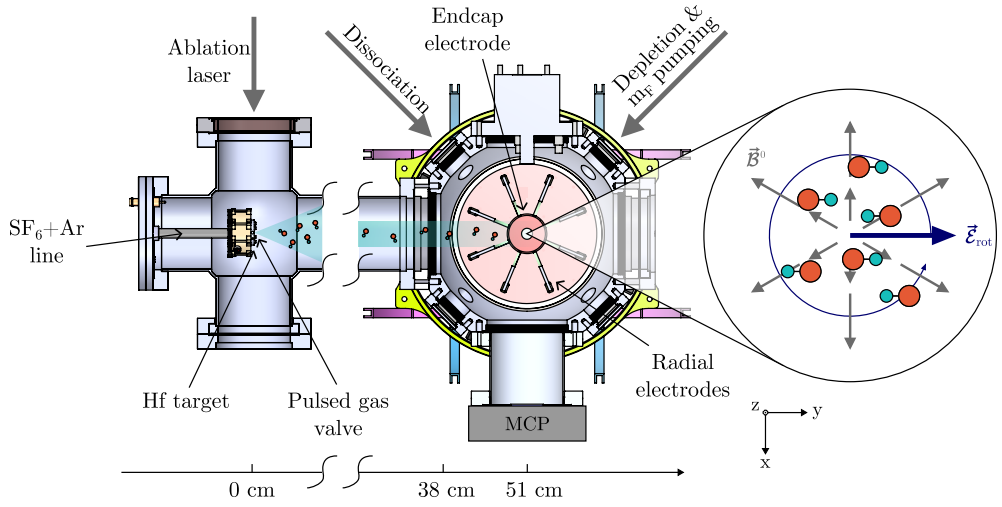

Figure 2.6: Schematic of experimental apparatus. On the left is the source chamber, where we produce neutral molecules. On the right is the main experimental chamber, containing the ion trap. The two chambers are connected by a differential pumping chamber with two small apertures at either end. The endcap electrodes of the ion trap have a hole in the center to allow optical access along the z direction (vertical in the lab). Inset shows fields applied during experimental sequence: the rotating electric bias field $\vec{\mathcal{E}}_{\rm rot}$, and the quadrupole magnetic field $\vec{\mathcal{B}}^0$. The molecular axis of each of the ions is either aligned or anti-aligned with $\vec{\mathcal{E}}_{\rm rot}$.

2.2.1 Experiment

Our experiment uses HfF^+ ions, confined in an ion trap and prepared in the metastable $^3\Delta_1$ state. Relevant molecular properties are given in Table 2.1. In the $^3\Delta_1$ state, one of the valence electrons is subject to a large intramolecular effective electric field $\mathcal{E}_{\rm eff} = 23\,\mathrm{GV\,cm^{-1}}$ [45], along the internuclear axis of the molecule. We orient this molecular axis in the lab frame by applying an external electric field which rotates to maintain confinement of the ions. We then prepare the electron spin of the molecule in a coherent superposition of states, corresponding to the spin of the eEDM-sensitive electron oriented either parallel or antiparallel to $\mathcal{E}_{\rm eff}$, and measure the energy difference between them using Ramsey spectroscopy. The eEDM will give a contribution to this energy proportional to $d_e\mathcal{E}_{\rm eff}$. To reject other unwanted contributions, we perform this measurement simultaneously on two spatially overlapping clouds of ions with their molecular axes aligned and

[7] In our third generation experiment we will switch to ThF^+ molecules where $^3\Delta_1$ is the ground electronic state, hopefully allowing us to increase the coherence time τ to 20 seconds.

anti-aligned with the externally applied field. The difference between the measured energies in each case is our science signal.

This section describes the apparatus and each of the steps used in state preparation and measurement of the ions. A summary of typical experimental parameters is given in Table 2.2.

2.2.1.1 Lasers

The experiment uses a total of 9 lasers; 5 pulsed lasers used for ablation, ionization, and photodissociation, and 4 CW lasers—which we denote $\mathcal{L}_{\text{trans}}^{961}$, $\mathcal{L}_{\text{vc}}^{818}$, $\mathcal{L}_{\text{op}}^{1082}$, $\mathcal{L}_{\text{depl}}^{814}$—used for state-preparation and readout. A summary is given in Table 2.3 and Fig. 2.7, and each is described in detail in the following sections. All lasers are locked to wavemeters using simple, $\sim 1\,\text{Hz}$ servo loops. The CW lasers are locked to within $\sim \pm 30\,\text{MHz}$, and the pulsed lasers to $\sim \pm 500\,\text{MHz}$.

2.2.1.2 Molecular beam and ionization

Our experiment begins with a pulsed beam of neutral molecules. We use a pulsed Nd:YAG laser to ablate a solid Hf rod into a pulsed supersonic expansion of Ar, seeded with 1% SF_6. Chemical reactions between the Hf plasma and the SF_6 produce neutral HfF which are entrained in the supersonic expansion and rovibrationally cooled by collisions with the Ar atoms to a temperature of $\sim 10\,\text{K}$. When they arrive in our main chamber, ~ 50 cm away, a pair of pulsed UV lasers at 309 nm and 368 nm excite a two-photon transition to a Rydberg state 54 cm^{-1} above the ionization threshold, from which they autoionize [39, 46]. The molecular ions are created in the first few rotational levels of $^1\Sigma^+(v = 0)$, the electronic and vibrational ground state of the molecule. The ions are stopped at the center of our RF ion trap by pulsed voltages on the radial trap electrodes, after which the confining potentials are immediately turned on. We typically trap $\sim 2 \times 10^4$ HfF^+ ions with a lifetime[8] of $\sim 5\,\text{s}$. The trap is described in detail in the next section.

[8] We note that the trap lifetime is limited by slow heating of the ions and is strongly dependent on the trapping parameters. The 5 s here is for the very shallow trap used during the Ramsey interrogation time.

Table 2.3: Photons used in our experimental sequence. All lasers address $v = 0$ state of ground and excited levels, except $\mathcal{L}_{\text{vc}}^{818}$ which addresses $v = 1$. $\mathcal{L}_{\text{trans}}^{961}$ and $\mathcal{L}_{\text{vc}}^{818}$ propagate along the trap z axis, all other lasers propagate in the x-y plane.

Name	Symbol	Transition	Power/Energy	λ (nm)	Polarization	Pulse Width
Ablation		–	10 mJ	532	linear	10 ns
Photoionization 1		$\Omega = 3/2 \leftarrow X^2\Delta_{3/2}$	30 µJ	309.388	linear	10 ns
Photoionization 2		Rydberg $\leftarrow \Omega = 3/2$	1.3 mJ	367.732	linear	10 ns
Transfer	$\mathcal{L}_{\text{trans}}^{961}$	$P(1)\ ^3\Pi_{0^+} \leftarrow X^1\Sigma^+$	600 mW	961.43495	linear	CW
m_F Pumping	$\mathcal{L}_{\text{op}}^{1082}$	$P(1)\ ^3\Pi_{0^-} \leftarrow\ ^3\Delta_1$	21 mW	1082.4137	circular	CW, strobed
m_F Depletion	$\mathcal{L}_{\text{depl}}^{814}$	$Q(1)^3\Sigma_{0^+}^- \leftarrow\ ^3\Delta_1$	550 mW	814.508	circular	CW, strobed
Vibrational Cleanup	$\mathcal{L}_{\text{vc}}^{818}$	$P(1)^3\Sigma_{0^+}^- \leftarrow\ ^3\Delta_1$	30 mW	818.37198	linear	CW
Dissociation 1		$\Omega = 2 \leftarrow\ ^3\Delta_1$	1.6 mJ	368.494	circular	10 ns
Dissociation 2		$? \leftarrow \Omega = 2$	25 mJ	266	circular	10 ns

2.2.1.3 Ion trap

Our linear Paul trap has 8 radial electrodes and 2 endcaps. The radial confinement is provided by driving the radial electrodes in a quadrupole configuration producing a field,

$$\vec{\mathcal{E}}_{\mathrm{RF}}(\vec{r},t) = \frac{V_{\mathrm{RF}}}{R_0^2}\cos(\omega_{\mathrm{RF}}t)(\vec{x}-\vec{y}), \tag{2.4}$$

where $\omega_{\mathrm{RF}} = 2\pi \times 50\,\mathrm{kHz}$, V_{RF} is the voltage applied on each electrode, $R_0 \sim 4.8\,\mathrm{cm}$ is the effective radius the RF trap, and $\vec{x}, \vec{y}$ are the radial position coordinates of the ions in the laboratory frame. Axial confinement is provided by DC voltages V_{DC} on a pair of endcaps, producing a field

$$\vec{\mathcal{E}}_{\mathrm{DC}}(\vec{r},t) = \frac{V_{\mathrm{DC}}}{Z_0^2}(\vec{x}+\vec{y}-2\vec{z}), \tag{2.5}$$

where $Z_0 \sim 17\,\mathrm{cm}$ is the effective height of the RF trap. We choose the values of V_{RF} and V_{DC} immediately after ionization to best match the spatial mode of the initial ion cloud, giving trap frequencies $\sim 5\,\mathrm{kHz}$ in all directions. We then linearly ramp the trapping voltages down over 10 ms to expand and cool the ion cloud. The ramp takes the trap frequencies to $\sim 2.8\,\mathrm{kHz}$ and $\sim 2.0\,\mathrm{kHz}$ in the radial and axial directions respectively.

In addition to the confinement fields, we also apply a rotating electric field $\vec{\mathcal{E}}_{\mathrm{rot}}$,

$$\vec{\mathcal{E}}_{\mathrm{rot}}(t) = \mathcal{E}_{\mathrm{rot}}\left[\hat{x}\cos(\omega_{\mathrm{rot}}t) + \tilde{R}\hat{y}\sin(\omega_{\mathrm{rot}}t)\right], \tag{2.6}$$

where $\omega_{\mathrm{rot}} = 2\pi \times 375\,\mathrm{kHz}$, $\tilde{R} = \pm 1$ indicates the rotation direction and $\mathcal{E}_{\mathrm{rot}} = |\vec{\mathcal{E}}_{\mathrm{rot}}|$ is typically $\sim 58\,\mathrm{V\,cm^{-1}}$. This field serves to orientate the molecular axis, and thus the effective electric field, of the ions and we do our spectroscopy in this rotating frame. $\vec{\mathcal{E}}_{\mathrm{rot}}$ causes an additional micromotion of the ions,

$$-\frac{e}{m\omega_{\mathrm{rot}}^2}\vec{\mathcal{E}}_{\mathrm{rot}} = -r_{\mathrm{rot}}\hat{\mathcal{E}}_{\mathrm{rot}}, \tag{2.7}$$

where $r_{\mathrm{rot}} \sim 0.5\,\mathrm{mm}$. The shape of the radial electrodes is optimized to minimize inhomogeneities in $\vec{\mathcal{E}}_{\mathrm{rot}}$ across the ion cloud [1].

2.2.1.4 Magnetic fields

Measuring the electron EDM also requires orienting the electron spin of the molecules which we do with an applied magnetic field $\vec{\mathcal{B}}^0$. In order for the unpaired electrons to experience a time-averaged interaction with the intramolecular effective electric field, this magnetic field must corotate with $\vec{\mathcal{E}}_{\rm rot}$. We achieve this using a pair of coils in anti-helmholtz configuration aligned along the axial direction, giving

$$\vec{\mathcal{B}}^0 = \tilde{B}\mathcal{B}^{\rm rev}_{2,0}(2\vec{z} - \vec{x} - \vec{y}). \tag{2.8}$$

Here $\mathcal{B}^{\rm rev}_{2,0}$ is typically $\sim 200\,\mathrm{mG\,cm^{-1}}$ and $\tilde{B} = \pm 1$ indicates the direction of the current in the coils, explained in more detail in Sec. 2.2.1.9. In the rotating and co-moving frame of the ions, this quadrupole magnetic field appears as a time-averaged magnetic bias,

$$\tilde{B}\mathcal{B}_{\rm rot} = \langle \vec{\mathcal{B}}^0 \cdot \vec{\mathcal{E}}_{\rm rot} \rangle = \tilde{B}\mathcal{B}^{\rm rev}_{2,0} r_{\rm rot}. \tag{2.9}$$

The coil pair is driven by a precision current source with 1 pA resolution, corresponding to $200\,\mathrm{fG\,cm^{-1}}$. We refer to the pair of coils that produces this field as the $\vec{\mathcal{B}}^0$-coils.

The apparatus also includes three pairs of coils setup along the lab frame $\hat{x}, \hat{y}, \hat{z}$ axes in Helmholtz configuration for tuning the magnetic field at the position of the ions. The z coil is driven by the second channel of the precision current supply used for the $\vec{\mathcal{B}}^0$-coils, the x and y coils are driven by a lower precision current supply. The magnetic field around the periphery of the trap is measured by an array of eight, 3-axis fluxgate magnetometers bolted to the outside of the main experimental chamber. We use these measurements to infer the magnetic field at the center of the trap. In contrast to other modern eEDM experiments [28, 47, 48], the apparatus includes no magnetic shielding as we are principally only sensitive to magnetic fields rotating at $\omega_{\rm rot}$, as discussed in detail in Chapter 3 of this document and Section VI A of the Systematics paper.

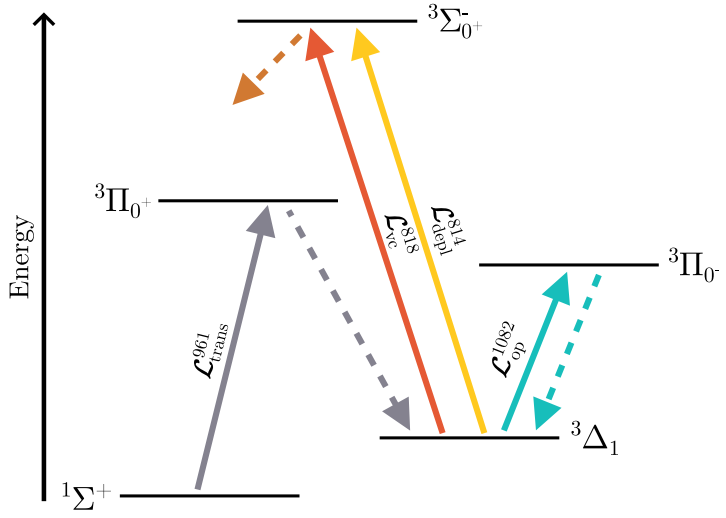

Figure 2.7: Cartoon depicting the transitions used during our state preparation. The $^3\Pi_{0^+}$ and $^3\Pi_{0^-}$ states decay preferentially to $^3\Delta_1$, while the $^3\Sigma^-_0$ state decays preferentially to $^1\Sigma^+$.

2.2.1.5 State preparation

Immediately after ionization, the HfF^+ ions are in the ground electronic and vibrational state ($^1\Sigma^+(v=0)$), primarily distributed over the lowest 4 rotational levels $J = 0$–3. We connect these rotational levels using microwaves and perform incoherent transfer to the eEDM-sensitive $^3\Delta_1(v=0, J=1)$ science state by using light from $\mathcal{L}^{961}_{\text{trans}}$ to drive the $^3\Pi_{0^+}(J=0) \leftarrow {}^1\Sigma^+$ transition, the excited state of which decays preferentially to $^3\Delta_1$. This light enters the chamber along the z-axis and is on for 80 ms beginning immediately after ionization. The decay from $^3\Pi_{0^+}$ puts population in several vibrational levels in $^3\Delta_1$, which can decay into the $v = 0$ science state if left untreated. We remove the population in higher vibrational levels by illuminating the cloud with $\mathcal{L}^{818}_{\text{vc}}$ light which connects $^3\Sigma^-_{0^+}(v=1, J=0) \leftarrow {}^3\Delta_1(v=1, J=1)$ at ~ 818 nm, preferentially decaying back to $^1\Sigma^+$. The $\mathcal{L}^{818}_{\text{vc}}$ laser also enters the chamber along the z axis and remains on for the duration of the experiment. Potential systematics associated with this light are discussed in Section VI B 2 of the Systematics paper.

After transferring the ions to the science state, we ramp on $\vec{\mathcal{E}}_{\text{rot}}$ in 5 ms. Figure 2.8 shows

the structure of the science state at $\mathcal{E}_{\mathrm{rot}} = 58\,\mathrm{V\,cm^{-1}}$. In this field, the stretched states of ${}^3\Delta_1(J = 1, F = 3/2)$ correspond to the molecule aligned or anti-aligned with the field. They form two pairs of levels—which we call the upper and lower doublet, highlighted in orange and blue respectively—with their molecular dipole, and thus $\mathcal{E}_{\mathrm{eff}}$, either aligned or anti-aligned with $\mathcal{E}_{\mathrm{rot}}$. Each doublet consists of one state with $m_F = 3/2$ and one with $m_F = -3/2$.

We polarize the molecules in the rotating frame by optically pumping them using $\mathcal{L}_{\mathrm{op}}^{1082}$ light addressing the ${}^3\Pi_{0^-}(v = 0, J = 0) \leftarrow {}^3\Delta_1(v = 0, J = 1)$ at 1082 nm. The light is circularly polarized with its k-vector in the plane of $\vec{\mathcal{E}}_{\mathrm{rot}}$. We use an AOM to strobe $\mathcal{L}_{\mathrm{op}}^{1082}$ synchronously with the rotation of $\vec{\mathcal{E}}_{\mathrm{rot}}$ on a 50% duty cycle[9] such that it drives either σ^+ or σ^- transitions to an $F' = 3/2$ manifold in the excited state. This eventually leaves population only in either the $m_F = 3/2$ or $m_F = -3/2$ states of ${}^3\Delta_1(v = 0, J = 1)$. We define the *preparation phase* of the experiment as the orientation of $\vec{\mathcal{E}}_{\mathrm{rot}}$ relative to the k-vector of the light when the light is on; *in* when $\vec{\mathcal{E}}_{\mathrm{rot}}$ is parallel, and *anti* when it is anti-parallel. This preparation phase can be changed by adjusting the timing of the strobing cycle. $\mathcal{L}_{\mathrm{op}}^{1082}$ is on for a total of 80 ms, starting 40 ms after trapping.

The final step of state preparation is applying $\mathcal{L}_{\mathrm{depl}}^{814}$ light at 814 nm. This laser is tuned to address the ${}^3\Sigma_{0^+}^-(v = 0, J = 0) \leftarrow {}^3\Delta_1(v = 0, J = 1)$, which preferentially decays to ${}^1\Sigma^+$ by a 10:1 ratio, having weaker coupling to the ${}^3\Delta_1$ state. $\mathcal{L}_{\mathrm{depl}}^{814}$ is circularly polarized with the same handedness and k-vector as $\mathcal{L}_{\mathrm{op}}^{1082}$. It is again strobed so as to only address and remove any residual population left over in other m_F states after $\mathcal{L}_{\mathrm{op}}^{1082}$ is turned off. $\mathcal{L}_{\mathrm{depl}}^{814}$ light is on for 7 ms, beginning 3 ms after $\mathcal{L}_{\mathrm{op}}^{1082}$ is turned off.

These steps leave the population in an incoherent mixture of one of the stretched states of the two doublets. The key difference from our previous measurement [38] is that the experiment

[9] We note that, although the light is on for 50% of each cycle, the micromotion-induced Doppler shifts mean it is only resonant with the ions for less than 5%.

proceeds on *both* doublets simultaneously. Our detection scheme [49], described in Sec. 2.2.1.7, allows us to read out each independently, enabling us to take advantage of common-mode noise cancellation.

2.2.1.6 Ramsey sequence

Immediately prior to the Ramsey sequence, we ramp the radial confinement of the ions down further, to trap frequencies of $\sim 1\,\mathrm{kHz}$. This reduces the density of the cloud and improves the coherence time due to mechanisms discussed in Section VI D 1 of the Systematics paper.

We apply a $\pi/2$ pulse to the ensemble of ions by temporarily ramping down the magnitude of $\vec{\mathcal{E}}_{\mathrm{rot}}$ from $\sim 58\,\mathrm{V\,cm^{-1}}$ to $\sim 7\,\mathrm{V\,cm^{-1}}$ in $16\,\mu\mathrm{s}$, holding it there for $1\,\mathrm{ms}$ and then ramping back up in a further $16\,\mu\mathrm{s}$. Reducing $\mathcal{E}_{\mathrm{rot}}$ increases a rotation-induced coupling between $m_F = \pm 3/2$ states in a doublet (see Sec. 2.2.3), causing the pure spin states in each doublet to evolve into a coherent superposition. We allow this superposition to evolve for a variable amount of time t_R—up to $3\,\mathrm{s}$—and then apply a second $\pi/2$ pulse to map the relative phase onto a population difference between the two states in a doublet.

2.2.1.7 Measurement

We project the ions into their final state by applying $\mathcal{L}^{814}_{\mathrm{depl}}$ again to remove population from one of the stretched states in each doublet. The *readout phase* is defined in the same way as the *preparation phase*; *in* for $\vec{\mathcal{E}}_{\mathrm{rot}}$ is parallel with the k-vector of the light when it is on and *anti* for antiparallel.

Finally, we detect and count the number of ions in the remaining stretched states via resonance-enhanced multiphoton dissociation [50], driven by two pulsed UV lasers at 368 nm and 266 nm. Immediately prior to the dissociation pulse, we ramp up both radial and axial confinement to compress the cloud and improve the dissociation efficiency. The dissociation pulse is timed so that $\vec{\mathcal{E}}_{\mathrm{rot}}$ is along $\tilde{I}\hat{y}$, parallel to the plane of a microchannel plate (MCP) and phosphor screen as-

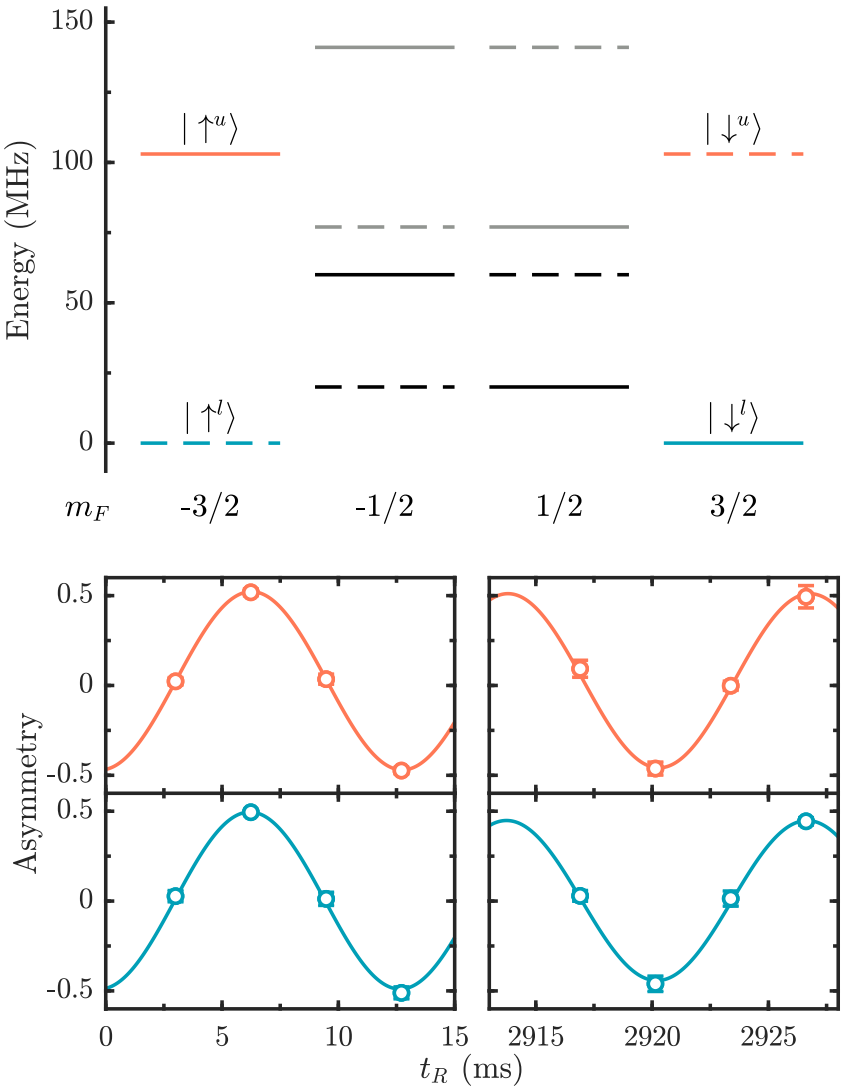

Figure 2.8: Ramsey spectroscopy in HfF^+. Top: level structure of the eEDM-sensitive $^3\Delta_1(v = 0, J = 1)$ manifold in external electric $\mathcal{E}_{\rm rot} \sim 58\,\mathrm{V\,cm^{-1}}$. Solid (dashed) lines correspond to states with $\Omega = +1(-1)$. Gray lines correspond to states which asymptote to $F = 1/2$ at zero field, all other states asymptote to $F = 3/2$. The upper (orange) and lower (blue) doublets used for the measurement, corresponding to $\mathcal{E}_{\rm eff}$ aligned and anti-aligned with the externally applied field respectively, are separated by $\sim 100\,\mathrm{MHz}$. The two states in each doublet are further split by the Zeeman energy, not resolvable on this scale, and interaction of the eEDM with $\mathcal{E}_{\rm eff}$. Bottom: example Ramsey fringes from our dataset. The fringes from the two doublets are collected simultaneously.

sembly. Here $\tilde{I} = \pm 1$ and $\hat{y}$ is defined by Fig. 2.6. Because the dissociation lasers enter at an angle to $\hat{y}$, there is considerable Doppler shift from the micromotion of the ions at 45° to the k-vector of

the light. To account for this we adjust the frequency of the 368 nm light by $\sim \pm 2$ GHz depending on the product $\tilde{R}\tilde{I}$ which gives the sign of the Doppler shift.

Each of the lasers is circularly polarized to drive transitions which preserve the orientation of the molecules during dissociation [1]. In this way the resultant Hf^+ ions from each doublet are ejected in opposite directions. The handedness of the dissociation lasers $\tilde{P}$ is determined by a $\lambda/2$ waveplate which can be moved into or out of the beam path on a motorized mount. Immediately after dissociation, we turn off the RF confinement and apply pulsed voltage on the radial electrodes to kick the ions towards the MCP. The Hf^+ ions from each doublet are imaged on opposite sides of the phosphor screen; the side each doublet is imaged on is set by the value of $\tilde{I}$. We time-gate the phosphor screen such that we only image the dissociated Hf^+ and not any remaining HfF^+ ions. We detect both Hf^+ and HfF^+ ions in time of flight. Technical details of our imaging and counting system are described in [49, 51].

Of the $\sim 2 \times 10^4$ trapped HfF^+ ions, we typically detect ~ 550 Hf^+ ions on each side of the screen at early time (~ 1100 total), and ~ 120 (~ 240 total) after $t_R \sim 3$ s. The latter is principally limited by the finite lifetime of the $^3\Delta_1$ state but with a contribution from ions being heated out of our shallow trapping potential during t_R.

2.2.1.8 Noise

Instability of the intensity of the pulsed lasers used for ablation, ionization and photodissociation means that the fluctuations in the number of Hf^+ ions detected at the end of each shot are $\sim 30\%$, roughly $3\times$ the quantum projection noise limit for 120 ions. However these sources of noise, and many others, are common mode; the exact same laser pulses address the ions which end up in the upper and lower doublets. If we measure the ion number when the Ramsey oscillations of the two doublets are close to in phase with one another then we can take advantage of excellent noise cancellation in the number difference [49] which we use to extract our science signal (see Sec 2.2.2). The two doublets oscillate at slightly different frequencies owing to a part in 230

difference in their magnetic moments and so we deliberately take our data at a *beat*; our early-time data is taken when the two doublets are in phase[10] and our late-time data ~ 230 oscillations later when they come back into phase again. The time of the second *beat* can be controlled by varying the oscillation frequency via the $\vec{\mathcal{B}}^0$-coils. In our final dataset, the noise in the science signal is roughly 30% above the shot noise limit.

2.2.1.9 Experimental protocol and switch states

In each shot of the experiment we can choose the preparation phase to be either *in* or *anti*. For a given choice of $\tilde{I}$, the direction of $\vec{\mathcal{E}}_{\rm rot}$ at the moment of dissociation, and $\tilde{P}$, the handedness of the dissociation laser polarization, the readout phase is constrained by the need to drive stretched-to-stretched transitions which preserve molecule orientation. We label each shot of the experiment with each of these phases. For example *in-anti* labels a shot where the cleanup (and optical pumping) laser are parallel to $\vec{\mathcal{E}}_{\rm rot}$ during state preparation but anti-parallel during readout.

To record a Ramsey fringe, we repeat our measurement at different free evolution times. For a given fringe, the phase of readout is kept fixed. At each Ramsey time, we take an even number of shots with each pair consisting of one shot with each phase of state preparation. This set of shots is called a point and a Ramsey fringe consists of 8 of these points taken at different t_R; we take 4 points at early Ramsey time, and 4 points at late Ramsey time, each consisting of two points on the sides of fringes and one point each on the top and bottom as shown in Fig. 2.8. The points on the sides of the fringes consist of 20 shots each, while the points on top and bottom consist of 8 shots each.

We record our data in 'blocks'. Each block is constructed from a set of $2^3 = 8$ fringes recorded in each possible combination of 3 experimental switches. Each switch corresponds to an

[10] Due to the finite length of the $\pi/2$ pulses, the doublets are already slightly out of phase at the earliest Ramsey times accessible to us. Systematic effects associated with this imperfection are discussed in Section VII in the Systematics paper.

experimental parameter whose sign can be reversed: $\tilde{B}$ the direction of the current in the $\vec{\mathcal{B}}^0$-coils, $\tilde{R}$ the direction of rotation of $\vec{\mathcal{E}}_{\rm rot}$, and $\tilde{I}$ the direction of $\vec{\mathcal{E}}_{\rm rot}$ relative to the y axis at the time of dissociation, corresponding to which side of the phosphor screen each of the doublets are imaged onto. Note that in our implementation of the $\tilde{I}$ switch, the direction of $\vec{\mathcal{E}}_{\rm rot}$ is reversed at all points in time so that the opposite switch is prepared and read out. A fourth experimental switch, $\tilde{P}$ the polarization of the dissociation light, is alternated every block.

We refer to each experimental configuration with $\{\tilde{B}, \tilde{R}, \tilde{I}, \tilde{P}\} = \pm 1$ as a switch state. In each block, the first Ramsey time is recorded for all switch states before moving onto the second Ramsey time for each switch state etc. The order of the switch states at each point is $\{\tilde{B}, \tilde{R}, \tilde{I}\}$ ={1,1,1}, {-1,1,1}, {1,-1,1}, {-1,-1,1}, {1,1,-1}, {-1,1,-1}, {1,-1,-1}, {-1,-1,-1}. Every other block, the order of switch states is reversed. In each switch state, we simultaneously collect data for molecules in each doublets, corresponding to orientation of the molecular axis with respect to the applied electric field which we represent by another switch $\tilde{D} = \pm 1$. The Ramsey times for each switch state are adjusted independently based on the data from the previous block to ensure that the 20-shot points are as close as possible to both the sides of the fringes, where our sensitivity is highest, and to the beat, where our noise cancellation is best and where various systematic shifts are minimized.

For the eEDM dataset, we collected 1370 blocks or $\sim$ 600 hours of data over a $\sim$ 2 month period of April–June 2022. During the data run, we took data with 3 different values of the $\mathcal{B}^{\rm rev}_{2,0}$, corresponding to fringe frequencies of $\sim$ 75, 105 and 151 Hz. About halfway through the dataset, we rotated the waveplates of $\mathcal{L}^{1082}_{\rm op}$, $\mathcal{L}^{814}_{\rm depl}$ and the dissociation lasers to reverse the handedness of the light from each.

2.2.1.10 Images to determine doublet positions

To determine where the dissociated Hf^+ ions from each doublet fall on the phosphor screen in each switch state, we take a series of images with no Ramsey sequence. For these images we prepare the stretched states as described in Section VII A of the Systematics paper but apply

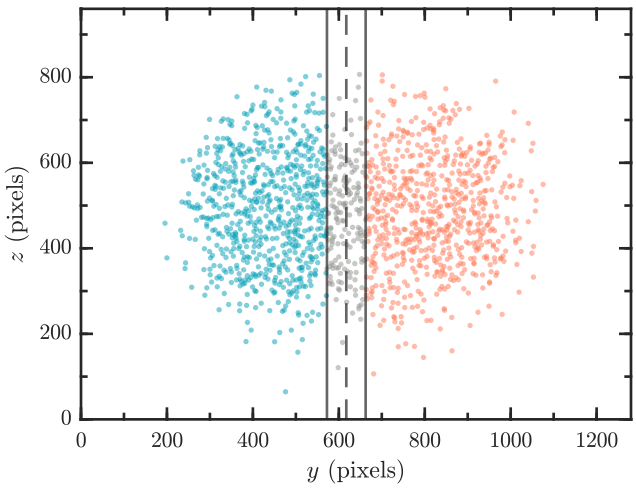

Figure 2.9: Example ion-detection data for a single shot of the experiment. Swatch (solid lines), from which ion counts are discarded, is defined by region ±45 pixels from center line (dashed line). Ions assigned to the upper and lower doublets are shown in orange and blue respectively.

no $\pi/2$ pulses before removing the population in one of the doublets using low-power $\mathcal{L}^{814}_{\text{depl}}$ light, tuned to resonance with the doublet to be depleted, and propagating along the z direction to avoid micromotion-induced Doppler shifts. We take 3 types of image per switch state: one where we deplete the lower Stark doublet, one where we deplete the upper Stark doublet, and one where the laser is tuned between the doublets to deplete both symmetrically. We use these three images to determine the center line between the two blobs for each switch state as described in Sec. 2.2.2.1. We repeated this imaging routine roughly every 10 blocks during the dataset to protect against alignment drifts. Potential effects of a systematic error in the determination of the center line are discussed in Section VII B 2 of the Systematics paper.

2.2.2 Data Analysis

2.2.2.1 Ion counting and asymmetry

Our experimental signal is dissociated Hf^+ ions read out via phosphorescence on an imaging microchannel plate (MCP). The images are processed asynchronously and we save a file which contains the locations of each bright spot which was determined to be an ion according to our

smoothing and noise-reducing processing algorithm. The data from a tyical shot is shown in Fig 2.9. The full eEDM dataset contains $\sim 10^8$ ion detection events.

We use this same algorithm to analyze the test images described in Sec. 2.2.1.10 and find a *center line* for each switch state. We use this center line when analyzing the Ramsey data to define a *swatch* which is a rectangular area, of fixed width, at the center of the image from which ion counts are discarded, as shown in Fig. 2.9. We do this because the doublets are not entirely separated on the screen, so in this area we cannot be sure that we will assign ions to the correct doublet. The extent to which we are able to isolate the two doublets is given by the imaging contrast C_{I}. As the swatch width increases, the imaging contrast improves but total ion number N decreases as we throw out more ions. For the final analysis of the dataset, we used a swatch of 90 pixels—to be compared with the total width covered by the detected ions, about 900 pixels—which roughly maximizes $C_{\mathrm{I}}\sqrt{N}$, proportional to our sensitivity. Potential systematics associated with the swatch width and imaging contrast are discussed in Section VII B 1 of the Sysetmatics paper.

Once we have our center line for each switch state we can properly count Hf^+ ions in our Ramsey data images and assign them to the correct doublet. For every image (which corresponds to a single run of the experiment), we end up with a number of ions in the upper doublet N^{u}, and number of ions in the lower doublet N^{l}.

For every switch state, we take data in both the in-in and anti-in (or the anti-anti and in-anti) combinations of preparation and readout phase. If the preparation and readout phase are the same (i.e. in-in and anti-anti), then the fringe formed as we vary t_R will have a π phase shift from the fringe formed when they are different (anti-in or in-anti). We will refer to in-in and anti-anti as "In" and in-anti and anti-in as "Anti". Now for each pair of shots, we can form our spin asymmetry,

$$\mathcal{A}_{\mathrm{u/l}} = \frac{N_{\mathrm{In}}^{\mathrm{u/l}} - N_{\mathrm{Anti}}^{\mathrm{u/l}}}{N_{\mathrm{In}}^{\mathrm{u/l}} + N_{\mathrm{Anti}}^{\mathrm{u/l}}}, \tag{2.10}$$

where the subscript refers to the preparation and readout phase combination. For each Ramsey time and switch state we take n shots and so can form $n/2$ asymmetries for each of the upper and

lower doublet. From these $n/2$ asymmetries we construct a mean $\mathcal{A}^{\mathrm{m}}_{\mathrm{u/l}}$, and from their scatter, a standard error on the mean $\delta\mathcal{A}_{\mathrm{u/l}}$.

We then form two 'meta' asymmetries by taking the difference (D) and sum (S) of the upper and lower asymmetries,

$$\begin{aligned}\mathcal{A}_{\mathrm{D}} &= \mathcal{A}_{\mathrm{u}} - \mathcal{A}_{\mathrm{l}},\\ \mathcal{A}_{\mathrm{S}} &= \mathcal{A}_{\mathrm{u}} + \mathcal{A}_{\mathrm{l}},\end{aligned} \tag{2.11}$$

with means $\mathcal{A}^{\mathrm{m}}_{\mathrm{D}}, \mathcal{A}^{\mathrm{m}}_{\mathrm{S}}$ and standard errors $\delta\mathcal{A}_{\mathrm{D}}, \delta\mathcal{A}_{\mathrm{S}}$. The $\delta\mathcal{A}_{\mathrm{D}}$ are reduced compared to $\delta\mathcal{A}_{\mathrm{S}}$ (and $\delta\mathcal{A}_{\mathrm{u/l}}$) due to common-mode cancellation of many sources of noise.

2.2.2.2 Least squares fitting

As mentioned previously, we perform our Ramsey experiment simultaneously on both doublets and use their opposing orientations at the time of dissociation to read them out on opposing sides on the imaging MCP screen. Because the data are acquired simultaneously, the difference asymmetry allows us to cancel much of the common-mode noise, leaving us with doublet-odd data with less scatter than the raw data. Unfortunately, the doublets are not fully separated on the screen, so we must be careful with how we fit our data.

For an ideal Ramsey fringe, with no leakage from the other doublet, we can define a functional form for the asymmetry,

$$h_{\mathrm{u/l}}(t_R) = C_{\mathrm{u/l}} e^{-\gamma_{\mathrm{u/l}} t_R} \cos(2\pi f_{\mathrm{u/l}} t_R + \phi_{\mathrm{u/l}}) + O_{\mathrm{u/l}}. \tag{2.12}$$

Here C is the initial fringe contrast, γ the contrast decay rate, f the fringe frequency, t_R the free evolution time, ϕ the initial phase, O the offset, and the subscripts indicate the upper or lower Stark doublet. In our fitting routine, we initially fit each fringe separately to this function. From the fit parameters we define the mean and difference parameters as

$$\begin{aligned}\alpha_{\mathrm{m}} &= \frac{\alpha_{\mathrm{u}} + \alpha_{\mathrm{l}}}{2},\\ \alpha_{\mathrm{d}} &= \frac{\alpha_{\mathrm{u}} - \alpha_{\mathrm{l}}}{2},\end{aligned} \tag{2.13}$$

with $\alpha \in \{C, \gamma, f, \phi, O\}$. Due to imperfect imaging contrast C_I, in reality each doublet's signal has a contribution from the other doublet. In this case, the measured asymmetries are

$$\begin{aligned} A_\mathrm{u} &= (\frac{1+C_\mathrm{I}}{2})h_\mathrm{u} + (\frac{1-C_\mathrm{I}}{2})h_\mathrm{l}, \\ A_\mathrm{l} &= (\frac{1-C_\mathrm{I}}{2})h_\mathrm{u} + (\frac{1+C_\mathrm{I}}{2})h_\mathrm{l}. \end{aligned} \tag{2.14}$$

Now our sum and difference asymmetries are

$$\begin{aligned} A_\mathrm{S} &= h_\mathrm{u} + h_\mathrm{l} \\ A_\mathrm{D} &= C_\mathrm{I}(h_\mathrm{u} - h_\mathrm{l}), \end{aligned} \tag{2.15}$$

which we can express in terms of the mean and difference fitting parameters,

$$\begin{aligned} A_\mathrm{S} = {} & (C_\mathrm{m} + C_\mathrm{d})e^{-2\gamma_\mathrm{m} t_R}\cos(2\pi(f_\mathrm{m} + f_\mathrm{d})t_R + (\phi_\mathrm{m} + \phi_\mathrm{d})) + (O_\mathrm{m} + O_\mathrm{d})... \\ & + (C_\mathrm{m} - C_\mathrm{d})e^{-2\gamma_\mathrm{d} t_R}\cos(2\pi(f_\mathrm{m} - f_\mathrm{d})t_R + (\phi_\mathrm{m} - \phi_\mathrm{d})) + (O_\mathrm{m} - O_\mathrm{d}), \\ A_\mathrm{D} = {} & C_\mathrm{I}((C_\mathrm{m} + C_\mathrm{d})e^{-2\gamma_\mathrm{m} t_R}\cos(2\pi(f_\mathrm{m} + f_\mathrm{d})t_R + (\phi_\mathrm{m} + \phi_\mathrm{d})) + (O_\mathrm{m} + O_\mathrm{d})... \\ & - (C_\mathrm{m} - C_\mathrm{d})e^{-2\gamma_\mathrm{d} t_R}\cos(2\pi(f_\mathrm{m} - f_\mathrm{d})t_R + (\phi_\mathrm{m} - \phi_\mathrm{d})) - (O_\mathrm{m} - O_\mathrm{d})). \end{aligned} \tag{2.16}$$

We use these two expressions to perform a simultaneous least-squares fit for the sum and difference asymmetries in each experimental switch state. The value of C_I, the imaging contrast, is fixed at 0.89 for this fit—determined as described in Section VII B 1 of the Systematics paper. The parameter uncertainties are extracted based solely on the standard errors of the asymmetries used in the fits. The resultant uncertainties on the fitted values of f_d and ϕ_d are close to the shot noise limit and much smaller than those on f_m and ϕ_m thanks to our simultaneous data collection and fitting routine, which cancels most of the common-mode noise. The outputs of these simultaneous fits are used for all further analysis.

2.2.2.3 Switch-parity channels

After fitting to each Ramsey fringe in a block to extract the 10 fitting parameters, we use the resulting 8 values of each parameter to form 8 linear combinations which we call switch-parity

channels. The switch-parity channels for the mean and difference parameters α_{m} and α_{d} which are odd under the product of switches $[\tilde{\mathcal{S}}_a\tilde{\mathcal{S}}_b...]$ are given by

$$\begin{aligned}\alpha^{\mathcal{S}_a\mathcal{S}_b\cdots} &= \frac{1}{8}\sum_{\tilde{B},\tilde{R},\tilde{I}=\pm1}[\tilde{\mathcal{S}}_a\tilde{\mathcal{S}}_b...]\alpha_{\mathrm{m}}(\tilde{B},\tilde{R},\tilde{I}),\\ \alpha^{D\mathcal{S}_a\mathcal{S}_b\cdots} &= \frac{1}{8}\sum_{\tilde{B},\tilde{R},\tilde{I}=\pm1}[\tilde{\mathcal{S}}_a\tilde{\mathcal{S}}_b...]\alpha_{\mathrm{d}}(\tilde{B},\tilde{R},\tilde{I}).\end{aligned} \tag{2.17}$$

So for example, C^{DBRI} is formed from adding together the measured C_{d} in all switch states for which the product $\tilde{B}\tilde{R}\tilde{I} = 1$, subtracting all switch states for which the product $\tilde{B}\tilde{R}\tilde{I} = -1$ and dividing by the number of switch states. f^{BR} is formed by adding together the f_{m} measured in all switch states for which the product $\tilde{B}\tilde{R} = 1$, subtracting the f_{m} measured in all switch states for which the product $\tilde{B}\tilde{R} = -1$ and, again, dividing by the total number of switch states. To avoid ambiguity, we label parity channels for the mean parameters α_{m} which are even under all switches with superscript 0; e.g. f^0 is the mean of the f_{m} measured in all switch states. We note that, because the measured $f_{\mathrm{u/l}}$ are defined as positive quantities (see Sec. 2.2.3), the $\tilde{B}$ switch is anomalous in that frequency contributions which change sign with $\tilde{B}$ appear in $\tilde{B}$-even channels while contributions which are independent of the $\tilde{B}$ switch appear in $\tilde{B}$-odd channels. In particular, the absolute sign of the contribution from the eEDM, which appears in f^{DB}, changes sign only with $\tilde{D}$. All other parity channels allow us to to diagnose experimental issues and identify sources of systematic error.

2.2.2.4 Blinding

We blinded the dataset by programming the fitting routine to add an unknown constant offset to the f^{DB} channel. This offset, drawn from a uniform distribution with a width of 10 mHz ($\sim 9\times10^{-28}\,e\,\mathrm{cm}$), was stored in an encrypted file and not removed until all statistical and systematic checks on the dataset had been completed, and the uncertainties finalized.

2.2.2.5 Data cuts

After completing the dataset, we applied cuts to the blinded data based on non-EDM channels indicating signal quality. Blocks with any individual fringe with late-time contrast below $C_{\text{late}} = 0.2$ were cut due to low signal to noise. By inspection of least-squares fits of individual fringes, this cut served as a good proxy for pathological fitting results. Blocks were also cut if they contained a fringe with a fitted difference frequency f_{d} in any switch state which was more than 3.5σ different from the mean fringe frequency for that switch state. The mean fringe frequencies were calculated over all blocks not removed by the late-time-contrast cut and which had the same value of $\vec{\mathcal{B}}^0$. They were constructed from the linear combinations, including the blinded offset on f^{DB}. This cut helped remove blocks where an experiment malfunction, e.g. laser unlocking, affected just one or two shots in a fringe. If our data were perfectly normally distributed, with no outliers, this would be expected to remove ~ 5 blocks, and decrease χ^2 by $\sim 0.7\%$. Figure 2.10 shows the shift in the center value, and the error bar of the eEDM channel, as a function of each of these two cuts. The first cut removed 26 blocks and the second a further 15, leaving 1329 blocks in the final dataset, with $\chi^2 = 1.07(4)$ for f^{DB}. Our final 1σ statistical error of 22.8 µHz has been relaxed by a factor $\sqrt{\chi^2} = 1.035$.

2.2.3 Effective Hamiltonian for Doublets

To an excellent approximation, we can model the evolution of either of the Stark doublets, shown in orange and blue in Fig. 2.8, as a two-level system. The effective Hamiltonian for each pair can be parameterized

$$H_{\text{eff}} = \frac{h}{2}\begin{pmatrix} f_0 & \Delta \\ \Delta & -f_0 \end{pmatrix}. \tag{2.18}$$

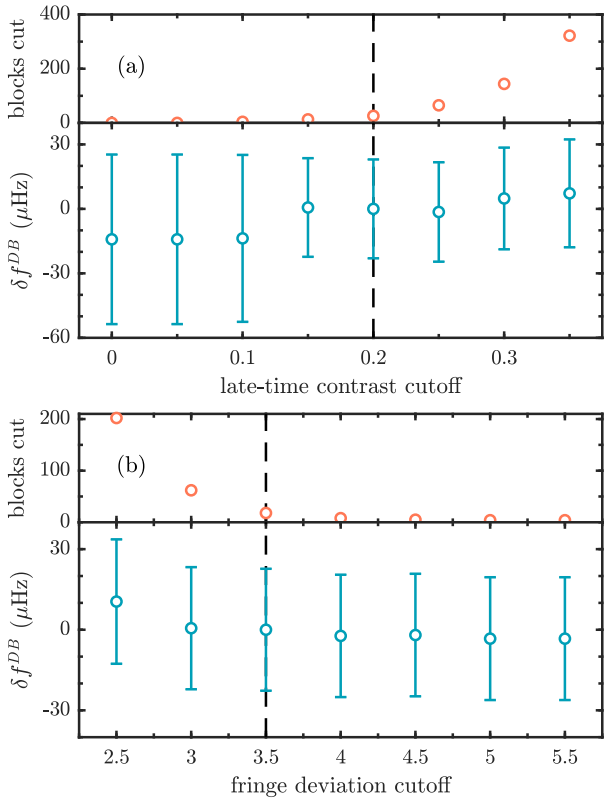

Figure 2.10: Change in f^{DB} over whole dataset as a function of cuts explained in text. (a) Late-time contrast cut. (b) Individual fringe outlier cut. In each plot, only one cut is applied. The error bars on f^{DB} are corrected by a factor of $\sqrt{\chi^2}$. Dashed lines indicate cuts used in final analysis.

This effective Hamiltonian acts on states $\begin{pmatrix} M_F = +3/2 \\ M_F = -3/2 \end{pmatrix}$.[11] The diagonal components f_0 contain all terms which directly shift the energies of the two states relative to one another, while the off-diagonal components Δ contain all terms which mix the two states. We can expand both f_0 and Δ in terms of their leading contributions,

$$f_0 = \tilde{B} f_0^0 + \delta\mathcal{F}_0, \tag{2.19}$$

$$\Delta = \tilde{R}\Delta^0 + \tilde{R}\tilde{D}\Delta^D + \delta\mathcal{D}. \tag{2.20}$$

[11] The order of the vectors in Equation 2.18 was not specified in the Systematics paper. The Systematics paper implicitly uses the opposite convention and has a few sign errors and missing factors of h that will be highlighted in footnotes of this document.

Here the quantities with tildes are equal to ± 1 and are determined by the experimental switch state, discussed in Sec. 2.2.1.9. The remaining parameters are defined in the next two paragraphs.

The principal contribution to f_0 is the Zeeman splitting $f_0^0 = -3g_F\mu_B\mathcal{B}_{\rm rot}/h \sim 100\,\text{Hz}$.[12] The off-diagonal component is dominated by two terms with similar magnitude, but different switch state dependence; Δ^0 and Δ^D, which both have magnitudes of about 1 Hz, represent a slight mixing of the two $M_F = \pm 3/2$ states in each doublet and arise at fourth order in perturbation theory in the full molecular Hamiltonian from the combined perturbations of rotation and Ω-doubling, breaking the degeneracy of either Stark doublet at $\mathcal{B}_{\rm rot} = 0$ [52, 53]. Δ^0 and Δ^D are given by

$$\begin{aligned} h\Delta^0 &= \frac{3\hbar\omega_{ef}}{2}\left(\frac{\hbar\omega_{\rm rot}}{d_{\rm mf}\mathcal{E}_{\rm rot}}\right)^3\left(\frac{18A_\parallel^2 - 19d_{\rm mf}^2\mathcal{E}_{\rm rot}^2}{A_\parallel^2 - d_{\rm mf}^2\mathcal{E}_{\rm rot}^2}\right), \\ h\Delta^D &= \frac{3\hbar\omega_{ef}}{2}\left(\frac{\hbar^3\omega_{\rm rot}^3}{d_{\rm mf}^2\mathcal{E}_{\rm rot}^2 A_\parallel}\right)\left(\frac{9A_\parallel^2 - 8d_{\rm mf}^2\mathcal{E}_{\rm rot}^2}{A_\parallel^2 - d_{\rm mf}^2\mathcal{E}_{\rm rot}^2}\right), \end{aligned} \tag{2.21}$$

where the various constants are defined in Table 2.1. These expressions are valid as long as $d_{\rm mf}\mathcal{E}_{\rm rot} \gg \hbar\omega_{ef}$ and $d_{\rm mf}\mathcal{E}_{\rm rot} \gg \hbar\omega_{\rm rot}$ or, in other words, if the molecule is fully polarized. The strong scaling of Δ with $\mathcal{E}_{\rm rot}$ allows us to perform off-resonant $\pi/2$ pulses by modulating the magnitude of $\mathcal{E}_{\rm rot}$ as described in Sec. 2.2.1.6.

The additional perturbations are given by

$$\delta\mathcal{F}_0(\tilde{B},\tilde{R},\tilde{I},\tilde{D}) = \sum_{\tilde{S}\in\mathcal{W}} \tilde{S}\delta f_0^s, \tag{2.22}$$

$$\delta\mathcal{D}(\tilde{B},\tilde{R},\tilde{I},\tilde{D}) = \sum_{\tilde{S}\in\mathcal{W}} \tilde{S}\delta\Delta^s, \tag{2.23}$$

where both summations are over $\mathcal{W}$, the set of all possible products of $\{\tilde{B},\tilde{R},\tilde{I}\,\tilde{D}\}$, and the superscript s on the δf_0^s and $\delta\Delta^s$ denote the switch state dependence of the perturbation *relative* to the largest term in each matrix element, f_0^0 and Δ^0 respectively. For our purposes, the most important

[12] Note that sign change and factor of h not included in the Systematics paper. See Subsection 4.6.2 for why this shift has a negative sign. The lack of a negative sign in the Systematics paper is the cause of considerable sign confusion.

perturbation is that due to the eEDM which contributes a diagonal term, $\tilde{D}\delta f_0^{DB} = 2\tilde{D}d_e\mathcal{E}_{\text{eff}}/h$[13]. Others which are important for our determination of d_e are discussed in detail in Section VI of the Systematics paper.

For each experimental switch state $(\tilde{B}, \tilde{R}, \tilde{I})$, and doublet $\tilde{D}$, we measure a frequency $f(\tilde{B}, \tilde{R}, \tilde{I}, \tilde{D})$ corresponding to the energy difference between the two eigenstates, which we define to be always positive. For typical experimental parameters, f_0^0 is roughly two orders of magnitude larger than any other term in the Hamiltonian, and so we can expand f about f_0^0,

$$\begin{aligned} f(\tilde{B}, \tilde{R}, \tilde{I}, \tilde{D}) = \Bigg| & \tilde{B}f_0^0 + \delta\mathcal{F}_0 + \frac{(\Delta^0)^2 + (\Delta^D)^2 + 2\tilde{D}\Delta^0\Delta^D + 2\tilde{R}(\Delta^0 + \tilde{D}\Delta^D)\delta\mathcal{D} + \delta\mathcal{D}^2}{2\tilde{B}f_0^0} \\ & - \delta\mathcal{F}_0\frac{(\Delta^0)^2 + (\Delta^D)^2 + 2\tilde{D}\Delta^0\Delta^D + 2\tilde{R}(\Delta^0 + \tilde{D}\Delta^D)\delta\mathcal{D} + \delta\mathcal{D}^2}{2f_0^{0\,2}} + ...\Bigg| \\ = |f_0^0| + \text{sgn}(f_0^0)\Bigg[& \tilde{B}\delta\mathcal{F}_0 + \frac{(\Delta^0)^2 + (\Delta^D)^2 + 2\tilde{D}\Delta^0\Delta^D + 2\tilde{R}(\Delta^0 + \tilde{D}\Delta^D)\delta\mathcal{D} + \delta\mathcal{D}^2}{2|f_0^0|} \\ & - \tilde{B}\delta\mathcal{F}_0\frac{(\Delta^0)^2 + (\Delta^D)^2 + 2\tilde{D}\Delta^0\Delta^D + 2\tilde{R}(\Delta^0 + \tilde{D}\Delta^D)\delta\mathcal{D} + \delta\mathcal{D}^2}{2|f_0^0|^2} + ...\Bigg] \end{aligned} \tag{2.24}$$

Note the factor of $\text{sgn}(f_0^0) = \text{sgn}(-3g_F\mu_B\mathcal{B}_{\text{rot}}/h) = -\text{sgn}(g_F)$, multiplying all but the first term in this expression. As we see in Chapter 4, we have measured $\text{sgn}(g_F) = -1$ so $\text{sgn}(f_0^0) = +1$.[14]

[13] The factor of 2 in this expression arises because our definition for the frequency of each fringe corresponds to the full energy difference between d_e aligned and anti-aligned with $\mathcal{E}_{\text{eff}}$. The systematics paper also reports this shift with a positive sign, though this is due to 1) the opposite convention for the order of the $M_F = \pm 3/2$ states in Equation 2.18 and 2) a sign error in the paper. See Subsection 4.6.2 for why the sign of the eEDM shift is positive. Also note the inclusion of h, absent in the Systematics paper.

[14] The systematics paper says $\text{sgn}(f_0^0) = -1$ because it uses the definition $f_0^0 = +3g_F\mu_B\mathcal{B}_{\text{rot}}/h$. I use the definition with a negative sign the equation for f_0^0, and do so consistently throughout this thesis. Where there are discrepancies, default to this thesis instead of the Systematics paper.

Chapter 3

Systematics

"I'm not dumb. I just have a command of thoroughly useless information."

- Bill Watterson, The Indispensable Calvin and Hobbes

As discussed in the previous chapter, the eEDM shift is $\tilde{D}$-odd and shows up in the f^{DB} frequency channel which we have measured with a 1σ statistical error of 22.8 μHz. One of our primary goals for the experiment was to understand and reduce the size of the systematic errors in our experiment so that they are each small compared to our statistical error bar. A complete description of our systematic error budget is given in the Systematics paper [31]. In this chapter, I will give an overview of our systematic errors and discuss some of those errors in more depth.

The systematic errors of our measurement can be nicely split into two camps. First are shifts in the frequency difference within each doublet that we measure during the Ramsey experiment. These shifts are the largest systematics in our experiment and will be the focus of this chapter. The other set of systematic errors are due to phase shifts of the Ramsey fringe at either early or late time. While these phase shifts change the measured frequency, the resulting frequency shifts are suppressed because we measure the phase at the beginning and end of our long coherence time. This is a key advantage we have over beam line experiments which cannot vary the coherence time of their measurements. As the systematics from phase errors are relatively small, I leave their discussion to Section VII of the Systematics paper [31].

3.1 Systematics due to Off Diagonal Terms

We know that the eEDM shift contributes to our measured frequency f^{DB}, but it is just part of the full expression which we can find from Equations 2.22- 2.24:

$$\begin{aligned} f^{DB} &= \frac{1}{16}\sum_{\tilde{B},\tilde{R},\tilde{I},\tilde{D}=\pm1}\tilde{B}\tilde{D}f(\tilde{B},\tilde{R},\tilde{I},\tilde{D}) \\ &= \frac{1}{16}\sum_{\tilde{B},\tilde{R},\tilde{I},\tilde{D}=\pm1}\Bigg[\tilde{B}\tilde{D}|f_0^0| + \tilde{D}\delta\mathcal{F}_0 \\ &\quad + \tilde{B}\tilde{D}\frac{(\Delta^0)^2+(\Delta^D)^2+2\tilde{D}\Delta^0\Delta^D+2\tilde{R}(\Delta^0+\tilde{D}\Delta^D)\delta\mathcal{D}+\delta\mathcal{D}^2}{2|f_0^0|} \\ &\quad - \tilde{D}\delta\mathcal{F}_0\frac{(\Delta^0)^2+(\Delta^D)^2+2\tilde{D}\Delta^0\Delta^D+2\tilde{R}(\Delta^0+\tilde{D}\Delta^D)\delta\mathcal{D}+\delta\mathcal{D}^2}{2|f_0^0|^2}+...\Bigg] \end{aligned} \tag{3.1}$$

The only terms that survive the summation are the ones which are not multiplied by $\tilde{B},\tilde{R},\tilde{I}$ or $\tilde{D}$:

$$\begin{aligned} f^{DB} &= \delta f_0^{DB} + \frac{\Delta^0\delta\Delta^{DB}+\Delta^D\delta\Delta^B}{|f_0^0|} - \delta f_0^{DB}\frac{(\Delta^0)^2+(\Delta^D)^2}{2|f_0^0|^2} - \delta f_0^B\frac{\Delta^0\Delta^D}{|f_0^0|^2} \\ &\quad + \frac{1}{16}\sum_{\tilde{B},\tilde{R},\tilde{I},\tilde{D}=\pm1}\left[\tilde{B}\tilde{D}\frac{\delta\mathcal{D}^2}{2|f_0^0|} - \tilde{D}\delta\mathcal{F}_0\frac{2\tilde{R}(\Delta^0+\tilde{D}\Delta^D)\delta\mathcal{D}+\delta\mathcal{D}^2}{2|f_0^0|^2}+...\right] \end{aligned} \tag{3.2}$$

The first term, δf_0^{DB}, contains the doublet-odd frequency shifts which show up directly in the measured f^{DB} channel.[1] This includes the eEDM shift $2\tilde{D}d_e\mathcal{E}_{\text{eff}}$ which we want to measure.

[1] As defined in Subsection 2.2.3, frequency shifts are labeled with a superscript that denotes the switch state dependence of the frequency shift *relative* to the largest frequency shift f_0^0. f_0^0 is $\tilde{B}$-odd, so δf_0^{DB} is $\tilde{D}$-odd but $\tilde{B}$-even. The same convention holds for the Δ terms where the largest off-diagonal coupling Δ^0 is $\tilde{R}$-odd. This convention is confusing and should be abolished in Generation 3, but as it is deeply entrenched in the Generation 2 documents I use it in my thesis. Note that every term Equation 3.2 has the "net" superscript DB. For example, the second and third terms $\Delta^0\delta\Delta^{DB}$ and $\Delta^D\delta\Delta^B$ each have one D and B in their superscripts, and therefore a "net" superscript DB. If the same letter appears twice in the superscript it cancels out. This means that the $\delta f_0^{DB}(\Delta^D)^2$ term has a "net" superscript DB as well.

All other terms in the above expression, including any other $\tilde{D}$-odd frequency shifts that are part of δf_0^{DB}, are systematic errors in our experiment.

All but the first term of Equation 3.2 are systematic shifts due to the nonzero off-diagonal couplings Δ. The largest of these terms are the $\tilde{R}$-odd $\Delta^0 \sim 0.6$ Hz and $\tilde{D}\tilde{R}$-odd $\Delta^D \sim -0.9$ Hz. In Subsection 2.2.3 it was explained that these couplings are calculated from fourth order perturbation theory which gives the expressions in Equations 2.21. The important part of these expressions is that Δ^0 is $\tilde{R}$-odd and is proportional to $\hbar\omega_{ef}\left(\frac{\hbar\omega_{\mathrm{rot}}}{d_{\mathrm{mf}}\mathcal{E}_{\mathrm{rot}}}\right)^3$, which is explained in Figure 3.1.

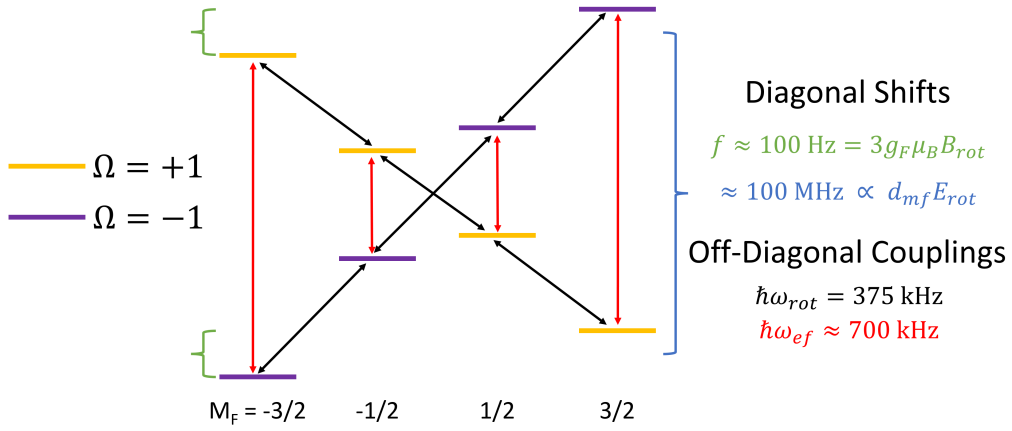

Figure 3.1: The level structure of $^3\Delta_1$ $v = 0, J = 1, F = 3/2$ state in HfF^+ in an external electric field $\mathcal{E}_{\mathrm{rot}} \sim 58$ V/cm and magnetic field $\mathcal{B}_{\mathrm{rot}} \sim 10$ mG. The energies of the eight states are given by the Stark shift, which splits the upper and lower doublets by ~ 100 MHz (blue bracket), and the Zeeman shift, which causes a ~ 100 Hz shift between the $M_F = \pm 3/2$ levels (green brackets). The shifts are not shown to scale. Pairs of states with the same Ω and $\Delta M_F = 1$ are mixed by the rotation matrix element $\hbar\omega_{\mathrm{rot}}$ (black lines) because the experiment is performed in a rotating frame. Pairs of states with the same M_F but different Ω values are mixed due to the Omega doubling matrix element $\hbar\omega_{ef}$ (red lines). When we construct the two-level effective Hamiltonian in Subsection 2.2.3, Δ^0 is the average off-diagonal coupling between the $M_F = \pm 3/2$ states within each doublet. These states are coupled by three rotation matrix elements and one Omega doubling matrix element, spanning energies on the scale of the Stark shift $d_{\mathrm{mf}}\mathcal{E}_{\mathrm{rot}}$. That is why fourth order perturbation theory gives the expression $\Delta^0 \propto \hbar\omega_{ef}\left(\frac{\hbar\omega_{\mathrm{rot}}}{d_{\mathrm{mf}}\mathcal{E}_{\mathrm{rot}}}\right)^3$. Note that Δ^0 is proportional to three powers of the rotation coupling which changes sign when the molecules are rotating clockwise vs counterclockwise. This explains why Δ^0 is $\tilde{R}$-odd. This diagram does not include the $F = 1/2$ states, which as seen in Figure 2.8 are closer in energy to the upper doublet. These states complicate the calculation and explain why the coupling has a large Δ^D term.

The model explained in Figure 3.1 can also guide us towards the off-diagonal coupling terms

besides Δ^0 and Δ^D which are significant. While the rotation matrix element mixes pairs of states with the same value of Ω and $\Delta M_F = 1$, the same can be done by a magnetic field that is perpendicular to the quantization axis defined by $\vec{\mathcal{E}}_{\text{rot}}$.[2] As $\vec{\mathcal{E}}_{\text{rot}}$ rotates in the xy-plane, magnetic fields along the z-axis of our experiment fit the bill.

There are two important sorts of uniform magnetic fields along the z-axis, those that reverse with $\tilde{B}$ and those that do not. Recall that we apply a magnetic field gradient $\vec{\mathcal{B}}^0 = \tilde{B}\mathcal{B}^{\text{rev}}_{2,0}(2\vec{z}-\vec{x}-\vec{y})$, where $\mathcal{B}^{\text{rev}}_{2,0} \sim 200$ mG/cm, via a pair of anti-Helmholtz coils.[3] $\mathcal{B}^{\text{rev}}_{2,0}$ is the largest part of the total magnetic field experienced by the molecules, $\vec{\mathcal{B}} = \tilde{B}\vec{\mathcal{B}}^0 + \delta\vec{\mathcal{B}}$. Similar to the notation for f and Δ explained in Subsection 2.2.3, the switch state dependence of the magnetic field will be written as:

$$\delta\vec{\mathcal{B}} = \sum_{\tilde{S}\in\mathcal{W}} \tilde{S}\delta\vec{\mathcal{B}}^s \tag{3.3}$$

The summation is over $\mathcal{W}$, the set of all possible products of $\{\tilde{B}, \tilde{D}, \tilde{R}, \tilde{I}\}$, and the superscript s denotes the switch state dependence of the field *relative* to $\vec{\mathcal{B}}^0$, which is $\tilde{B}$-odd. This means $\mathcal{B}_z$ is the $\tilde{B}$-odd magnetic field along the z-axis, which can be generated if the anti-Helmholtz coils are misaligned, while $\mathcal{B}^B_z$ is the $\tilde{B}$-even background field.[4] See Appendix A for how we measured $\mathcal{B}_z < 88$ mG and $\mathcal{B}^B_z < 80$ mG in our experiment.

These magnetic fields along the z-axis cause off-diagonal couplings between the same pairs of states coupled by the rotation matrix element. We can naively estimate the magnitude of Δ induced by $\mathcal{B}_z$ or $\mathcal{B}^B_z$ by replacing one of the three rotation matrix elements $\hbar\omega_{\text{rot}}$ with $g_F\mu_B\mathcal{B}_z$ or $g_F\mu_B\mathcal{B}^B_z$. This would tell us that there are contributions to Δ that are $\dfrac{g_F\mu_B\mathcal{B}_z}{\hbar\omega_{\text{rot}}} = \dfrac{1}{982}$ and

[2] See Chapter 2 of Willaim Cairncross's thesis [1] for a detailed explanation of how magnetic and electric fields cause diagonal and off-diagonal matrix elements.

[3] See Subsection 2.3.5 of Tanya Roussy's thesis [2] for a complete description of the coils used in our experiment.

[4] As I made clear in a previous footnote, I do not like this confusing notation. I strongly encourage everyone still working on the JILA eEDM experiment to change this notation for the next measurement.

$\frac{g_F\mu_B\mathcal{B}_z^B}{\hbar\omega_{\rm rot}} = \frac{1}{1080}$ times ~ 1 Hz, assuming that the magnetic fields are as large as our measurements allow them to be. A more careful calculation by current JILA EDM graduate student Anzhou Wang tells us that this misses a factor of three because the magnetic field matrix element can replace any one of the three rotation matrix elements. This results in $\tilde{B}$-even and $\tilde{B}$-odd components of Δ that are ~ 327 and 360 times smaller than 1 Hz. These Δs are $\tilde{R}$-even because they now include only two rotation matrix elements, and they can either be $\tilde{D}$-even or $\tilde{D}$-odd since we start with Δ^0 and Δ^D of roughly the same magnitude. This means we should expect $\delta\Delta^R$, $\delta\Delta^{BR}$, $\delta\Delta^{DR}$ and $\delta\Delta^{DBR}$ all to be roughly ~ 3 mHz, given our limits on $\mathcal{B}_z$ and $\mathcal{B}_z^B$.

The second term of Equation 3.2 contains $\delta\Delta^{DB}$ and $\delta\Delta^B$. These $\delta\Delta$s must be $\tilde{R}$ and $\tilde{B}$-odd, which can be done if the fourth order perturbation is composed of one Omega doubling matrix element, one $\tilde{B}$-even Zeeman matrix element, one $\tilde{B}$-odd Zeeman matrix element and one rotation matrix element. These couplings, made from two Zeeman matrix elements, will be $\frac{1}{6}\frac{\hbar\omega_{\rm rot}}{g_F\mu_B\mathcal{B}_z}\frac{\hbar\omega_{\rm rot}}{g_F\mu_B\mathcal{B}_z^B} \sim 1.8\times10^5$ times smaller than Δ^0 and Δ^D. The factor of 6 comes from the six unique ways that $g_F\mu_B\mathcal{B}_z$ and $g_F\mu_B\mathcal{B}_z^B$ can replace the three $\hbar\omega_{\rm rot}$ matrix elements, meaning that $\delta\Delta^B$ and $\delta\Delta^{DB}$ are both about 6 μHz.

Knowing the magnitude of the Δs, together with the fact that $|f_0^0| \sim 100$ Hz, we can evaluate the terms in Equation 3.2 to see how large the systematic effect is from each term. The first term, δf_0^{DB}, contains all of the $\tilde{D}$-odd shifts including the eEDM shift. This term will be discussed in Section 3.2. The second and third terms in Equation 3.2 can be grouped with the largest terms in $\tilde{B}\tilde{D}\delta\mathcal{D}^2$, where $\delta\mathcal{D}$ is the sum of all of the Δ switch states except Δ^0 and Δ^D. These shifts together are:

$$\frac{\Delta^0\delta\Delta^{DB} + \Delta^D\delta\Delta^B + \delta\Delta^{DR}\delta\Delta^{BR} + \delta\Delta^R\delta\Delta^{DBR}}{|f_0^0|} = \frac{30 g_F^2\mu_B^2\mathcal{B}_z\mathcal{B}_z^B\Delta^0\Delta^D}{h^2 f_{\rm rot}^2|f_0^0|} \tag{3.4}$$

On the right side of this equation we have used the approximate values of the six $\delta\Delta$ terms de-

termined previously. Note that the four terms on the left hand side of the above equation are not independent – their errors are correlated so we have taken the sum of their magnitudes instead of the usual quadrature sum for uncorrelated errors. When we evaluate this term with the largest allowed values of $\mathcal{B}_z$ and $\mathcal{B}_z^B$ we find that it has a magnitude of ~ 150 nHz, comfortably smaller than our statistical error bar and smaller than the 400 nHz we report in the Systematics paper.[5]

The next terms in Equation 3.2 are:

$$-\delta f_0^{DB}\frac{(\Delta^0)^2+(\Delta^D)^2}{2|f_0^0|^2}-\delta f_0^B\frac{\Delta^0\Delta^D}{|f_0^0|^2}\approx-\frac{\delta f_0^{DB}}{10^4}+\frac{\delta f_0^B}{10^4} \tag{3.5}$$

The first term simply tells us that our measurement of f^{DB} gives us 99.99% of the $\tilde{D}$-odd frequency shifts instead of the entire shift, a small correction that we can safely ignore. The second term tells us that we have a systematic from the frequency shifts that are even in all of our switches, divided by 10,000. As we will see in Section 3.2.2, the root cause of many systematic errors in our experiment is that a part in ~ 460 of δf_0^B shifts leak into our measured f^{DB}. The second term in the above equation tells us that this leakage is about 5% larger than we would otherwise expect. As we later constrain δf_0^B to be ~ 3.5 mHz,[6] we get an additional systematic shift on the order of ~ 210 nHz. This shift is not included in the Systematics paper, though we do mention that there are effects at the $\lesssim 200$ nHz level that we ignore.

The last term in Equation 3.2 is a sum over a term that is proportional to $\delta\mathcal{F}_0$. As discussed in Subsection 3.4.2, the largest frequency shift outside of f_0^0 is $\delta f_0^{BR}\approx 210$ mHz. This means that the largest systematic effects from the $\delta\mathcal{F}_0$ term are:

[5]There are multiple reasons for the discrepancy with the Systematics paper. The first is that we did not include the factors of 3 and 6 found by Anzhou Wang discussed above. The second is that we did not properly find the limits on $\mathcal{B}_z$ and $\mathcal{B}_z^B$ as discussed in Appendix A. We also did not include the terms proportional to $\Delta^0\delta\Delta^{DB}$ or $\Delta^D\delta\Delta^B$. It is fortuitous that the magnitude of the systematic does not vary substantially when correcting these oversights.

[6]This number was found by adding in quadrature all of the shifts in f^B in sections VI A and VI B of the Systematics paper. Those shifts will be discussed later in this chapter.

$$-f^{BR}\frac{\Delta^0\delta\Delta^{DR}+\Delta^D\delta\Delta^R}{|f_0^0|^2}=-\frac{f^{BR}}{|f_0^0|^2}\frac{6g_F\mu_B\mathcal{B}_z\Delta^0\Delta^D}{hf_{\rm rot}} \tag{3.6}$$

On the right hand side we have replaced the $\delta\Delta$ terms with the order of magnitude estimates we found previously. We can evaluate this expression to find that f^{BR} leaking into the eEDM channel gives us a ~ 70 nHz shift, smaller than the 200 nHz shift we report in the Systematics paper.

The updated values of the systematic effects in Equations 3.4 and 3.6 are not significant enough to change the net systematic or total error bars of our experiment, but these more reliable calculations may be helpful for when these effects are evaluated in our future measurement.

3.2 Doublet-odd Frequency Shifts

In Section 3.1 we saw that all of the terms in Equation 3.2 except for the first lead to systematics that are comfortably small compared to our statistical uncertainty. The first term, δf_0^{DB}, contains all of the $\tilde{D}$-odd frequency shifts. This includes the T-symmetry violating eEDM shift $2\tilde{D}d_e\mathcal{E}_{\rm eff}$ that we want to measure. HfF^+ is also sensitive to a T-symmetry violating pseudoscalar-scalar electron-nucleon coupling, $\mathcal{C}_S$ [54, 55]. This shows up as a $\tilde{D}$-odd frequency shift $2W_S\mathcal{C}_S$ where $W_S/h = -51$ kHz in HfF^+ [56]. While $\mathcal{C}_S$ does not get the same attention as d_e, we are equally interested in measuring these two T-symmetry violating effects.[7]

Other than T-symmetry violating effects, the only $\tilde{D}$-odd shifts are magnetic.[8] Therefore now is a good time to explain in detail the Zeeman effect in our experiment. This explanation will

[7] We actually measure a linear combination of d_e and $\mathcal{C}_S$. Our measurement alone cannot determine the value of either parameter. It is possible, if unlikely, that d_e and $\mathcal{C}_S$ are large enough for us to measure but the effects cancel in HfF^+. This is one reason why it is good that experiments to measure these quantities are done with different molecules. I will only mention $\mathcal{C}_S$ again briefly in Chapter 6.

[8] Berry's phase effects, which are discussed in Section 3.5, are inherently $\tilde{D}$-even. Berry's phase, magnetic and T-symmetry violating effects are the *only* shifts that can create an energy difference between pairs of $M_F = \pm F$ states for which all other quantum numbers are the same.

follow the introduction to Section VI A of the Systematics paper quite closely.

3.2.1 Zeeman Shifts

The Zeeman Hamiltonian for the $^3\Delta_1$ $v = 1, J = 1, F = 3/2$ state of HfF^+ is given as:

$$\begin{aligned} H_Z &= -(\vec{\mu}_0 + \tilde{D}\vec{\mu}_D) \cdot \vec{\mathcal{B}} \\ &= -M_F \mu_B (g_F + \tilde{D}\delta g_F) \hat{\mathcal{E}}_{\text{rot}} \cdot \vec{\mathcal{B}} \end{aligned} \tag{3.7}$$

Here $\vec{\mu}_0$ is the part of the magnetic moment that is common to both doublets and $\vec{\mu}_D$ is the differential part. The magnetic moments of the upper and lower doublets are quite similar for our typical experimental parameters; their difference is usually only a part in ~ 460. In the second line we use the fact that both magnetic moments track the quantization axis defined by $\hat{\mathcal{E}}_{\text{rot}}$.

As discussed in Section 3.1, we express the magnetic field as a sum of two parts, $\vec{\mathcal{B}} = \tilde{B}\vec{\mathcal{B}}^0 + \delta\vec{\mathcal{B}}$. The first part is the idealized applied quadrupole magnetic field gradient which switches perfectly with $\tilde{B}$, and the second part $\delta\vec{\mathcal{B}}$ represents any additional magnetic field experienced by the molecules. We are particularly interested in $\delta\vec{\mathcal{B}}^B$, the magnetic field which does not switch sign with $\tilde{B}$, causing shifts in f^B and f^{DB}.[9] To first order[10] these are:

$$h\delta f^B = -3 g_F \mu_B \hat{\mathcal{E}} \cdot \delta\vec{\mathcal{B}}^B \tag{3.8}$$

$$h\delta f^{DB} = -3 \delta g_F \mu_B \hat{\mathcal{E}} \cdot \delta\vec{\mathcal{B}}^B \tag{3.9}$$

[9] Note that a magnetic field with switch state dependence S will cause shifts in f^S and f^{DS} as given by Equations 3.8 and 3.9. With an exception discussed in Subsection 3.2.3, magnetic fields are necessarily $\tilde{D}$-even as the ions in each doublet are overlapped in space and time.

[10] There is a $\lesssim 5\%$ correction to these shifts from the mixing within each doublet described in Section 2.2.3. These effects are not included in our systematic uncertainty budget.

In these equations $\hat{\mathcal{E}}$ is the unit vector pointing along the total electric field $\vec{\mathcal{E}}$.

As will be calculated in Subsection 4.6.7, the differential magnetic moment $\vec{\mu}_D$ arises primarily from the mixing of $J = 1$ and $J = 2$ levels induced by the electric and magnetic fields:

$$\delta g_F \approx -\frac{d_{\mathrm{mf}} G_{\parallel} |\vec{\mathcal{E}}|}{20B} \tag{3.10}$$

The values of the molecular constants in this equation are given in Table 2.1. There are ~ 10 % corrections due to the mixing of adjacent M_F levels in the rotating frame and interactions with other electronic states, as explained by [57]. We can use this equation together with Equation 3.9 to find expressions for the $\tilde{B}$-even time averaged frequency shifts we measure in the experiment:

$$h \langle \delta f^B \rangle = -3 g_F \mu_B \langle \hat{\mathcal{E}} \cdot \delta \vec{\mathcal{B}}^B \rangle \tag{3.11}$$

$$h \langle \delta f^{DB} \rangle = -3 \frac{\delta g_F}{|\vec{\mathcal{E}}|} \mu_B \langle \vec{\mathcal{E}} \cdot \delta \vec{\mathcal{B}}^B \rangle \tag{3.12}$$

Appreciating the subtle differences in these equations is incredibly important for understanding the systematic shifts in our experiment. The Zeeman shift that is common to the two doublets is proportional to the time average of the magnetic field $\delta \vec{\mathcal{B}}^B$ in the direction of the quantization axis $\hat{\mathcal{E}}$. On the other hand, the differential Zeeman shift is proportional to the time average of the magnetic field $\delta \vec{\mathcal{B}}^B$ dotted into the the entire electric field $\vec{\mathcal{E}}$. Note that $\dfrac{\delta g_F}{|\vec{\mathcal{E}}|}$ is independent of the electric field due to Equation 3.10 and is just a constant. This difference between whether $\hat{\mathcal{E}}$ or $\vec{\mathcal{E}}$ is included in the time average is the source of most of our magnetic systematic errors.

Going forward it will be useful to expand $\delta \vec{\mathcal{B}}^B$ as:

$$\delta\vec{\mathcal{B}}^B(\vec{x},\vec{y},\vec{z}) = \sum_{l=1,2,\ldots}\sum_{m=-l}^{l}\mathcal{B}_{l,m}\vec{\nabla}r^l\mathcal{Y}_{l,m} \tag{3.13}$$

Here $\vec{x}$, $\vec{y}$ and $\vec{z}$ and the ion's position relative to the trap center, $\mathcal{B}_{l,m}$ is the coefficient of each component and $\mathcal{Y}_{l,m}$ are the seminormalized real spherical harmonics:

$$\mathcal{Y}_{l,m} = \sqrt{\frac{4\pi}{2l+1}} \times \begin{cases} \frac{i}{\sqrt{2}}(Y_l^m - (-1)^m Y_l^{-m}) & \text{if } m < 0 \\ Y_l^0 & \text{if } m = 0 \\ \frac{1}{\sqrt{2}}(Y_l^{-m} + (-1)^m Y_l^m) & \text{if } m > 0 \end{cases}. \tag{3.14}$$

The $\vec{\nabla}r^l\mathcal{Y}_{l,m}$ for $l \leq 3$ are given in Table 3.1.

Table 3.1: Magnetic Field Expansion. Estimated sizes of components are given in parentheses.

Coefficient	$\vec{\nabla}r^l\mathcal{Y}_{l,m}$
Uniform fields ($\lesssim 10\,\mathrm{mG}$)[11]	
$\mathcal{B}_{1,-1}$	$\hat{y}$
$\mathcal{B}_{1,0}$	$\hat{z}$
$\mathcal{B}_{1,1}$	$\hat{x}$
First-order gradients ($\lesssim 10\,\mathrm{mG\,cm^{-1}}$) [12]	
$\mathcal{B}_{2,-2}$	$\sqrt{3}(y\hat{x} + x\hat{y})$
$\mathcal{B}_{2,-1}$	$\sqrt{3}(z\hat{y} + y\hat{z})$
$\mathcal{B}_{2,0}$	$-x\hat{x} - y\hat{y} + 2z\hat{z}$
$\mathcal{B}_{2,1}$	$\sqrt{3}(z\hat{x} + x\hat{z})$
$\mathcal{B}_{2,2}$	$\sqrt{3}(x\hat{x} - y\hat{y})$
Second-order gradients ($\lesssim 10\,\mathrm{mG\,cm^{-2}}$)	
$\mathcal{B}_{3,-3}$	$\frac{3}{2}\sqrt{\frac{5}{2}}(2xy\hat{x} + (x-y)(x+y)\hat{y})$
$\mathcal{B}_{3,-2}$	$\sqrt{15}(yz\hat{x} + xz\hat{y} + xy\hat{z})$
$\mathcal{B}_{3,-1}$	$\sqrt{\frac{3}{2}}(-xy\hat{x} + \frac{1}{2}(-x^2 - 3y^2 + 4z^2)\hat{y} + 4yz\hat{z}$
$\mathcal{B}_{3,0}$	$-3(xz\hat{x} + yz\hat{y} + \frac{1}{2}(x^2 + y^2 - 2z^2)\hat{z})$
$\mathcal{B}_{3,1}$	$\sqrt{\frac{3}{2}}(\frac{1}{2}(-3x^2 - y^2 + 4z^2)\hat{x} - xy\hat{y} + 4xz\hat{z})$
$\mathcal{B}_{3,2}$	$\sqrt{15}(xz\hat{x} - yz\hat{y} + \frac{1}{2}(x-y)(x+y)\hat{z})$
$\mathcal{B}_{3,3}$	$\frac{3}{2}\sqrt{\frac{5}{2}}((x-y)(x+y)\hat{x} - 2xy\hat{y})$

3.2.2 Zeeman Shift from $\vec{\mathcal{E}}_{\text{rot}}$ and $\vec{\mathcal{B}}_{2,0}$

The largest electric field that the molecules experience is $\vec{\mathcal{E}}_{\text{rot}} = \mathcal{E}_{\text{rot}}[\cos(\omega_{\text{rot}}t)\hat{x} + \sin(\omega_{\text{rot}}t)\hat{y}]$. This field causes the molecules to undergo a circular micromotion with radius $r_{\text{rot}} = \dfrac{e}{m\omega_{\text{rot}}^2}$, where $e > 0$ and m are the charge and mass of HfF^+ respectively. As discussed in Section 2.1, there is no induced Zeeman shift if the molecules are rotating in a uniform magnetic field $\vec{\mathcal{B}}_{1,m}$. We can now see that this is because $\langle \vec{\mathcal{E}}_{\text{rot}} \cdot \vec{\mathcal{B}}_{1,m} \rangle = \langle \hat{\mathcal{E}}_{\text{rot}} \cdot \vec{\mathcal{B}}_{1,m} \rangle = 0$ for all allowed values of $m = \pm 1, 0$. In fact, the only magnetic field with $l \leq 3$ which causes a nonzero time-averaged shift in any frequency channel is the intentionally applied $\vec{\mathcal{B}}_{2,0}$. This leads to frequency shifts:

$$h\langle f^0 \rangle = -3g_F\mu_B \langle \hat{\mathcal{E}}_{\text{rot}} \cdot \vec{\mathcal{B}}_{2,0}^{\text{rev}} \rangle = -3g_F\mu_B \mathcal{B}_{2,0}^{\text{rev}} r_{\text{rot}} \tag{3.15}$$

$$h\langle \delta f^D \rangle = -3\frac{\delta g_F}{\mathcal{E}_{\text{rot}}}\mu_B \langle \vec{\mathcal{E}}_{\text{rot}} \cdot \vec{\mathcal{B}}_{2,0}^{\text{rev}} \rangle = -3\delta g_F \mu_B \mathcal{B}_{2,0}^{\text{rev}} r_{\text{rot}} \tag{3.16}$$

Note that in this case that $\langle \hat{\mathcal{E}} \cdot \vec{\mathcal{B}} \rangle = \langle \vec{\mathcal{E}} \cdot \vec{\mathcal{B}} \rangle / |\vec{\mathcal{E}}|$. This gives us the "usual" case where the $\tilde{D}$-odd shift is $\dfrac{g_F}{\delta g_F} \sim -460$ times smaller than the $\tilde{D}$-even shift.[13] We reliably see in our experiment that when $f^0 \approx 100$ Hz, we measure $f^D \approx -210$ mHz.

While this combination of ideal electric and magnetic fields does not give rise to $\tilde{D}$-odd frequency shifts, it is never that easy in real life. There will inevitably be a magnetic field gradient $\vec{\mathcal{B}}_{2,0}$ that does not reverse sign with $\tilde{B}$, $\vec{\mathcal{B}}_{2,0}^{\text{nr}}$. This non-reversing field can arise from either an

[11] We used an array of magnetometers around our apparatus to shim the magnetic fields to about 10 mG, though we were unsure if we could trust the measurement of magnetometers outside of our vacuum chamber. We were able to confirm that $\mathcal{B}_{1,1}$ and $\mathcal{B}_{1,-1}$ were less than about 10 mG at the location of the ions by intentionally applying a large second harmonic of the electric field and measuring the resulting shifts from the Zeeman effect described in Subsection 3.3.3. In Appendix A we find that $\mathcal{B}_z < 80$ mG and $\mathcal{B}_z^B < 88$ mG.

[12] See Section VI A 4 of the Systematics paper for how we approximated the first- and second-order magnetic field gradients.

[13] See Subsection 4.6.7 if you would like an explanation of why $\dfrac{g_F}{\delta g_F}$ is negative.

imperfection in how we reverse the current in the coils that drives $\vec{\mathcal{B}}^{\rm rev}_{2,0}$ or from a background magnetic field gradient. In either case we get the frequency shifts:

$$h\left\langle \delta f^{B}\right\rangle = -3g_F\mu_B\left\langle \hat{\mathcal{E}}_{\rm rot}\cdot\vec{\mathcal{B}}^{\rm nr}_{2,0}\right\rangle = -3g_F\mu_B\mathcal{B}^{\rm nr}_{2,0}r_{\rm rot} \tag{3.17}$$

$$h\left\langle \delta f^{DB}\right\rangle = -3\frac{\delta g_F}{\mathcal{E}_{\rm rot}}\mu_B\left\langle \vec{\mathcal{E}}_{\rm rot}\cdot\vec{\mathcal{B}}^{\rm nr}_{2,0}\right\rangle = -3\delta g_F\mu_B\mathcal{B}^{\rm nr}_{2,0}r_{\rm rot} \tag{3.18}$$

The latter of these two shifts is a systematic error, caused by a non-reversing magnetic field gradient interacting with the slight difference in g-factors between the two doublets. The magnitude of this systematic shift in f^{DB} will be $\left\langle \delta f^{D}\right\rangle \dfrac{\mathcal{B}^{\rm nr}_{2,0}}{\mathcal{B}^{\rm rev}_{2,0}} \approx 210$ mHz $\times\dfrac{\mathcal{B}^{\rm nr}_{2,0}}{\mathcal{B}^{\rm rev}_{2,0}}$.

We go to great lengths to suppress this worrying systematic shift. First note that every time we take a block of data, we measure all 16 frequency channels made from the $\tilde{B}$, $\tilde{D}$, $\tilde{R}$ and $\tilde{I}$ switches. This includes f^B, which according to Equation 3.17 contains a shift proportional to $\mathcal{B}^{\rm nr}_{2,0}$. If we assume that this is the only shift in f^B, an assumption that we carefully check,[14] we can use our measurement of f^B in order to shim the currents through the $\vec{\mathcal{B}}^0$ coils in the subsequent block to bring $\mathcal{B}^{\rm rev}_{2,0}$ as close to zero as we can. This shimming procedure was quite successful; the magnitude of the largest f^B measured in any block was 35 mHz while the median magnitude was 2.3 mHz. These correspond to non-reversing magnetic fields that give rise to systematics of 75 and 5 μHz per block.

To remove the systematic effect more completely, we also can correct our measurement of

[14] This is a two part assumption. The first part is that Equation 3.17 is the only frequency shift in our experiment that is even with respect to all of our switch states, which will be evaluated in Sections 3.3 and 3.5. The second assumption is that our measurement of f^B does not contain significant shift due to the mixing terms like the ones in Equation 3.2. Since Δ^0 and Δ^D are similar in magnitude, the shifts caused by the mixing terms in f^B will be similar in magnitude to the ones discussed in Section 3.1. Those showed up at the $\sim$ 100s nHz level, and are therefore small enough to ignore.

f^{DB} using our measured value of f^B:

$$f^{DB}_{\text{corrected}} = f^{DB} - \frac{\delta g_F}{g_F} f^B \tag{3.19}$$

Note that the two approaches, shimming the magnetic field and correcting the measurement, are mathematically equivalent approaches to removing the systematic. We do both. Because we shimmed the non-reversing magnetic field before we corrected f^{DB}, the average correction over the whole dataset was just 90 nHz.

There are two more comments to make about this systematic effect. The first is that, in order for our correction to be successful, we need to know $\frac{\delta g_F}{g_F}$ quite accurately. This is an experimentally measured quantity with the data shown in Figure 3.2. The second point is that, while we have successfully stomped out this systematic, we now have a host of new problems. Any shift δf^B which does not have an associated $\tilde{D}$-odd shift that is $\frac{\delta g_F}{g_F}$ times smaller will cause a systematic error in our measurement of the eEDM. These shifts can be magnetic in cases where $\langle \hat{\mathcal{E}} \cdot \vec{\mathcal{B}} \rangle \neq \langle \vec{\mathcal{E}} \cdot \vec{\mathcal{B}} \rangle / |\vec{\mathcal{E}}|$, which will be addressed in Section 3.3. Additionally, Berry's phase can cause shifts that are even with respect to all of switch states without any $\tilde{D}$-odd effect, which are discussed in Section 3.5.

3.2.3 Imperfect Doublet Overlap

Before moving onto Zeeman effects that cause shifts in f^B and f^{DB} that may not be cancelled out perfectly, it is worth asking if there are any Zeeman shifts that are inherently $\tilde{D}$-odd. We assume throughout the rest of this thesis that the cloud of upper doublet molecules is overlapped in space and time with the cloud of lower doublet molecules. If this is the case the magnetic fields seen by the ions are inherently $\tilde{D}$-even and the only way to cause $\tilde{D}$-odd Zeeman shifts is via the small difference in g-factor δg.

But what if the clouds are in slightly different places $\langle r_i \rangle^D$? Or what if the doublet clouds have different sizes $\langle r_i^2 \rangle^D$? In this case $\tilde{B}$-even magnetic fields that cause first- and second-order

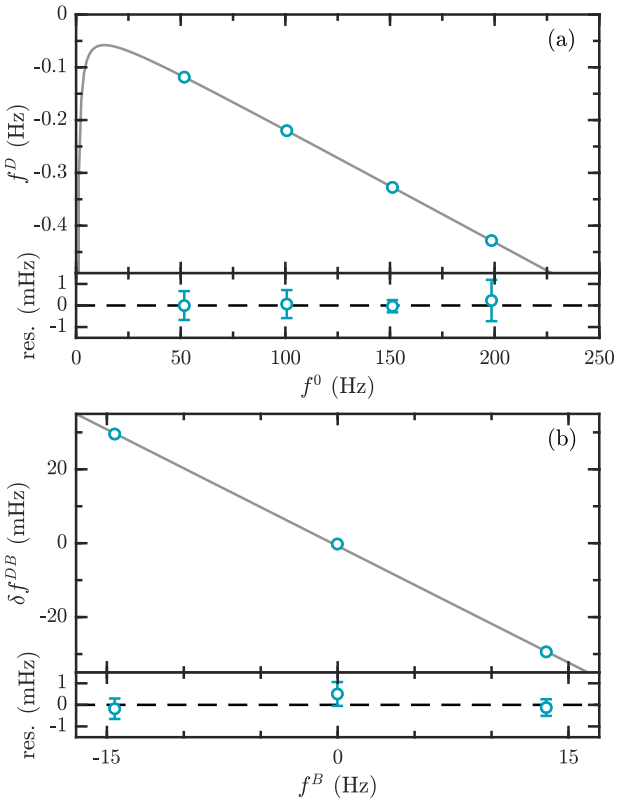

Figure 3.2: Measurement of $\frac{\delta g_F}{g_F}$. (a) f^D vs f^0 for various values of the applied quadrupole magnetic field, $\vec{\mathcal{B}}^0$. Data taken at $\mathcal{E}_{\rm rot} \sim 58\,{\rm V\,cm^{-1}}$. Fit is to $f^D = \frac{\delta g_F}{g_F} f^0 + \frac{\Delta^0 \Delta^D}{f^0}$, giving $\frac{\delta g_F}{g_F} = -0.002\,149(3)$, $\Delta^0\Delta^D = -0.39(4)\,{\rm Hz}^2$. (b) Change in f^{DB} vs f^B induced by introducing a large non-reversing $\mathcal{B}_{2,0}$. Fitted gradient is equal to $\frac{\delta g_F}{g_F} - \frac{\Delta^0\Delta^D}{f^{0\,2}}$ and when combined with value of $\Delta^0\Delta^D$ from (a) gives $\frac{\delta g_F}{g_F} = -0.002\,13(2)$, in excellent agreement. Note that this is the only effect we ever saw cause a shift in f^{DB}. Under each plot we show the residuals after fits are subtracted.

gradients in f^B would lead directly to $\tilde{D}$-odd systematic shifts:

$$\delta f^{DB} = \sum_{i=x,y,z} \langle r_i \rangle^D \frac{\partial f^B}{\partial r_i} + \langle r_i^2 \rangle^D \frac{\partial^2 f^B}{\partial r_i^2} \tag{3.20}$$

We measured these gradients by moving the ions around in the trap and found $\frac{\partial f^B}{\partial r_i} \sim 40$ mHz/cm and $\frac{\partial^2 f^B}{\partial r_i^2} \sim 10$ mHz/cm^2. In order to keep the systematics shifts at least an order of magnitude smaller than our systematic error bar, we need $\langle r_i \rangle^D \lesssim 1\times10^{-4}$ cm and $\langle r_i^2 \rangle^D \lesssim 5\times10^{-4}$

Table 3.2: f^B Curavatures with and without Permanent Magnets

Effect	x	y	z
$\frac{\partial f^B}{\partial r_i}$ without Magnets (mHz/cm)	18(2)	47(2)	47(2)
$\frac{\partial^2 f^B}{\partial r_i^2}$ without Magnets (mHz/cm^2)	-2(10)	9(10)	-4(4)
$\frac{\partial f^B}{\partial r_i}$ with Magnets (mHz/cm)	-1090(10)	450(10)	-1500(20)
$\frac{\partial^2 f^B}{\partial r_i^2}$ with Magnets (mHz/cm^2)	250(50)	-170(30)	-1210(20)

cm^2.

We took two approaches to measure these $\tilde{D}$-odd moments of the doublet clouds. The first approach, which I will discuss now, did not work. It was fun though, and I want to record it in my thesis. Our idea was to place permanent magnets – found in the hallways of JILA holding up posters – around our ion trap to induce $\tilde{B}$-even gradients in f^B. This was after we completed our ~ 650 hour long dataset, so we really hoped that this would not permanently magnetize our apparatus if we needed to retake any data.[15] With the magnets in place we repeated our measurements of $\frac{\partial f^B}{\partial r_i}$ and $\frac{\partial^2 f^B}{\partial r_i^2}$. An example of the gradients we measured along the z-axis is shown in Figure 3.3. The gradients created by this particular orientation of magnets is summarized in Table 3.2

After measuring the curvatures we took a few hours of precision data with the magnets still in

[15]Putting the magnets above the vacuum chamber was easy. Three magnets were stacked together and they sat in a small cardboard box that rested on the vacuum chamber. The cardboard box was there so the magnets would not sit directly on our permanent vacuum chamber and possibly permanently magnetize it. Getting the other set of permanent magnets below the vacuum chamber was trickier, as it was very hard to reach into the space and place anything precisely. I ended up stacking the cardboard box that contains the permanent magnets on top of a pile of paper towels. I could adjust the number of paper towels to change the magnets' height, and attempted to have the top of the cardboard box rest directly against the bottom of the vacuum chamber. I should clarify that this was done when I was left alone in lab for a week or so, as I think Tanya Roussy and Luke Caldwell have no desire to claim this work as their own. I, on the other hand, made sure this brilliant stroke of engineering for a precision measurement is permanently recorded in my thesis.

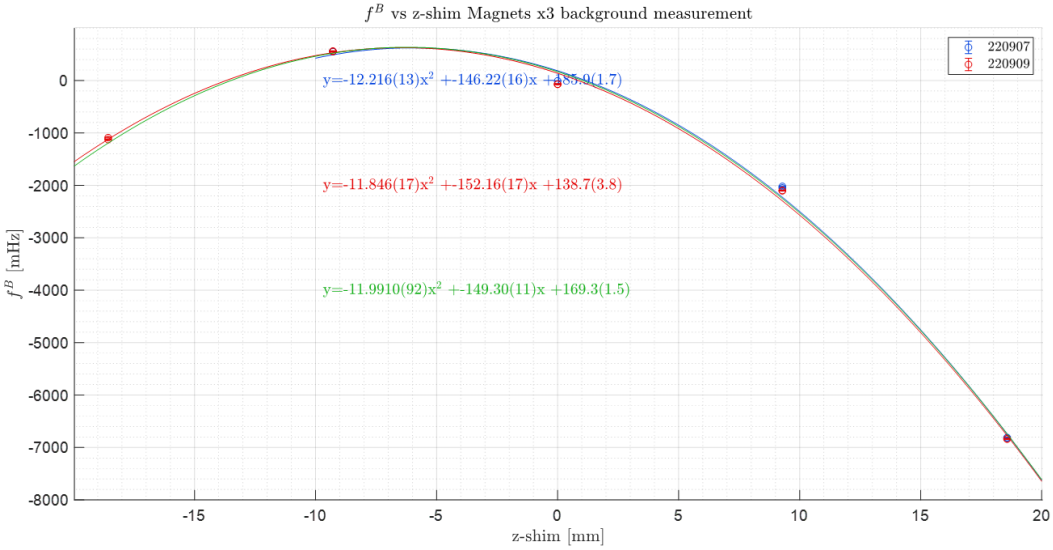

Figure 3.3: Three permanent magnets were placed above and below the ion trap, generating a curvature in f^B via the Zeeman effect. We moved the center of the ion trap to different positions along the z-axis and measured f^B on two different days, the 7th and 9th of September 2022. On both days we saw $\frac{\partial^2 f^B}{\partial z^2} \sim 1200$ mHz/cm^2 and $\frac{\partial f^B}{\partial z} \sim 1500$ mHz/cm, both much larger values than background values of $\frac{\partial^2 f^B}{\partial z^2} \sim 5$ mHz/cm^2 and $\frac{\partial f^B}{\partial z} \sim 47$ mHz/cm. For a full comparison of the curvatures with and without the magnets in all three directions, see Table 3.2.

place and the ions at the center of the trap. We measured $f^{DB} = 90(627)$ μHz, showing no evidence of a shift in f^{DB} from our central value -15(23) μHz. In principle, we can use this measurement to set a limit on a linear combination of the six $\tilde{D}$-odd sizes $\langle r_i \rangle^D$ and $\langle r_i^2 \rangle^D$. If we took more precision data with different values of $\frac{\partial f^B}{\partial r_i}$ and $\frac{\partial^2 f^B}{\partial r_i^2}$, and continued not to see shifts in f^{DB}, we perhaps could set sufficiently small limits on $\langle r_i \rangle^D$ and $\langle r_i^2 \rangle^D$.

In practice, this was quite difficult. We were limited in terms of where we could physically place the permanent magnets by our apparatus. As can be seen in Figure 2.6, the vacuum chamber extends to both sides of the ion trap along the y-axis, meaning it was especially difficult to make large gradients $\frac{\partial f^B}{\partial y}$ and $\frac{\partial^2 f^B}{\partial y^2}$. Additionally, we were nervous about using magnets that were too large around our trap in case the apparatus became permanently magnetized. This could have been disastrous if for any reason we needed to take more precision EDM data. In the end we came

up with a number of arguments for how $\langle r_i \rangle^D$ and $\langle r_i^2 \rangle^D$ could arise in our experiment and why they must be small. See Section VI D 2 of the Systematics paper for that discussion. Via those arguments we conservatively constrain the net systematic shift to be 3.5 μHz at most.

3.3 Systematics from Magnetic Shifts in f^B and f^{DB}

The correction to f^{DB} discussed in Subsection 3.2.2 relies on the assumption that all shifts in f^B are magnetic and appear $\frac{\delta g_F}{g_F}$ times smaller in f^{DB}. However, we saw that this assumption fails for any Zeeman shifts caused by electric and magnetic fields where $\langle \hat{\mathcal{E}} \cdot \vec{\mathcal{B}} \rangle \neq \langle \vec{\mathcal{E}} \cdot \vec{\mathcal{B}} \rangle / |\vec{\mathcal{E}}|$. In this case we would have:

$$\begin{aligned} f^{DB}_{\text{corrected}} &= f^{DB} - \frac{\delta g_F}{g_F} f^B \\ &= 2d_e \mathcal{E}_{\text{eff}} - 3\delta g_F \mu_B \frac{\langle \vec{\mathcal{E}} \cdot \vec{\mathcal{B}} \rangle}{|\vec{\mathcal{E}}|} - \frac{\delta g_F}{g_F} \left(-3 g_F \mu_B \langle \hat{\mathcal{E}} \cdot \vec{\mathcal{B}} \rangle \right) \\ &= 2d_e \mathcal{E}_{\text{eff}} - 3\delta g_F \mu_B \frac{\langle \vec{\mathcal{E}} \cdot \vec{\mathcal{B}} \rangle}{|\vec{\mathcal{E}}|} + 3\delta g_F \mu_B \langle \hat{\mathcal{E}} \cdot \vec{\mathcal{B}} \rangle \\ &= 2d_e \mathcal{E}_{\text{eff}} + 3\delta g_F \mu_B \left(\langle \hat{\mathcal{E}} \cdot \vec{\mathcal{B}} \rangle - \frac{\langle \vec{\mathcal{E}} \cdot \vec{\mathcal{B}} \rangle}{|\vec{\mathcal{E}}|} \right) \end{aligned} \tag{3.21}$$

In order to minimize this systematic shift we need to find all possible combinations of electric and magnetic fields where $\langle \hat{\mathcal{E}} \cdot \vec{\mathcal{B}} \rangle \neq \langle \vec{\mathcal{E}} \cdot \vec{\mathcal{B}} \rangle / |\vec{\mathcal{E}}|$. Luke Caldwell approached this problem analytically while I simulated the shifts numerically. These methods will be discussed in the next two subsections.

3.3.1 Analytic Approach to Zeeman Systematics

The ideal electric field in our experiment is $\vec{\mathcal{E}} = \vec{\mathcal{E}}_{\text{rot}} + \vec{\mathcal{E}}_{\text{RF}} + \vec{\mathcal{E}}_{\text{DC}}$, where the three electric fields are given by Equations 2.4 – 2.6 and the largest of which is $\vec{\mathcal{E}}_{\text{rot}}$. As discussed in Subsection 2.2.1.3, we create $\vec{\mathcal{E}}_{\text{rot}} \sim 58$ V/cm by applying voltages ~ 350 V to eight radial electrodes. Those voltages which oscillate at 375 kHz are generated by DDS (direct digital synthesis) boards and amplified

by high-powered op-amps. The op-amps inevitably add harmonic distortions when generating the voltages to apply $\vec{\mathcal{E}}_{\text{rot}}$, which we can write as:

$$\vec{\mathcal{E}}_{\text{nh}}(t) = \mathcal{E}_{\text{nhx}} \cos\left(n\omega_{\text{rot}}t + \phi_{\text{nx}}\right)\hat{x} + \mathcal{E}_{\text{nhy}} \cos\left(n\omega_{\text{rot}}t + \phi_{\text{ny}}\right)\hat{y} + \mathcal{E}_{\text{nhz}} \cos\left(n\omega_{\text{rot}}t + \phi_{\text{nz}}\right)\hat{z} \tag{3.22}$$

The other predominant imperfection in our electric field is the ellipticity of $\vec{\mathcal{E}}_{\text{rot}}$. This can arise either because the voltages on the eight radial electrodes are unequal or the electrodes are slightly out of place. We can write the ellipticity as:

$$\vec{\mathcal{E}}_{\epsilon}(t) = \mathcal{E}_{\epsilon}\Big(\cos\left(2\theta - \omega_{\text{rot}}t\right)\hat{x} + \sin\left(2\theta - \omega_{\text{rot}}t\right)\hat{y}\Big) \tag{3.23}$$

The strategy now is to analytically calculate the micromotion of the HfF^+ molecules in the electric field $\vec{\mathcal{E}} = \vec{\mathcal{E}}_{\text{rot}} + \kappa\delta\vec{\mathcal{E}}$, where $\delta\vec{\mathcal{E}}$ represents all perturbations to the idealized rotating electric field. This runs into a chicken and egg problem because $\vec{\mathcal{E}}_{\text{RF}}$ and $\vec{\mathcal{E}}_{\text{DC}}$ both vary spatially, as seen in Equations 2.4 and 2.5. We want to find the ion trajectories from the electric field, but we need the ion trajectories to know the magnitude of $\vec{\mathcal{E}}_{\text{RF}}$ and $\vec{\mathcal{E}}_{\text{DC}}$. To get around this obstacle we approximate the effects of the spatial variance with time-varying fields:

$$\vec{\mathcal{E}}_{\text{sec}} = \mathcal{E}_{\text{secx}} \cos\left(\omega_{\text{secx}}t + \phi_{\text{secx}}\right)\hat{x} + \mathcal{E}_{\text{secy}} \cos\left(\omega_{\text{secy}}t + \phi_{\text{secy}}\right)\hat{y} + \mathcal{E}_{\text{secz}} \cos\left(\omega_{\text{secz}}t + \phi_{\text{secz}}\right)\hat{z} \tag{3.24}$$

$$\begin{aligned}\vec{\mathcal{E}}_{\text{RFeff}} = {} & \mathcal{E}_{\text{RFeffx}} \cos\left(\omega_{\text{secx}}t + \phi_{\text{secx}}\right) \cos\left(\omega_{\text{RF}}t + \phi_{\text{RF}}\right)\hat{x} \\ & + \mathcal{E}_{\text{RFeffy}} \cos\left(\omega_{\text{secy}}t + \phi_{\text{secy}}\right) \cos\left(\omega_{\text{RF}}t + \phi_{\text{RF}}\right)\hat{y} \\ & + \mathcal{E}_{\text{RFeffz}} \cos\left(\omega_{\text{secz}}t + \phi_{\text{secz}}\right) \cos\left(\omega_{\text{RF}}t + \phi_{\text{RF}}\right)\hat{z}\end{aligned} \tag{3.25}$$

Equation 3.24 is an electric field that causes the secular motion of the trapped ions. Equation 3.25 is meant to capture the RF micromotion – it is large when the RF field is large and the secular motion is at its maximum. This captures most of the effects of our electric fields, though it does not include pondermotive forces. We note that those forces are included in the numerical model described in Subsection 3.3.2.

Once we have the particle trajectories, we consider the molecules' motion through a magnetic field $\vec{\mathcal{B}} = \vec{\mathcal{B}}_{2,0} + \kappa\delta\vec{\mathcal{B}}$, where $\delta\vec{\mathcal{B}}$ are the zero, first and second order magnetic field gradients listed in Table 3.1 other than $\vec{\mathcal{B}}_{2,0}$. The calculated trajectory allows us to write down the time-dependent magnetic field experienced by a HfF^+ molecule. We can finally calculate $\langle\hat{\mathcal{E}}\cdot\vec{\mathcal{B}}\rangle$ and $\langle\vec{\mathcal{E}}\cdot\vec{\mathcal{B}}\rangle$, where the time average is over an integer number of periods of all relevant frequencies. We keep terms up to $\mathcal{O}(\kappa^2)$ before setting $\kappa = 1$.

As mentioned before, the only frequency shift that is zeroth order in κ is the one from $\vec{\mathcal{E}}_{\text{rot}}$ interacting with $\vec{\mathcal{B}}_{2,0}$. There are no frequency shifts first order in κ. This means that there are no frequency shifts from $\vec{\mathcal{E}}_{\text{rot}}$ interacting with one field in $\delta\vec{\mathcal{B}}$ or from one field in $\delta\vec{\mathcal{E}}$ interacting with $\vec{\mathcal{B}}_{2,0}$. There are a host of frequency shifts that are second order in κ, listed in Tables 3.3 – 3.5. Note that these table only include up to the the $n = 4$th harmonic, a choice which will be justified in Subsection 3.3.4.

3.3.2 Numerical Approach to Zeeman Systematics

In addition to the analytic approach of finding which combinations of electric and magnetic fields generate Zeeman shifts, we wanted to approach the problem numerically as well. The idea was to calculate the trajectory of HfF^+ ions in the full electric and magnetic fields at small discrete time steps. We then found the electric and magnetic fields at the ion locations, which allowed us to calculate $\hat{\mathcal{E}}\cdot\vec{\mathcal{B}}$ and $\vec{\mathcal{E}}\cdot\vec{\mathcal{B}}$ at each time step. The values were then averaged over the entire trajectory, giving us values for $\langle\hat{\mathcal{E}}\cdot\vec{\mathcal{B}}\rangle$ and $\langle\vec{\mathcal{E}}\cdot\vec{\mathcal{B}}\rangle$.

Table 3.3: Analytically Calculated Zeeman Shifts, Part 1

Number	$\langle \hat{\mathcal{E}} \cdot \vec{\mathcal{B}} \rangle$	$\langle \vec{\mathcal{E}} \cdot \vec{\mathcal{B}} \rangle / \mathcal{E}_{\mathrm{rot}}$	$\frac{\langle \vec{\mathcal{E}} \cdot \vec{\mathcal{B}} \rangle / \mathcal{E}_{\mathrm{rot}}}{\langle \hat{\mathcal{E}} \cdot \vec{\mathcal{B}} \rangle}$
1	$-\frac{\mathcal{B}_{1,1}\mathcal{E}_{2\mathrm{hx}} \cos\phi_{2\mathrm{x}}}{4\mathcal{E}_{\mathrm{rot}}}$	0	0
2	$\frac{\mathcal{B}_{1,1}\mathcal{E}_{2\mathrm{hy}} \sin\phi_{2\mathrm{y}}}{4\mathcal{E}_{\mathrm{rot}}}$	0	0
3	$\frac{\mathcal{B}_{1,-1}\mathcal{E}_{2\mathrm{hy}} \cos\phi_{2\mathrm{y}}}{4\mathcal{E}_{\mathrm{rot}}}$	0	0
4	$\frac{\mathcal{B}_{1,-1}\mathcal{E}_{2\mathrm{hx}} \sin\phi_{2\mathrm{x}}}{4\mathcal{E}_{\mathrm{rot}}}$	0	0
5	$\frac{\sqrt{3}\mathcal{B}_{2,2}\mathcal{E}_{3\mathrm{hx}} r_{\mathrm{rot}} \cos\phi_{3\mathrm{x}}}{4\mathcal{E}_{\mathrm{rot}}}$	0	0
6	$-\frac{\sqrt{3}\mathcal{B}_{2,2}\mathcal{E}_{3\mathrm{hy}} r_{\mathrm{rot}} \sin\phi_{3\mathrm{y}}}{4\mathcal{E}_{\mathrm{rot}}}$	0	0
7	$-\frac{\sqrt{3}\mathcal{B}_{2,-2}\mathcal{E}_{3\mathrm{hy}} r_{\mathrm{rot}} \cos\phi_{3\mathrm{y}}}{4\mathcal{E}_{\mathrm{rot}}}$	0	0
8	$-\frac{\sqrt{3}\mathcal{B}_{2,-2}\mathcal{E}_{3\mathrm{hy}} r_{\mathrm{rot}} \sin\phi_{3\mathrm{y}}}{4\mathcal{E}_{\mathrm{rot}}}$	0	0
9	$-\frac{5\mathcal{B}_{2,0}\mathcal{E}_{3\mathrm{hx}}\mathcal{E}_{\epsilon} r_{\mathrm{rot}} \cos(2\theta + \phi_{3\mathrm{x}})}{18\mathcal{E}_{\mathrm{rot}}^2}$	0	0
10	$\frac{5\mathcal{B}_{2,0}\mathcal{E}_{3\mathrm{hy}}\mathcal{E}_{\epsilon} r_{\mathrm{rot}} \sin(2\theta + \phi_{3\mathrm{y}})}{18\mathcal{E}_{\mathrm{rot}}^2}$	0	0
11	$-\frac{5\mathcal{B}_{2,0}\mathcal{E}_{2\mathrm{hx}}\mathcal{E}_{4\mathrm{hx}} r_{\mathrm{rot}} \cos(\phi_{2\mathrm{x}} - \phi_{4\mathrm{x}})}{128\mathcal{E}_{\mathrm{rot}}^2}$	0	0
12	$\frac{5\mathcal{B}_{2,0}\mathcal{E}_{2\mathrm{hy}}\mathcal{E}_{4\mathrm{hy}} r_{\mathrm{rot}} \cos(\phi_{2\mathrm{y}} - \phi_{4\mathrm{y}})}{128\mathcal{E}_{\mathrm{rot}}^2}$	0	0
13	$-\frac{5\mathcal{B}_{2,0}\mathcal{E}_{2\mathrm{hy}}\mathcal{E}_{4\mathrm{hx}} r_{\mathrm{rot}} \sin(\phi_{2\mathrm{y}} - \phi_{4\mathrm{x}})}{128\mathcal{E}_{\mathrm{rot}}^2}$	0	0
14	$-\frac{5\mathcal{B}_{2,0}\mathcal{E}_{2\mathrm{hx}}\mathcal{E}_{4\mathrm{hy}} r_{\mathrm{rot}} \sin(\phi_{2\mathrm{x}} - \phi_{4\mathrm{y}})}{128\mathcal{E}_{\mathrm{rot}}^2}$	0	0
15	$-\frac{3\sqrt{\frac{5}{2}}\mathcal{B}_{3,3}\mathcal{E}_{4\mathrm{hx}} r_{\mathrm{rot}}^2 \cos\phi_{4\mathrm{x}}}{8\mathcal{E}_{\mathrm{rot}}}$	0	0
16	$\frac{3\sqrt{\frac{5}{2}}\mathcal{B}_{3,-3}\mathcal{E}_{4\mathrm{hy}} r_{\mathrm{rot}}^2 \cos\phi_{4\mathrm{y}}}{8\mathcal{E}_{\mathrm{rot}}}$	0	0
17	$\frac{3\sqrt{\frac{5}{2}}\mathcal{B}_{3,-3}\mathcal{E}_{4\mathrm{hx}} r_{\mathrm{rot}}^2 \sin\phi_{4\mathrm{x}}}{8\mathcal{E}_{\mathrm{rot}}}$	0	0
18	$\frac{3\sqrt{\frac{5}{2}}\mathcal{B}_{3,3}\mathcal{E}_{4\mathrm{hy}} r_{\mathrm{rot}}^2 \sin\phi_{4\mathrm{y}}}{8\mathcal{E}_{\mathrm{rot}}}$	0	0

Table 3.4: Analytically Calculated Zeeman Shifts, Part 2

Number	$\langle\hat{\mathcal{E}}\cdot\vec{\mathcal{B}}\rangle$	$\langle\vec{\mathcal{E}}\cdot\vec{\mathcal{B}}\rangle/\mathcal{E}_{\rm rot}$	$\frac{\langle\vec{\mathcal{E}}\cdot\vec{\mathcal{B}}\rangle/\mathcal{E}_{\rm rot}}{\langle\hat{\mathcal{E}}\cdot\vec{\mathcal{B}}\rangle}$
19	$-\frac{\mathcal{B}_{2,0}\mathcal{E}_{\rm 2hz}^2 r_{\rm rot}}{4\mathcal{E}_{\rm rot}^2}$	$-\frac{\mathcal{B}_{2,0}\mathcal{E}_{\rm 2hz}^2 r_{\rm rot}}{4\mathcal{E}_{\rm rot}^2}$	1
20	$-\frac{\mathcal{B}_{2,0}\mathcal{E}_{\rm 3hz}^2 r_{\rm rot}}{9\mathcal{E}_{\rm rot}^2}$	$-\frac{\mathcal{B}_{2,0}\mathcal{E}_{\rm 3hz}^2 r_{\rm rot}}{9\mathcal{E}_{\rm rot}^2}$	1
21	$-\frac{\mathcal{B}_{2,0}\mathcal{E}_{\rm 4hz}^2 r_{\rm rot}}{16\mathcal{E}_{\rm rot}^2}$	$-\frac{\mathcal{B}_{2,0}\mathcal{E}_{\rm 4hz}^2 r_{\rm rot}}{16\mathcal{E}_{\rm rot}^2}$	1
22	$-\frac{\mathcal{B}_{2,0}\mathcal{E}_{\rm secz}^2 r_{\rm rot}\omega_{\rm rot}^2}{\mathcal{E}_{\rm rot}^2\omega_{\rm secz}^2}$	$-\frac{\mathcal{B}_{2,0}\mathcal{E}_{\rm secz}^2 r_{\rm rot}\omega_{\rm rot}^2}{\mathcal{E}_{\rm rot}^2\omega_{\rm secz}^2}$	1
23	$-\frac{\mathcal{B}_{2,0}\mathcal{E}_{\rm RFeffz}^2 r_{\rm rot}\omega_{\rm rot}^2}{4\mathcal{E}_{\rm rot}(\omega_{\rm RF}-\omega_{\rm secz})^2}$	$-\frac{\mathcal{B}_{2,0}\mathcal{E}_{\rm RFeffz}^2 r_{\rm rot}\omega_{\rm rot}^2}{4\mathcal{E}_{\rm rot}(\omega_{\rm RF}-\omega_{\rm secz})^2}$	1
24	$-\frac{\mathcal{B}_{2,0}\mathcal{E}_{\rm RFeffz}^2 r_{\rm rot}\omega_{\rm rot}^2}{4\mathcal{E}_{\rm rot}(\omega_{\rm RF}+\omega_{\rm secz})^2}$	$-\frac{\mathcal{B}_{2,0}\mathcal{E}_{\rm RFeffz}^2 r_{\rm rot}\omega_{\rm rot}^2}{4\mathcal{E}_{\rm rot}(\omega_{\rm RF}+\omega_{\rm secz})^2}$	1
25	$\frac{3\sqrt{15}\mathcal{B}_{3,2}\mathcal{E}_{\rm 2hz} r_{\rm rot}^2\cos\phi_{\rm 2z}}{8\mathcal{E}_{\rm rot}}$	$\frac{3\sqrt{15}\mathcal{B}_{3,2}\mathcal{E}_{\rm 2hz} r_{\rm rot}^2\cos\phi_{\rm 2z}}{8\mathcal{E}_{\rm rot}}$	1
26	$-\frac{3\sqrt{15}\mathcal{B}_{3,-2}\mathcal{E}_{\rm 2hz} r_{\rm rot}^2\sin\phi_{\rm 2z}}{8\mathcal{E}_{\rm rot}}$	$-\frac{3\sqrt{15}\mathcal{B}_{3,-2}\mathcal{E}_{\rm 2hz} r_{\rm rot}^2\sin\phi_{\rm 2z}}{8\mathcal{E}_{\rm rot}}$	1
27	$-\frac{3\sqrt{3}\mathcal{B}_{2,2}\mathcal{E}_{\epsilon} r_{\rm rot}\cos 2\theta}{2\mathcal{E}_{\rm rot}}$	$-\frac{2\sqrt{3}\mathcal{B}_{2,2}\mathcal{E}_{\epsilon} r_{\rm rot}\cos 2\theta}{\mathcal{E}_{\rm rot}}$	$\frac{4}{3}$
28	$-\frac{3\sqrt{3}\mathcal{B}_{2,-2}\mathcal{E}_{\epsilon} r_{\rm rot}\sin 2\theta}{2\mathcal{E}_{\rm rot}}$	$-\frac{2\sqrt{3}\mathcal{B}_{2,-2}\mathcal{E}_{\epsilon} r_{\rm rot}\sin 2\theta}{\mathcal{E}_{\rm rot}}$	$\frac{4}{3}$
29	$\frac{3\sqrt{\frac{5}{2}}\mathcal{B}_{3,3}\mathcal{E}_{\rm 2hx} r_{\rm rot}^2\cos\phi_{\rm 2x}}{4\mathcal{E}_{\rm rot}}$	$\frac{9\sqrt{\frac{5}{2}}\mathcal{B}_{3,3}\mathcal{E}_{\rm 2hx} r_{\rm rot}^2\cos\phi_{\rm 2x}}{8\mathcal{E}_{\rm rot}}$	$\frac{3}{2}$
30	$\frac{3\sqrt{\frac{5}{2}}\mathcal{B}_{3,-3}\mathcal{E}_{\rm 2hy} r_{\rm rot}^2\cos\phi_{\rm 2y}}{4\mathcal{E}_{\rm rot}}$	$\frac{9\sqrt{\frac{5}{2}}\mathcal{B}_{3,-3}\mathcal{E}_{\rm 2hy} r_{\rm rot}^2\cos\phi_{\rm 2y}}{8\mathcal{E}_{\rm rot}}$	$\frac{3}{2}$
31	$-\frac{3\sqrt{\frac{5}{2}}\mathcal{B}_{3,-3}\mathcal{E}_{\rm 2hx} r_{\rm rot}^2\sin\phi_{\rm 2x}}{4\mathcal{E}_{\rm rot}}$	$-\frac{9\sqrt{\frac{5}{2}}\mathcal{B}_{3,-3}\mathcal{E}_{\rm 2hx} r_{\rm rot}^2\sin\phi_{\rm 2x}}{8\mathcal{E}_{\rm rot}}$	$\frac{3}{2}$
32	$\frac{3\sqrt{\frac{5}{2}}\mathcal{B}_{3,3}\mathcal{E}_{\rm 2hy} r_{\rm rot}^2\sin\phi_{\rm 2y}}{4\mathcal{E}_{\rm rot}}$	$\frac{9\sqrt{\frac{5}{2}}\mathcal{B}_{3,3}\mathcal{E}_{\rm 2hy} r_{\rm rot}^2\sin\phi_{\rm 2y}}{8\mathcal{E}_{\rm rot}}$	$\frac{3}{2}$

Table 3.5: Analytically Calculated Zeeman Shifts, Part 3

Number	$\langle\hat{\mathcal{E}}\cdot\vec{\mathcal{B}}\rangle$	$\langle\vec{\mathcal{E}}\cdot\vec{\mathcal{B}}\rangle/\mathcal{E}_{\rm rot}$	$\frac{\langle\vec{\mathcal{E}}\cdot\vec{\mathcal{B}}\rangle/\mathcal{E}_{\rm rot}}{\langle\hat{\mathcal{E}}\cdot\vec{\mathcal{B}}\rangle}$
33	$\frac{\mathcal{B}_{2,0}\mathcal{E}_{\rm 2hx}^2 r_{\rm rot}}{16\mathcal{E}_{\rm rot}^2}$	$\frac{\mathcal{B}_{2,0}\mathcal{E}_{\rm 2hx}^2 r_{\rm rot}}{8\mathcal{E}_{\rm rot}^2}$	2
34	$\frac{\mathcal{B}_{2,0}\mathcal{E}_{\rm 2hy}^2 r_{\rm rot}}{16\mathcal{E}_{\rm rot}^2}$	$\frac{\mathcal{B}_{2,0}\mathcal{E}_{\rm 2hy}^2 r_{\rm rot}}{8\mathcal{E}_{\rm rot}^2}$	2
35	$\frac{\mathcal{B}_{2,0}\mathcal{E}_{\rm 3hx}^2 r_{\rm rot}}{36\mathcal{E}_{\rm rot}^2}$	$\frac{\mathcal{B}_{2,0}\mathcal{E}_{\rm 3hx}^2 r_{\rm rot}}{18\mathcal{E}_{\rm rot}^2}$	2
36	$\frac{\mathcal{B}_{2,0}\mathcal{E}_{\rm 3hy}^2 r_{\rm rot}}{36\mathcal{E}_{\rm rot}^2}$	$\frac{\mathcal{B}_{2,0}\mathcal{E}_{\rm 3hy}^2 r_{\rm rot}}{18\mathcal{E}_{\rm rot}^2}$	2
37	$\frac{\mathcal{B}_{2,0}\mathcal{E}_{\rm 4hx}^2 r_{\rm rot}}{64\mathcal{E}_{\rm rot}^2}$	$\frac{\mathcal{B}_{2,0}\mathcal{E}_{\rm 4hx}^2 r_{\rm rot}}{32\mathcal{E}_{\rm rot}^2}$	2
38	$\frac{\mathcal{B}_{2,0}\mathcal{E}_{\rm 4hy}^2 r_{\rm rot}}{64\mathcal{E}_{\rm rot}^2}$	$\frac{\mathcal{B}_{2,0}\mathcal{E}_{\rm 4hy}^2 r_{\rm rot}}{32\mathcal{E}_{\rm rot}^2}$	2
39	$\frac{\mathcal{B}_{2,0}\mathcal{E}_{\epsilon}^2 r_{\rm rot}}{2\mathcal{E}_{\rm rot}^2}$	$\frac{\mathcal{B}_{2,0}\mathcal{E}_{\epsilon}^2 r_{\rm rot}}{\mathcal{E}_{\rm rot}^2}$	2
40	$\frac{\mathcal{B}_{2,0}\mathcal{E}_{\rm secx}^2 r_{\rm rot}\omega_{\rm rot}^2}{4\mathcal{E}_{\rm rot}^2\omega_{\rm secx}^2}$	$\frac{\mathcal{B}_{2,0}\mathcal{E}_{\rm secx}^2 r_{\rm rot}\omega_{\rm rot}^2}{2\mathcal{E}_{\rm rot}^2\omega_{\rm secx}^2}$	2
41	$\frac{\mathcal{B}_{2,0}\mathcal{E}_{\rm secy}^2 r_{\rm rot}\omega_{\rm rot}^2}{4\mathcal{E}_{\rm rot}^2\omega_{\rm secy}^2}$	$\frac{\mathcal{B}_{2,0}\mathcal{E}_{\rm secy}^2 r_{\rm rot}\omega_{\rm rot}^2}{2\mathcal{E}_{\rm rot}^2\omega_{\rm secy}^2}$	2
42	$\frac{\mathcal{B}_{2,0}\mathcal{E}_{\rm RFeffx}^2 r_{\rm rot}\omega_{\rm rot}^2}{16\mathcal{E}_{\rm rot}^2(\omega_{\rm RF}-\omega_{\rm secx})^2}$	$\frac{\mathcal{B}_{2,0}\mathcal{E}_{\rm RFeffx}^2 r_{\rm rot}\omega_{\rm rot}^2}{8\mathcal{E}_{\rm rot}^2(\omega_{\rm RF}-\omega_{\rm secx})^2}$	2
43	$\frac{\mathcal{B}_{2,0}\mathcal{E}_{\rm RFeffx}^2 r_{\rm rot}\omega_{\rm rot}^2}{16\mathcal{E}_{\rm rot}^2(\omega_{\rm RF}+\omega_{\rm secx})^2}$	$\frac{\mathcal{B}_{2,0}\mathcal{E}_{\rm RFeffx}^2 r_{\rm rot}\omega_{\rm rot}^2}{8\mathcal{E}_{\rm rot}^2(\omega_{\rm RF}+\omega_{\rm secx})^2}$	2
44	$\frac{\mathcal{B}_{2,0}\mathcal{E}_{\rm RFeffy}^2 r_{\rm rot}\omega_{\rm rot}^2}{16\mathcal{E}_{\rm rot}^2(\omega_{\rm RF}-\omega_{\rm secy})^2}$	$\frac{\mathcal{B}_{2,0}\mathcal{E}_{\rm RFeffy}^2 r_{\rm rot}\omega_{\rm rot}^2}{8\mathcal{E}_{\rm rot}^2(\omega_{\rm RF}-\omega_{\rm secy})^2}$	2
45	$\frac{\mathcal{B}_{2,0}\mathcal{E}_{\rm RFeffy}^2 r_{\rm rot}\omega_{\rm rot}^2}{16\mathcal{E}_{\rm rot}^2(\omega_{\rm RF}+\omega_{\rm secy})^2}$	$\frac{\mathcal{B}_{2,0}\mathcal{E}_{\rm RFeffy}^2 r_{\rm rot}\omega_{\rm rot}^2}{8\mathcal{E}_{\rm rot}^2(\omega_{\rm RF}+\omega_{\rm secy})^2}$	2
46	0	$-\frac{3\sqrt{\frac{3}{2}}\mathcal{B}_{3,1}\mathcal{E}_{\rm 2hx}r_{\rm rot}^2\cos\phi_{\rm 2x}}{8\mathcal{E}_{\rm rot}}$	∞
47	0	$\frac{3\sqrt{\frac{3}{2}}\mathcal{B}_{3,-1}\mathcal{E}_{\rm 2hy}r_{\rm rot}^2\cos\phi_{\rm 2y}}{8\mathcal{E}_{\rm rot}}$	∞
48	0	$\frac{3\sqrt{\frac{3}{2}}\mathcal{B}_{3,-1}\mathcal{E}_{\rm 2hx}r_{\rm rot}^2\sin\phi_{\rm 2x}}{8\mathcal{E}_{\rm rot}}$	∞
49	0	$\frac{3\sqrt{\frac{3}{2}}\mathcal{B}_{3,1}\mathcal{E}_{\rm 2hy}r_{\rm rot}^2\sin\phi_{\rm 2y}}{8\mathcal{E}_{\rm rot}}$	∞

The numerical simulations added a level of realism not included in the analytic approach. The simulations always included $\vec{\mathcal{E}}_{\text{rot}}$ and the full DC and RF electric fields which give rise to pondermotive potentials. In many of the simulations the electric fields were written as the perfectly uniform fields given by Equations 2.4 – 2.6. Some of the more detailed simulations instead calculated the electric fields from voltages applied to our ten electrodes, with voltage to electric field conversion factors given in Appendix C.4 of William Cairncross's thesis [1]. The resulting electric fields were less homogeneous and more accurately represented the fields experienced by our ions. We did not see any significant difference between the two methods of simulating electric fields, which is convenient because the simpler fields are faster to simulate and indicate that the analytic approach does not miss anything important in this instance.

In addition to the three standard electric fields, a numerical simulation typically included one additional electric field perturbation such as an ellipticity or harmonic along a particular axis. The simulation also included typically included $\tilde{B}\mathcal{B}_{2,0}^{\text{rev}}$ and one more of the magnetic fields in Table 3.1 that would not change sign with $\tilde{B}$. As these are numerical simulations, particular values for the magnitudes and phases for each field were chosen.

After selecting the fields, a time step Δt and integration time T_{int} were chosen. Δt was selected so it was small compared to the inverse of the largest frequency in the simulation. T_{int} was chosen to include many secular frequencies ~ 1 kHz, as that was always the slowest characteristic frequency of the system. As long as $N_{\text{steps}} = \dfrac{T_{\text{int}}}{\Delta t} \gg 1$, it did not matter if T_{int} was an integer number of every characteristic period of the simulation.

Next we specified how many individual ion trajectories were being calculated. This was typically an integer multiple of 16, as the computer I was working on had 16 cores that could calculate the trajectories in parallel. We split the ions into equal groups of four where $(\tilde{B}, \tilde{R}) = (+1,+1), (+1,-1), (-1,+1)$ and $(-1,-1)$. Each individual ion was given a random initial position in three dimensions drawn from a normal distribution centered around zero with a width set to set

to give the ion cloud a 1σ radius of about 1 cm. The initial velocity was determined the same way except that it had a $\tilde{R}$-odd offset so that at $t = 0$ the molecules were already moving in circles with $\vec{\mathcal{E}}_{\rm rot}$.

The trajectories of the 16N ions were then individually calculated. These trajectories include the force from the magnetic field but did not include ion-ion interactions. Ion-ion interactions were the largest effect on the trajectories that were not considered by the numerical simulations. A two dimensional cut of a standard ion trajectory is shown in Figure 3.4. After calculating the ions' positions at each time step, $\vec{\mathcal{E}}$, $\hat{\mathcal{E}}$ and $\vec{\mathcal{B}}$ were found at each of those points in space and time. The dot products $\vec{\mathcal{E}} \cdot \vec{\mathcal{B}}$ and $\hat{\mathcal{E}} \cdot \vec{\mathcal{B}}$ were then found at each time step for every ion. Finally the averages $\langle \vec{\mathcal{E}} \cdot \vec{\mathcal{B}} \rangle$ and $\langle \hat{\mathcal{E}} \cdot \vec{\mathcal{B}} \rangle$ were found for each ion by summing the individual dot products and dividing by $N_{\rm steps}$.

The average frequency f and $\tilde{D}$-odd frequency f^D were calculated from each ion trajectory. By taking appropriate linear combinations of the data taken with different values of $\tilde{B}$ and $\tilde{R}$, the $\tilde{D}$, $\tilde{B}$ and $\tilde{R}$-odd frequency channels were constructed. This let us identify the magnitude and switch dependence of the Zeeman shifts present in the simulation.

With this method, we confirmed many of the shifts identified analytically in Tables 3.3 – 3.5. Take, for example, the first shift listed in the tables. It says that a second harmonic of the electric field along x will interact with a magnetic field along x to give a Zeeman shift that is entirely doublet even.[16] We confirmed this shift by applying the fields in question and seeing a shift in f^B that varied with the magnitudes $\mathcal{B}_{1,1}$ and $\mathcal{E}_{\rm 2hx}$, in addition to the phase of the second harmonic $\cos \phi_{\rm 2x}$.

I checked many of the systematic effects in Table 3.3–3.5 this way and did not find any surprises. These effects will be discussed in the next two subsections.

[16] Recall that the shift is entirely doublet even up to the two $\lesssim 10\%$ effects listed in Subsection 3.2.1. We should expect the doublet-odd shift to be $\sim 0.1 \times \dfrac{\delta g_F}{g_F}$ times the size of the doublet-even shift.

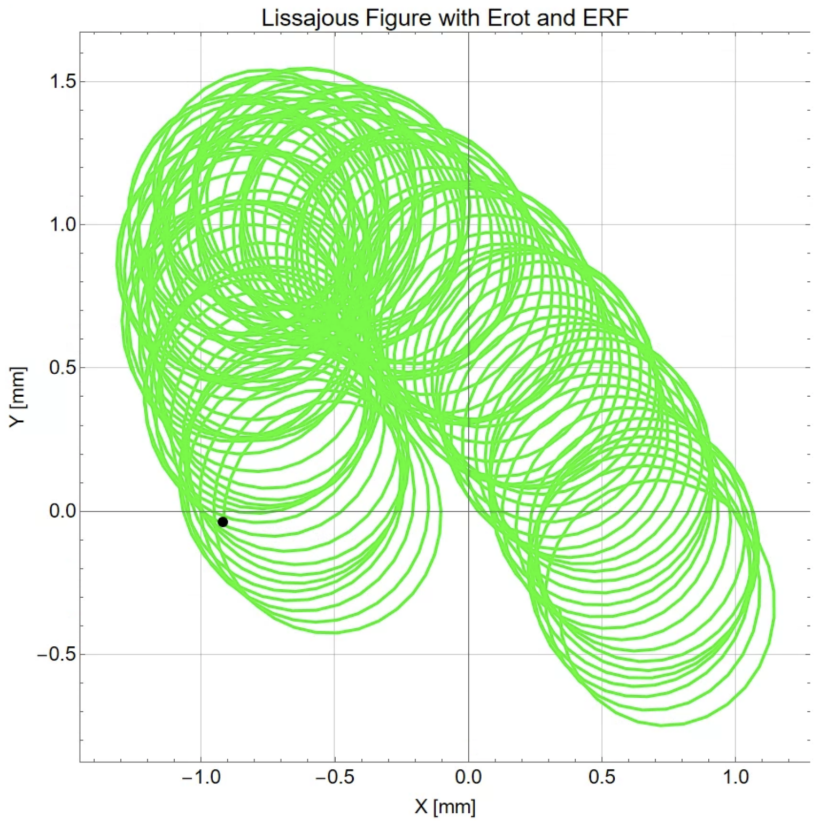

Figure 3.4: A two dimensional cut of a standard ion trajectory. At t=0 the ion's position is given by the black dot, and its trajectory follows the green trace. The molecule traces out many circles with radius ≈ 0.5 mm due to $\vec{\mathcal{E}}_{\rm rot}$. The molecule also undergoes slower oscillations in the xy-plane as the ion undergoes secular motion, moving around $x = y = 0$ due to the ion trapping fields.

3.3.3 Uniform Magnetic Field + Second Harmonic Systematic

Our task now is to show that all of the systematic effects from the entries in Tables 3.3–3.5 are small compared to our statistical error bar 22.8 μHz. This is easy for entries 19 through 26 as they have $\langle \hat{\mathcal{E}} \cdot \vec{\mathcal{B}} \rangle = \langle \vec{\mathcal{E}} \cdot \vec{\mathcal{B}} \rangle / |\vec{\mathcal{E}}|$ and their $\tilde{D}$-odd shift is cancelled by our shimming/correction procedure. It is worth noting that many of these shifts can be grouped. For example, the Zeeman shifts numbered 1 through 4 are all caused by a uniform magnetic field in the xy-plane interacting with a second harmonic of $\mathcal{E}_{\rm rot}$ in the xy-plane. This subsection will focus on this group of systematic shifts in detail, and the next subsection will address the rest of the effects.

Consider the simplified case where the total electric field is equal to $\vec{\mathcal{E}}_{\rm rot}$ plus a second har-

monic in the xy-plane:

$$\vec{\mathcal{E}} = \mathcal{E}_{\text{rot}} \begin{pmatrix} \cos(\omega_{\text{rot}} t) \\ \sin(\omega_{\text{rot}} t) \\ 0 \end{pmatrix} + \begin{pmatrix} \mathcal{E}_{\text{2hx}} \cos(2\omega_{\text{rot}} t + \phi_{\text{2hx}}) \\ \mathcal{E}_{\text{2hy}} \cos(2\omega_{\text{rot}} t + \phi_{\text{2hy}}) \\ 0 \end{pmatrix} \tag{3.26}$$

We can now find $\hat{\mathcal{E}}$ by expanding to first order in $1/\mathcal{E}_{\text{rot}}$:

$$\begin{aligned} \hat{\mathcal{E}} \simeq & \begin{pmatrix} \cos(\omega_{\text{rot}} t) \\ \sin(\omega_{\text{rot}} t) \\ 0 \end{pmatrix} + \frac{1}{2\mathcal{E}_{\text{rot}}} \begin{pmatrix} \mathcal{E}_{\text{2hx}} \cos(2\omega_{\text{rot}} t + \phi_{\text{2hx}}) \\ \mathcal{E}_{\text{2hy}} \cos(2\omega_{\text{rot}} t + \phi_{\text{2hy}}) \\ 0 \end{pmatrix} \\ & + \frac{\mathcal{E}_{\text{2hx}}}{4\mathcal{E}_{\text{rot}}} \begin{pmatrix} -\cos(4\omega_{\text{rot}} t + \phi_{\text{2hx}}) - \cos(\phi_{\text{2hx}}) \\ -\sin(4\omega_{\text{rot}} t + \phi_{\text{2hx}}) + \sin(\phi_{\text{2hx}}) \\ 0 \end{pmatrix} + \frac{\mathcal{E}_{\text{2hy}}}{4\mathcal{E}_{\text{rot}}} \begin{pmatrix} -\sin(4\omega_{\text{rot}} t + \phi_{\text{2hy}}) + \sin(\phi_{\text{2hy}}) \\ \cos(4\omega_{\text{rot}} t + \phi_{\text{2hy}}) + \cos(\phi_{\text{2hx}}) \\ 0 \end{pmatrix} \end{aligned} \tag{3.27}$$

Note that $\vec{\mathcal{E}}$ is made of terms that oscillate at ω_{rot} and $2\omega_{\text{rot}}$. When we take the dot product of $\vec{\mathcal{E}}$ and $\vec{\mathcal{B}} = \begin{pmatrix} \mathcal{B}_{\text{x}} \\ \mathcal{B}_{\text{y}} \\ 0 \end{pmatrix}$, all of the terms still oscillate at ω_{rot} or $2\omega_{\text{rot}}$. These terms will go to zero when time averaged, resulting in no $\tilde{D}$-odd Zeeman shift. However, $\hat{\mathcal{E}}$ and $\vec{\mathcal{B}}$ both have constant terms. This means $\langle \hat{\mathcal{E}} \cdot \vec{\mathcal{B}} \rangle \neq 0$ and we will get the $\tilde{D}$-even Zeeman shifts in entries 1-4 of Table 3.3.

We confirmed that this shift exists experimentally by applying a magnetic field $\mathcal{B}_{\text{x}} \sim \pm 0.2$ Gauss and a second harmonic of the electric field with $\mathcal{E}_{\text{2hy}} \sim 100$ V/m and $\phi_{\text{2hy}} \sim \frac{\pi}{4}$.[17] As seen in Figure 3.5, we saw no significant shift in f^{DB} but a $\sim \pm 8.5$ Hz shift in f^{B}.[18]

[17] Getting a value for the phase ϕ_{2hy} is a bit complicated because it is defined relative to $\mathcal{E}_{\text{rot}}$ which has a $\tilde{R}$-odd phase. See Subsection 4.6.4 for discussion, but $\phi_{\text{2hy}} \sim \frac{\pi}{4}$ is a reasonably good approximation as the $\tilde{R}$-odd part of

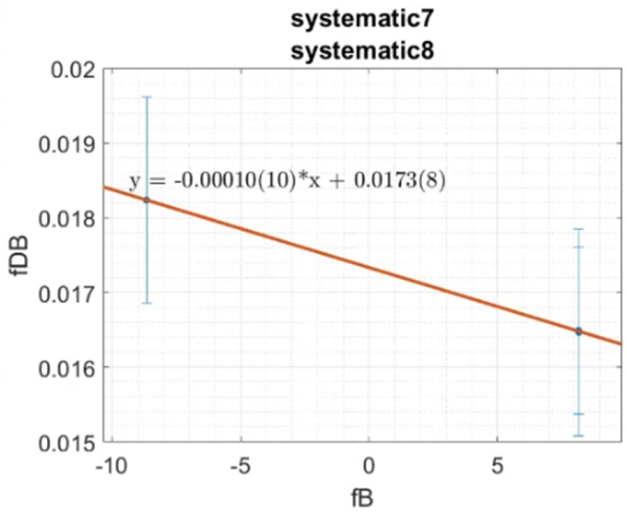

Figure 3.5: We applied a magnetic field $\mathcal{B}_{\mathrm{x}} \sim \pm 0.2$ Gauss and a second harmonic of the electric field with $\mathcal{E}_{\mathrm{2hy}} \sim 50$ V/m and $\phi_{\mathrm{2hy}} \sim \frac{\pi}{4}$. The plot shows the resulting f^B and f^{DB} in Hz, where f^{DB} includes the 16.1 mHz blind. Error bars of f^B are too small to resolve on this scale. Data with $\mathcal{B}_{\mathrm{x}} \sim +0.2$ Gauss is on the right with $f^B \sim 8$ Hz, and data with $\mathcal{B}_{\mathrm{x}} \sim -0.2$ Gauss is on the left with $f^B \sim -9$ Hz. This confirms the predicted $\tilde{D}$-even Zeeman shift.

The remaining challenge is to set a limit on the magnitude of this effect while we took the eEDM data set. See Appendix B for how we set limits on the harmonics of $\mathcal{E}_{\mathrm{rot}}$ in our apparatus. We carefully shimmed the second harmonic voltage on each electrode and found that the residual magnitude was $\lesssim 11$ mV, about than 30,000 times smaller than the voltages we apply to generate $\mathcal{E}_{\mathrm{rot}}$. Since we do not know if those voltages constructively or destructively interfere to generate a second harmonic in the xy-plane, we conservatively assume that the magnitdue in x and y is less than 2.5 mV/cm, 24,000 times smaller than $\mathcal{E}_{\mathrm{rot}}$. In this case we would expect shifts of about 80 mHz/G along both the x and y-axes.

After our harmonic shimming procedure we deliberately applied large magnetic fields ~ 2 Gauss along x and y and observed shifts in f^B to be 103(1) mHz/G along x and 46(9) mHz/G

$\mathcal{E}_{\mathrm{rot}}$'s phase is small.

[18] We took this data on January 27th 2022. At the time we thought that all Zeeman shifts effected the upper and lower doublets differently by the same ratio $\frac{\delta g_F}{g_F}$. This was quite a surprise. The magnitude of the shift in f^B is about three times larger than predicted, but the magnitude and phase of the second harmonic were not carefully calibrated at the time.

along y, see Figure 3.6. These shifts indicate that the estimate of the second harmonic in Appendix B is accurate. We were then able to apply a large second harmonic in the xy-plane in order to measure $\mathcal{B}_{\mathrm{x}}$ and $\mathcal{B}_{\mathrm{y}}$. We used this measurement to shim the current in our x and y Helmholtz coils, described in Section 2.3.5 of Tanya Roussy's thesis [2], to keep these background fields below 10 mG.

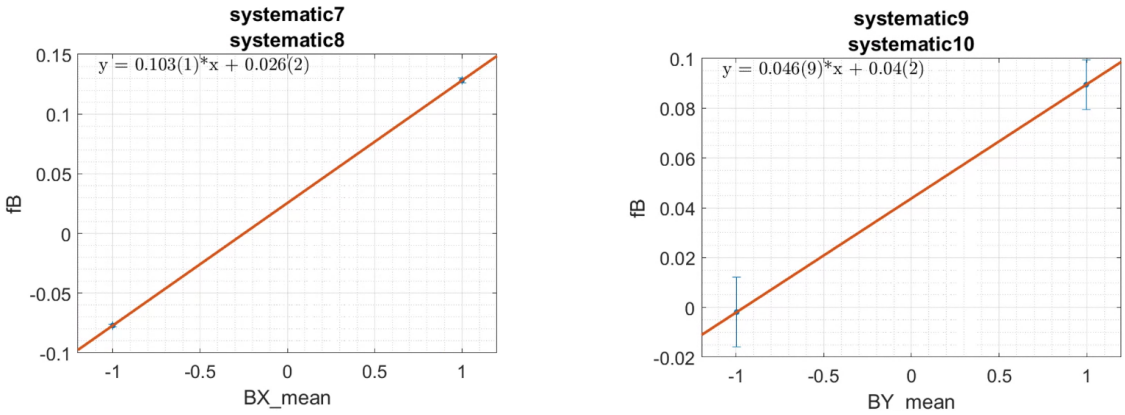

(a) f^B (Hz) vs $\mathcal{B}_{\mathrm{x}}$ (G) (b) f^B (Hz) vs $\mathcal{B}_{\mathrm{y}}$ (G)

Figure 3.6: We took data with (a) $\mathcal{B}_{\mathrm{x}} = \pm 1$ G and (b) $\mathcal{B}_{\mathrm{y}} = \pm 1$ G. Note the difference in scale of f^B of the two graphs. We saw shifts in f^B in both cases that are likely from the residual second harmonic of $\mathcal{E}_{\mathrm{rot}}$ after it was shimmed away.

The background magnetic field and second harmonic can drift throughout our dataset, so we redid these measurements about once a week while we were taking eEDM data. We did not measure any drifts outside of the aforementioned upper bounds. We therefore set a conservative upper limit of the uniform magnetic field in the xy-plane + second harmonic in the xy-plane shift in f^B to be 100 mHz/G $\times$ 10 mG = 1 mHz. Because there is no corresponding shift in f^{DB}, this shift in f^B will cause a slight error in our shimming/correction procedure. This results in a systematic shift with magnitude 1 mHz $\times \dfrac{\delta g_F}{g_F} = 2.2\ \mu$Hz. This is comfortably smaller than our statistical error bar 22.8 μHz.

3.3.4 Other Systematics from Zeeman Shifts

The previous subsection addressed entries 1 through 4 of Tables 3.3–3.5. We know entries 19 through 26 will not cause a systematic shift because $\langle \hat{\mathcal{E}} \cdot \vec{\mathcal{B}} \rangle = \langle \vec{\mathcal{E}} \cdot \vec{\mathcal{B}} \rangle / |\vec{\mathcal{E}}|$ in those cases. That leaves 37 Zeeman shifts to check. If I addressed those shifts in as much detail as I did 1 through 4, this chapter would go on for quite a while. Instead I will group them together in Table 3.6 and discuss the 15 remaining entries briefly. The effects in this table have all sines and cosines removed because we assume the phases are optimally bad. Electric fields along the x or y-axes have been grouped together, as have magnetic fields $\mathcal{B}_{l,\pm m}$.

Entries 5-8 are $\tilde{D}$-even Zeeman shifts from a third harmonic in the xy-plane interacting with a magnetic field gradient in the xy-plane. As discussed in Appendix B, we measured these third harmonics to be ~ 1.3 V/m, and as discussed in Section VI A 4 of the Systematics paper we found $\mathcal{B}_{2,\pm 2} \lesssim 10$ mG/cm. Plugging these values into the expression in Table 3.6, we find a shift in f^B with magnitude 0.7 mHz corresponding to a systematic in f^{DB} of 1.5 μHz.

Entries 9-10 are interesting because they are proportional to $\mathcal{B}_{2,0}$. This must be a $\tilde{B}$-even magnetic field gradient in order to show up as a systematic, and from Subsection 3.2.2 we know that this is $\mathcal{B}^{\rm nr}_{2,0}$. Over the entire dataset the median $\mathcal{B}^{\rm nr}_{2,0} \approx 0.8\,\mu$G/m. These entries are also proportional to the ellipticity $\mathcal{E}_\epsilon$, which we measure in Subsection 3.5.3 to be about 1.7 V/m. This gives an absolutely tiny shift in f^B of 1×10^{-7} μHz and systematic in f^{DB} of about 2×10^{-10} μHz.

Entries 11-14 are also proportional to $\mathcal{B}^{\rm nr}_{2,0}$ and are also tiny. They are in fact smaller because of the larger number in their denominator. We calculate the shift in f^B to be 9×10^{-10} μHz and the associated systematic 2×10^{-12} μHz.

Entries 15-18 are larger than 9-14 but still are not particularly worrying. We calculate the shift in f^B to be 22 μHz and the associated systematic 5×10^{-2} μHz.

Entries 19-26 do not cause systematics as they have $\langle \hat{\mathcal{E}} \cdot \vec{\mathcal{B}} \rangle = \langle \vec{\mathcal{E}} \cdot \vec{\mathcal{B}} \rangle / |\vec{\mathcal{E}}|$. Any shift caused

Table 3.6: Analytically Calculated Zeeman Shifts Grouped Together

Number in Tables 3.3–3.5	$\langle\hat{\mathcal{E}}\cdot\vec{\mathcal{B}}\rangle$	$\langle\vec{\mathcal{E}}\cdot\vec{\mathcal{B}}\rangle/\mathcal{E}_{\rm rot}$	$\frac{\langle\vec{\mathcal{E}}\cdot\vec{\mathcal{B}}\rangle/\mathcal{E}_{\rm rot}}{\langle\hat{\mathcal{E}}\cdot\vec{\mathcal{B}}\rangle}$	Systematic (μHz)
1-4	$\frac{\mathcal{B}_{1,\pm1}\mathcal{E}_{\rm 2hxy}}{4\mathcal{E}_{\rm rot}}$	0	0	2.2
5-8	$\frac{\sqrt{3}\mathcal{B}_{2,\pm2}\mathcal{E}_{\rm 3hxy}r_{\rm rot}}{4\mathcal{E}_{\rm rot}}$	0	0	1.5
9-10	$\frac{5\mathcal{B}_{2,0}\mathcal{E}_{\rm 3hxy}\mathcal{E}_{\epsilon}r_{\rm rot}}{18\mathcal{E}_{\rm rot}^2}$	0	0	2×10^{-10}
11-14	$\frac{5\mathcal{B}_{2,0}\mathcal{E}_{\rm 2hxy}\mathcal{E}_{\rm 4hxy}r_{\rm rot}}{128\mathcal{E}_{\rm rot}^2}$	0	0	2×10^{-12}
15-18	$\frac{3\sqrt{\frac{5}{2}}\mathcal{B}_{3,\pm3}\mathcal{E}_{\rm 4hxy}r_{\rm rot}^2}{8\mathcal{E}_{\rm rot}}$	0	0	5×10^{-2}
19-21	$-\frac{\mathcal{B}_{2,0}\mathcal{E}_{\rm nhz}^2r_{\rm rot}}{\mathrm{n}^2\mathcal{E}_{\rm rot}^2}$	$-\frac{\mathcal{B}_{2,0}\mathcal{E}_{\rm nhz}^2r_{\rm rot}}{\mathrm{n}^2\mathcal{E}_{\rm rot}^2}$	1	
22	$-\frac{\mathcal{B}_{2,0}\mathcal{E}_{\rm secz}^2r_{\rm rot}\omega_{\rm rot}^2}{\mathcal{E}_{\rm rot}^2\omega_{\rm secz}^2}$	$-\frac{\mathcal{B}_{2,0}\mathcal{E}_{\rm secz}^2r_{\rm rot}\omega_{\rm rot}^2}{\mathcal{E}_{\rm rot}^2\omega_{\rm secz}^2}$	1	
23-24	$-\frac{\mathcal{B}_{2,0}\mathcal{E}_{\rm RFeffz}^2r_{\rm rot}\omega_{\rm rot}^2}{4\mathcal{E}_{\rm rot}(\omega_{\rm RF}\pm\omega_{\rm secz})^2}$	$-\frac{\mathcal{B}_{2,0}\mathcal{E}_{\rm RFeffz}^2r_{\rm rot}\omega_{\rm rot}^2}{4\mathcal{E}_{\rm rot}(\omega_{\rm RF}\pm\omega_{\rm secz})^2}$	1	
25-26	$\frac{3\sqrt{15}\mathcal{B}_{3,\pm2}\mathcal{E}_{\rm 2hz}r_{\rm rot}^2}{8\mathcal{E}_{\rm rot}}$	$\frac{3\sqrt{15}\mathcal{B}_{3,\pm2}\mathcal{E}_{\rm 2hz}r_{\rm rot}^2}{8\mathcal{E}_{\rm rot}}$	1	
27-28	$-\frac{3\sqrt{3}\mathcal{B}_{2,\pm2}\mathcal{E}_{\epsilon}r_{\rm rot}}{2\mathcal{E}_{\rm rot}}$	$-\frac{2\sqrt{3}\mathcal{B}_{2,\pm2}\mathcal{E}_{\epsilon}r_{\rm rot}}{\mathcal{E}_{\rm rot}}$	$\frac{4}{3}$	1.7
29-32	$\frac{3\sqrt{\frac{5}{2}}\mathcal{B}_{3,\pm3}\mathcal{E}_{\rm 2hxy}r_{\rm rot}^2}{4\mathcal{E}_{\rm rot}}$	$\frac{9\sqrt{\frac{5}{2}}\mathcal{B}_{3,\pm3}\mathcal{E}_{\rm 2hxy}r_{\rm rot}^2}{8\mathcal{E}_{\rm rot}}$	$\frac{3}{2}$	2×10^{-2}
33-38	$\frac{\mathcal{B}_{2,0}\mathcal{E}_{\rm nhxy}^2r_{\rm rot}}{4\mathrm{n}^2\mathcal{E}_{\rm rot}^2}$	$\frac{\mathcal{B}_{2,0}\mathcal{E}_{\rm nhxy}^2r_{\rm rot}}{2\mathrm{n}^2\mathcal{E}_{\rm rot}^2}$	2	8×10^{-12}
39	$\frac{\mathcal{B}_{2,0}\mathcal{E}_{\epsilon}^2r_{\rm rot}}{2\mathcal{E}_{\rm rot}^2}$	$\frac{\mathcal{B}_{2,0}\mathcal{E}_{\epsilon}^2r_{\rm rot}}{\mathcal{E}_{\rm rot}^2}$	2	5×10^{-10}
40-41	$\frac{\mathcal{B}_{2,0}\mathcal{E}_{\rm secxy}^2r_{\rm rot}\omega_{\rm rot}^2}{4\mathcal{E}_{\rm rot}^2\omega_{\rm secxy}^2}$	$\frac{\mathcal{B}_{2,0}\mathcal{E}_{\rm secxy}^2r_{\rm rot}\omega_{\rm rot}^2}{2\mathcal{E}_{\rm rot}^2\omega_{\rm secxy}^2}$	2	1×10^{-5}
42-45	$\frac{\mathcal{B}_{2,0}\mathcal{E}_{\rm RFeffxy}^2r_{\rm rot}\omega_{\rm rot}^2}{16\mathcal{E}_{\rm rot}^2(\omega_{\rm RF}\pm\omega_{\rm secxy})^2}$	$\frac{\mathcal{B}_{2,0}\mathcal{E}_{\rm RFeffxy}^2r_{\rm rot}\omega_{\rm rot}^2}{8\mathcal{E}_{\rm rot}^2(\omega_{\rm RF}\pm\omega_{\rm secxy})^2}$	2	3×10^{-6}
46-49	0	$\frac{3\sqrt{\frac{3}{2}}\mathcal{B}_{3,\pm1}\mathcal{E}_{\rm 2hxy}r_{\rm rot}^2}{8\mathcal{E}_{\rm rot}}$	∞	1×10^{-2}

by these effects will be corrected as discussed in Subsection 3.2.2.

Entries 27 and 28 are unique because they are the only second order shifts in κ with $\frac{\langle \vec{\mathcal{E}} \cdot \vec{\mathcal{B}} \rangle / \mathcal{E}_{\rm rot}}{\langle \hat{\mathcal{E}} \cdot \vec{\mathcal{B}} \rangle} = \frac{4}{3}$. This means the correction will account for 75% of the shift these effects cause in f^{DB}, but the rest of the shift leads to a systematic. By plugging in the limits for the parameters in this shift, as we have been been doing for the last few paragraphs, we calculate the shift in f^B to be 5 mHz. However as we mention in Section VI A 5 of the Systematics paper, we measured this shift with a five times larger ellipticity than is usually present in our experiment. We did not see any shift in f^B due to this effect and the 1σ upper limit was 12 mHz, so we set a more stringent limit on the effect at 2.4 mHz. This corresponds to a systematic uncertainty in f^{DB} of 1.7 μHz.

Entries 29 through 32 are interesting as well for being the only shifts with $\frac{\langle \vec{\mathcal{E}} \cdot \vec{\mathcal{B}} \rangle / \mathcal{E}_{\rm rot}}{\langle \hat{\mathcal{E}} \cdot \vec{\mathcal{B}} \rangle} = \frac{3}{2}$. These shifts, however, are naturally smaller than 27 and 28 because they are proportional to a higher order gradient and the second harmonic that we shimmed particularly well. We calculate the shift in f^B to be 17 μHz, corresponding to a systematic error of about 20 nHz.

Entries 33 through 45 are all predictably small because they are proportional to $\mathcal{B}^{\rm nr}_{2,0}$. Their associated systematic shifts can be found in Table 3.6.[19]

Entries 46 through 49 are Zeeman shifts which are entirely $\tilde{D}$-odd. These effects show up directly as systematics! Fortunately they are only 14 nHz, small enough to sweep under the rug. If they were much larger this would be a difficult systematic to diagnose as we blinded our measurements of f^{DB} and they do not show up in any other frequency channel.

Note that our choice to only include up to the fourth harmonic in $\mathcal{E}_{\rm rot}$ is sensible. As seen in Appendix B, higher harmonics generally have smaller amplitudes. In addition, we can see in Table

[19]Note that the largest systematic shifts from entries 33 through 38 are from n=3 due to the third harmonic being significantly larger than the shimmed second harmonic, see Appendix B. The shift due to n=3 is the systematic shift reported in Table 3.6. The magnitude of the RF electric field reported in Table 2.2 was used for $\mathcal{E}_{\rm RFeffxy}$. $\mathcal{E}_{\rm secxy}$ was found using dimensional analysis assuming a secular frequency of 1.3 kHz.

3.6 that the third and fourth harmonics generally couple to higher order magnetic field gradients and larger powers of $r_{\rm rot}$. Since $\mathcal{B}_{1,m} > \mathcal{B}_{2,m} r_{\rm rot} > \mathcal{B}_{3,m} r_{\rm rot}^2$, we can safely assume that magnetic systematics caused by the fifth harmonic or higher will be smaller than the largest effects in Table 3.6.

3.4 Other Noteworthy Magnetic Shifts

In Sections 3.2 and 3.3 I addressed the Zeeman shifts which are doublet odd and show up as systematic effects or appear in the f^B frequency channel, leading to systematics via our correction on f^{DB}. In this section I will discuss a few other magnetic shifts that do not cause systematic errors in our experiment but are interesting nonetheless.

3.4.1 Axial Magnetic Field and f^R

$\vec{\mathcal{E}}_{\rm rot}$ causes the molecules to trace out circles in the xy-plane with radius $r_{\rm rot}$. A magnetic field along the z-axis will slightly modify the radius of that rotation due to the $\vec{v} \times \vec{\mathcal{B}}$ force:

$$r_{\rm rot} = \frac{e\mathcal{E}_{\rm rot}}{m\omega_{\rm rot}^2} + \tilde{R}\frac{ev\mathcal{B}_{\rm z}}{m\omega_{\rm rot}^2} \simeq \frac{e\mathcal{E}_{\rm rot}}{m\omega_{\rm rot}^2} + \tilde{R}\frac{e^2\mathcal{E}_{\rm rot}\mathcal{B}_{\rm z}}{m^2\omega_{\rm rot}^3} \tag{3.28}$$

Since $\vec{v}$ is $\tilde{R}$-odd, the $\vec{v} \times \vec{\mathcal{B}}$ force causes a $\tilde{R}$-odd change in the radius. The effect depends on the velocity of the ions, which in turn depends on the radius because $\omega_{\rm rot}$ is fixed. This makes the math more complicated, but we can approximate the velocity as $v = \omega_{\rm rot} r_{\rm rot} \simeq \omega_{\rm rot}\frac{e\mathcal{E}_{\rm rot}}{m\omega_{\rm rot}^2} = \frac{e\mathcal{E}_{\rm rot}}{m\omega_{\rm rot}}$ as long as $\mathcal{B}_{\rm z} \ll \frac{m\omega_{\rm rot}}{e} \sim 5$ Tesla so it only causes a small perturbation to $r_{\rm rot}$.

The change in $r_{\rm rot}$ causes a $\tilde{R}$-odd frequency shift as the molecules move through $\mathcal{B}_{2,0}^{\rm rev}$:

$$hf = -3g_F\mu_B\mathcal{B}_{2,0}^{\rm rev} r_{\rm rot} \simeq -3g_F\mu_B\mathcal{B}_{2,0}^{\rm rev}\left(\frac{e\mathcal{E}_{\rm rot}}{m\omega_{\rm rot}^2} + \tilde{R}\frac{e^2\mathcal{E}_{\rm rot}\mathcal{B}_{\rm z}}{m^2\omega_{\rm rot}^3}\right) \tag{3.29}$$

We measured this effect with $\mathcal{B}_{2,0}^{\rm rev} \approx 230$ mG/cm, which generates $f^0 \sim 150$ Hz, and $\mathcal{B}_{\rm z} \sim \pm 10$

Gauss. The data is shown in Figure 3.7. With this value of $\mathcal{B}^{\text{rev}}_{2,0}$ we predict f^R to have a slope of -3.1 mHz/G, which is consistent with our measurement $-2.98(9)$ mHz/G. This is the first shift that we as a group could not initially explain that I understood before anyone else, so it gets a page in my thesis.

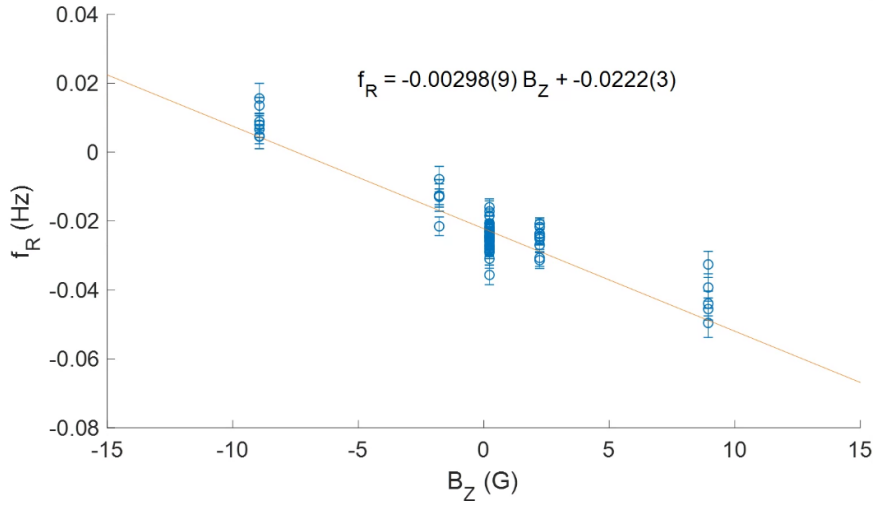

Figure 3.7: We applied a large non-reversing $\mathcal{B}_z$ of ± 10 G. We observed a shift in f^R of $-2.98(9)$ mHz/G, consistent with the explanation that $\mathcal{B}_z$ modifies the size of r_{rot}.

3.4.2 Charging Currents

The largest magnetic field we intentionally apply to our molecules is the quadrupole magnetic field that reverses sign with $\tilde{B}$. The largest magnetic field that we unintentionally apply is created by the currents which drive the oscillating voltages V_{rot} to create $\mathcal{E}_{\text{rot}}$. The voltages have amplitude $V_{\text{rot}} \sim 350$ V and oscillate at $f_{\text{rot}} = 375$ kHz. They are applied to our eight radial electrodes which are shown in Figure 3.8.

The radial electrodes, which we sometimes call "fins" due to their peculiar shape, are numbered $n = 1$ through 8 in Figure 3.8. We apply $\tilde{R}$-odd voltages to the electrodes with a phase shift of $\frac{\pi}{4}$ between neighboring electrodes:[20]

[20] The actual phases of V^n_{rot} are discussed in Subsection 4.6.4. These toy phases are simpler to consider and are sufficient to model the Zeeman shift caused by the charging currents.

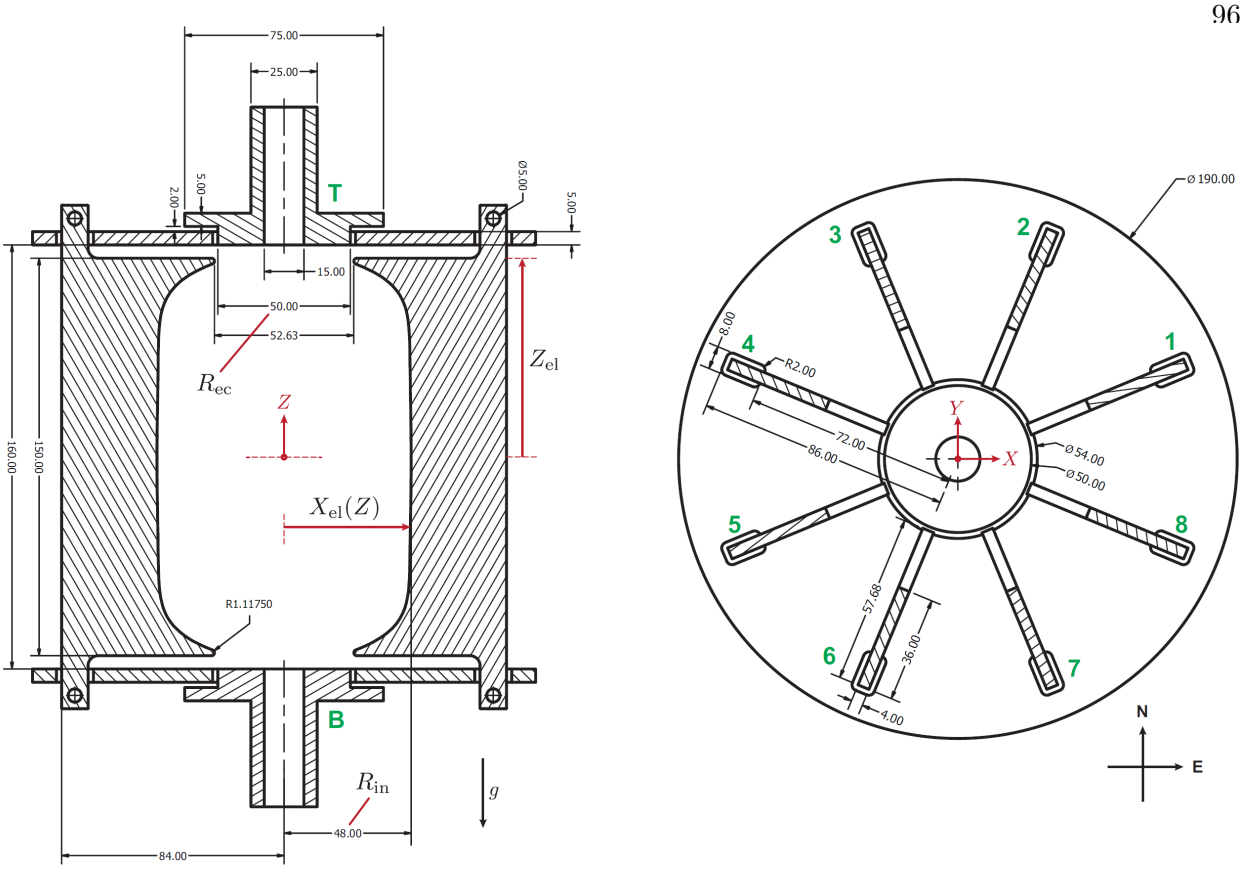

Figure 3.8: Key dimensions of our ion trap, all dimensions in millimeters. The radial electrodes, two of which are shown in detail on the left, have a peculiar shape to make the $\vec{\mathcal{E}}_{\text{rot}}$ as uniform as possible at the center of the trap. Note that the electrodes have "tabs" at the top and bottom that reach beyond the top (T) and bottom (B) endcaps. The electrodes can be charged and discharged through either or both of these notches. A full description of the radial electrode design can be found in Chapter 4 of William Cairncross's thesis [1], which is the source of this image.

$$V_{\text{rot}}^{n} = V_{\text{rot}} \cos\left(\tilde{R}\omega_{\text{rot}} t - \frac{n\pi}{4} + \pi\right) \tag{3.30}$$

Ignoring the spatial inhomogeneities that are discussed in Chapter 4 of William Cairncross's thesis [1], these voltages applied to our radial electrodes creates an electric field $\vec{\mathcal{E}}_{\text{rot}} = \mathcal{E}_{\text{rot}}\Big(\cos(\omega_{\text{rot}} t)\hat{x} + \tilde{R}\sin(\omega_{\text{rot}} t)\hat{y}\Big)$ as we would expect.

Originally we charged and discharged all eight of our electrodes from the top and bottom simultaneously. That is, we connected the output of the op-amp which generates V_{rot}^{n} to both the

top and bottom tabs of fin n. The idea was to minimize the current flowing through the electrodes as V_{rot} varied, therefore reducing the resulting magnetic field. However, due to differences in the resistances of the electrical feedthroughs above and below each fin, this resulted in all eight fins generating an unpredictable magnetic field. These resistances were small but had substantial fractional variations, which meant each electrode had a different proportion of current above and below them.

Rather than attempt to model the resulting magnetic field, we decided to connect the op-amps of the odd numbered fins only to the top of the odd numbered electrodes. The even numbered fins were charged and discharged from the bottom. This meant we knew exactly which direction the current was traveling as each fin charged and discharged. We can create a simple model of the magnetic field by assuming that the eight radial electrodes have a height z_0 and are centered at $z = 0$. We also assume the radial electrodes have capacitance C_{fin} which is constant as a function of height so $C_{\text{fin}} = \dfrac{dC_{\text{fin}}}{dz} z_0$. With these assumptions and the relationship $I = C\dfrac{dV}{dt}$ we reach the following expression for the currents on each fin:

$$I^n_{\text{rot}} = \tilde{R}\frac{dC_{\text{fin}}}{dz} V_{\text{rot}}\omega_{\text{rot}} \sin\left(\tilde{R}\omega_{\text{rot}}t - \frac{n\pi}{4} + \pi\right)\left(z \mp \frac{z_0}{2}\right) \tag{3.31}$$

The $\mp$ symbol is minus for odd radial electrodes that are charged from the top and plus for even radial electrodes that are charged from the bottom.

We can now calculate the magnetic field at the center of the trap. To keep the expression simple we assume the radial electrodes are infinitely long thin wires that are a distance R_{trap} from the trap center. If this is true we find that the magnetic field $\vec{\mathcal{B}}_{\text{cc}}$ created by the charging currents is:

$$\vec{\mathcal{B}}_{\rm cc} = \frac{2V_{\rm rot}\mu_0\omega_{\rm rot}\dfrac{dC_{\rm fin}}{dz}z}{\pi R_{\rm trap}} \begin{pmatrix} \tilde{R}\cos\left(\omega_{\rm rot}t\right) \\ \sin\left(\omega_{\rm rot}t\right) \\ 0 \end{pmatrix} = \mathcal{B}_{\rm cc}z \begin{pmatrix} \tilde{R}\cos\left(\omega_{\rm rot}t\right) \\ \sin\left(\omega_{\rm rot}t\right) \\ 0 \end{pmatrix} \tag{3.32}$$

According to this equation the magnetic field caused by the charging currents rotates with a frequency equal to $f_{\rm rot}$ and is parallel to $\vec{\mathcal{E}}_{\rm rot}$ for $z\tilde{R} > 0$ and antiparallel for $z\tilde{R} < 0$.[21]

While this model captures the general behavior of $\vec{\mathcal{B}}_{\rm cc}$, we can calculate its amplitude more precisely. We used Comsol Multiphysics to simulate where the charge accumulates on the fins as a function of height.[22] We found that each fin has a total capacitance of about 9.7 pF and we found the current through each fin as a function of height, shown in Figure 3.9.

We then calculated the magnetic field from these current distributions assuming the fins were thin wires with finite length z_0. It was initially unclear what value to use as the distance between the eight imaginary thin wires and the center of the trap. To be safe we did the calculation twice with the radius set to 48 and 84 mm, two reasonable radii shown in the bottom left of Figure 3.8. These calculations predicted the $\mathcal{B}_{\rm cc} = 2.9$ and 1.1 mG/m respectively. Because the magnetic field is $\tilde{R}$-odd and $\tilde{B}$-even, this corresponds to a slope $\dfrac{df^{BR}}{dz}$ between 31.8 and 12.4 mHz/mm. This compares very well with our observed data, shown in Figure 3.10, where we see a shift of 12.69(6) mHz/mm. This perhaps indicates that the majority of the charge moves along the back of the radial electrodes.

There are a few comments worth making about this shift before moving on. The first is that while the shift ideally goes to zero at the center of the ion trap, we measure $f^{BR} \sim 210$ mHz. This could easily be explained by differences in capacitances of the wiring inside the vacuum chamber

[21] This magnetic field has a nonzero curl; see Section 5.1.2 for a discussion of this field and Maxwell's equations.

[22] These simulations used a realistic rendering of the entire ion trap. It was important to include the voltages applied to all eight radial electrodes when calculating the capacitance as this effected how much charge needed to accumulate on a given fin to reach a given voltage.

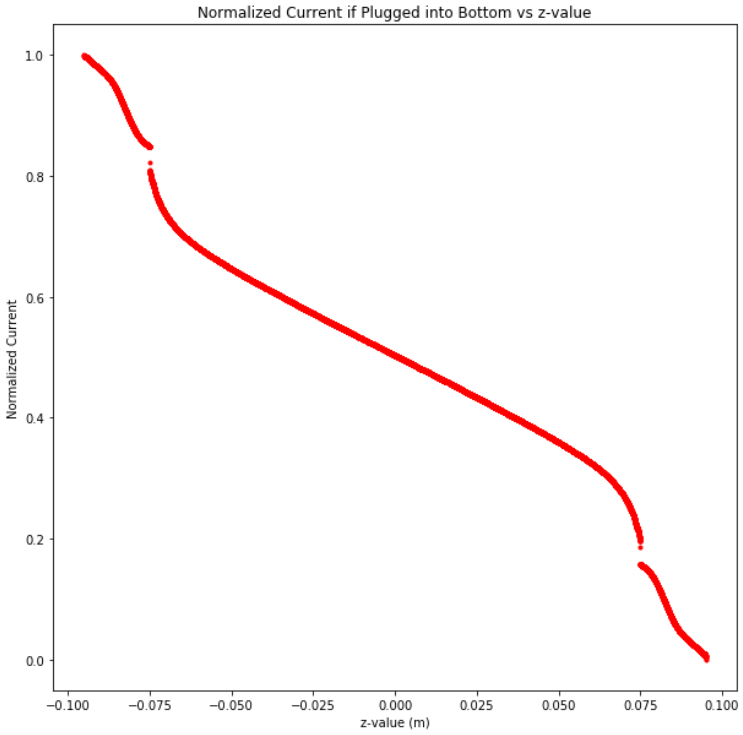

Figure 3.9: This graph shows the percentage of the current that drives V_{rot} through a radial electrode that is plugged in from the bottom. For the fin to reach V_{rot} charge must be distributed roughly evenly in z. Therefore 100% of the current goes through the bottom layer of the fin, and there is less and less current as we move up the fin. The curves of the graph are explained by different heights of the radial electrode having different capacitances which were calculated in Comsol Multiphysics. The two discontinuities occur at points where where the fins suddenly jut out toward the center of the trap, see Figure 3.8.

between the eight op-amps and fins.

This shift is entirely $\tilde{R}$-odd and shows up in f^{BR}, so it does not contribute to our systematic error budget. Additionally, because this magnetic field is parallel or antiparallel to $\vec{\mathcal{E}}_{\text{rot}}$, it has $\frac{\langle \vec{\mathcal{E}} \cdot \vec{\mathcal{B}} \rangle / |\mathcal{E}|}{\langle \hat{\mathcal{E}} \cdot \vec{\mathcal{B}} \rangle} = 1$. This means that there will be a ~ 460 times smaller shift that appears in f^{DBR}. Even if somehow a small part of the shift is $\tilde{R}$-even and appears in f^{B}, which could happen because of the $\tilde{R}$-odd $\mathcal{E}_{\text{rot}}$ phases discussed in Subsection 4.6.4, it will not cause a systematic error in our experiment because the effect is taken care of by our shimming/correction procedure.

There is the possibility that this frequency shift will be used intentionally in our third gen-

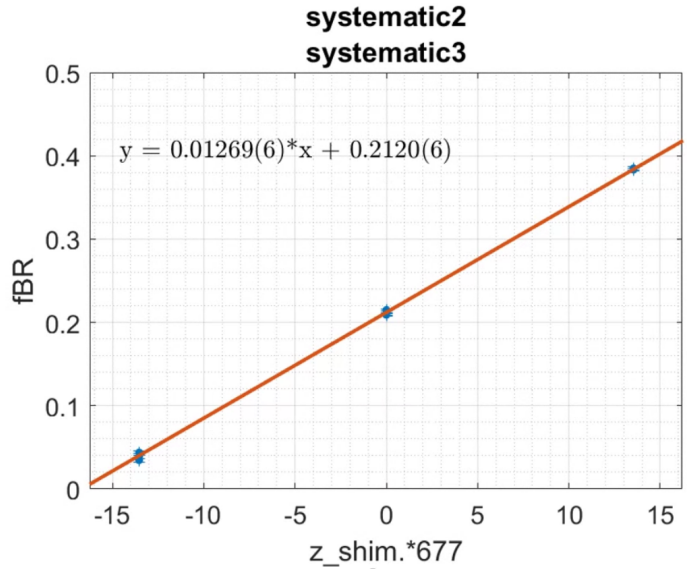

Figure 3.10: The y-axis reports f^{BR} in Hz and the x-axis gives the position of the ion cloud along z in mm. We observe a gradient $\frac{df^{BR}}{dz}$ of 12.69(6) mHz/mm which agrees well with our model.

eration experiment to measure the eEDM. This will be addressed in Section 5.1.3.

3.4.3 Other Zeeman Shifts

For a discussion of other miscellaneous Zeeman shifts, see Section 3.11 of Tanya Roussy's thesis [2].

3.5 Berry's Phase

Other than Zeeman shifts, the only effect that can cause a frequency shift that shows up in f^B is Berry's phase.[23] Berry's phase shifts are almost on equal footing in importance with the Zeeman effect in terms of our systematics, but I have relegated them to the fifth section of this chapter. This is an interesting choice on my part, as when I give talks about the experiment the Berry's phase shift described in Subsection 3.5.3 is usually the only systematic effect I mention.

[23] I mention at the beginning of this chapter that I leave discussion of systematics due to phase shifts to the Systematics paper. In this section I describe how we can continuously accumulate a Berry's phase which shows up in our experiment as a frequency shift that can cause systematic errors. Hopefully this clarifies any confusion.

Unlike Zeeman shifts, Berry's phase is an inherently $\tilde{D}$-even effect so it is a bit less worrisome. It can only causes systematic shifts by changing f^B and spoiling our correction to f^{DB} described in Subsection 3.2.2. That said, Berry's phase is an important effect that we spent many collective months (years?) worrying about for the generation two measurement.

As a note, I wrote Chapter 4 to be an independent paper which does not reference any other chapter in this thesis on the off chance we decide to publish it. It explains how we measure the sign of g_F using Berry's phase, so it contains an explanation of Berry's phase I will describe Berry's phase from scratch in this section as well, please forgive the repetition. This explanation is also similar to the one given in Section VI B of the Systematics paper in case you would like to read a third version.

3.5.1 Berry's Phase Overview

Our quantization axis defined by $\vec{\mathcal{E}}_{\text{rot}}$ completes $f_{\text{rot}} = 375,000$ rotations per second in the xy-plane. As $\vec{\mathcal{E}}_{\text{rot}}$ traces out closed loops, the quantum state accumulates a geometric phase of:

$$\phi_{geo} = \Delta M_F \Omega_s \tag{3.33}$$

During our spectroscopy the molecules are in a superposition of $M_F = \pm 1.5$ states, so the molecules will accumulate a relative phase shift of $3\Omega_s$. Here Ω_s is the solid angle traced out by the electric field, as shown in Figure 3.11, which is a signed quantity. If the electric field rotates perfectly in the xy-plane, $\Omega_s = \mp 2\pi$ for $\tilde{R} = \pm 1$. In this ideal case the difference of ϕ_{geo} between the two M_F states is $\mp 6\pi$, meaning that the Berry's phase is not observable as it is an integer number of 2π phase shifts. But if we intentionally tilt the electric field up out of the xy-plane by a small angle α as shown in Figure 3.11, we induce a measurable phase shift that will be accumulated every $T_{\text{rot}} = 1/f_{\text{rot}}$. For small tilts, this will appear as a frequency shift for each M_F state given by:

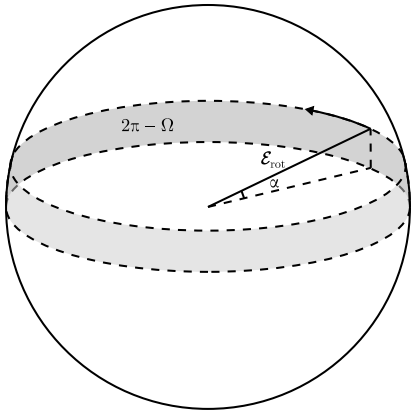

Figure 3.11: Ideally, the quantization axis defined by $\vec{\mathcal{E}}_{\text{rot}}$ rotates perfectly in the xy-plane and traces out a solid angle of $-2\pi\tilde{R}$. If $\vec{\mathcal{E}}_{\text{rot}}$ is tilted up by a small angle α, it will deviate from the ideal solid angle by an amount Ω. This image has been reproduced from [31].

$$f_{\text{Berry}} \approx -\frac{3f_{\text{rot}}}{2\pi}\int_0^{T_{\text{rot}}} \alpha(t)\dot{\phi}(t)dt \tag{3.34}$$

Here $\alpha(t)$ is the tilt of the quantization axis out of the xy-plane and $\dot{\phi}(t)$ is the azimuthal angular velocity. If neither parameter depends on time, we find that:

$$f_{\text{Berry}} = -3f_{\text{rot}}\alpha\tilde{R} \tag{3.35}$$

At first glance it is reassuring that f_{Berry} is $\tilde{R}$-odd, which is the case because $\dot{\phi}(t)$ is $\tilde{R}$-odd. However we will soon see that our imperfections to the electric field, the ellipticity and various harmonics of $\mathcal{E}_{\text{rot}}$, can themselves be $\tilde{R}$-odd. This results in $\tilde{R}$-even shifts which generally appear in f^B.

3.5.2 Gravity

The only way $\vec{\mathcal{E}}_{\text{rot}}$ can have a constant tilt α out of the xy-plane is due to gravity. This is because the ions sit at the point in the trap where the average net force is equal to zero. Since gravity pulls the ions downward there is an average electric field pointing up to cancel its effect. This

field $\vec{\mathcal{E}}_{\text{grav}} = \frac{mg}{e}\hat{z} \sim 20\,\mu\text{V/m}$. This causes a tilt in our total electric field $\alpha = \arctan\left(\frac{\mathcal{E}_{\text{rot}}}{\mathcal{E}_{\text{grav}}}\right) \sim 3.3 \times 10^{-7}$, resulting in a shift $f^{BR} \sim 4$ mHz.[24] This shift is completely $\tilde{R}$-odd so it does not cause a systematic effect.

All other Berry's phase shifts discussed in this section are caused by electric fields that oscillate along the z-axis interacting with another electric field in the xy-plane which together cause an average tilt $\langle\alpha\rangle$.

3.5.3 Ellipticity plus Axial Second Harmonic

The simplest way to get a nonzero value of $\langle\alpha\rangle$ is from a second harmonic of $\mathcal{E}_{\text{rot}}$ along the z-axis and an ellipticity of $\mathcal{E}_{\text{rot}}$. Ignoring the trapping electric fields, this gives us a total electric field:

$$\vec{\mathcal{E}}(t) = \begin{pmatrix} \mathcal{E}_{\text{rot}}\cos\left(\omega_{\text{rot}}t + \frac{\pi}{12} + \tilde{R}\frac{7\pi}{4}\right) + \mathcal{E}_{\epsilon}\cos\left(2\theta\tilde{R} - \omega_{\text{rot}}t - \frac{\pi}{12} - \tilde{R}\frac{7\pi}{4}\right) \\ \mathcal{E}_{\text{rot}}\tilde{R}\sin\left(\omega_{\text{rot}}t + \frac{\pi}{12} + \tilde{R}\frac{7\pi}{4}\right) + \mathcal{E}_{\epsilon}\tilde{R}\sin\left(2\theta\tilde{R} - \omega_{\text{rot}}t - \frac{\pi}{12} - \tilde{R}\frac{7\pi}{4}\right) \\ \mathcal{E}_{2\text{hz}}\cos\left(2\omega_{\text{rot}}t + \phi_{2f}\right) \end{pmatrix} \tag{3.36}$$

The peculiar choice of $\mathcal{E}_{\text{rot}}$ phase $\frac{\pi}{12} + \tilde{R}\frac{7\pi}{4}$ was used in our experiment to ensure that the ions of the upper and lower doublet land on different sides of our MCP, as explained in Section 2.2. See Subsection 4.6.4 for how we confirmed the values of these phases. Here there is an ellipticity $\mathcal{E}_{\epsilon}$ along an angle θ from the x-axis and a second harmonic along the z-axis with phase ϕ_{2f}.

As we see in Subsection 4.6.3, we can combine Equations 3.34 and 3.36 to find frequency shifts that show up in f^B and f^{BR}:[25]

[24] It would be really cool if we could measure this and see gravity's effect on molecular ions. 4 mHz is a large enough shift for us to easily resolve, but it shows up in the same frequency channel as the ~ 200 mHz shift caused by the charging currents described in Subsection 3.4.2. If only we could turn our apparatus upside down.

[25] Note that we get a $\tilde{R}$-odd $\langle\alpha\rangle$, and therefore a $\tilde{R}$-even frequency shift, even though we assume that $\vec{\mathcal{E}}_{2\text{hz}}$ is $\tilde{R}$-even. If we relax this assumption we find that the resulting frequency shifts are split between f^B and f^{BR} as well.

$$f^B = -\frac{9\mathcal{E}_{2\mathrm{hz}}\mathcal{E}_\epsilon f_{\mathrm{rot}}}{2\mathcal{E}_{\mathrm{rot}}^2}\cos(2\theta)\sin(\phi_{2f} - \frac{\pi}{6}) \tag{3.37}$$

$$f^{BR} = -\frac{9\mathcal{E}_{2\mathrm{hz}}\mathcal{E}_\epsilon f_{\mathrm{rot}}}{2\mathcal{E}_{\mathrm{rot}}^2}\sin(2\theta)\sin(\phi_{2f} + \frac{\pi}{3}) \tag{3.38}$$

While we are not particularly bothered by the shift in f^{BR}, the shift in f^B leads to a systematic that is $\frac{\delta g_F}{g_F}$ times smaller. Assuming the worst cases for the phases, that the entire shift shows up in f^B, we have a systematic shift with magnitude $\frac{9\mathcal{E}_{2\mathrm{hz}}\mathcal{E}_\epsilon f_{\mathrm{rot}}}{2\mathcal{E}_{\mathrm{rot}}^2}\frac{\delta g_F}{g_F}$.

We know the magnitude of all of these terms, including $\mathcal{E}_{2\mathrm{hz}}$ from Appendix B, except for $\mathcal{E}_\epsilon$. To find $\mathcal{E}_\epsilon$ we initially applied $\mathcal{E}_{2\mathrm{hz}} \sim 4$ V/m and $\mathcal{E}_\epsilon/\mathcal{E}_{\mathrm{rot}} \sim 7 \times 10^{-3}$ to make sure that we saw shifts in f^B and f^{BR}. In the data in Figure 3.12 we fixed the angle of the ellipticity $\theta = -\frac{\pi}{8}$ and scanned ϕ_{2f}. We saw both frequencies vary sinusoidally with the magnitudes we expected.

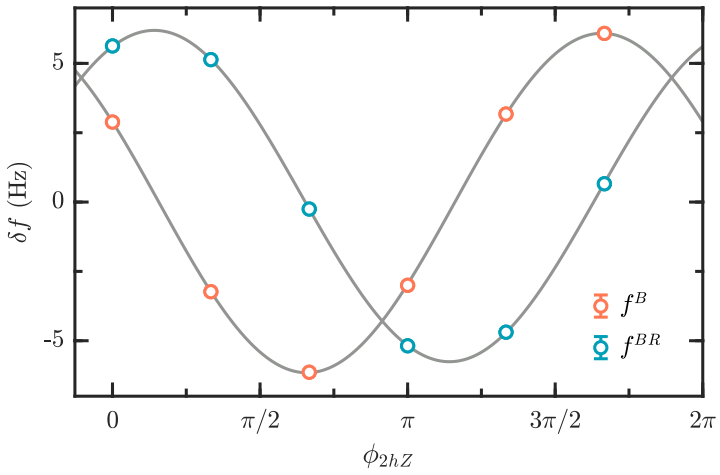

Figure 3.12: Measurement of Berry's phase shift in f^B and f^{BR}. We applied an ellipticity with magnitude $\mathcal{E}_\epsilon/\mathcal{E}_{\mathrm{rot}} \sim 7 \times 10^{-3}$ and phase $\theta = -\frac{\pi}{8}$. We also applied a second harmonic along the z-axis with magnitude $\mathcal{E}_{2\mathrm{hz}} \sim 4$ V/m and scanned its phase. We see the sinusoidal frequency shifts predicted in Equations 3.37 and 3.38.

We then repeated the measurement without intentionally applying an ellipticity and saw a smaller sinusoidal effect in both frequency channels, shown in Figure 3.13. We inferred from this

measurement that the natural scale of the ellipticity in our trap is $\mathcal{E}_\epsilon/\mathcal{E}_{\rm rot} = 3 \times 10^{-4}$. This let us put a limit on the shift in f^B to be 0.8 mHz, corresponding to a systematic effect of 1.7 μHz.

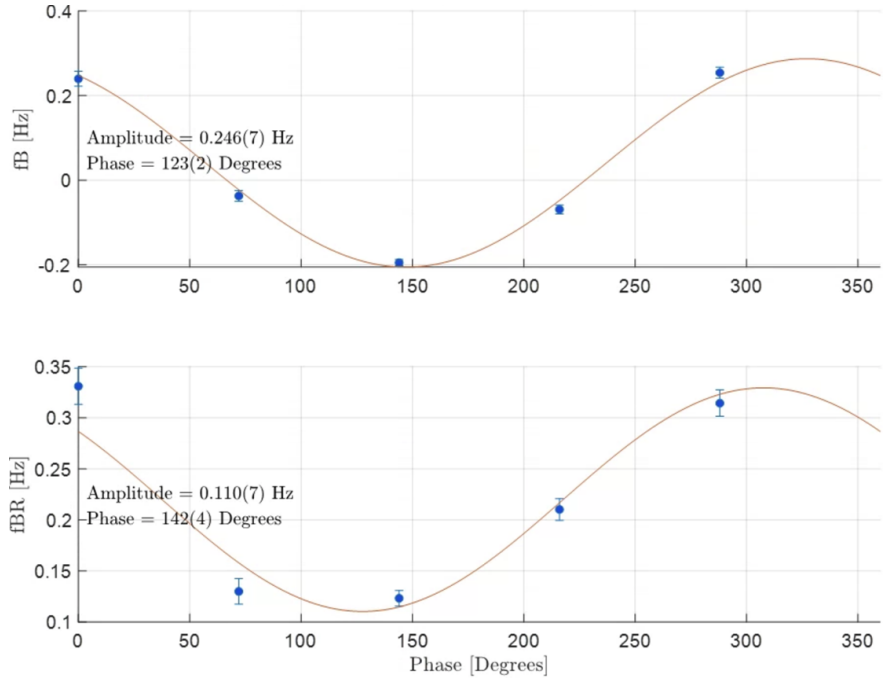

Figure 3.13: To measure $\mathcal{E}_\epsilon$ we applied a second harmonic along the z-axis with magnitude $\mathcal{E}_{\rm 2hz} \sim 4$ V/m and scanned its phase. We see sinusoidal shifts in f^B and f^{BR} indicating that there is a nonzero $\mathcal{E}_\epsilon/\mathcal{E}_{\rm rot} \sim 3 \times 10^{-4}$.

3.5.4 nth Harmonic along z plus (n-1) or (n+1)th Harmonic in the xy-plane

Generally, we can get a Berry's phase shift from the combination of two harmonics when one is along the z-axis and the other is in the xy-plane:

$$\delta\vec{\mathcal{E}}_{x,y} = \mathcal{E}_{nhx}\cos(n\omega_{\rm rot}t + \phi_{nhx})\hat{x} + \mathcal{E}_{nhy}\cos(n\omega_{\rm rot}t + \phi_{nhy})\hat{y} \tag{3.39}$$

$$\delta\vec{\mathcal{E}}_{z} = \mathcal{E}_{mhz}\cos(m\omega_{\rm rot}t + \phi_{mhz})\hat{z} \tag{3.40}$$

In these equations m and n are both integers. The combination of these perturbations will result

in a non-zero time-averaged frequency shift at first order provided m and n differ by ± 1. The shift is given by:

$$\delta f = \mp \frac{3\mathcal{E}_{mhz} f_{\rm rot}(n \pm 2)}{4\mathcal{E}_{\rm rot}^2} \left(\mathcal{E}_{nhx} \cos(\phi_{nhx} - \phi_{mhz}) \pm \mathcal{E}_{nhy} \sin(\phi_{nhy} - \phi_{mhz})\right) \tag{3.41}$$

Here the $\pm$ correspond to $m = n \pm 1$. Depending on the $\tilde{R}$ dependence of the various phases, this shift could appear in either f^B or f^{BR}. We note that the frequency shift corresponding to the first harmonic on the endcap and second harmonic radially, $m = 1$, $n = 2$, is zero, and so the next largest shifts are expected to come from effects involving the third harmonic or higher.

We measured the voltages of up to the 17th harmonics and put constraints on the various electric fields in Appendix B. We can plug the electric field measurements in Table B.1 into Equation 3.41 to find the magnitude of shifts that appear in f^B or f^{BR}. The results are shown in Table 3.7. The quadrature sum of all shifts in this table is 1.4 mHz. Assuming the worst case, that the shift is entirely in f^B, we are left with a 3.0 μHz systematic error in f^{DB}.

3.5.5 Other Berry's Phase Effects

The systematics paper discusses two more sources of Berry's phase. They are caused by 1) an AC Stark shift from our only laser that is on during the Ramsey time (Section VI B 2) and 2) the molecular cloud's axial slosh (Section VI B 3). I do not have much to add about these effects other than to point out that I think Luke Caldwell was clever to realize that there could be a Berry's phase shift from our laser at all.

3.6 Systematics Summary and Result

To end the chapter I include Table 3.8 which summarizes the systematic errors in our experiment. This table does include the smaller value for the axial magnetic field systematic discussed in Section 3.1. The section listed in the table below refers to the relevant section of the Systematics

Table 3.7: Constraints on Berry's phase frequency contributions to f^B or f^{BR} due to possible combinations of radial and axial field imperfections from harmonic distortion in amplifiers used to drive radial electrodes. All entries are in µHz. This table is an extension of Table VI in the Systematics paper.

	n_z															
$n_{x,y}$	2	3	4	5	6	7	8	9	10	11	12	13	14	15	16	17
2	0	17	0	0	0	0	0	0	0	0	0	0	0	0	0	0
3	11	0	95	0	0	0	0	0	0	0	0	0	0	0	0	0
4	0	22	0	87	0	0	0	0	0	0	0	0	0	0	0	0
5	0	0	75	0	83	0	0	0	0	0	0	0	0	0	0	0
6	0	0	0	31	0	38	0	0	0	0	0	0	0	0	0	0
7	0	0	0	0	139	0	947	0	0	0	0	0	0	0	0	0
8	0	0	0	0	0	13	0	24	0	0	0	0	0	0	0	0
9	0	0	0	0	0	0	545	0	556	0	0	0	0	0	0	0
10	0	0	0	0	0	0	0	16	0	35	0	0	0	0	0	0
11	0	0	0	0	0	0	0	0	90	0	200	0	0	0	0	0
12	0	0	0	0	0	0	0	0	0	33	0	30	0	0	0	0
13	0	0	0	0	0	0	0	0	0	0	143	0	107	0	0	0
14	0	0	0	0	0	0	0	0	0	0	0	37	0	41	0	0
15	0	0	0	0	0	0	0	0	0	0	0	0	144	0	155	0
16	0	0	0	0	0	0	0	0	0	0	0	0	0	9	0	11
17	0	0	0	0	0	0	0	0	0	0	0	0	0	0	105	0

paper.

When we removed the blind from our data we found that:

$$f^{DB} = -14.6 \pm 22.8_{\text{stat}} + 6.9_{\text{syst}}\ \mu\text{Hz} \tag{3.42}$$

We divide this result by $-2\mathcal{E}_{\text{eff}}\dfrac{\text{sgn}(g_F)}{h} \simeq 1.11 \times 10^{31}\ \dfrac{\mu\text{Hz}}{\text{e cm}}$ and we find a value for the eEDM:

$$d_e = \Big(1.3 \pm 2.0 \pm 0.6\Big) \times 10^{-30}\ \text{e cm} \tag{3.43}$$

The combined statistical and systematic uncertainty $\sigma_{d_e} = 2.1 \times 10^{-30}$ e cm improves on the ACME collaboration's result, which was previously the world leading measurement, by a factor of ~ 2.

Table 3.8: Uncertainty Budget

Effect	Section	Correction (μHz)	Uncertainty (μHz)
Magnetic			
Non-reversing $\vec{\mathcal{B}}^0$	VI A 1	0.1	< 0.1
Second harmonic of $\mathcal{E}_{\text{rot}}$ and transverse magnetic field	VI A 3		2.2
Third harmonic of $\mathcal{E}_{\text{rot}}$ and magnetic field gradients	VI A 4		1.5
Higher harmonics of $\mathcal{E}_{\text{rot}}$ and higher-order magnetic field gradients	VI A 4		< 0.1
Ellipticity of $\mathcal{E}_{\text{rot}}$ and magnetic field gradients	VI A 5		1.7
Berry's phase			
Phase modulation due to axial secular motion	VI B 3		3.4
Axial 2nd harmonic with ellipticity of $\mathcal{E}_{\text{rot}}$	VI B 4		1.7
Higher harmonics of $\mathcal{E}_{\text{rot}}$	VI B 5		3.0
Rotation induced mixing			
Leaking of f^{BR}	VI C 1		0.1
Axial magnetic fields	VI C 2		0.2
Other frequency			
Imperfect overlap of spatial distributions	VI D 2		3.5
Phase			
Improperly characterized imaging contrast	VII B 1		0.7
Swatch position	VII B 2		1.2
Total systematic		0.1	6.9
Statistical			22.8
Total		0.1	23.8

We can translate our result to an upper bound on d_e with 90% confidence:

$$|d_e| < 4.1 \times 10^{-30} \text{ e cm} \tag{3.44}$$

Per Equation 1.6, this result rules out the existence of certain beyond the Standard Model particles with masses up to 40 TeV, well beyond the direct reach of the Large Hadron Collider [30].

Chapter 4

Sign of the G-Factor

"Absolute sign determinations are extremely difficult to perform; there are too many ways one can overlook one minus sign out of the many which may be present."

- Larry A. Cohen, John H. Martin, and Norman F. Ramsey. "Signs of rotational g factors." Physical Review A 19.2 (1979): 433.

4.1 Introduction

The imbalance between matter and anti-matter in the universe can only be explained if the combined charge and parity (CP) symmetry is violated [24]. While the Standard Model does violate CP symmetry in the quark sector, it is not enough to explain the predominance of matter over antimatter [58]. Many extensions of the Standard Model incorporate novel CP violation that would induce a non-zero, and potentially measurable, electric dipole moment of the electron (eEDM) [29, 59, 60].

We recently made the most precise measurement of the eEDM to date using electrons confined inside HfF^+ molecular ions, subjected to a huge intra-molecular electric field, and evolving coherently for up to three seconds [27]. Like the other leading eEDM measurement made by the ACME collaboration, we performed our measurement in the $^3\Delta_1$ electronic state of a diatomic molecule, a state which is sensitive to the eEDM but relatively immune to magnetic effects [28]. The magnetic

g-factor g_F is suppressed in $^3\Delta_1$ states because two units of orbital angular momentum with $g = 1$ point opposite to one unit of spin angular momentum with $g \approx 2.002$.

The small g-factor of $^3\Delta_1$ is a powerful tool to suppress systematic errors in our measurements [31,61]. However, its small size makes the sign of g_F difficult to predict, especially in HfF^+ where the magnetic moment of the fluorine nucleus is comparable in size to the residual electronic magnetic moment. It is also a tricky parameter to extract experimentally, as only absolute magnitudes of energy differences are directly observable in standard Ramsey precession experiments.[1]

In both experiments, the sign of g_F is critical because it is necessary to find the sign of the eEDM. In the HfF^+ experiment the eEDM shows up as

$$d_e = \frac{-\mathrm{sgn}(g_F) h f^{DB}}{2\mathcal{E}_{\mathrm{eff}}} \tag{4.1}$$

where d_e is the eEDM, f^{DB} is a particular linear combination of frequencies that we measured (see Subsection 4.3.2) and $\mathcal{E}_{\mathrm{eff}} = +23$ GV/cm is the effective electric field of HfF^+ [36, 42, 43, 45].[2]

Once an experiment finds a non-zero value of d_e, knowing its sign will be crucial to compare with other measurements to confirm the result. At JILA, we plan to make our next generation measurement of the eEDM in the $^3\Delta_1$ state of ThF^+ molecules, while the ACME collaboration's upcoming measurement continues to use the $^3\Delta_1$ state of ThO [62]. In order to accurately determine

[1] Suppose you can apply pi/2 pulses around any axis on the Bloch sphere with states $|a\rangle$ and $|b\rangle$, with the initial quantum state $|\psi(t=0)\rangle = |a\rangle$. Consider an experiment where you first apply a pi/2 pulse to rotate about the +x axis, wait for the state to pick up a phase shift of $\pi/2$, and then apply another pi/2 pulse around the +y axis. The population will end up in $|a\rangle$ if $E_a > E_b$ or in $|b\rangle$ if $E_a < E_b$. However, it is not clear that you can determine the direction of the axis of rotation if you do not already know which state has more energy than the other. In any case, when we apply pi/2 pulses by reducing the magnitude of the rotating electric field, we cannot control the rotation axis in the Bloch sphere.

[2] See Appendix 4.6.2 for a discussion of the sign of $\mathcal{E}_{\mathrm{eff}}$.

the sign of our result, this chapter will detail how we experimentally determined the sign of g_F of the $^3\Delta_1$ state in HfF^+. This method can be used in the near future to do the same for ThF^+.

4.2 Possible Methods of Measuring the Sign of g_F

Determining the magnitude of a $^3\Delta_1$ state's g-factor can be done by measuring the magnitude of the energy difference between $\pm M_F$ states in the presence of a known magnetic field. That alone will not provide information about the g-factor's sign. A generic technique that can work for $^3\Delta_1$ states is microwave spectroscopy between neighboring rotational levels that are typically spaced tens of GHz apart. Consider the $J = 1$ and $J = 2$ rotational levels of a $^3\Delta_1$ state with nuclear spin $I = \frac{1}{2}$ as is the case in HfF^+ and ThF^+ and shown in Figure 4.1. The diagonal Stark and Zeeman shifts of the fully stretched states in a given rotational level are given by:

$$\begin{aligned} E_{\text{Stark+Zeeman}}(\Omega, J, I = \frac{1}{2}, F = J + \frac{1}{2}, M_F = \pm F) \\ = -\big(D_\parallel \mathcal{E}_z \Omega + (3g_F - g_N \frac{m_e}{m_p})\mu_B \mathcal{B}_z\big) \frac{M_F}{F(F + 0.5)} \end{aligned} \tag{4.2}$$

In this equation $D_\parallel$ is the effective molecular dipole moment, g_F is the g-factor of the $^3\Delta_1$ state, $g_N \approx 5.25$ is the magnetic moment of the fluorine nucleus, and m_e and m_p are the masses of the electron and proton. $\mathcal{E}_z$ and $\mathcal{B}_z$ are the components of the electric and magnetic fields respectively along the quantization axis that give rise to the diagonal shifts, which in our experiment are $\mathcal{E}_{\text{rot}}$ and $\mathcal{B}_{\text{rot}}$. If we perform microwave spectroscopy between two stretched states of $J = 1$ and $J = 2$ as shown in Figure 4.1, in addition to the energy offset due to the rotational and hyperfine splittings, we find an energy difference of:

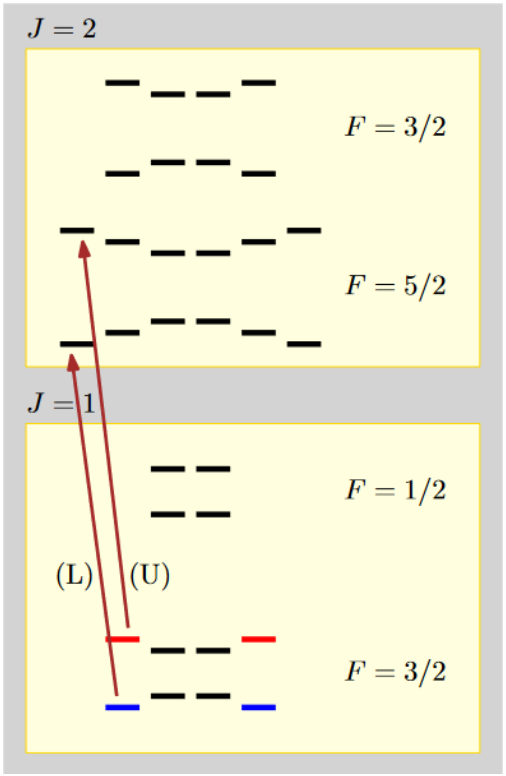

Figure 4.1: A schematic of the $J = 1$ and $J = 2$ rotational energy levels of the $^3\Delta_1$ state with $I = 0.5$ in the presence of an electric field. This is in the limit where the hyperfine structure is large compared to the Stark splitting, which is large compared to the omega doublet splitting. The red lines show transitions between the lower (L) and upper (U) stretched states. Measuring either transition in the presence of a magnetic field can determine the sign of the state's g-factor. This image has been reproduced from [4].

$$E(\Omega=-1, J=2, I=\frac{1}{2}, F=\frac{5}{2}, M_F=-\frac{5}{2}) \; - \; E(\Omega=-1, J=1, I=\frac{1}{2}, F=\frac{3}{2}, M_F=-\frac{3}{2})$$
$$= \frac{(3g_F - g_N\frac{\mu_N}{\mu_B})\mu_B\mathcal{B}_z - D_\parallel\mathcal{E}_z}{6} + \text{Constant} \tag{4.3}$$

The above equation gives the energy difference of the transition labeled (L) in Figure 4.1. For a fixed value of $\mathcal{E}_z$, the energy difference becomes a constant plus two terms - one that's proportional to the sign of g_F and another that depends on very accurately known constants. By measuring this transition frequency with positive and negative values of $\mathcal{B}_z$, the offset can be removed and the sign of g_F determined. A challenge of this method is that one needs to know which fully stretched M_F state is initially prepared. If the initial state is prepared via optical pumping, the absolute sign of the optical pumping laser's helicity must be known.

While this method could be used in a number of instances, it is not feasible in our apparatus. In order to isolate the sign of g_F, the magnitude of the Zeeman shift must be larger than the noise in the shift due to the electric field. In the part of our dataset where we applied 151 Hz frequency shifts, the measured frequencies had a 1σ spread of 143 mHz that can be attributed to noise in $\mathcal{E}_{\text{rot}}$. This part in 1000, or 60 mV/cm, electric field noise together with $D_\parallel = 1.97$ MHz / (V/cm) gives about 20 kHz of noise in Equation 4.3. In order for the Zeeman shift to have a comparable magnitude, we would need a reversible $\mathcal{B}_{\text{rot}} \sim 10$ Gauss, which is roughly three orders of magnitude larger than we typically apply.

This method could be implemented at the ACME experiment where they apply static electric and magnetic fields that do not rotate and therefore can be more stable. With a reasonably large ~ 100 G magnetic field[3], they would expect to see a $\pm 1.4/6$ MHz $\approx \pm 230$ kHz shift. This would require electric field stability at the V/cm level or better to see this signal and determine the sign of their g-factor, which seems attainable.[4]

[3] 1000 Amp*turns and 10 cm radius coils gives a 90 G field at the center of Helmholtz coils

[4] Note that ACME's molecule, ThO, does not have any hyperfine structure, simplifying Equation 4.3 as $g_N = 0$.

Alternatively, the sign of the g-factor can be measured via Ramsey spectroscopy between any two states that are separated in energy by both a magnetic and non-magnetic effect like Berry's phase. For example, suppose two states $\pm M_F$ are separated by a Zeeman shift of $\sim -\text{sgn}(g_F)100$ Hz. If a non-magnetic then effect lifts the $+M_F$ state 10 Hz above the $-M_F$ state, the sign of the g-factor can be determined by observing if the magnitude of the shift becomes 110 or 90 Hz.

One downside of this approach is that not many experiments are set up to apply readily measurable Berry's phase shifts. Fortunately, performing our spectroscopy in a bias field $\mathcal{E}_{\text{rot}}$ that rotates at 100s of kHz allows us to quite easily apply large Berry's phase shifts. It can be difficult to get the sign of a Berry's phase shift correct, which is crucial for this measurement, so it is re-derived in Appendix 4.6.1. In Section 4.3 we will introduce the JILA eEDM experiment. In Section 4.4 we will explain the results of Berry's phase measurements that reveal the sign of g_F in HfF^+.

4.3 The JILA eEDM Experiment

4.3.1 Experimental Overview

We trap $\sim 20,000$ HfF^+ molecular ions in a two-dimensional Paul trap. We populate the stretched states of the lowest rovibrational level of the $^3\Delta_1$ electronic state in the presence of a rotating bias field $\vec{\mathcal{E}}_{\text{rot}}$ with magnitude $\mathcal{E}_{\text{rot}} \approx 60$ V/cm, see Figure 4.2. $\vec{\mathcal{E}}_{\text{rot}}$ rotates in the xy-plane with frequency $f_{\text{rot}} = 375$ kHz, causing the ions to move circularly with radius $r_{\text{rot}} \approx 0.5$ mm. $\vec{\mathcal{E}}_{\text{rot}}$ also polarizes the molecules and defines the quantization axis for our spectroscopy. A magnetic field causes a Zeeman shift between the stretched $M_F = \pm 1.5$ states with an absolute value of ~ 100 Hz, which we measure via Ramsey spectroscopy. For details on how we used HfF^+ in this platform to measure the eEDM, see [2, 27, 31] and Chapter 2 of this thesis.

4.3.2 Experimental Switches and Frequency Channels

As is common in precision measurements, we greatly benefit from experimental "switches". By measuring Ramsey fringes in different configurations we can isolate the eEDM induced shift

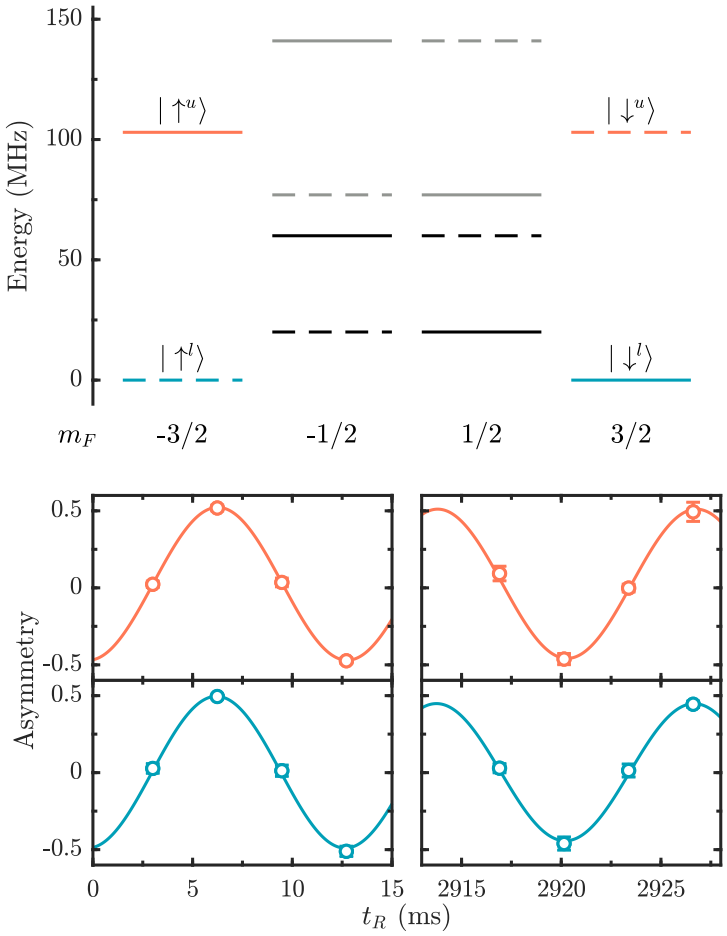

Figure 4.2: Top: The level structure of $^3\Delta_1 v = 0, J = 1$ state in HfF^+ in an external electric field $\mathcal{E}_{\text{rot}} \sim 58$ V/cm. The energy levels are similar to the $^3\Delta_1, v = 0, J = 1$ state in ThF^+. Grey lines correspond to states which asymptote to $F = \frac{1}{2}$ as $\mathcal{E}_{\text{rot}}$ tends toward zero, and all other states asymptote to $F = \frac{3}{2}$. Solid (dashed) lines correspond to states with $\Omega = +1$ (-1), see Appendix 4.6.2. The upper (orange) and lower (blue) doublets of the $F = \frac{3}{2}$ state are split by ~ 100 MHz by $\mathcal{E}_{\text{rot}}$. We can split the $M_F = \pm\frac{3}{2}$ states with a Zeeman shift and/or a Berry's phase, typically on the order of ~ 100 Hz. If the eEDM is nonzero it will cause an energy splitting in the upper and lower doublets of the same size but opposite sign. Bottom: We simultaneously perform Ramsey measurements within each doublet to measure the ~ 100 Hz energy difference. The points are from example HfF^+ Ramsey fringes; the curves are fits. This image has been reproduced from [31].

from much larger spurious effects. Our recent measurement had five switches, but only three that are relevant for determining the sign of the eEDM and the g-factor: $\tilde{D} = \pm 1$, whether we take data in the upper or lower doublet of $^3\Delta_1$ as shown in Figure 4.2; $\tilde{B} = \pm 1$, whether the magnetic field is parallel or anti-parallel to $\vec{\mathcal{E}}_{\rm rot}$; $\tilde{R} = \pm 1$, whether the rotation of the electric field points up or down via the right hand rule. For a description of the other switch states, see [2, 31].

Combining these three switches we make $2^3 = 8$ Ramsey measurements of the energy difference between the stretch states shown in Figure 4.2. We fit the Ramsey fringes to sine waves, and we label the eight fit frequencies as $f^{\tilde{D}=\pm1,\tilde{B}=\pm1,\tilde{R}=\pm1}$.

The $\sim$ 100 Hz energy difference that we measure is caused by the Zeeman shift between $M_F = \pm 1.5$ states and therefore changes sign when we reverse $\tilde{B}$. We do not know this energy difference's absolute sign unless we know $\mathrm{sgn}(g_F)$. We arbitrarily constrain all of the fit frequencies to be positive. We then construct eight frequency channels:

$$\begin{pmatrix} f \\ f^D \\ f^B \\ f^{DB} \\ f^R \\ f^{DR} \\ f^{BR} \\ f^{DBR} \end{pmatrix} = \frac{1}{8} \begin{pmatrix} 1 & 1 & 1 & 1 & 1 & 1 & 1 & 1 \\ 1 & -1 & 1 & -1 & 1 & -1 & 1 & -1 \\ 1 & 1 & -1 & -1 & 1 & 1 & -1 & -1 \\ 1 & -1 & -1 & 1 & 1 & -1 & -1 & 1 \\ 1 & 1 & 1 & 1 & -1 & -1 & -1 & -1 \\ 1 & -1 & 1 & -1 & -1 & 1 & -1 & 1 \\ 1 & 1 & -1 & -1 & -1 & -1 & 1 & 1 \\ 1 & -1 & -1 & 1 & -1 & 1 & 1 & -1 \end{pmatrix} \begin{pmatrix} f^{+1,+1,+1} \\ f^{-1,+1,+1} \\ f^{+1,-1,+1} \\ f^{-1,-1,+1} \\ f^{+1,+1,-1} \\ f^{-1,+1,-1} \\ f^{+1,-1,-1} \\ f^{-1,-1,-1} \end{pmatrix} \tag{4.4}$$

The presence of D or R in the superscript of a frequency channel indicates that it is the difference between the upper and lower doublet or between the two rotation directions. The absence of superscript D or R conversely indicates that it is the average of the doublets or rotation directions. However, because $\tilde{B}$ determines the sign of the energy difference and we have already taken the

absolute value, the inclusion or absence of B has the opposite meaning. For example, f^{BR} is the average of the $\tilde{B}$ and $\tilde{D}$ switches, but the difference between rotation up and rotation down.

As derived in Appendix 4.6.2, f^{DB}, the difference frequency between the upper and lower doublet and average of the other switches, tells us the value of the eEDM. It is clear from Equation 4.1 that in order to extract the sign of d_e we need to know the sign of g_F. Intuitively, this is for the same reason that we need to know the sign of the Berry's phase effect to determine the sign of g_F - because we only measure the magnitude of the splitting between $M_F = \pm\frac{3}{2}$ states, we need to know the sign of the Zeeman effect to know the sign of the eEDM.

4.3.3 Berry's Phase in JILA eEDM

During the Ramsey spectroscopy, the quantization axis defined by $\vec{\mathcal{E}}_{\text{rot}}$ completes on the order of 10^5 rotations in the xy-plane per second. As $\vec{\mathcal{E}}_{\text{rot}}$ traces out closed loops, the quantum state accumulates a geometric phase of:

$$\phi_{geo} = M_F \Omega_s \tag{4.5}$$

During our spectroscopy the molecules are in a superposition of $M_F = \pm 1.5$ states, so the molecules will accumulate a relative phase shift of $3\Omega_s$. Here Ω_s is the solid angle traced out by the electric field, as shown in Figure 4.3, which is a signed quantity. If the electric field rotates perfectly in the xy-plane, $\Omega_s = \mp 2\pi$ for $\tilde{R} = \pm 1$. In this ideal case the difference of ϕ_{geo} between the two M_F states is $\mp 6\pi$, meaning that the Berry's phase is not observable as it is an integer number of 2π phase shifts. But if we intentionally tilt the electric field out of the xy-plane by a small angle α, we induce a measurable phase shift that will be accumulated every $T_{\text{rot}} = 1/f_{\text{rot}}$. For small tilts, this will appear as a frequency shift for each M_F state given by:

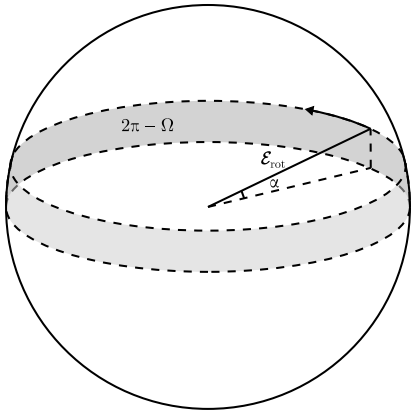

Figure 4.3: Ideally, the quantization axis defined by $\vec{\mathcal{E}}_{\text{rot}}$ rotates perfectly in the xy-plane and traces out a solid angle of $-2\pi\tilde{R}$. If $\vec{\mathcal{E}}_{\text{rot}}$ is tilted up by a small angle α, it will deviate from the ideal solid angle by an amount Ω. This image has been reproduced from [31].

$$f_{\text{Berry}} \approx -\frac{M_F f_{\text{rot}}}{2\pi} \int_0^{T_{\text{rot}}} \alpha(t)\dot{\phi}(t)dt \tag{4.6}$$

Here $\alpha(t)$ is the tilt of the quantization axis out of the xy-plane and $\dot{\phi}(t)$ is the azimuthal angular velocity. If neither parameter depends on time, we find that:

$$f_{\text{Berry}} = -M_F f_{\text{rot}} \alpha \tilde{R} \tag{4.7}$$

In order to measure the sign of the g-factor, we cannot simply apply a constant tilt to $\vec{\mathcal{E}}_{\text{rot}}$ as shown in Figure 4.3 since the average force on our trapped ions must equal zero.[5] Attempting to tilt $\vec{\mathcal{E}}_{\text{rot}}$ upwards would simply lift the center of the ion trap. However, we can generate a Berry's phase by applying an electric field along the z-axis that time averages to zero. A combination of fields that gives a nonzero Berry's phase is an electric field along z that oscillates at twice the rotation frequency along with an elliptical rotating field:

[5]There is always a small electric field pointing up to balance the force of gravity. This slightly tilts $\vec{\mathcal{E}}_{\text{rot}}$ and generates a small Berry's phase that we cannot tune, which is not particularly useful for measuring the sign of g_F. For further discussion of the effect of gravity on Berry's phase, see [31].

$$\vec{\mathcal{E}}(t) = \begin{pmatrix} \mathcal{E}_{\text{rot}} \cos\left(\omega_{\text{rot}} t + \phi_R + \tilde{R}\phi_0\right) + \mathcal{E}_\epsilon \cos\left(2\theta\tilde{R} - \omega_{\text{rot}} t - \phi_R - \tilde{R}\phi_0\right) \\ \mathcal{E}_{\text{rot}}\tilde{R} \sin\left(\omega_{\text{rot}} t + \phi_R + \tilde{R}\phi_0\right) + \mathcal{E}_\epsilon \tilde{R} \sin\left(2\theta\tilde{R} - \omega_{\text{rot}} t - \phi_R - \tilde{R}\phi_0\right) \\ \mathcal{E}_{\text{2hz}} \cos\left(2\omega_{\text{rot}} t + \phi_{2f}\right) \end{pmatrix} \tag{4.8}$$

$\mathcal{E}_\epsilon$ is the magnitude of the ellipticity and $\mathcal{E}_{\text{2hz}}$ is the magnitude second harmonic that oscillates at $2\omega_{\text{rot}}$ along the z axis. Note that both magnitudes are defined to be positive. At $t = 0$, $\vec{\mathcal{E}}_{\text{rot}}$ points in the xy-plane at an angle $\phi_0 + \tilde{R}\phi_R$ from the positive x-axis. The long axis of the ellipticity points at an angle θ in the xy-plane and the second harmonic has a phase of ϕ_{2f}. By applying this combination of fields, we see in Appendix 4.6.3 that we generate a Berry's phase that will appear as a frequency shift in f^B and f^{BR} and depend on the sign of g_F.

$$f^B = \frac{9\mathcal{E}_{\text{2hz}}\mathcal{E}_\epsilon f_{\text{rot}}}{2\mathcal{E}_{\text{rot}}^2} \text{sgn}(g_F) \sin\left(2\theta - 2\phi_0\right) \sin\left(\phi_{2f} - 2\phi_R\right) \tag{4.9}$$

$$f^{BR} = -\frac{9\mathcal{E}_{\text{2hz}}\mathcal{E}_\epsilon f_{\text{rot}}}{2\mathcal{E}_{\text{rot}}^2} \text{sgn}(g_F) \cos\left(2\theta - 2\phi_0\right) \cos\left(\phi_{2f} - 2\phi_R\right) \tag{4.10}$$

In order to measure the sign of the g-factor, we need to apply these fields with known phases and see how f^B and f^{BR} change as we scan the phase of the second harmonic for a fixed value of the ellipticity.[6] We can then compare the two observed sine waves to the above equations for $\text{sgn}(\text{g}_\text{F}) = \pm 1$ to see which value is correct for each of our molecules.

4.4 Results

As discussed in Appendix 4.6.4, we take all of our data with $\phi_0 = \frac{7\pi}{4}$ and $\phi_R = \frac{\pi}{12}$,[7] so the above equations simplify to:

[6] Alternatively, we could fix ϕ_{2f} and scan θ, but it is easier to scan ϕ_{2f} experimentally.

[7] These seemingly arbitrary choices of ϕ_0 and ϕ_R ensure that at the time of dissociation the molecules are oriented to optimize our imaging contrast.

$$f^B = \frac{9\mathcal{E}_{2\mathrm{hz}}\mathcal{E}_\epsilon f_{\mathrm{rot}}}{2\mathcal{E}_{\mathrm{rot}}^2}\mathrm{sgn}(g_F)\cos(2\theta)\sin(\phi_{2f} - \frac{\pi}{6}) \tag{4.11}$$

$$f^{BR} = \frac{9\mathcal{E}_{2\mathrm{hz}}\mathcal{E}_\epsilon f_{\mathrm{rot}}}{2\mathcal{E}_{\mathrm{rot}}^2}\mathrm{sgn}(g_F)\sin(2\theta)\sin(\phi_{2f} + \frac{\pi}{3}) \tag{4.12}$$

We took data with our usual values of $\mathcal{E}_{\mathrm{rot}} = 58$ V/cm and $f_{\mathrm{rot}} = 375$ kHz, and applied $\mathcal{E}_\epsilon \sim 400$ mV/cm at an angle of $\theta = \frac{\pi}{8}$. We also applied a second harmonic along the z-axis $\mathcal{E}_{2\mathrm{hz}} \sim 40$ mV/cm and scanned its phase ϕ_{2f}. We therefore expect the data, which are shown in Figure 4.4, to behave as follows:

$$f^B = \frac{9\mathcal{E}_{2\mathrm{hz}}\mathcal{E}_\epsilon f_{\mathrm{rot}}}{2\sqrt{2}\mathcal{E}_{\mathrm{rot}}^2}\mathrm{sgn}(g_F)\sin(\phi_{2f} - \frac{\pi}{6}) \tag{4.13}$$

$$f^{BR} = \frac{9\mathcal{E}_{2\mathrm{hz}}\mathcal{E}_\epsilon f_{\mathrm{rot}}}{2\sqrt{2}\mathcal{E}_{\mathrm{rot}}^2}\mathrm{sgn}(g_F)\sin(\phi_{2f} + \frac{\pi}{3}) \tag{4.14}$$

We see that the data conform to a sine waves with amplitudes similar to those predicted by Equations 4.13 and 4.14. The phase of the sine waves predicted by these equations depend on the sign of the g-factor, and it is obvious from both frequency channels in Figure 4.4 that $\mathrm{sgn}(g_F) = -1$.

We can confirm our assignment by considering data where the ellipticity is rotated by 90 degrees, so $\theta = -\frac{\pi}{8}$ as shown in Figure 4.5. While there is a slight phase offset between the predicted and measured values of f^B and f^{BR} on the order of a few degrees, that is explained by the imprecision in determining ϕ_0 and ϕ_R as explained in Appendix 4.6.4. It is again clear that $\mathrm{sgn}(g_F) = -1$ fits the data.

The data in Figures 4.4 and 4.5 are conclusive, but the result is obscured by a haze of math. Instead of splitting the data into frequency channels as described in Equation 4.4, we can focus

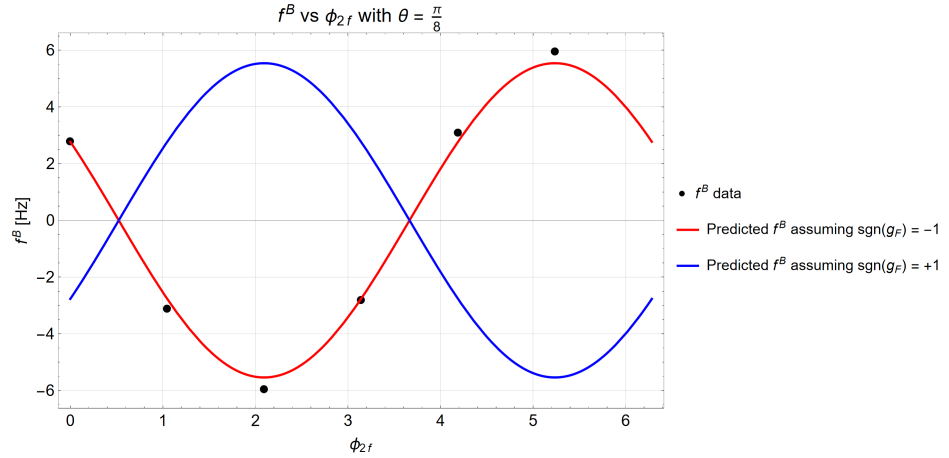

(a)

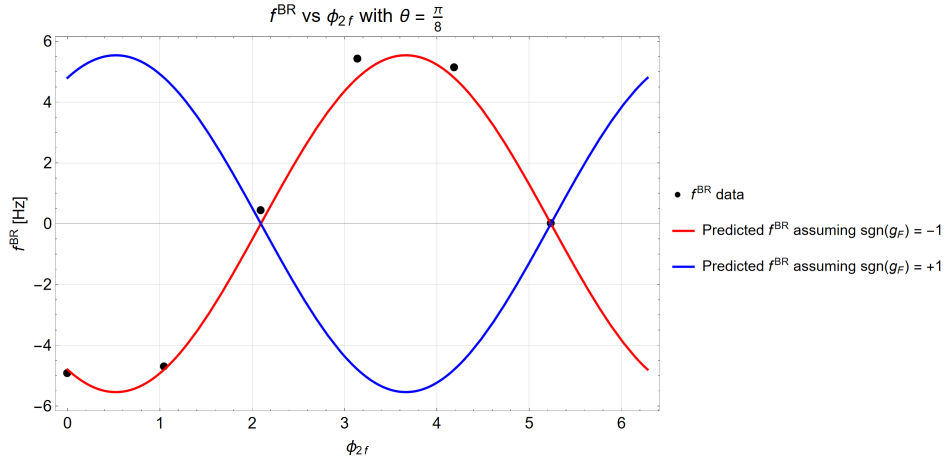

(b)

Figure 4.4: f^B (a) and f^{BR} (b) data taken with applied ellipticity at angle $\theta = \dfrac{\pi}{8}$ and different phases of the second harmonic along the z-axis. The data points in both graphs have error bars on the order of 10 mHz that are too small to resolve at this scale. Equations 4.13 (a) and 4.14 (b) are plotted with both signs of g_F, there is no fitting. Both datasets clearly show that $\text{sgn}(g_F) = -1$.

on the absolute magnitude of the energy differences measured directly. Consider the eight energy differences when $\tilde{B} = \pm 1$, $\tilde{R} = \pm 1$, and when the time-average of α, the angle of the total electric field above the xy-plane, is positive or negative. To simplify the notation, we introduce the notation $\tilde{\alpha} = \pm 1$ for these two cases respectively.

We have $\tilde{\alpha} = +1$ when $\vec{\mathcal{E}}_{2\text{hz}}$ points downward when the elliptical electric field points along its

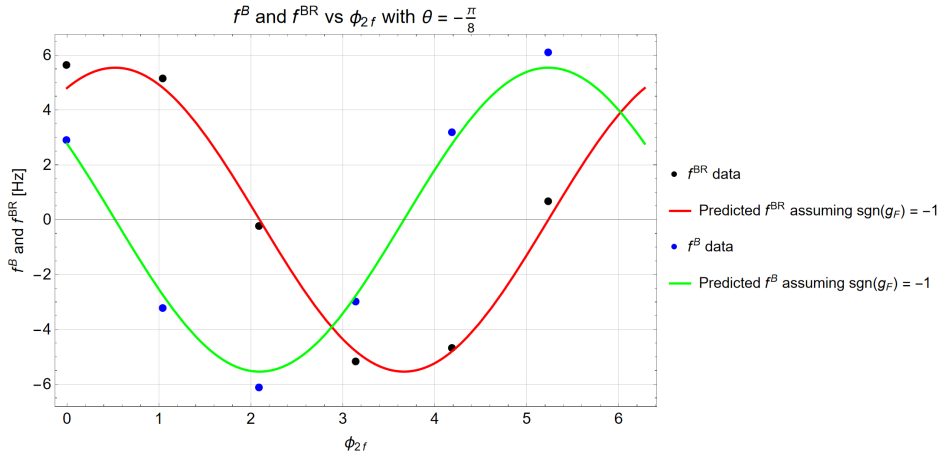

Figure 4.5: f^B and f^{BR} data taken with applied ellipticity at angle $\theta = -\frac{\pi}{8}$ and different phases of the second harmonic along the z-axis. The data points in both graphs have error bars on the order of 10 mHz that are too small to resolve at this scale. Equations 4.13 (a) and 4.14 (b) are plotted with $\text{sgn}(g_F) = -1$, which we found from the data with $\theta = \frac{\pi}{8}$ shown in Figure 4.4. This dataset also shows that $\text{sgn}(g_F) = -1$.

major axis, forming a small downward angle. When the elliptical $\vec{\mathcal{E}}_{\text{rot}}$ rotates 90 degrees, $\vec{\mathcal{E}}_{\text{2hz}}$ will point upward as the $\vec{\mathcal{E}}_{\text{rot}}$ points along its minor axis, forming a larger upward angle. Therefore the time-averaged $\bar{\alpha}$ is positive in this case.[8]

The sign of the Zeeman shift is $-\text{sgn}(g_F)\tilde{B}$,[9] while the sign of the Berry's phase shift is $-\tilde{\alpha}\tilde{R}$, as given by Equation 4.7.[10] When the Zeeman and Berry's phase shifts have the same sign, the absolute energy difference will increase. Therefore, the entries in Figure 4.6 will be larger/smaller (~ 159 or ~ 143 Hz) when $-\text{sgn}(g_F)\tilde{B} \times -\tilde{\alpha}\tilde{R} = \text{sgn}(g_F)\tilde{\alpha}\tilde{B}\tilde{R} = \pm 1$. The top left entry in Figure 4.6 is one of the smaller entries, with $\tilde{\alpha}\tilde{B}\tilde{R} = (+1)(+1)(+1) = +1$, so it must be that $\text{sgn}(g_F) = -1$. Checking any of the other seven entries gives the same result, all without the potential confusion

[8] For our data in Figure 4.6, we use data where ϕ_{2f} is 15 degrees away from the value where $\bar{\alpha}$ is at its maximal or minimal value. This marginally reduces the magnitude of the Berry's phase shift, but does not change the analysis.

[9] We assume that energy shifts are positive when the $M_F = \frac{3}{2}$ state has more energy than the $M_F = -\frac{3}{2}$ state, as we do elsewhere.

[10] While in this case α and $\dot{\phi}$ depend on time so we have to use the more general Equation 4.6, Equation 4.7 gives the correct sign if we replace α with the time-averaged $\bar{\alpha}$. This helps clarify the underlying physics.

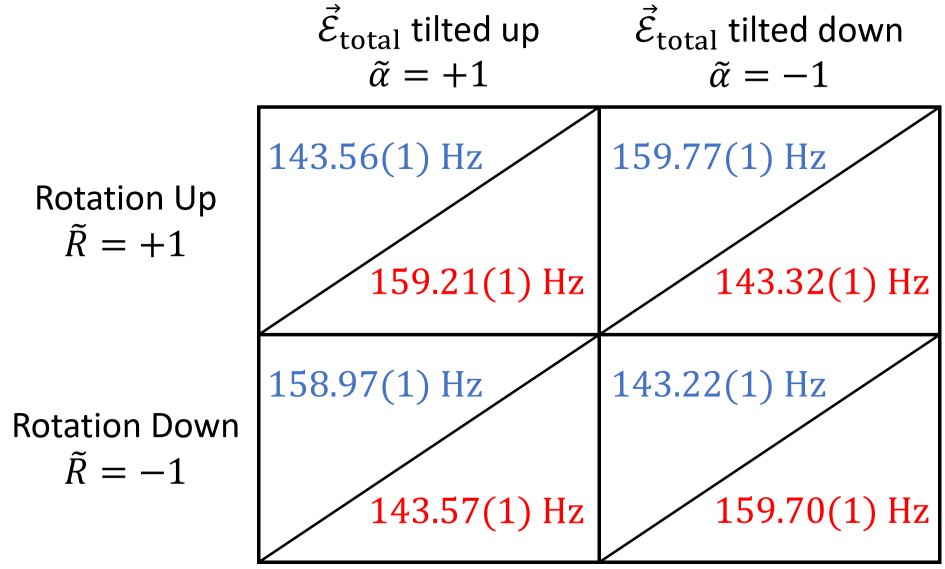

Figure 4.6: Absolute energy differences measured with a Zeeman shift plus Berry's phase, as a function of $\tilde{B}$, $\tilde{R}$ and $\tilde{\alpha}$. Blue frequencies in the top left of each box have $\tilde{B} = +1$, red frequencies in the bottom right have $\tilde{B} = -1$. The ~ 8 Hz Berry's phase shift has the same/opposite sign as the ~ 151 Hz Zeeman shift when $\text{sgn}(g_F)\tilde{\alpha}\tilde{B}\tilde{R} = \pm 1$, giving absolute energy differences of 151 + 8 = 159 Hz or 151 - 8 = 143 Hz. All eight of these entries imply that $\text{sgn}(g_F) = -1$.

of defining f^B and f^{BR}. This method still relies on knowing the rotation direction, magnetic field direction and relative orientation of electric fields of each of our fringes, but it is hopefully more intuitive.

We can now plug in the sign of g_F into Equation 4.1 and find a sign-sensitive relationship in our HfF^+ experiment:

$$d_e = \frac{h f^{DB}}{2\mathcal{E}_{\text{eff}}} \tag{4.15}$$

h is positive and $\mathcal{E}_{\text{eff}} = +23$ GV/cm in our molecule, so d_e has the same sign as f^{DB}.

It is important that the signed quantities have the same signs in our code, which is addressed in Appendix 4.6.5. For a full list of the quantities whose sign we need to define correctly in order to arrive at these two equations, see Appendix 4.6.6. Given that the sign of g_F is negative, we

can also confirm the calculation from second order perturbation theory that $\frac{\delta g_F}{g_F}$ is positive. See Appendix 4.6.7 for that discussion.

4.5 Conclusion

By applying a Zeeman shift in addition to an energy difference with a known sign between the $\pm M_F$ states via Berry's phase, we were able to determine that the sign of the g-factor in the $^3\Delta_1$ state of HfF^+ is negative. As Norman Ramsey said, there are many places to go wrong when determining absolute energy differences, but we are confident in our assignment. This method will be repeated for the $^3\Delta_1$ state of ThF^+, and can be checked by anyone who has enough time on their hands to inspect this thesis chapter diligently.

4.6 Appendices for Sign of the G Factor

4.6.1 Appendix 1: Berry's Phase Derived

Our method of determining the sign of g_F relies on us applying an energy shift of known sign between the $M_F = \pm\frac{3}{2}$ states via Berry's phase. Simply using an equation like Equation 4.7 is tempting but possibly misleading because the sign of the solid angle can depend on convention. To confirm the sign of the Berry's phase shift, we will derive Berry's phase from purely quantum mechanical arguments. This treatment will largely follow this paper [63] by Meyer, Leanhardt, Cornell and Bohn.

Consider a spin-$\frac{1}{2}$ system[11] in the presence of a magnetic field with the time-dependant Hamiltonian:

$$H(t) = -\vec{\mu}_m \cdot \vec{\mathcal{B}}(t) = -\frac{g\mu_B \mathcal{B}}{2}\vec{\sigma} \cdot \hat{\mathcal{B}}(t) = \frac{\hbar}{2}\omega_L \vec{\sigma} \cdot \hat{\mathcal{B}}(t) \tag{4.16}$$

[11] The authors of [63] treat both a spin-$\frac{1}{2}$ and a spin-j system, and they show that the sign of the effect is the same in both cases.

We are assuming that the magnitude of the magnetic field does not change, but its direction varies. This Hamiltonian introduces the Larmor frequency $\omega_L = -\frac{g\mu_B \mathcal{B}}{\hbar}$. We define the lab-frame Cartesian coordinates (ξ, η, ζ), and allow the magnetic field to rotate around the ζ axis at a constant angle θ_r. In a time t the magnetic field rotates an angle $\phi = \omega_r t\tilde{R}$ in the lab frame, where ω_r is an unsigned (always positive) quantity defined by $\vec{\omega}_r = \tilde{R}\omega_r\hat{\zeta}$. The rotating magnetic field defines the rotating-frame coordinates (x, y, z) as shown in Figure 4.7.

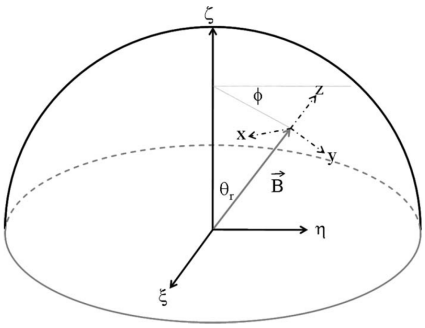

FIG. 1. The axis of rotation with laboratory-fixed coordinates $\{\xi, \eta, \zeta\}$ as well as the field coordinates defined by $\{x, y, z\}$. The field direction rotates about the ζ-axis with angular frequency ω_r.

Figure 4.7: Image and caption are from [63].

We can write the magnetic field in the lab frame as:

$$\vec{\mathcal{B}}(t) = (\mathcal{B}_\xi(t), \mathcal{B}_\eta(t), \mathcal{B}_\zeta(t)) = \mathcal{B}(\sin\theta_r \cos\omega_r t, \tilde{R}\sin\theta_r \sin\omega_r t, \cos\theta_r) \tag{4.17}$$

We can find an explicit representation of the Hamiltonian in Equation 4.16 in the lab-frame by plugging in the magnetic field as written in Equation 4.17 and using the explicit forms of the Pauli matrices. The Hamiltonian acts on the lab-frame basis vectors $|m_\zeta = \pm\frac{1}{2}\rangle$, and is written as:

$$H(t) = \frac{\hbar\omega_L}{2}\begin{pmatrix} \cos\theta_r & \sin\theta_r e^{-i\tilde{R}\omega_r t} \\ \sin\theta_r e^{i\tilde{R}\omega_r t} & -\cos\theta_r \end{pmatrix} \tag{4.18}$$

The goal now is to find the eigenvalues of this Hamiltonian. We'll start by writing a general

ansatz for the wave function in this basis:

$$|\psi(t)\rangle = \begin{pmatrix} \alpha(t)e^{-i\omega_+ t} \\ \beta(t)e^{-i\omega_- t} \end{pmatrix} \tag{4.19}$$

$\omega_\pm$ are the currently unspecified frequencies of the eigenvectors, which we'll solve for shortly. We can now plug this ansatz and the Hamiltonian in Equation 4.18 into the time-dependent Schrodinger equation:

$$i\hbar\frac{\partial}{\partial t}\begin{pmatrix} \alpha(t)e^{-i\omega_+ t} \\ \beta(t)e^{-i\omega_- t} \end{pmatrix} = \frac{\hbar\omega_L}{2}\begin{pmatrix} \cos\theta_r & \sin\theta_r e^{-i\tilde{R}\omega_r t} \\ \sin\theta_r e^{i\tilde{R}\omega_r t} & -\cos\theta_r \end{pmatrix}\begin{pmatrix} \alpha(t)e^{-i\omega_+ t} \\ \beta(t)e^{-i\omega_- t} \end{pmatrix} \tag{4.20}$$

After a few lines of algebra we find that:

$$i\hbar\frac{\partial}{\partial t}\begin{pmatrix} \alpha(t) \\ \beta(t) \end{pmatrix} = \hbar\begin{pmatrix} \frac{\omega_L}{2}\cos\theta_r - \omega_+ & \frac{\omega_L}{2}\sin\theta_r e^{-i(\tilde{R}\omega_r+\omega_- -\omega_+)t} \\ \frac{\omega_L}{2}\sin\theta_r e^{i(\tilde{R}\omega_r+\omega_- -\omega_+)t} & -\frac{\omega_L}{2}\cos\theta_r - \omega_- \end{pmatrix}\begin{pmatrix} \alpha(t) \\ \beta(t) \end{pmatrix} \tag{4.21}$$

This is progress because we now have something resembling the Schrodinger equation, although the vectors and Hamiltonian both depend on time. We can simplify this if we chose $\omega_\pm = \pm\tilde{R}\frac{\omega_r}{2}$, as this makes the Hamiltonian time-independent:

$$i\hbar\frac{\partial}{\partial t}\begin{pmatrix} \alpha(t) \\ \beta(t) \end{pmatrix} = \hbar\begin{pmatrix} \frac{\omega_L}{2}\cos\theta_r - \tilde{R}\frac{\omega_r}{2} & \frac{\omega_L}{2}\sin\theta_r \\ \frac{\omega_L}{2}\sin\theta_r & -\frac{\omega_L}{2}\cos\theta_r + \tilde{R}\frac{\omega_r}{2} \end{pmatrix}\begin{pmatrix} \alpha(t) \\ \beta(t) \end{pmatrix} \tag{4.22}$$

Recall that this is in the lab-frame basis. It's also clear that we can split this Hamiltonian into Zeeman and rotating parts:

$$H_{\text{dressed,lab}} = H_{Z,\text{lab}} + H_{r,\text{lab}} \tag{4.23}$$

$$H_{Z,\text{lab}} = \frac{\hbar\omega_L}{2}\begin{pmatrix}\cos\theta_r & \sin\theta_r \\ \sin\theta_r & -\cos\theta_r\end{pmatrix} \tag{4.24}$$

$$H_{r,\text{lab}} = -\tilde{R}\frac{\hbar\omega_r}{2}\begin{pmatrix}+1 & 0 \\ 0 & -1\end{pmatrix} = -\tilde{R}\hbar\omega_r m_\zeta \begin{pmatrix}1 & 0 \\ 0 & 1\end{pmatrix} \tag{4.25}$$

Now that we have a Hamiltonian, it's tempting to read off the energy shift due to the part of the Hamiltonian that arises from rotation.[12] However, we do our spectroscopy in the rotating frame so we need to change the Hamiltonian's basis. We can immediately write the Zeeman shift in the rotating basis, even though it's not particularly interesting for us at the moment:

$$H_{Z,\text{rot}} = \frac{\hbar\omega_L}{2}\begin{pmatrix}1 & 0 \\ 0 & -1\end{pmatrix} \tag{4.26}$$

This Hamiltonian acts on basis vectors $|m_z = \pm\frac{1}{2}\rangle$. To write H_r in the rotating frame, we need to transform from the $|sm_\zeta\rangle$ basis to the $|sm_z\rangle$ basis. We can do this by rotating through the Euler angles $(0, \theta_r, 0)$: [13]

$$R(0,\theta_r,0) = e^{-i\theta_R J_\eta} = \text{Exp}\left[-i\theta_R\begin{pmatrix}0 & -\frac{i}{2} \\ \frac{i}{2} & 0\end{pmatrix}\right] = \begin{pmatrix}\cos\left(\frac{\theta_r}{2}\right) & -\sin\left(\frac{\theta_r}{2}\right) \\ \sin\left(\frac{\theta_r}{2}\right) & \cos\left(\frac{\theta_r}{2}\right)\end{pmatrix} \tag{4.27}$$

We can then write:

[12] It's worth noting that this Hamiltonian is exact, there is no assumption that $\omega_r \ll \omega_L$ as is usually the case when discussing Berry's phase geometrically.

[13] [63] uses Wigner matrices instead of the generators of rotations. I believe the approach I have taken here is easier to follow.

$$\begin{pmatrix} +_z \\ -_z \end{pmatrix} = R \begin{pmatrix} +_\zeta \\ -_\zeta \end{pmatrix} = \begin{pmatrix} \cos\left(\frac{\theta_r}{2}\right) & -\sin\left(\frac{\theta_r}{2}\right) \\ \sin\left(\frac{\theta_r}{2}\right) & \cos\left(\frac{\theta_r}{2}\right) \end{pmatrix} \begin{pmatrix} +_\zeta \\ -_\zeta \end{pmatrix} \tag{4.28}$$

Note that because the matrix R is invertible, we can find the Hamiltonian in the rotating frame:

$$H_{r,rot} = RH_{r,lab}R^{-1} = \tilde{R}\frac{\hbar\omega_r}{2} \begin{pmatrix} -\cos\theta_r & -\sin\theta_r \\ -\sin\theta_r & \cos\theta_r \end{pmatrix} \tag{4.29}$$

We can read off the diagonal Berry's phase shift as $-\tilde{R}m_F\omega_r\cos\theta_r$. We are interested in evaluating the Berry's phase for $\theta_r = \frac{\pi}{2} - \alpha$, where α is a small angle. When α is positive it denotes a small angle above the xy-plane. In this case we have:

$$\omega_{\text{Berry}} = -\tilde{R}m_F\omega_r\cos\left(\frac{\pi}{2} - \alpha\right) \approx -\tilde{R}m_F\omega_r\alpha \tag{4.30}$$

In the last step we used the first term from the following Taylor expansion: $\cos\left(\frac{\pi}{2} - \alpha\right) = \alpha - \alpha^3/6 + \alpha^5/120 + ...$ Since α is small we can keep just the first term, and this justifies the overall sign in Equation 4.7.

4.6.2 Appendix 2: Relating d_e to f^{DB}

We define the internuclear axis $\hat{n}$ to point from the lighter fluorine towards the heavier nucleus as shown in Figure 4.8.[14] The electronic angular momentum projections Λ, Σ and $\Omega = \Lambda + \Sigma$ are positive if they point along $\hat{n}$. In the $^3\Delta_1$ state where $|\Lambda| = 2$, $|\Sigma| = 1$ and $|\Omega| = 1$, Λ and Σ must point in the opposite directions. This gives rise to the $\Omega = \pm 1$ states shown in Figure 4.8.

[14] This is a common convention, but it is not universal.

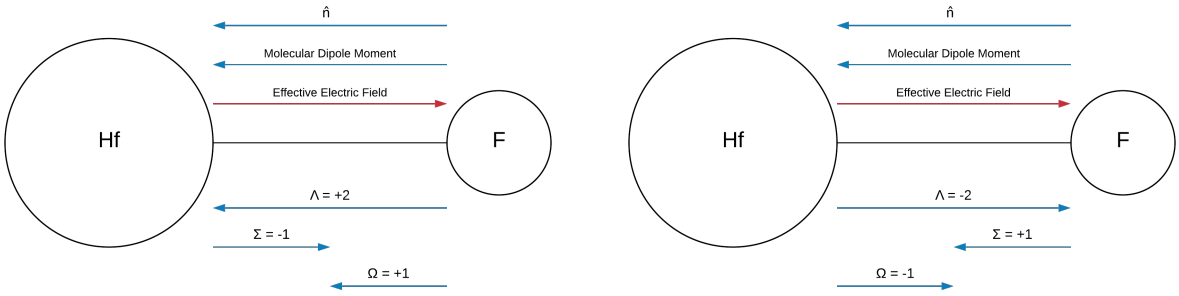

Figure 4.8: The two possible configurations of Quantum numbers in $^3\Delta_1$. Note that the (Hf nucleus + core of electrons) has a positive charge and the (F nucleus + core of electrons) has a negative charge. The directions of the molecular dipole moment and effective electric field therefore follow from the above definitions.

We can now justify the assignment of $\Omega = \pm 1$ in the level diagram shown in Figure 4.2. In the absence of an external electric field, the states with well defined Ω shown in Figure 4.8 are fully mixed and the eigenstates have well defined parity. In the presence of $\vec{\mathcal{E}}_{\text{rot}}$, which defines our quantization axis, $|^3\Delta_1, \Omega, J, F, M_F\rangle$ states are well defined. F is the total angular momentum and is always positive, while M_F is positive if it points along $\vec{\mathcal{E}}_{\text{rot}}$, the quantization axis.

Consider the particular rotational ground state ($R = 0$ so $J = \Omega + R = \Omega$) $|^3\Delta_1, 1, 1, \frac{3}{2}, \frac{3}{2}\rangle$. Since $F = J + I = \Omega + \frac{1}{2}$ we know that M_F points along the same direction as Ω. We also know that Ω points along $\hat{n}$ and that M_F points along $\hat{\mathcal{E}}_{\text{rot}}$, so it must be that $\hat{n} \parallel \hat{\mathcal{E}}_{\text{rot}}$. As we can see in Figure 4.8, $\hat{n}$ is parallel to the molecular dipole moment $\vec{d}_{mf}$ so we have $\hat{\mathcal{E}}_{\text{rot}} \parallel \vec{d}_{mf}$. This means the $|^3\Delta_1, 1, 1, \frac{3}{2}, \frac{3}{2}\rangle$ state has a negative Stark shift $E_{\text{Stark}} = -\vec{d}_{mf} \cdot \vec{\mathcal{E}}_{\text{rot}} = -d_{mf}\mathcal{E}_{\text{rot}}$ and we can identify it as part of the lower doublet, as shown in Figure 4.2. We can repeat a similar process to identify the value of Ω in the remainder of the states in the upper and lower doublets.

This procedure is important because the shift due to the eEDM depends on Ω. The shift is given by:

$$\langle H_{\text{edm}} \rangle = -d_e \mathcal{E}_{\text{eff}} \Omega \tag{4.31}$$

This relationship is given by [36][15], but also intuitively makes sense if we naively imagine that there is an actual electric field pointing from the positively charged hafnium nucleus to the negatively charged fluorine nucleus as shown in Figure 4.8. We define the electron's EDM d_e to be positive if $\vec{d_e} \parallel \vec{s}$. In our molecule that means $\hat{d}_e \parallel \hat{\Sigma} \parallel -\hat{\Omega}$. We should expect there to be an energy shift $\langle H_{\text{edm}} \rangle = -\vec{d_e} \cdot \vec{\mathcal{E}}_{\text{eff}} = -d_e \mathcal{E}_{\text{eff}}(-\hat{\Omega}) \cdot (-\hat{n}) = -d_e \mathcal{E}_{\text{eff}} \Omega$ as given by [36].

The above argument is appealing and lands at the right answer, but only fortuitously. Drawing an effective electric field from one nucleus to another in Figure 4.8 is useful but misleading. The energy shift due to the eEDM only occurs when one of HfF^+'s valence electrons is very close to the hafnium nucleus, where the electric field points radially outward and causes the electron to move at relativistic speeds [64,65]. Instead, the proper treatment is to calculate the magnitude and sign of the effective electric field, as is done for HfF^+ in the following papers [36, 42, 43, 45].

While theorists are consistent in determining the magnitude of $\mathcal{E}_{\text{eff}}$ for HfF^+, approximately 23 GV/cm, they are maddeningly unclear when it comes to the sign. For example, one author has published that our $\mathcal{E}_{\text{eff}}$ is both positive and negative [43,45]. The confusion only gets worse when we look at review articles which compare the signs of $\mathcal{E}_{\text{eff}}$ between different molecules. We can compare the signs of $\mathcal{E}_{\text{eff}}$ for HfF^+, ThO and YbF, the molecules employed by the three currently leading eEDM experiments. While an overall sign change between review articles could be explained by different conventions, relative sign changes abound. In one article the signs of $\mathcal{E}_{\text{eff}}$ in all three molecules are the same [35], in another YbF has a different sign than the others [56], and in a third HfF^+ is the odd molecule out [17]. This spans the space of possibilities!

I have adopted the convention of Alexander Petrov who reports that $\mathcal{E}_{\text{eff}} = +23$ GV/cm in HfF^+ [36]. His article is relatively clear when it comes to the sign conventions and explicitly gives Equation 4.31 which we can consistently apply to see how the eEDM shows up in our experiment.

[15] Note that I have written the above equation with a minus sign that does not appear in [36] because we define the internuclear axis $\hat{n}$ to point in opposite directions and the sign of Ω depends on $\hat{n}$.

This has the perk of agreeing with John Bohn's sign convention, and he's on my committee [35,66].

We measure the eEDM induced shift in the presence of a magnetic field while minimizing Berry's phase, which can contribute systematic errors to our measurement [31]. The magnetic field interacts with our molecule's magnetic dipole moment $\vec{\mu}_F$, which we define such that $\mu_F = g_F \mu_B > 0$ when $\vec{\mu}_F$ is parallel to the molecule's total angular momentum F. Note that the Bohr magneton μ_B is defined to be a positive quantity, while the g-factor can be positive or negative. As the quantization axis in our experiment is defined by $\vec{\mathcal{E}}_{\rm rot}$, we have $\vec{\mu}_F = g_F \mu_B M_F \hat{\mathcal{E}}_{\rm rot}$.

We apply a magnetic field $\vec{\mathcal{B}}_{\rm rot}$ that is parallel or antiparallel ($\tilde{B} = \pm 1$) to $\vec{\mathcal{E}}_{\rm rot}$ which causes a Zeeman shift of:

$$H_{\rm Zeeman} = -\vec{\mu}_F \cdot \vec{\mathcal{B}}_{\rm rot} = -g_F \mu_B M_F \hat{\mathcal{E}}_{\rm rot} \cdot \vec{\mathcal{B}}_{\rm rot} = -g_F \mu_B M_F \mathcal{B}_{\rm rot} \tilde{B} \tag{4.32}$$

We can now create an effective Hamiltonian for the upper and lower doublets using Equations 4.31 and 4.32:

$$H_{\rm eff} = \frac{1}{2} \begin{pmatrix} -3(g_F + \delta g_F \tilde{D}) \mu_B \mathcal{B}_{\rm rot} \tilde{B} + 2 d_e \mathcal{E}_{\rm eff} \tilde{D} & h(\Delta + \Delta^D \tilde{D}) \\ h(\Delta + \Delta^D \tilde{D}) & 3(g_F + \delta g_F \tilde{D}) \mu_B \mathcal{B}_{\rm rot} \tilde{B} - 2 d_e \mathcal{E}_{\rm eff} \tilde{D} \end{pmatrix} \tag{4.33}$$

In addition to the expected Zeeman and eEDM shifts, we have also included a $\tilde{D}$ odd Zeeman shift to account for the fact that the upper and lower doublets have slightly different values of g_F. We define g_F to be the average g-factor of the two doublets, while $\delta g_F = \dfrac{g_F^{\rm upper} - g_F^{\rm lower}}{2}$. We define Δ and Δ^D similarly to account for a $\tilde{D}$-odd mixing between the states within the two doublets. This effective Hamiltonian acts on states $\begin{pmatrix} M_F = +3/2 \\ M_F = -3/2 \end{pmatrix}$.

If we diagonalize this Hamiltonian and solve for the energy difference, we find that:

$$E_{M_F=1.5} - E_{M_F=-1.5} = -3(g_F + \delta g_F \tilde{D})\mu_B \mathcal{B}_{\rm rot}\tilde{B} - \frac{[h(\Delta + \Delta^D \tilde{D})]^2 \tilde{B}}{\frac{3}{2}(g_F + \delta g_F \tilde{D})\mu_B \mathcal{B}_{\rm rot}} + 2d_e \mathcal{E}_{\rm eff}\tilde{D} \tag{4.34}$$

While finding this energy difference we have dropped a term that is proportional to $(d_e\mathcal{E}_{\rm eff})^2$ and used a binomial approximation where we assumed that:

$$\left|\frac{2d_e\mathcal{E}_{\rm eff}}{(g_F \pm \delta g_F)\mu_B\mathcal{B}_{\rm rot}}\right|, \left(\frac{h(\Delta \pm \Delta^D)}{\frac{3}{2}(g_F \pm \delta g_F)\mu_B\mathcal{B}_{\rm rot}}\right)^2 \ll 1 \tag{4.35}$$

Our new result tells us that the numerator of the first term is smaller than 40 μHz, while the denominator is $\sim$ 100 Hz [27]. The numerator of the second term is $\sim$ 1 Hz, making the entire term $\sim 10^{-4}$. The second term is larger than the first, but is still much smaller than 1 so the approximation is a good one.

As explained in Subsection 4.3.2, we always record a positive value of the energy. Since the leading term in Equation 4.34 is the largest, we take the absolute value of the energy difference by multiplying by the sign of the leading term $-\text{sgn}(g_F)\tilde{B}$:

$$\begin{aligned}|\Delta E| = {} & 3|g_F|\mu_B\mathcal{B}_{\rm rot} + 3\delta g_F \mu_B \mathcal{B}_{\rm rot}\text{sgn}(g_F)\tilde{D} \\ & + h^2\text{sgn}(g_F)\frac{\Delta^2 + \tilde{D}\Delta\Delta^D + (\Delta^D)^2}{\frac{3}{2}(g_F + \tilde{D}\delta g_F)\mu_B\mathcal{B}_{\rm rot}} - 2d_e\mathcal{E}_{\rm eff}\text{sgn}(g_F)\tilde{B}\tilde{D}\end{aligned} \tag{4.36}$$

We can immediately see that the only $\tilde{B}\tilde{D}$-odd shift is caused by the eEDM. From Equation 4.4, we find that

$$hf^{DB} = -2d_e\mathcal{E}_{\rm eff}\text{sgn}(g_F) \tag{4.37}$$

This is equivalent to Equation 4.1, which is what we wanted to show.

4.6.3 Appendix 3: Calculating Berry's Phase from 2H and Ellipticity

We generate a Berry's phase by having $\vec{\mathcal{E}}_{\text{rot}}$ trace out an elliptical Lissajous figure in xy-plane and apply also a 2nd harmonic of $\mathcal{E}_{\text{rot}}$ in the axial direction, as described in Equation 4.8. To calculate the expected Berry's phase shift, we need expressions for $\alpha(t)$ and $\dot{\phi}(t)$ to compute the integral in Equation 4.6:

$$\alpha(t) = \frac{\mathcal{E}_{\text{z}}(t)}{\sqrt{\mathcal{E}_{\text{x}}^2(t) + \mathcal{E}_{\text{y}}^2(t)}} = \frac{\mathcal{E}_{\text{2hz}}}{\mathcal{E}_{\text{rot}}} \cos\left(2\omega_{\text{rot}} t + \phi_{2f}\right)\left(1 - \frac{\mathcal{E}_{\epsilon}}{\mathcal{E}_{\text{rot}}} \cos\left(2\tilde{R}(\theta - \phi_0) - 2(\phi_R + \omega_{rot} t)\right)\right) \tag{4.38}$$

$$\dot{\phi}(t) = \frac{\partial}{\partial t} \arctan\left(\frac{\mathcal{E}_{\text{y}}(t)}{\mathcal{E}_{\text{x}}(t)}\right) = \tilde{R}\omega_{rot} - \frac{2\tilde{R}\omega_{rot}\mathcal{E}_{\epsilon}}{\mathcal{E}_{\text{rot}}} \cos\left(2\tilde{R}(\theta - \phi_0) - 2(\phi_R + \omega_{rot} t)\right) \tag{4.39}$$

In both equations we assume that $\mathcal{E}_{\text{rot}}$ is large compared to the other electric fields. We can then plug these expressions into Equation 4.6 and integrate:

$$f_{\text{Berry}} = \frac{3\mathcal{E}_{\text{2hz}}\mathcal{E}_{\epsilon} f_{\text{rot}} M_F \tilde{R}}{2\mathcal{E}_{\text{rot}}^2} \cos\left(2\tilde{R}(\theta - \phi_0) + \phi_{2f} - 2\phi_R\right) \tag{4.40}$$

We can now construct an effective Hamiltonian like in Appendix 4.6.2, except this time we will include the Berry's phase shift and ignore all $\tilde{D}$-odd effects:

$$H_{\text{eff}} = \begin{pmatrix} \text{Diag} & \frac{h\Delta}{2} \\ \frac{h\Delta}{2} & -\text{Diag} \end{pmatrix} \tag{4.41}$$

The diagonal term is expressed below so everything fits nicely between the margins of this page:

$$\text{Diag} = -\frac{3}{2} g_F \mu_B B_{rot} \tilde{B} + h\frac{9\mathcal{E}_{\text{2hz}}\mathcal{E}_{\epsilon} f_{\text{rot}}}{4\mathcal{E}_{\text{rot}}^2} \cos\left(2\tilde{R}(\theta - \phi_0) + \phi_{2f} - 2\phi_R\right)\tilde{R} \tag{4.42}$$

Again, the effective Hamiltonian acts on states $\begin{pmatrix} M_F = +3/2 \\ M_F = -3/2 \end{pmatrix}$. Solving for the difference in the diagonalized energies, we get:

$$|\Delta E| = 3|g_F|\mu_B\mathcal{B}_{\rm rot} - \frac{9h\mathcal{E}_{\rm 2hz}\mathcal{E}_\epsilon f_{\rm rot}}{2\mathcal{E}_{\rm rot}^2}\cos\left(2\tilde{R}(\theta-\phi_0)+\phi_{2f}-2\phi_R\right)\tilde{B}\tilde{R}\,\mathrm{sgn}(g_F) + \frac{h^2\Delta^2}{6|g_F|\mu_B\mathcal{B}_{\rm rot}} \quad (4.43)$$

Note that the the Berry's phase shift is $\tilde{B}$-odd, but has a complicated $\tilde{R}$ dependence. This means we should expect the Berry's phase to show up in both f^B and f^{BR}. We can use Equation 4.4 to find:

$$f^B = \frac{9\mathcal{E}_{\rm 2hz}\mathcal{E}_\epsilon f_{\rm rot}}{2\mathcal{E}_{\rm rot}^2}\mathrm{sgn}(g_F)\sin\left(2\theta-2\phi_0\right)\sin\left(\phi_{2f}-2\phi_R\right) \quad (4.44)$$

$$f^{BR} = -\frac{9\mathcal{E}_{\rm 2hz}\mathcal{E}_\epsilon f_{\rm rot}}{2\mathcal{E}_{\rm rot}^2}\mathrm{sgn}(g_F)\cos\left(2\theta-2\phi_0\right)\cos\left(\phi_{2f}-2\phi_R\right) \quad (4.45)$$

4.6.4 Appendix 4: $\mathcal{E}_{\rm rot}$ Phases in HfF+ Experiment

It is easier to compare the above equations to our experiment if we replace ϕ_0 and ϕ_R with ϕ_{up} and ϕ_{down}:

$$\phi_{up} = \phi_0 + \phi_R \quad (4.46)$$

$$\phi_{down} = \phi_0 - \phi_R \quad (4.47)$$

Substituting these into Equations 4.44 and 4.45 gives us:

$$f^B = \frac{9\mathcal{E}_{2\mathrm{hz}}\mathcal{E}_\epsilon f_{\mathrm{rot}}}{2\mathcal{E}_{\mathrm{rot}}^2}\mathrm{sgn}(g_F)\sin\left(2\theta - \phi_{up} - \phi_{down}\right)\sin\left(\phi_{2f} - \phi_{up} + \phi_{down}\right) \tag{4.48}$$

$$f^{BR} = -\frac{9\mathcal{E}_{2\mathrm{hz}}\mathcal{E}_\epsilon f_{\mathrm{rot}}}{2\mathcal{E}_{\mathrm{rot}}^2}\mathrm{sgn}(g_F)\cos\left(2\theta - \phi_{up} - \phi_{down}\right)\cos\left(\phi_{2f} - \phi_{up} + \phi_{down}\right) \tag{4.49}$$

In order to use these equations to find $\mathrm{sgn}(g_F)$, we need to know all four phases in the above equations. The x and y axes are defined as shown in Figure 4.9, with the z-axis pointing out of the page. θ, the angle which defines the strong axis of the ellipse, is equal to zero when pointing along $+\hat{x}$ and increases as it rotates toward the $+\hat{y}$ axis. We define ϕ_{up} and ϕ_{down}, the direction of $\mathcal{E}_{\mathrm{rot}}$ at t=0 for each rotation direction, the same way. ϕ_{2f} is the phase of the second harmonic at t=0.

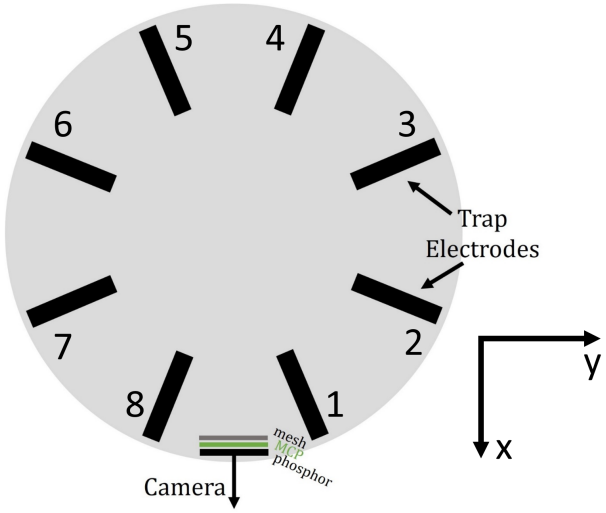

Figure 4.9: The eight radial electrodes are numbered 1 through 8. There are two "endcap" electrodes in and out of the page to apply fields along the z-axis.

The equations for f^B and f^{BR} do not depend on the choice of t=0, so we chose 1 ms after the first $\frac{\pi}{2}$ pulse in our Ramsey sequence as it is a convenient time to trigger our oscilloscopes that measure the voltages on our electrodes. We can measure ϕ_{up} and ϕ_{down} by simply measuring the voltages on all eight radial electrodes and finding the direction $\mathcal{E}_{\mathrm{rot}}$ points at this time. We find that $\phi_{up} = \frac{11\pi}{6}$ and $\phi_{down} = \frac{10\pi}{6}$ to within 5 degrees, which means $\phi_0 = \frac{7\pi}{4}$ and $\phi_R = \frac{\pi}{12}$.

When we apply the second harmonic field along the z-direction, we can control its phase in our software. We find that when we program the computer to generate the field with "zero" phase, 1 ms after the first $\frac{\pi}{2}$ pulse the electric field is at its maximum pointing upwards. We also verified that inputting a 30 degree phase shift into our software is equivalent to a +30 degree phase shift. This means that the phase in our control software is equivalent to the phase in Equation 4.8.

Finally, we can verify that we know θ by observing the voltages that generate $\mathcal{E}_{\text{rot}}$ on our eight radial electrodes. For example, if we apply an ellpiticity with $\theta = 0$ we expect that the voltages on electrodes 1, 4, 5 and 8 in Figure 4.9 will now have slightly larger amplitudes, while the amplitude of the voltages on the remaining electrodes will decrease. This procedure went as expected.

We can therefore use the fixed values of ϕ_{up} and ϕ_{down} and choose values of θ and ϕ_{2f} to generate a Berry's phase. By choosing a value of θ and scanning ϕ_{2f}, we should expect to see sine waves in f^B and f^{BR} with phases that are completely known except for the sign of the g-factor.

4.6.5 Appendix 5: Defining the Frequency Channels

We need to know how our code constructs f^B, f^{BR} and f^{DB} in order to accurately interpret their signs. This involves understanding the Matlab code generate_lcoms_common.m which creates the frequency channels from the raw data.

We take data through our homemade Labview code in 2^4 experimental configurations, by taking every combination of magnetic field (B), rotation direction (R), imaging chop (I) and depletion phase (P). In each of these configurations, we take data for both the upper and lower doublet (D), giving us data for $2^5 = 32$ total Ramsey fringes. As in Subsection 4.3.2, we are not interested in the I or P chops in order to find the sign of the g-factor or eEDM. We can narrow our focus to the 8 data sets made by switching B, R and D.

Labview saves the eight data sets with labels $f^{\tilde{D}=\pm1,\tilde{B}=\pm1,\tilde{R}=\pm1}$, but it mislabels the the rotation switch. That is, data taken with $\vec{\mathcal{E}}_{\text{rot}}$ rotating up are labeled $\tilde{R} = -1$ and data taken with

$\vec{\mathcal{E}}_{\rm rot}$ rotating down are labeled $\tilde{R} = +1$. This is a bit awkward, but as I will describe this error is later corrected in the data analysis.

Matlab imports the eight data sets, analyzes each one and fits a positive frequency for each switch state, as discussed in Subsection 4.3.2. Matlab then creates a doublet even and doublet odd frequency four the four experimental configurations $\tilde{B}, \tilde{R} = \pm 1$:

$$f_{ML}^{\tilde{B}=\pm1,\tilde{R}=\pm1} = \frac{f^{\tilde{D}=+1,\tilde{B}=\pm1,\tilde{R}=\pm1} + f^{\tilde{D}=-1,\tilde{B}=\pm1,\tilde{R}=\pm1}}{2} \tag{4.50}$$

$$f_{ML}^{D,\tilde{B}=\pm1,\tilde{R}=\pm1} = \frac{f^{\tilde{D}=+1,\tilde{B}=\pm1,\tilde{R}=\pm1} - f^{\tilde{D}=-1,\tilde{B}=\pm1,\tilde{R}=\pm1}}{2} \tag{4.51}$$

This is done when the data is processed in a subroutine called fit_fringe_common_v6.m, see where it defines the variables b_mean and b_diff. At this point, Matlab still has the sign of $\tilde{R}$ backwards as it has inherited Labview's error.

Matlab now constructs the four doublet even linear combinations, f f^B, f^R and f^{BR}, out of its four values $f_{ML}^{\tilde{B}=\pm1,\tilde{R}=\pm1}$. It does the same for the four doublet odd linear combinations out of the four values $f_{ML}^{D,\tilde{B}=\pm1,\tilde{R}=\pm1}$, all of which is done in generate_lcoms_common.m. If inspected closely, the matrices of ones and minus ones in the code that generate the eight frequency channels seem to have the wrong signs. However, these "errors" must have been intentional as they fix the rotation sign error that is inherited from Labview.[16]

The result is that the frequency channels are defined with the proper signs as given in Equation 4.4. f is the average of the absolute fitted frequencies, which are all defined to be positive. f^B is the sum of the fitted frequencies with $\vec{\mathcal{E}}_{\rm rot} \parallel \vec{\mathcal{B}}_{\rm rot}$ minus the sum of the fitted frequencies

[16]This is done without any comment in the code or, as far as I can tell, the lab notebook. Why not just fix the mistake in Labview? Or at least make the correction when the data is first imported?

with $\vec{\mathcal{E}}_{\rm rot} \parallel -\vec{\mathcal{B}}_{\rm rot}$. f^R is the sum of the fitted frequencies with the rotation direction of $\vec{\mathcal{E}}_{\rm rot}$ up by the right hand rule minus the sum of the fitted frequencies with $\vec{\mathcal{E}}_{\rm rot}$ rotating down. f^D is the sum of the fitted frequencies of the upper doublet minus the sum of the fitted frequencies of the lower doublet. For a frequency channel with multiple superscript letters like f^{DB}, we add up the frequency channels with positive $\tilde{B}\tilde{D}$ and subtract the frequency channels with negative $\tilde{B}\tilde{D}$. In all cases, we divide by the number of frequency channels in the linear combination.

4.6.6 Appendix 6: Table of Signs

Here I provide a list of definitions of signed quantities used in determining the sign of the g-factor, gathered here in one table. For the entries f^B, f^{BR} and f^{DB}, the note points to the relevant Matlab code which creates the linear combination of frequencies.

Table 4.1: List of quantities whose signs matter for determining the sign of the g-factor

Quantity	Description	Notes
$\tilde{B}$	+1 for $\vec{\mathcal{B}}_{\rm rot} \parallel \vec{\mathcal{E}}_{\rm rot}$, -1 for $\vec{\mathcal{B}}_{\rm rot} \parallel -\vec{\mathcal{E}}_{\rm rot}$	Magnetic Field Chop
$\tilde{R}$	+1 for Up, -1 for Down	Rotation Chop
$\tilde{D}$	+1 for Upper, -1 for Lower	Doublet Chop
Labview B Sign	+1	Labview knows B Sign
Labview R Sign	-1	Labview is wrong about R sign
Labview D Sign	+1	Labview knows D Sign
sgn(f^B)	$f^{\tilde{B}=+1} - f^{\tilde{B}=-1}$	See generate_lcoms_common.m
sgn(f^{BR})	$f^{\tilde{B}=+1,\tilde{R}=+1} - f^{\tilde{B}=-1,\tilde{R}=+1} - f^{\tilde{B}=+1,\tilde{R}=-1} + f^{\tilde{B}=-1,\tilde{R}=-1}$	See generate_lcoms_common.m
sgn(f^{DB})	$f^{\tilde{D}=+1,\tilde{B}=+1} - f^{\tilde{D}=-1,\tilde{B}=+1} - f^{\tilde{D}=+1,\tilde{B}=-1} + f^{\tilde{D}=-1,\tilde{B}=-1}$	See fit_fringe_common_v6.m
$\vec{d}$	points from -q to +q	Implies $U_{dip} = -\vec{d} \cdot \vec{E}$
$\mathcal{E}_{\rm eff}$	+ 23 GV/cm	See Appendix 4.6.2
$\hat{n}$	points from F to Hf nuclei	The internuclear axis
$\vec{\mu}$	points normal to current loop	Implies $U_{dip} = -\vec{\mu} \cdot \vec{B}$
$\vec{\mu}_F$	$\mu_F = g_F \mu_B > 0$ when $\vec{\mu}_F \| \vec{F}$	This defines the sign of the g_F
f_{Berry}	$= -m_F f_{\rm rot} \alpha \tilde{R}$	Sign of Berry's phase shift
ϕ_{up}	330 degrees	Initial $\vec{\mathcal{E}}_{\rm rot}$ phase when $\tilde{R} = +1$
ϕ_{down}	300 degrees	Initial $\vec{\mathcal{E}}_{\rm rot}$ phase when $\tilde{R} = -1$

4.6.7 Appendix 7: The sign of δg_F in HfF$^+$

From Equation 4.36 we can read that $f = 3|g_F|\mu_B\mathcal{B}_{\rm rot}$ and $f^D = 3\delta g_F \mu_B \mathcal{B}_{\rm rot}{\rm sgn}(g_F)$. Therefore we have:

$$\frac{f^D}{f} = \frac{3\delta g_F \mu_B \mathcal{B}_{\rm rot}{\rm sgn}(g_F)}{3|g_F|\mu_B\mathcal{B}_{\rm rot}} = \frac{\delta g_F}{|g_F|{\rm sgn}(g_F)} = \frac{\delta g_F}{g_F} \tag{4.52}$$

We can compare this expression with the Figure 6a in the systematics paper [31], repeated here as Figure 4.10.

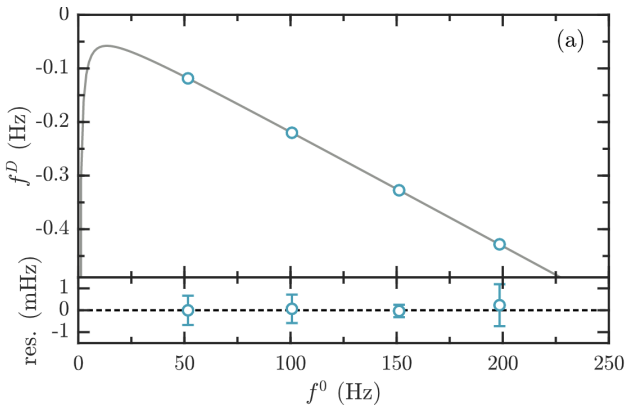

Figure 4.10: Repetition from systematics paper caption: f^D vs f^0 for various values of the applied quadrupole magnetic field, $\vec{\mathcal{B}}^0$. Data taken at $\mathcal{E}_{\rm rot} \sim 58$ V/cm. Fit is to $f^D = \frac{\delta g_F}{g_F} f^0 + \frac{\Delta^0\Delta^D}{f^0}$, giving $\frac{\delta g_F}{g_F} = -0.002149(3)$, $\Delta^0\Delta^D = -0.39(4)$Hz^2.

We've concluded in Section 4.4 that g_F is negative, and as we can see from Figure 4.10 $\frac{\delta g_F}{g_F}$ is negative as well. Therefore δg_F is a positive quantity. We can compare this experimentally determined sign to theory by evaluating the leading order term of δg_F from our Hamiltonian as follows.

δg_F primarily comes from a difference in the sign of the mixing terms between the upper and lower doublets to $J = 2$. We can start by finding $g^{(2)}_{\rm upper}$ and $g^{(2)}_{\rm lower}$, where the superscript (2) denotes that these are calculated from 2nd order perturbation theory:

$$
\begin{aligned}
g^{(2)}_{\text{upper}} &= \frac{\Delta E^{(2)}_{\text{upper},M_F=3/2} - \Delta E^{(2)}_{\text{upper},M_F=-3/2}}{-3\mu_B \mathcal{B}_{\text{rot}}} \\
&= \Bigg(\sum_{n\in J=2} \frac{|\left\langle \text{upper}, M_F = 1.5\right| H_{\text{stark}} + H_{\text{zeeman}} \left|n\right\rangle|^2}{-4B} \\
&\quad - \sum_{n\in J=2} \frac{|\left\langle \text{upper}, M_F = -1.5\right| H_{\text{stark}} + H_{\text{zeeman}} \left|n\right\rangle|^2}{-4B} \Bigg) / (-3\mu_B \mathcal{B}_{\text{rot}})
\end{aligned} \tag{4.53}
$$

Note that we define the g-factor of the upper doublet to be the difference in energy of the two stretched states divided by $-3\mu_B\mathcal{B}_{\text{rot}}$, which is the term for a Zeeman shift sans g_F. There's a similar expression for $g^{(2)}_{\text{lower}}$. Also note that we're approximating the energy difference as $-4B$ because the only relevant states $|n\rangle$ are in the $J = 2$ rotational level and $E(J = 1) - E(J = 2) = 2B - 6B = -4B$.

Now we need to evaluate the matrix elements, where $H_{\text{stark}} + H_{\text{zeeman}} = -\vec{D}\cdot\vec{E} - \vec{\mu}\cdot\vec{B}$. Here's an equation from chapter 2 of Will Cairncross's thesis, which I've checked with Brown and Carrington [1, 67]:

$$
\begin{aligned}
&\langle J, F, M_F, \Omega | H_{\text{stark}} + H_{\text{zeeman}} | J', F', M'_F, \Omega' \rangle \\
&\quad = \big(- D_{\|}\mathcal{E}_{\text{rot}} - G_{\|}\mathcal{B}_{\text{rot}}\mu_B\Omega \big)(-1)^{F-M_F} \begin{pmatrix} F & 1 & F' \\ -M_F & 0 & M'_F \end{pmatrix} \\
&\qquad \times (-1)^{F'+J+1.5}\sqrt{(2F+1)(2F'+1)} \begin{Bmatrix} J' & F' & 0.5 \\ F & J & 1 \end{Bmatrix} \\
&\qquad \times \sum_{q=-1}^{1} \left((-1)^{J-\Omega} \begin{pmatrix} J & 1 & J' \\ -\Omega & q & \Omega' \end{pmatrix} \sqrt{(2J+1)(2J'+1)} \right)
\end{aligned} \tag{4.54}
$$

Note that $G_{\|} = 3g_F - g_N\dfrac{m_e}{m_p}$. This expression only applies for the simplified case where the electric and magnetic fields are along the quantization axis and only applies within the $^3\Delta_1$, $v = 0$ manifold. For the full expression, see Equation 2.15 in Will Cairncross's thesis [1].

The above equation does not mix terms with different values of M_F or Ω, which means there are only a few terms that appear in the sums in Equation 4.53. Writing those terms out we get:

$$\begin{aligned} g^{(2)}_{\text{upper}} = & \frac{|\langle 1, 1.5, 1.5, -1| H_{\text{stark}} + H_{\text{zeeman}} |2, 1.5, 1.5, -1\rangle|^2}{-4B(-3\mu_B \mathcal{B}_{\text{rot}})} \\ & + \frac{|\langle 1, 1.5, 1.5, -1| H_{\text{stark}} + H_{\text{zeeman}} |2, 2.5, 1.5, -1\rangle|^2}{-4B(-3\mu_B \mathcal{B}_{\text{rot}})} \\ & - \frac{|\langle 1, 1.5, -1.5, 1| H_{\text{stark}} + H_{\text{zeeman}} |2, 1.5, -1.5, 1\rangle|^2}{-4B(-3\mu_B \mathcal{B}_{\text{rot}})} \\ & - \frac{|\langle 1, 1.5, -1.5, 1| H_{\text{stark}} + H_{\text{zeeman}} |2, 2.5, -1.5, = 1\rangle|^2}{-4B(-3\mu_B \mathcal{B}_{\text{rot}})} \\ & = -\frac{D_\parallel \mathcal{E}_{\text{rot}} G_\parallel}{20B} \end{aligned} \tag{4.55}$$

A similar calculation for $g^{(2)}_{\text{lower}}$ gives:

$$g^{(2)}_{\text{lower}} = \frac{D_\parallel \mathcal{E}_{\text{rot}} G_\parallel}{20B} \tag{4.56}$$

We can put them together to find $\delta g^{(2)}_F$:

$$\delta g^{(2)}_F = \frac{g^{(2)}_{\text{upper}} - g^{(2)}_{\text{lower}}}{2} = -\frac{D_\parallel \mathcal{E}_{\text{rot}} G_\parallel}{20B} \tag{4.57}$$

At the start of this appendix, we found experimentally that δg_F is positive. The relationship $G_\parallel = 3g_F - g_N \dfrac{m_e}{m_p}$ tells us that $G_\parallel$ is positive as well. We can take the sign of the terms in Equation 4.57 and we find that:

$$\text{sgn}(\delta g^{(2)}_F) = \text{sgn}\left(-\frac{D_\parallel \mathcal{E}_{\text{rot}} G_\parallel}{20B} \right) = -\frac{\text{sgn}(D_\parallel)\text{sgn}(\mathcal{E}_{\text{rot}})\text{sgn}(G_\parallel)}{\text{sgn}(B)} = -\frac{(+1)(+1)(-1)}{(+1)} = +1 \tag{4.58}$$

So we expect the sign of $\delta g_F^{(2)}$ to be positive, which makes sense because we found δg_F to be positive experimentally.

Since we've made it this far, we may as well calculate $\frac{\delta g_F^{(2)}}{g_F}$ from $G_\parallel = 3g_F - g_N\frac{m_e}{m_p}$:

$$\frac{\delta g_F^{(2)}}{g_F} = -\frac{D_\parallel \mathcal{E}_{\rm rot} G_\parallel}{20B}\frac{3}{G_\parallel + g_N\frac{m_e}{m_p}} = -\frac{3D_\parallel \mathcal{E}_{\rm rot}}{20B\left(1+\frac{g_N m_e}{G_\parallel m_p}\right)} \approx -\frac{D_\parallel \mathcal{E}_{\rm rot}}{5.102B} = -4.298\times 10^{-5}\frac{\mathcal{E}_{\rm rot}}{\rm V/cm} \tag{4.59}$$

Note that in the last step, I've plugged in experimental values as reported in [31]. Using the value in generation 2 of $\mathcal{E}_{\rm rot} = 58$ V/cm, we find that:

$$\frac{\delta g_F^{(2)}}{g_F} = -0.00249 \tag{4.60}$$

This has the same sign as and is 16% larger than the measured value $-0.002149(3)$ from Figure 4.10. The discrepancy in magnitude arises at least in part from the fact that we have ignored smaller perturbations. A more complete calculation was done by Alexander Petrov [57] who included perturbations due to the rotation Hamiltonian and higher order effects that couple to the $^3\Delta_2$, $^3\Pi_{0^+}$ and $^3\Pi_{0^-}$ electronic states. Petrov claims that his numerical results are within 5% of the analytical formulas we presented in our systematics paper [31], and he found a value of:

$$\frac{\delta g_F}{g_F} = -\frac{1}{473} \approx -0.002114 \tag{4.61}$$

Petrov's result is much closer to the measured value $-0.002149(3)$ than the second order perturbation result I calculated in this appendix.

Chapter 5

Magnetic Shielding

"Science is magic that works."

- Kurt Vonnegut, Cat's Cradle.

One of the main challenges of measuring the eEDM is measuring the energy shift $d_e\mathcal{E}_{\text{eff}}$ in the face of the much larger Zeeman effect. As explained in Section 2.1, our experiment 1) uses a molecule with a small value of g_F, 2) makes a differential measurement between the upper and lower doublets, pairs of states with similar magnetic sensitivities but opposite eEDM shifts, and 3) uses a rotating quantization axis to average out shifts caused by uniform magnetic fields. There is a fourth, and perhaps obvious, strategy to minimize the systematic errors caused by the Zeeman effect. That is to surround the apparatus with magnetic shielding to passively reduce the magnitude of the field and therefore all associated systematic shifts. Fortunately, the first three methods to minimize magnetic systematics were sufficient in our first and second generation measurements of the eEDM at JILA. As discussed in Chapter 3, the total magnetic systematic error in generation two was just a few μHz, almost an order of magnitude smaller than our statistical error bar.

The absence of magnetic shielding in our previous measurements makes us unique among modern EDM experiments. Two of the leading electron EDM measurements, the ACME collaboration and the Imperial College eEDM experiment, have both required multiple layers of magnetic shielding from their outset [47, 68]. Regrettably, our experiment will need magnetic shielding in its

next iteration. We want our third generation measurement to have an order of magnitude smaller statistical and systematic error bars, the latter of which we can no longer achieve without shielding the magnetic field in our lab.

5.1 Generation Three JILA eEDM Experiment

5.1.1 Desired Statistical Sensitivity

The goal of the third generation measurement at JILA is to improve our sensitivity to the eEDM by another order of magnitude. As seen in Table 3.8, our leading source of error in generation two was statistical. To reduce the statistical error we can refer to Equation 2.3, which indicates we will need to increase a combination of the effective electric field $\mathcal{E}_{\text{eff}}$, the coherence time τ and the number of molecules we measure N.

There is not a clear path forward to substantially improving any of these quantities if we stick with HfF^+. $\mathcal{E}_{\text{eff}}$ is a fixed quantity and τ is limited to about 3 seconds due to the finite lifetime of the $^3\Delta_1$ state. It should be possible to increase N by improving the state preparation efficiency of $^3\Delta_1$ as described in Subsection 2.2.1.5; we only move $\gtrsim 20\%$ of the HfF^+ molecules we trap from the electronic ground state to $^3\Delta_1$. If we improve the efficiency to $\sim 90\%$ we would gain roughly a factor of four in ion number, doubling our statistical sensitivity. It is not exactly clear how we would improve this efficiency but it should be possible. Alternatively, we could just take more hours of data. The ~ 650 hours of data that Tanya Roussy, Luke Caldwell and I took over ~ 2.5 months could be extended indefinitely, or at least until the equipment/grad students/postdocs break.

Our plan is to work smarter instead of longer hours. The third generation experiment will be made with ThF^+ molecular ions instead of HfF^+. This switch has involved a significant overhead in order to learn how to produce, trap and manipulate the quantum states of this new molecule [3, 4]. However, we are optimistic that the payoff will be worth it.

The $^3\Delta_1$ state of ThF^+ has $\mathcal{E}_{\text{eff}} = 35$ GV/cm, about 1.5 times larger than HfF^+ [69,70]. That

means in order to measure the eEDM 10 times more precisely, we only need a ~ 6.7 times smaller error bar in our frequency measurement. The key advantage of ThF^+ is that $^3\Delta_1$ is its electronic ground state, so τ will not be limited by a finite lifetime. We hope to achieve $\tau \sim 20$ seconds for our generation three measurement.

In the generation two apparatus a longer coherence time τ means that we have to spend more time waiting for the experiment to run and therefore measure fewer ions N. If we assume the best case that the "dead time" between the end of one measurement and the beginning of the coherence time of the subsequent clouds of ions is minimal, increasing our coherence time only improves our statistical sensitivity by $\sqrt{\tau}$. This means an increase of coherence time from 3 to 20 seconds would only net us a factor of $\sqrt{20/3} = 2.6$ in sensitivity. In order to improve our statistical sensitivity even further, we have completely redesigned our ion trap. Instead of trapping a single cloud of ions, we will trap many ion clouds and make semi-continuous measurements of the eEDM.

See Figure 5.1 which shows the design of the "Bucket Brigade" ion trap. The eight radial electrodes in the generation two ion trap shown in Figure 3.8 are replaced with eight long rod electrodes that run the length of the new trap, from the bottom left to bottom right of the Figure 5.1. The two endcap electrodes from generation two are replaced with a series of ring electrodes whose voltages can be set to create many ion traps along the length of the rods.

We create a neutral beam of ThF molecules which are ionized and trapped on one end of the Bucket Brigade. We do all of the state preparation and begin the Ramsey evolution at this initial location. We will then slowly move the center of the ion trap by varying the voltages on the ring electrodes to the other end of the Bucket Brigade, where after the coherence time τ the Ramsey measurement is completed. However, once the ions have moved far enough,[1] another "bucket" of ions is prepared in the state preparation region. In this way many buckets of ions are prepared

[1] How far is far enough between buckets of ions? This is currently an open question, look to a future JILA EDM thesis for the answer.

and shuttled from one end of the ion trap to the other in unison, and we can make measurements semi-continuously. This will substantially increase the number of ions N we measure in a given amount of time.

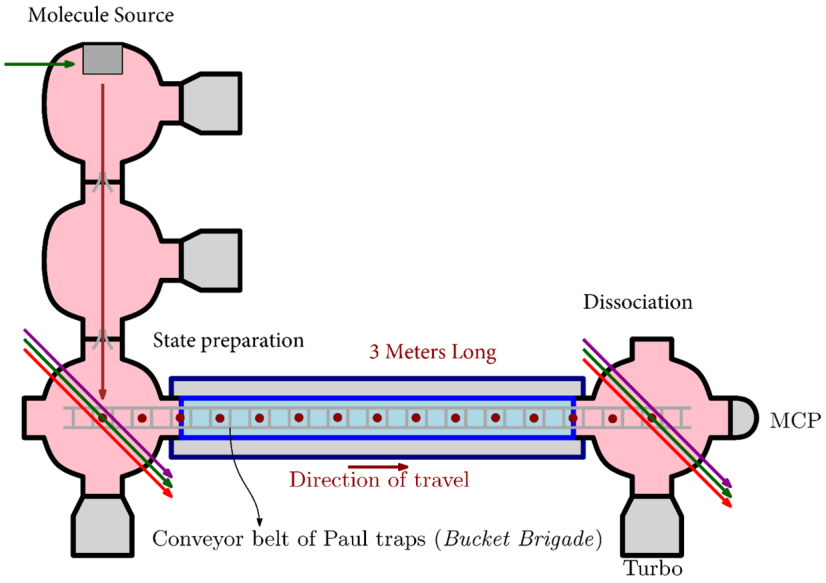

Figure 5.1: A conceptual drawing of the Bucket Brigade for our generation three eEDM measurement. We plan to trap many buckets of ions simultaneously, all moving from the state preparation region on the left to the dissociation region on the right. While the ions move in parallel they are undergoing their ~ 20 second coherence time. This image was made by Kia Boon Ng [4].

For significantly more detailed explanations of our next EDM experiment, please see the theses recently written by Kia Boon Ng [4] and Noah Scholssberger [3].

5.1.2 One of Maxwell's Equations

Before jumping into more details about generation three, it will help to discuss one of Maxwell's equations:

$$\vec{\nabla} \times \vec{\mathcal{B}} = \mu_0 \vec{j} + \frac{1}{c^2} \frac{\partial \vec{\mathcal{E}}}{\partial t} \tag{5.1}$$

In our experiment the largest electric field is $\vec{\mathcal{E}}_{\text{rot}} = \mathcal{E}_{\text{rot}}\Big(\cos(\omega_{\text{rot}}t)\hat{x} + \tilde{R}\sin(\omega_{\text{rot}})\hat{y}\Big)$. According to the above equation this will lead to time-varying magnetic field gradients:

$$\begin{pmatrix} \frac{\partial \mathcal{B}_y}{\partial z} - \frac{\partial \mathcal{B}_z}{\partial y} \\ \frac{\partial \mathcal{B}_z}{\partial x} - \frac{\partial \mathcal{B}_x}{\partial z} \\ \frac{\partial \mathcal{B}_x}{\partial y} - \frac{\partial \mathcal{B}_y}{\partial x} \end{pmatrix} = \frac{\omega_{\text{rot}}\mathcal{E}_{\text{rot}}}{c^2} \begin{pmatrix} -\sin(\omega_{\text{rot}}t) \\ \tilde{R}\cos(\omega_{\text{rot}}t) \\ 0 \end{pmatrix} \tag{5.2}$$

Because our experiment relies on $\vec{\mathcal{E}}_{\text{rot}}$ we cannot remove these magnetic field gradients from our experiment. Note that the above equation does not uniquely determine any of the six gradients, they must be determined by the boundary conditions of our experiment.

We saw the effect of these gradients in generation two; they were discussed in Subsection 3.4.2 under the name $\vec{\mathcal{B}}_{\text{cc}}$. In that section we said that:

$$\vec{\mathcal{B}}_{\text{cc}} = \mathcal{B}_{\text{cc}} z \begin{pmatrix} \tilde{R}\cos\left(\omega_{\text{rot}}t\right) \\ \sin\left(\omega_{\text{rot}}t\right) \\ 0 \end{pmatrix} \tag{5.3}$$

This is equivalent to Equation 5.2 with boundary conditions that set $\frac{\partial \mathcal{B}_z}{\partial y} = \frac{\partial \mathcal{B}_z}{\partial x} = \frac{\partial \mathcal{B}_x}{\partial y} = \frac{\partial \mathcal{B}_y}{\partial x} = 0$. We can see that by applying these boundary conditions to Equation 5.2 and integrate along z to find that:

$$\begin{pmatrix} \mathcal{B}_y \\ \mathcal{B}_x \\ 0 \end{pmatrix} = -\frac{\omega_{\text{rot}}\mathcal{E}_{\text{rot}} z}{c^2} \begin{pmatrix} \sin(\omega_{\text{rot}}t) \\ \tilde{R}\cos(\omega_{\text{rot}}t) \\ 0 \end{pmatrix} \tag{5.4}$$

Noting that the first and second entries of the vectors are flipped from their usual order, we can compare to Equation 5.3 to find $\mathcal{B}_{\text{cc}} = -\frac{\omega_{\text{rot}}\mathcal{E}_{\text{rot}}}{c^2}$. When we plug in the generation two values we

find that $|\mathcal{B}_{\rm cc}| = 1.6$ mG/m, which is about 50% larger than the value 1.1 mG/m we measured in Section 3.4.2. This indicates that there were magnetic field gradients $\frac{\partial \mathcal{B}_z}{\partial y}$ and $\frac{\partial \mathcal{B}_z}{\partial x}$ possibly as large as 0.5 mG/m that we did not consider in generation two. The systematics shifts created by these magnetic field gradients will be discussed in Subsection 5.2.2.

Because we plan to keep $\mathcal{E}_{\rm rot}$ and $\omega_{\rm rot}$ roughly the same magnitude, a choice we discuss in Subsection 5.2.1, we should expect similarly sized magnetic field gradients in generation three. These gradients will be more problematic in generation three because instead of sitting at one point the molecules will move up to three meters along the z-axis! These gradients will be referenced multiple times during the rest of this chapter.

5.1.3 Methods of Generating f^0

The combined improvements of $\mathcal{E}_{\rm eff}$, τ and N should give us a factor of ~ 10 improvement in the statistical sensitivity of our next eEDM measurement. The larger value of $\mathcal{E}_{\rm eff}$ means we can achieve this factor of 10 by reducing our statistical uncertainty by a factor of $10/1.5 = 6.7$, corresponding to an uncertainty of about 3.5 μHz. This new sensitivity is crucial, but only matters if our systematic error bar shrinks as well. As seen in Table 3.8, our largest individual systematic error was 3.5 μHz. To keep our total systematic error ~ 3 times smaller than our statistical error, we want our each of our individual systematic errors to be no larger than 500 nHz at most.[2]

As we saw in Chapter 3, the magnitude of a given systematic effect depends on our method of generating $f^0 \approx 100$ Hz.[3] In generation two f^0 was produced by the $\tilde{B}$-odd Zeeman shift caused by our molecules rotating in the magnetic field gradient $\vec{\mathcal{B}}_{2,0}$. This effect has $\frac{\langle \vec{\mathcal{E}} \cdot \vec{\mathcal{B}} \rangle / |\mathcal{E}|}{\langle \hat{\mathcal{E}} \cdot \vec{\mathcal{B}} \rangle} = 1$, so it also

[2] Assuming that all systematic errors are uncorrelated, there need to be 49 individual 500 nHz systematics to result in a total systematic error bar of 3.5 μHz, the size of our desired statistical error bar. We do not want the total systematic error bar to be this large, but a few ~ 500 nHz systematic errors are fine.

[3] f^0 is the name for the channel that measures the ~ 100 Hz Zeeman shift. In other JILA EDM documents it has been called f and f_0.

causes a $\tilde{D}$-odd shift that is $\frac{\delta g_F}{g_F}$ times smaller. We saw in Subsection 3.2.2 that all other frequency shifts with the same ratio of f^D/f^0 did not cause an appreciable systematic shift because of our shimming/correction procedure. This means that the magnitude of systematic effects in generation 3 will depend on the method we choose for generating f^0. For example, if we generate f^0 with Berry's phase then all Berry's phase shifts and magnetic effects with $\frac{\langle \vec{\mathcal{E}} \cdot \vec{\mathcal{B}} \rangle / |\mathcal{E}|}{\langle \hat{\mathcal{E}} \cdot \vec{\mathcal{B}} \rangle} = 0$ will not cause a systematic error.[4]

As a group we have put a substantial amount of thought into how we want to generate f^0 in generation 3, evidenced by chapter 8 of Kia Boon Ng's thesis which is titled "Generating f^0 in the Bucket Brigade" [4]. He details five plans for generating f^0 which are listed in Table 5.1, focusing on how to implement each plan while keeping the required fields homogeneous enough to maintain $\tau \gtrsim 20$ seconds.

Table 5.1: Kia Boon's Plans to Generate f^0

Plan	Description	$\frac{f^D}{f^0}$ value
A	Zeeman shift from $\mathcal{B}_{2,0}$ plus $\mathcal{E}_{\text{rot}}$	$\frac{\delta g_F}{g_F}$
B	Berry's Phase from $\mathcal{E}_\epsilon$ plus $\mathcal{E}_{\text{2hz}}$	0
C	Zeeman shift from $\mathcal{B}_{1,\pm1}$ plus $\mathcal{E}_{\text{2hxy}}$	0
D	Zeeman shift from $\mathcal{B}_{2,\pm2}$ plus $\mathcal{E}_\epsilon$	$\frac{4}{3}\frac{\delta g_F}{g_F}$
E	Zeeman shift from $\mathcal{B}_{\text{rot}}$ plus $\mathcal{E}_{\text{rot}}$	$\frac{\delta g_F}{g_F}$

Plans A through D make use of frequency shifts already discussed in Chapter 3. Plan E relies on a magnetic field $\vec{\mathcal{B}}_{\text{rot}}$ that rotates in the xy-plane at a frequency f_{rot} so that it is always parallel or anti-parallel to $\vec{\mathcal{E}}_{\text{rot}}$ depending on $\tilde{B}$. This is a similar field to $\vec{\mathcal{B}}_{\text{cc}}$ which also rotates in

[4] This is true for the magnetic effects up to the small corrections discussed in Subsection 3.2.1 and [57]. In practice, these shifts would cause negligible systematics unless things go horribly wrong.

the xy-plane at $f_{\rm rot}$. The differences are 1) that $\vec{\mathcal{B}}_{\rm cc}$ is parallel or anti-parallel to $\vec{\mathcal{E}}_{\rm rot}$ depending on $\tilde{R}$ instead of $\tilde{B}$, 2) $\vec{\mathcal{B}}_{\rm cc}$ is a magnetic field gradient along the z-axis while $\vec{\mathcal{B}}_{\rm rot}$ is spatially uniform over the Bucket Brigade and 3) $\vec{\mathcal{B}}_{\rm cc}$ is applied unintentionally due to the charging currents while $\vec{\mathcal{B}}_{\rm rot}$ would be applied by intentionally sending additional current through the radial electrodes. In order to apply a ~ 100 Hz frequency shift with $\vec{\mathcal{B}}_{\rm rot}$ we do not want $\vec{\mathcal{B}}_{\rm cc}$ interfering and causing the frequency shift to be $\tilde{R}$-odd or having a spatial gradient. The implementation of $\vec{\mathcal{B}}_{\rm rot}$ with minimal $\vec{\mathcal{B}}_{\rm cc}$ is depicted in Figure 5.2 and can be created with the following voltages and currents applied to the eight radial electrodes:

$$V^n_{\rm rot} = V_{\rm rot}\cos\left(\tilde{R}\omega_{\rm rot}t - \frac{n\pi}{4} + \pi\right) \tag{5.5}$$

$$I^n_{\rm rot} = \tilde{B}I_{\rm rot}\sin\left(\tilde{R}\omega_{\rm rot}t - \frac{n\pi}{4} + \pi\right) \tag{5.6}$$

Note that $I^n_{\rm rot}$ are the intentionally applied currents that flow through the eight rods to create $\vec{\mathcal{B}}_{\rm rot}$, they are not the currents that charge the rods and give rise to $V^n_{\rm rot}$. When these voltages and currents are applied to the rods they create the following electric and magnetic fields:

$$\vec{\mathcal{E}}_{\rm rot} = \mathcal{E}_{\rm rot}\Big(\cos(\omega_{\rm rot}t)\hat{x} + \tilde{R}\sin(\omega_{\rm rot}t)\hat{y}\Big) \tag{5.7}$$

$$\vec{\mathcal{B}}_{\rm rot} = \mathcal{B}_{\rm rot}\tilde{B}\Big(\cos(\omega_{\rm rot}t)\hat{x} + \tilde{R}\sin(\omega_{\rm rot}t)\hat{y}\Big) \tag{5.8}$$

Assuming that the rods are infinitely long,[5] we find that $\mathcal{B}_{\rm rot} = \dfrac{2I_{\rm rot}\mu_0}{\pi R_0}$, where R_0 is the radius of the Bucket Brigade. For $R_0 = 5.85$ cm, the value of our current design [3], we need a reasonable

[5]While this is a better approximation in generation three then in generation two, it should not be taken too seriously. It is sufficient to find the approximate value of $I_{\rm rot}$.

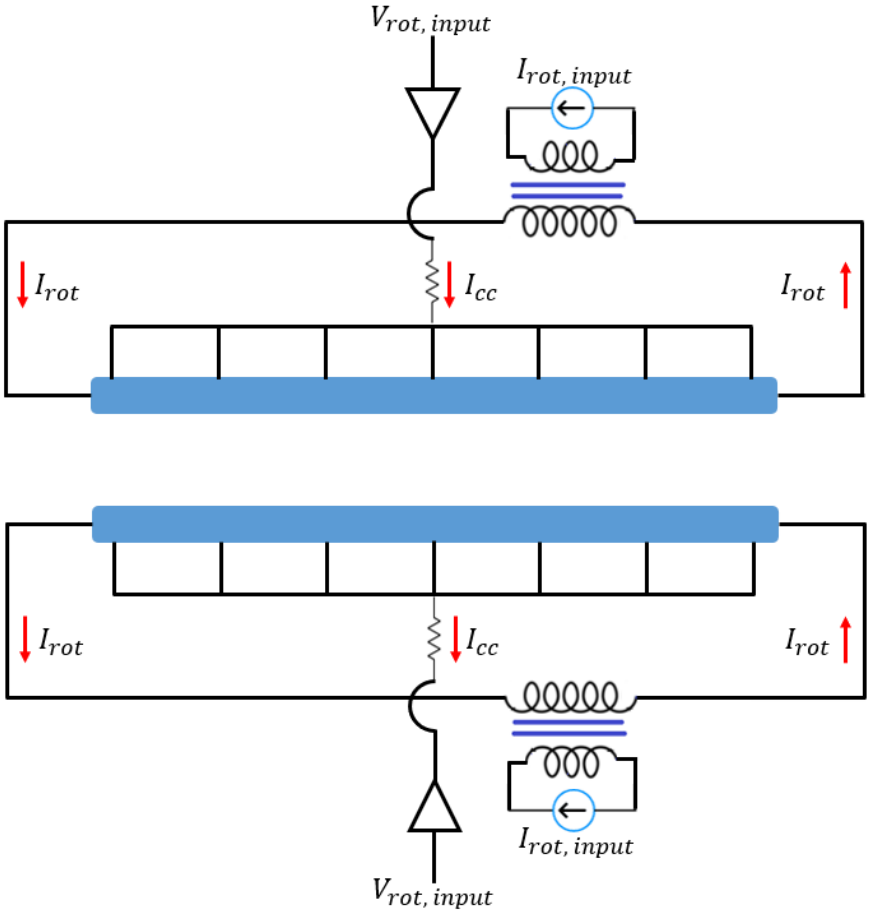

Figure 5.2: If we choose to generate f^0 via plan E this is our design to generate $\vec{\mathcal{B}}_{\rm rot}$ without $\vec{\mathcal{B}}_{\rm cc}$. The eight rods in the Bucket Brigade, two of which are shown in blue, have finite capacitance. If they are charged from one side a magnetic field $\vec{\mathcal{B}}_{\rm cc}$ will arise as described in Subsection 3.4.2. We can minimize this field by charging the radial electrodes via the charging current $I_{\rm cc}$ which connects to many points spaced along the rods and is generated by the amplified $V_{\rm rot}$. This minimizes the current traveling along the rods and therefore $\vec{\mathcal{B}}_{\rm cc}$. In order to create $\vec{\mathcal{B}}_{\rm rot}$ we can apply the currents $I_{\rm rot}$ in Equation 5.6 to run all the way though the electrodes. Since these currents do not need to induce a voltage in the rods, they will have the same magnitude as a function of z and $\vec{\mathcal{B}}_{\rm rot}$ will not have a spatial gradient.

$I_{\rm rot} = 12$ mA to apply $\mathcal{B}_{\rm rot} = 1.6$ mG and a Zeeman shift of 100 Hz.

5.1.4 Choosing a Method to Generate f^0

Now that all five plans listed in Table 5.1 have been explained, we can see which would be best in terms of limiting our systematic error. Plan B, where we generate $f^0 \sim 100$ Hz via a second harmonic and ellipticity to create a Berry's phase shift, at first appears promising. Berry's phase

does not cause a $\tilde{D}$-odd shift so there would be no need to worry about higher harmonics causing additional small Berry's phase shifts, and we would not need to apply a correction to our eEDM frequency channel. Additionally, some of the Zeeman effects which are currently systematics have $\frac{\langle \vec{\mathcal{E}} \cdot \vec{\mathcal{B}} \rangle / |\mathcal{E}|}{\langle \hat{\mathcal{E}} \cdot \vec{\mathcal{B}} \rangle} = 0$ so they will not cause systematic errors either. The only systematic errors from frequency shifts that we need to mind are magnetic and the experiment could be done inside some serious magnetic shielding.

There are two problems with this approach. The first is that the Zeeman shift from our molecules rotating inside the magnetic field gradient $\vec{\mathcal{B}}_{2,0}$ would cause a systematic $3\delta g_F \mu_B \mathcal{B}_{2,0} r_{\rm rot}$. Unlike all of the magnetic systematics listed in Table 3.6, this systematic effect is not multiplied by an electric field imperfection divided by $\mathcal{E}_{\rm rot}$. That will make this the most worrying Zeeman shift and require $\mathcal{B}_{2,0} < 75$ nG/cm for the effect to be 500 nHz or less. As we will soon see, this would be the most stringent restriction on the allowed magnetic fields by far! The second problem is that, as described in Subsection 5.1.2, we cannot completely remove magnetic field gradients from our apparatus. As discussed in Subsection 5.2.2, the largest Zeeman effects caused by these gradients have $\frac{\langle \vec{\mathcal{E}} \cdot \vec{\mathcal{B}} \rangle / |\mathcal{E}|}{\langle \hat{\mathcal{E}} \cdot \vec{\mathcal{B}} \rangle} = 1$ and would therefore cause systematic errors.

While these considerations eliminate plan B, they have also pushed us away from plans C and D. Plan C, to generate a Zeeman shift with $\frac{\langle \vec{\mathcal{E}} \cdot \vec{\mathcal{B}} \rangle / |\mathcal{E}|}{\langle \hat{\mathcal{E}} \cdot \vec{\mathcal{B}} \rangle} = 0$, suffers the same strict magnetic shielding requirements. Plan D generates $f^0 \sim 100$ Hz with $\frac{\langle \vec{\mathcal{E}} \cdot \vec{\mathcal{B}} \rangle / |\mathcal{E}|}{\langle \hat{\mathcal{E}} \cdot \vec{\mathcal{B}} \rangle} = \frac{4}{3}$ and could possibly be simpler to apply over a two or three meter long region,[6] but it still requires $\mathcal{B}_{2,0} < 225$ nG/cm. As we see in Subsection 5.2.1, this somewhat relaxed requirement is still three orders of magnitude more demanding then if we pick a plan with $\frac{\langle \vec{\mathcal{E}} \cdot \vec{\mathcal{B}} \rangle / |\mathcal{E}|}{\langle \hat{\mathcal{E}} \cdot \vec{\mathcal{B}} \rangle} = 1$. From this point on we assume that we generate f^0 from either plan A or E, where one of $\mathcal{B}_{2,0}$ or $\mathcal{B}_{\rm rot}$ causes a $f^0 \sim 100$ Hz Zeeman shift via the interaction with $\mathcal{E}_{\rm rot}$.

[6] Plan D involves an ellipticity interacting with a magnetic field gradient $\mathcal{B}_{2,\pm 2}$ which is entirely in the xy-plane. The ellipticity could be intentionally applied by "displacing" one or more of the rod electrodes and the magnetic field gradient could be created by a single current carrying wire that runs the length of the Bucket Brigade.

5.2 Magnetic Systematics in Generation 3

One of the downsides of ThF^+ is that its g-factor $|g_F| = 0.0149(3)$ in the $^3\Delta_1$ electronic state is nearly five times larger than in HfF^+ [62].[7] Its differential g-factor is larger as well, with $|\delta g_F| \sim 5.7$ times larger than in HfF^+, see Figure 5.3. This larger magnetic sensitivity and the fact that the molecules will move over a 2 or 3 meter long region during the coherence time make magnetic systematics more worrying in our next measurement. I will first discuss how the magnetic systematic effects that worried us in generation two translate to our new experiment in Subsection 5.2.1, and then discuss the new magnetic systematics we expect to encounter in Subsections 5.2.2 and 5.2.3.

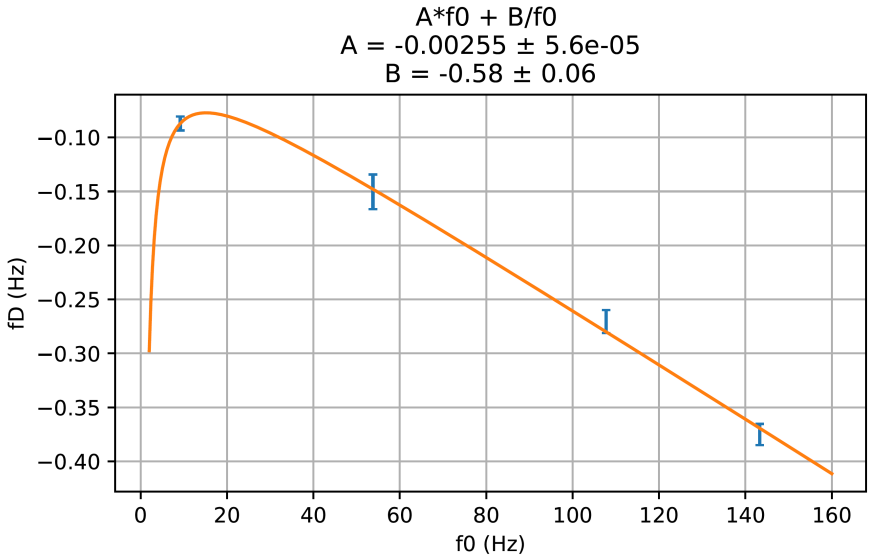

Figure 5.3: A measurement of f^D vs f^0 in ThF^+ for various values of the applied magnetic field. Data is taken with $\mathcal{E}_{\text{rot}} = 60$ V/cm. The data is fit to $\text{A}f^0 + \text{B}/f^0$, where $\text{A} = \dfrac{\delta g_F}{g_F}$ and $\text{B} = \Delta\Delta^D$. The parameter A is equal to $\dfrac{\delta g_F}{g_F} = -0.00255(6)$, comparable to $\dfrac{\delta g_F}{g_F}$ in HfF^+. This fit combined with the measured value $|g_F| = 0.0149(3)$ gives $|\delta g_F| = 3.8(1) \times 10^{-6}$, about 5.7 times larger than in HfF^+. This image was made by current JILA eEDM graudate student Sun Yool Park.

[7] Note that the sign of g_F in ThF^+ is still unknown. This can be determined by repeating the method described in Chapter 4.

5.2.1 Known Magnetic Systematics from Generation 2

5.2.1.1 Overview

The magnetic systematics in generation two, discussed in Section 3.3, concerned electric and magnetic field imperfections in a small ~ 1 cm^3 region of space. In generation three our molecules will move in a similarly sized ion cloud over a two to three meter long distance down the Bucket Brigade. Fortunately, this does not complicate the systematics in Table 3.6 because they are proportional to the average electric and magnetic field imperfections experienced by the ions. That means the restrictions on these fields in generation three will be averaged over the entire length of the Bucket Brigade, assuming the ions move at a uniform velocity.

As discussed earlier in this chapter we have a ~ 5.7 times larger δg_F and want to keep each systematic smaller than 500 nHz. The largest magnetic systematics in generation two were ~ 2 μHz. If we have the same field imperfections in our Bucket Brigade these will cause systematic shifts greater than 10 μHz, over twenty times larger than we want to allow!

We would like the magnitude of these systematics to drop by at least a factor of ~ 20, which we can accomplish in one of two ways. The first method is to reduce the magnitude of the stray electric fields relative to $\mathcal{E}_{\rm rot}$, which we plan to keep ~ 60 V/cm. The ellipticity is largely constrained by geometric imperfections that we expect to be similar in magnitude to our generation two ion trap. We do have a plan to reduce the harmonics of $\mathcal{E}_{\rm rot}$ by replacing the op-amps which generated $V_{\rm rot}$ in generation two with resonant transformer circuits. These circuits generate a large voltage at their resonant frequency $f_{\rm rot}$ and suppress the off-resonant harmonics. The circuits have been built with a new resonant frequency $f_{\rm rot} \sim 150$ kHz and are currently in use, and they are described in Chapter 4 of Noah Schlossberger's thesis [3].

While the circuits have been successful in suppressing harmonics, the lower value of $f_{\rm rot} \sim 150$ kHz has increased $r_{\rm rot} = \dfrac{e\mathcal{E}_{\rm rot}}{4\pi^2 m f_{\rm rot}^2}$ by a factor of 5 relative to $r_{\rm rot}$ in generation two. This will cause the systematic effects due to magnetic field gradients to grow as they scale like $\mathcal{B}_{l,m} r_{\rm rot}^{l-1}$.

The lower frequency has also caused larger pondermotive forces which have caused trouble in our current generation three ion trap. In order to solve both of these problems we plan on rebuilding the resonant circuits with $f_{\rm rot} \sim 375$ kHz. This will result in $r_{\rm rot} \sim 0.4$ mm, a slightly smaller value than in generation two due to the higher mass of ThF^+. Because the new resonant circuit has not been built yet we do not know the values of the harmonic electric fields. To be overly cautious, I assume that the harmonics will have the same values in generations two and three for the rest of this section.

While we hope to have smaller electric field imperfections, the other option for reducing the Zeeman systematics is to reduce the magnitude of the magnetic field and its gradients in the ion trap. We can determine the required magnetic field limits by investigating the largest effects in Table 3.6 and the off diagonal effects in Subsection 3.1.

5.2.1.2 Uniform Magnetic Fields

The magnitude of the only systematic effect in Table 3.6 caused by a uniform magnetic field is $3\delta g_F \mu_B \frac{\mathcal{B}_{1,\pm1}\mathcal{E}_{\rm 2hxy}}{4\mathcal{E}_{\rm rot}}$, which caused a 2.2 μHz systematic in generation two. Assuming a similar value of $\frac{\mathcal{E}_{\rm 2hxy}}{\mathcal{E}_{\rm rot}} \sim 4.2 \times 10^{-5}$ and accounting for the larger value of δg_F, we require $\mathcal{B}_{1,\pm1} = \mathcal{B}_{\rm xy} < 0.25$ mG. Magnetic fields along the z-axis in generation two caused systematics by creating off-diagonal mixing terms Δ that had switch state dependencies other than Δ^0 and Δ^D. In generation three we need to consider all magnetic fields that are perpendicular to $\vec{\mathcal{E}}_{\rm rot}$, not just $\mathcal{B}_{1,0} = \mathcal{B}_{\rm z}$. If we choose plan E and apply f^0 via a rotating magnetic field $\vec{\mathcal{B}}_{\rm rot}$, there will inevitably be a portion of that field that is perpendicular to $\vec{\mathcal{E}}_{\rm rot}$. We next consider the systematics caused by both of these perpendicular magnetic fields which will be grouped together with the label $\mathcal{B}_\perp$.

In general the systematics described in Section 3.1 due to Δ will be larger in generation three. This is because Δ^0 and Δ^D are both proportional to the Ω-doubling constant ω_{ef}, as shown in Equation 2.21, which is ~ 7 times larger in ThF^+ than it was in HfF^+. Assuming that $f_{\rm rot} = 375$ kHz in generation three, Δ^0 and Δ^D will be ~ 5 Hz. We can first consider the systematic effects

from the terms in Equation 3.4 which are:

$$\frac{\Delta^0\delta\Delta^{DB} + \Delta^D\delta\Delta^B + \delta\Delta^{DR}\delta\Delta^{BR} + \delta\Delta^R\delta\Delta^{DBR}}{|f_0^0|} = \frac{30 g_F^2 \mu_B^2 \mathcal{B}_\perp \mathcal{B}_\perp^B \Delta^0 \Delta^D}{h^2 f_{\text{rot}}^2 |f_0^0|} \tag{5.9}$$

See Section 3.1 for how we arrived at the right hand side of this equation. Using $\Delta^0 \sim \Delta^D \sim 5$ Hz as we expect in generation three, we find that the shift has a magnitude of $23\frac{\text{nHz}}{\text{mG}^2}\mathcal{B}_\perp\mathcal{B}_\perp^B$.

In order to keep this combined systematic effect smaller than 500 nHz, we require $\mathcal{B}_\perp\mathcal{B}_\perp^B \lesssim 20$ mG^2. If we follow plan A and we do not apply $\vec{\mathcal{B}}_{\text{rot}}$ then we are only concerned with magnetic fields along the z-axis. In this case we will intentionally apply a magnetic field gradient along z $\mathcal{B}_{2,0}$ that flips with the magnetic field. Therefore the ions will experience an average magnetic field $\mathcal{B}_\perp = \mathcal{B}_{2,0} z_{\text{offset}}$ as they move through the Bucket Brigade. z_{offset} is the distance between the center of the Bucket Brigade and the location where the applied magnetic field along z goes to zero. Assuming that we reduce the background field $\mathcal{B}_z^B$ to $\lesssim 1$ mG by magnetic shielding, then we require $\mathcal{B}_{2,0} z_{\text{offset}} < 20$ mG.

If we choose plan E we also have to consider $\mathcal{B}_\perp$ due to imperfect alignment between $\vec{\mathcal{E}}_{\text{rot}}$ and $\vec{\mathcal{B}}_{\text{rot}}$. As discussed in Subsection 5.1.3 we only need $\mathcal{B}_{\text{rot}} \sim 1.6$ mG in order to create a ~ 100 Hz frequency shift. Even if we messed up $\vec{\mathcal{B}}_{\text{rot}}$ so badly that $\mathcal{B}_\perp = \mathcal{B}_\perp^B = 1.6$ mG, Equation 5.9 would still only result in a ~ 60 nHz systematic shift. Because this shift is small enough to not be a problem and plan E does not involve applying large $\mathcal{B}_z$ gradients, this systematic shift would not be very concerning if we generate f^0 with $\vec{\mathcal{B}}_{\text{rot}}$. Limiting $\mathcal{B}_z \lesssim 1$ mG would be more than good enough to keep this systematic shift small.

The last systematic we need to consider from $\mathcal{B}_z$ is the shift proportional to f^{BR}, which we assume will still be our largest frequency channel outside of f^0, given in Equation 3.6. We find that we need $f^{BR}\mathcal{B}_\perp \lesssim 0.6$ mG Hz. It is hard to predict how large f^{BR} will be in generation three due to the charging currents, so it will be important to check this requirement in the future. If we assume

$f^{BR} \sim 200$ mHz like in generation two, we need $\mathcal{B}_\perp \lesssim 3$ mG. Recall that this is the magnetic field that is perpendicular to $\vec{\mathcal{E}}_{\rm rot}$ and switches sign with $\tilde{B}$. This should be straightforward if we choose plan E, but if we choose plan A we would require $\mathcal{B}_{2,0} z_{\rm offset} < 3$ mG unless f^{BR} is smaller in generation three.

5.2.1.3 Magnetic Field Gradients

Table 3.6 has two more magnetic systematic effects that are a few μHz in size, both from first order magnetic field gradients. They are $3\delta g_F \mu_B \frac{\sqrt{3}\mathcal{B}_{2,\pm2}\mathcal{E}_{\rm 3hxy} r_{\rm rot}}{4\mathcal{E}_{\rm rot}}$ and $3\delta g_F \mu_B \frac{\sqrt{3}\mathcal{B}_{2,\pm2}\mathcal{E}_{\epsilon} r_{\rm rot}}{2\mathcal{E}_{\rm rot}}$, which caused systematics of 1.5 and 1.7 μHz respectively in generation two. Assuming the generation two values for $\mathcal{E}_{\rm 3hxy}$ and $\mathcal{E}_\epsilon$, we require $\mathcal{B}_{2,\pm2} < 0.25$ mG/cm. This provides the strongest restriction on first order magnetic field gradients as we will shim $\mathcal{B}_{2,0}$ to zero.[8] To be safe, we would like all first order gradients $\mathcal{B}_{2,m} < 0.25$ mG/cm.

Table 3.6 does include frequency shifts caused by second order magnetic field gradients $\mathcal{B}_{3,m}$, though they only caused systematics on the order of 10s of nHz in generation two. In order to keep these systematics less than 500 nHz in generation three, we require $\mathcal{B}_{3,m} \lesssim 25$ mG/cm^2. Note that if we apply magnetic shielding to keep the zero and first order gradients of the magnetic field less than 0.25 mG and 0.25 mG/cm respectively, it would be very odd if $\mathcal{B}_{3,m} \lesssim 25$ mG/cm^2. We can make the argument stronger by noting that the ions will always be more than 10 cm from the magnetic shielding,[9] so we would expect higher order gradients to fall at least as fast as $\frac{0.25 \text{ mG/cm}}{(10 \text{ cm})^n}$ with

[8] If we go with plan E and generate $f^0 \sim 100$ Hz via $\mathcal{B}_{\rm rot}$, shimming f^B to zero by changing the value of $\mathcal{B}^B_{\rm rot}$ will likely leave nonzero values of $\mathcal{B}^B_{\rm rot}$ and $\mathcal{B}^B_{2,0}$. At first glance this appears to cause systematics due to effects 9-14 and 33-45 in Table 3.6 which are proportional to $\mathcal{B}_{2,0}$ but have $\frac{\langle \vec{\mathcal{E}} \cdot \vec{\mathcal{B}} \rangle / |\mathcal{E}|}{\langle \hat{\mathcal{E}} \cdot \vec{\mathcal{B}} \rangle} \neq 1$. However, the shimming procedure will guarantee that $\mathcal{B}^B_{\rm rot} = -\mathcal{B}^B_{2,0} r_{\rm rot}$. Additionally, Table 3.6 does not include frequency shifts caused by $\mathcal{B}_{\rm rot}$. Since $\mathcal{B}_{2,0} r_{\rm rot}$ looks exactly like a rotating magnetic field to the ions (see Figure 2.4) Table 3.6 would include duplicates of all entries proportional to $\mathcal{B}_{2,0}$ with $\mathcal{B}_{2,0} r_{\rm rot}$ replaced by $\mathcal{B}_{\rm rot}$. Therefore the frequency shifts from $\mathcal{B}_{2,0}$ will cancel with shifts caused by $\mathcal{B}_{\rm rot}$ and there will be no resulting systematics.

[9] As discussed in Sections 5.4 and 5.5 we expect the innermost magnetic shield to have $R_1 = 25$ cm, so 10 cm is conservative. The shield will be the nearest object to the ions that is magnetic.

higher orders of gradient n. All that is to say that if we constrain the zero and first order gradients of the magnetic field to be < 0.25 mG and < 0.25 mG/cm respectively, and we do not increase the size of $r_{\rm rot}$ by using a lower value of $f_{\rm rot}$, systematics from higher order gradients should be negligible.

5.2.2 Maxwell Systematics

Figure 5.2 outlines a potential plan to control the magnetic field gradients guaranteed in our experiment by Maxwell in Equation 5.1. Since we are not sure if we will implement this plan, and even if we do there is no guarantee how well it will work, we now consider the systematic effects caused by any of the magnetic gradients created by $\vec{\mathcal{E}}_{\rm rot}$.

From Equation 5.2 we see that $\vec{\mathcal{E}}_{\rm rot}$ can lead to four[10] magnetic field gradients, where the total "Maxwell" magnetic field is:

$$\vec{\mathcal{B}}_{\rm Maxwell} = \begin{pmatrix} -\tilde{R}z\mathcal{B}_{x\partial z}\cos\left(\omega_{\rm rot}t\right) \\ -z\mathcal{B}_{y\partial z}\sin\left(\omega_{\rm rot}t\right) \\ \tilde{R}x\mathcal{B}_{z\partial x}\cos\left(\omega_{\rm rot}t\right) + y\mathcal{B}_{z\partial y}\sin\left(\omega_{\rm rot}t\right) \end{pmatrix} \tag{5.10}$$

While only the differences in these amplitudes is fixed by Equation 5.2, we can expect that they are each $\sim \dfrac{\omega_{\rm rot}\mathcal{E}_{\rm rot}}{c^2} = 1.6$ mG/m.

What frequency shifts are created by this magnetic field gradient? Using $\vec{\mathcal{E}}_{\rm rot}$ as defined in Equation 5.7, we arrive at a $\tilde{D}$-even frequency shift of $-3g_F\mu_B\left\langle\hat{\mathcal{E}}_{\rm rot}\cdot\vec{\mathcal{B}}_{\rm Maxwell}\right\rangle/h = -1.5g_F\mu_B(\mathcal{B}_{x\partial z}+\mathcal{B}_{y\partial z})z\tilde{R}/h \sim -\dfrac{3g_F\mu_B\omega_{\rm rot}\mathcal{E}_{\rm rot}}{hc^2}z\tilde{R}$, which has a magnitude of about 1 Hz/cm. Since $\dfrac{\left\langle\vec{\mathcal{E}}\cdot\vec{\mathcal{B}}\right\rangle/|\mathcal{E}|}{\left\langle\hat{\mathcal{E}}\cdot\vec{\mathcal{B}}\right\rangle} = 1$ in this case, there will also be a $\tilde{D}$-odd shift that is smaller by a factor of $\dfrac{\delta g_F}{g_F}$. Fortunately this will not cause a systematic if we choose plans A or E, but it does mean that our ions would have their

[10] Because $\vec{\mathcal{E}}_{\rm rot}$ has no component along the z-axis, we assume that the two remaining magnetic field gradients are each zero.

Ramsey frequency vary by ~ 200 Hz over a 2 meter long Bucket Brigade! If we engineer so most of the gradients are in $\mathcal{B}_{z\partial x}$ or $\mathcal{B}_{z\partial y}$, we can make the gradient small. This may be a necessity as we need the frequency to be large compared to Δ for the entire coherence time or else the $M_F = \pm 1.5$ stretched states will mix.

If we gloss over the problem of the frequency going through zero, when we average the effect over the entire Bucket Brigade there will be a frequency shift of $1\frac{\text{Hz}}{\text{cm}}\, z_0 \tilde{R}$ where z_0 is the distance between the center of the Bucket Brigade and the position along the z-axis where the Maxwell magnetic field goes to zero. We think those locations should be near one another since the apparatus will be mostly symmetric, but a z_0 of at least few centimeters would not be surprising given that the length of the entire apparatus will be a few meters.

In order to see how this frequency gradient can cause systematic effects I have repeated the procedure outlined in Section 3.3. I numerically and analytically searched for frequency shifts caused by $\vec{\mathcal{B}}_{\text{Maxwell}}$ and stray electric fields. Table 5.2 contains all of the shifts found by the analytic method up to $\mathcal{O}(\kappa^2)$, which were verified numerically.[11]

Shifts number 1-4 in Table 5.2 cause a systematic shift because they cause a $\tilde{D}$-even but not $\tilde{D}$-odd shift. The four shifts can suggestively be rewritten as $\frac{\left(\mathcal{B}_{x\partial z} - \mathcal{B}_{y\partial z}\right)\mathcal{E}_{3\text{hx}} z_0 \cos\phi_{3\text{x}}}{8\mathcal{E}_{\text{rot}}}$ and $\frac{\left(\mathcal{B}_{y\partial z} - \mathcal{B}_{x\partial z}\right)\mathcal{E}_{3\text{hy}} z_0 \sin\phi_{3\text{y}}}{8\mathcal{E}_{\text{rot}}}$. In this form it is perhaps clear why we ignored this systematic in generation two. Assuming that our ion trap is rotationally symmetric about the z-axis, there are no major differences between x and y, $\mathcal{B}_{x\partial z}$ and $\mathcal{B}_{y\partial z}$ will have the same magnitude and sign causing these frequency shifts to cancel. And even if the effect does not cancel and we suppose somehow that $\mathcal{B}_{x\partial z} - \mathcal{B}_{y\partial z} \sim \frac{\omega_{\text{rot}}\mathcal{E}_{\text{rot}}}{c^2} = 1.6$ mG/m, the systematic in generation two is still just 1.2 μHz/meter times z_0. Per Figure 3.8 the entire generation two ion trap was 160 mm tall, meaning z_0 should be much smaller than 80 mm. Assuming the worst case where $z_0 = 80$ mm, the systematic shift

[11] For curious graduate students in the JILA EDM group, or in case these systematic effects are dramatically larger than anticipated, I have recorded the shifts up to $\mathcal{O}(\kappa^3)$ in the group meeting slides on November 13th 2023.

Table 5.2: Analytically Calculated Zeeman Shifts from $\vec{\mathcal{B}}_{\text{Maxwell}}$

Number	$\langle\hat{\mathcal{E}}\cdot\vec{\mathcal{B}}\rangle$	$\langle\vec{\mathcal{E}}\cdot\vec{\mathcal{B}}\rangle/\mathcal{E}_{\text{rot}}$	$\dfrac{\langle\vec{\mathcal{E}}\cdot\vec{\mathcal{B}}\rangle/\mathcal{E}_{\text{rot}}}{\langle\hat{\mathcal{E}}\cdot\vec{\mathcal{B}}\rangle}$
1	$\dfrac{\mathcal{B}_{x\partial z}\mathcal{E}_{3\text{hx}}z_0\cos\phi_{3\text{x}}}{8\mathcal{E}_{\text{rot}}}$	0	0
2	$-\dfrac{\mathcal{B}_{y\partial z}\mathcal{E}_{3\text{hx}}z_0\cos\phi_{3\text{x}}}{8\mathcal{E}_{\text{rot}}}$	0	0
3	$-\dfrac{\mathcal{B}_{x\partial z}\mathcal{E}_{3\text{hy}}z_0\sin\phi_{3\text{y}}}{8\mathcal{E}_{\text{rot}}}$	0	0
4	$\dfrac{\mathcal{B}_{y\partial z}\mathcal{E}_{3\text{hy}}z_0\sin\phi_{3\text{y}}}{8\mathcal{E}_{\text{rot}}}$	0	0
5	$\dfrac{\mathcal{B}_{x\partial z}\mathcal{E}_{2\text{hz}}r_{\text{rot}}\cos\phi_{2\text{z}}}{16\mathcal{E}_{\text{rot}}}$	$\dfrac{\mathcal{B}_{x\partial z}\mathcal{E}_{2\text{hz}}r_{\text{rot}}\cos\phi_{2\text{z}}}{16\mathcal{E}_{\text{rot}}}$	1
6	$-\dfrac{\mathcal{B}_{y\partial z}\mathcal{E}_{2\text{hz}}r_{\text{rot}}\cos\phi_{2\text{z}}}{16\mathcal{E}_{\text{rot}}}$	$-\dfrac{\mathcal{B}_{y\partial z}\mathcal{E}_{2\text{hz}}r_{\text{rot}}\cos\phi_{2\text{z}}}{16\mathcal{E}_{\text{rot}}}$	1
7	$-\dfrac{\mathcal{B}_{z\partial x}\mathcal{E}_{2\text{hz}}r_{\text{rot}}\cos\phi_{2\text{z}}}{4\mathcal{E}_{\text{rot}}}$	$-\dfrac{\mathcal{B}_{z\partial x}\mathcal{E}_{2\text{hz}}r_{\text{rot}}\cos\phi_{2\text{z}}}{4\mathcal{E}_{\text{rot}}}$	1
8	$\dfrac{\mathcal{B}_{z\partial y}\mathcal{E}_{2\text{hz}}r_{\text{rot}}\cos\phi_{2\text{z}}}{4\mathcal{E}_{\text{rot}}}$	$\dfrac{\mathcal{B}_{z\partial y}\mathcal{E}_{2\text{hz}}r_{\text{rot}}\cos\phi_{2\text{z}}}{4\mathcal{E}_{\text{rot}}}$	1
9	$-\dfrac{\mathcal{B}_{x\partial z}\mathcal{E}_{\epsilon}z_0\cos 2\theta}{4\mathcal{E}_{\text{rot}}}$	$-\dfrac{\mathcal{B}_{x\partial z}\mathcal{E}_{\epsilon}z_0\cos 2\theta}{2\mathcal{E}_{\text{rot}}}$	2
10	$\dfrac{\mathcal{B}_{y\partial z}\mathcal{E}_{\epsilon}z_0\cos 2\theta}{4\mathcal{E}_{\text{rot}}}$	$\dfrac{\mathcal{B}_{y\partial z}\mathcal{E}_{\epsilon}z_0\cos 2\theta}{2\mathcal{E}_{\text{rot}}}$	2

would only be 100 nHz in generation two.

While we were safe to ignore these shifts in generation two, it is not so easy in generation three. All magnetic effects are inherently 5.7 times larger, our desired uncertainty is 10 times smaller and the ion trap will be multiple meters long. This time around the shift will be 6.7 μHz/meter if $\mathcal{B}_{x\partial z}-\mathcal{B}_{y\partial z}\sim\dfrac{\omega_{\text{rot}}\mathcal{E}_{\text{rot}}}{c^2}=1.6$ mG/m. In order to keep this shift smaller than 500 nHz we must keep $\left(\mathcal{B}_{x\partial z}-\mathcal{B}_{y\partial z}\right)z_0\lesssim 0.1$ mG.[12] This should not be particularly challenging, but it will need to be confirmed experimentally.

Shifts number 5-8 in Table 5.2 are interesting because they are proportional to r_{rot} instead

[12]This constraint assumes the generation two value for $\mathcal{E}_{3\text{hxy}}$. If this harmonic is suppressed in generation three, which it should be due to the resonant circuits discussed in Subsection 5.2.1, this restraint will be relaxed.

of z_0. Fortunately they will not cause systematic errors because they each have $\frac{\langle \vec{\mathcal{E}} \cdot \vec{\mathcal{B}} \rangle / |\mathcal{E}|}{\langle \hat{\mathcal{E}} \cdot \vec{\mathcal{B}} \rangle} = 1$.

Shifts 9 and 10 in Table 5.2 can be combined to get $\frac{\left(\mathcal{B}_{y\partial z} - \mathcal{B}_{x\partial z}\right)\mathcal{E}_\epsilon z_0 \cos 2\theta}{4\mathcal{E}_{\rm rot}}$. Like shifts 1 through 4 this effect goes to zero if the ion trap is symmetric between x and y. Assuming this is not the case, generation two would have had a systematic of 3.3 μHz/meter and is still small enough to ignore. In the worst case described above, the systematic shift would be less than 300 nHz and is likely much smaller. For generation three I expect this systematic to be more worrying than shifts 1 through 4 because while we have a plan to reduce the third harmonic, the ellipticity will likely have the same magnitude as in generation two. If that is the case and if $\mathcal{B}_{x\partial z} - \mathcal{B}_{y\partial z} \sim \frac{\omega_{\rm rot}\mathcal{E}_{\rm rot}}{c^2} = 1.6$ mG/m, this shift will be 18.8 μHz/meter times z_0. This will require $\left(\mathcal{B}_{x\partial z} - \mathcal{B}_{y\partial z}\right) z_0 \lesssim 0.04$ mG, a more demanding constraint then before. This will require a bit of thought and effort to achieve, but should not be an intractable obstacle.

5.2.3 Systematics from Spatial Gradients

The last category of magnetic systematics to consider are those that are caused by spatial inhomogeneities in our electric and magnetic fields. In generation two our ion cloud sat at the same point in space, and we could verify the temporal stability of $V_{\rm rot}$ and the current that drove $\vec{\mathcal{B}}_{2,0}$. In generation three it will be inevitable that spatial inhomogeneities in $\vec{\mathcal{E}}_{\rm rot}$ and either $\vec{\mathcal{B}}_{2,0}$ or $\vec{\mathcal{B}}_{\rm rot}$ which can lead to systematic errors. Because the frequency shift caused by $\vec{\mathcal{B}}_{2,0}$ depends on $r_{\rm rot}$ which is a function of $\mathcal{E}_{\rm rot}$, we will start by considering the simpler case where our frequency shift is caused by $\vec{\mathcal{B}}_{\rm rot}$.

We start by considering the simplest case where $\mathcal{B}_{\rm rot}$ is uniform over the entire length of the Bucket Brigade L but $\mathcal{E}_{\rm rot}$ is larger by $\mathcal{E}_{\rm bump}$ for a small region of the Bucket Brigade L_E, as shown in Figure 5.4. This change in $\mathcal{E}_{\rm rot}$ magnitude will not change the $\tilde{D}$-even frequencies because $\langle \vec{\mathcal{B}} \cdot \hat{\mathcal{E}} \rangle$ will be the same size throughout the Bucket Brigade. On the other hand the $\tilde{D}$-odd frequencies will change size because $\langle \vec{\mathcal{B}} \cdot \vec{\mathcal{E}} \rangle$ is not the same over the entire ion trap.[13] Assuming that the ions

[13] See Subsection 3.2.1 for an explanation of this difference between $\tilde{D}$-even and $\tilde{D}$-odd Zeeman shifts.

move with a uniform velocity, we measure:

$$\frac{f^D}{f^0} = \frac{\delta g_F}{g_F}\left(1 + \frac{L_E \mathcal{E}_{\text{bump}}}{L\mathcal{E}_{\text{rot}}}\right) \tag{5.11}$$

Note that this can cause an increase in $\frac{f^D}{f^0}$ because $\mathcal{E}_{\text{bump}}$ is a signed quantity. In the case where $L_E = L$, this equation tells us that $\frac{\delta g_F}{g_F}$ is proportional to $\mathcal{E}_{\text{rot}}$, which we found in Equation 4.57.

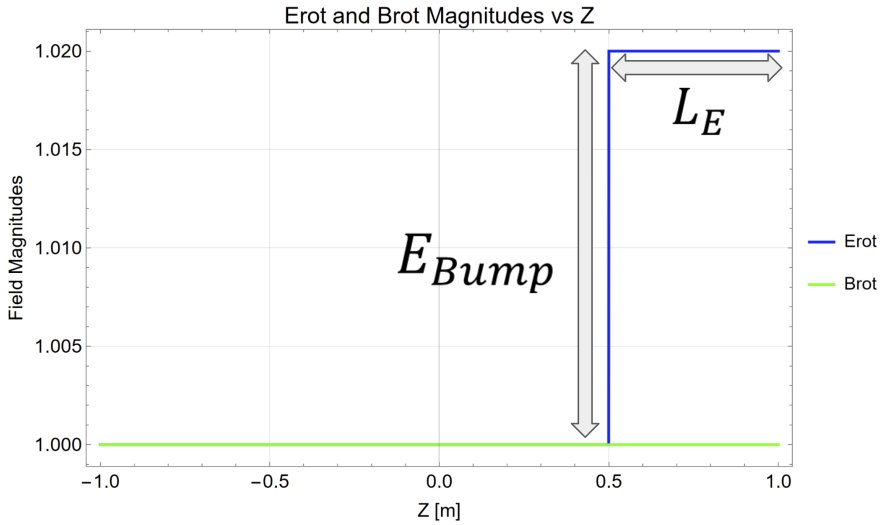

Figure 5.4: $\mathcal{B}_{\text{rot}}$ is uniform over the $L = 2$ meter long Bucket Brigade, but $\mathcal{E}_{\text{rot}}$ is larger by $\mathcal{E}_{\text{bump}}$ for a region $L_E < L$. This changes the ratio f^D/f^0.

On its own, $\mathcal{E}_{\text{bump}}$ is not problematic. It will change our measured value of $\frac{f^D}{f^0}$, but as long as it is stable over time we will take all of our data with the same ratio.[14] Spatial variations in the magnitude of $\mathcal{E}_{\text{rot}}$ are most likely to come from geometric imperfections of the rods, i.e. the rods are closer together on one end of the Bucket Brigade then the other, which will be stable over time.

Spatial variation in $\mathcal{E}_{\text{rot}}$ and $\mathcal{B}_{\text{rot}}$ at the same time is more worrying. Now we assume that the magnitude of $\mathcal{B}_{\text{rot}}$ changes by $\mathcal{B}_{\text{bump}}$ for a region L_B as shown in Figure 5.5. Let L_{EB} be the length of the region where the two bumps overlap. In the case of Figure 5.5 $L_{EB} = 0$, but in general the

[14]This modification of $\frac{f^D}{f^0}$ is similar to an effect of the trapping electric fields described in Section VI A 6 of the Systematics paper [31].

bumps can be centered anywhere in the region L and the two bumps can partially or completely overlap. In this case the change in $\frac{f^D}{f^0}$ is more complicated. Expanding in powers of $\frac{\mathcal{B}_{\text{bump}}}{\mathcal{B}_{\text{rot}}}$, we find that:

$$\frac{f^D}{f^0} = \frac{\delta g_F}{g_F}\left(1 + \frac{\mathcal{E}_{\text{bump}}}{\mathcal{E}_{\text{rot}}}\left(\frac{L_E}{L} + \frac{\mathcal{B}_{\text{bump}}}{\mathcal{B}_{\text{rot}}}\frac{LL_{EB} - L_E L_B}{L^2} + \mathcal{O}\left(\frac{\mathcal{B}_{\text{bump}}}{\mathcal{B}_{\text{rot}}}\right)^2\right)\right) \tag{5.12}$$

Note that this equation reduces to Equation 5.11 when $\mathcal{B}_{\text{bump}} = 0$, as expected.

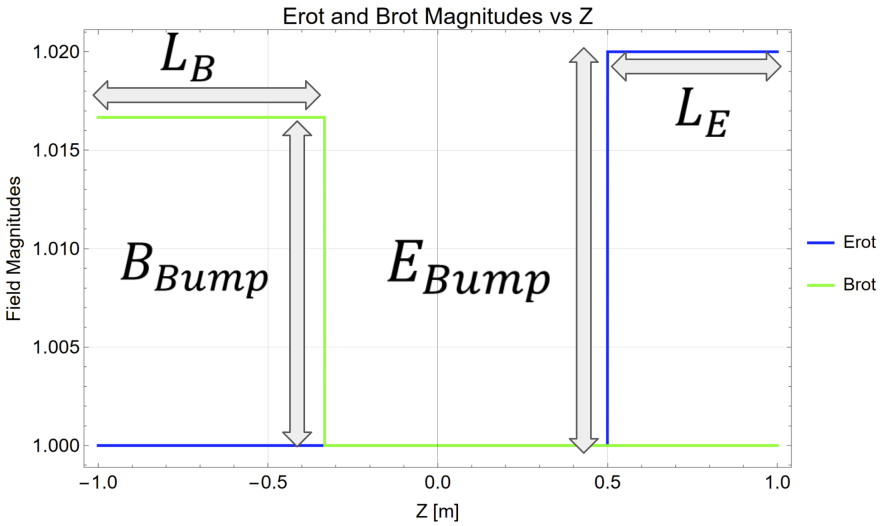

Figure 5.5: $\mathcal{E}_{\text{rot}}$ is larger than its usual value by $\mathcal{E}_{\text{bump}}$ for a region $L_E < L$ and $\mathcal{B}_{\text{rot}}$ is larger than its usual value by $\mathcal{B}_{\text{bump}}$ for a region $L_B < L$. This changes the ratio f^D/f^0 and can cause a systematic shift.

The scary part of Equation 5.12 is that $\mathcal{B}_{\text{bump}}$ should be replaced by $\tilde{B}\mathcal{B}_{\text{bump}} + \mathcal{B}^B_{\text{bump}}$ as in general the $\mathcal{B}_{\text{rot}}$ non-uniformity will have $\tilde{B}$-even and $\tilde{B}$-odd components. The $\tilde{B}$-even component $\mathcal{B}^B_{\text{bump}}$ will cause a shift in f^{DB} with magnitude:

$$\delta f^{DB} = f^0 \frac{\delta g_F}{g_F}\frac{\mathcal{E}_{\text{bump}}}{\mathcal{E}_{\text{rot}}}\frac{\mathcal{B}^B_{\text{bump}}}{\mathcal{B}_{\text{rot}}} \tag{5.13}$$

Note that we have dropped the factor of $\frac{LL_{EB} - L_E L_B}{L^2}$ from Equation 5.12 because the spatial inhomogeneities of the fields will not be perfect bumps and this order one number will be replaced

by another order one number. What makes this systematic effect worrying is that there will not be an analogous shift in f^B that occurs without the factor of $\frac{\delta g_F}{g_F}$. That is because this effect is inherently $\tilde{D}$-odd like the $\tilde{D}$-odd cloud size effect described in Subsection 3.2.3 – the $\tilde{D}$-odd frequency changes suddenly due to the bump in $\mathcal{E}_{\rm rot}$ while the $\tilde{D}$-even frequency is unaffected.

If there are inhomogeneities in $\mathcal{B}_{\rm rot}$ we do have a method to measure them. We can move the ions to a certain point in the trap, perform the entire Ramsey sequence by applying the $\pi/2$ pulses with the molecules in place, and then read out the frequency f^0. This works because the frequency depends only on $\mathcal{B}_{\rm rot}$ and not $\mathcal{E}_{\rm rot}$ in this case, and we can map out the variation in $\mathcal{B}_{\rm rot}$. Unfortunately, given the method for creating $\mathcal{B}_{\rm rot}$ in Figure 5.2, it may be difficult to correct for gradients in $\mathcal{B}_{\rm rot}$. After mapping out $\mathcal{B}_{\rm rot}$ we could then measure variations in $\mathcal{E}_{\rm rot}$ by looking for variations in $\frac{f^D}{f^0}$ as a function of ion position. Assuming we have $f^0 = 100$ Hz, we need to keep $\frac{\mathcal{E}_{\rm bump}}{\mathcal{E}_{\rm rot}}\frac{\mathcal{B}^B_{\rm bump}}{\mathcal{B}_{\rm rot}} < 2\times10^{-6}$ in order to keep the systematic effect less than 500 nHz.

As mentioned before, the story becomes more complicated if we use $\mathcal{B}_{2,0}$ instead of $\mathcal{B}_{\rm rot}$ to generate $f^0 \sim 100$ Hz because the frequency shift which is proportional to $\mathcal{B}_{2,0}r_{\rm rot}$ depends on the magnitude of $\mathcal{E}_{\rm rot}$. However, this does not significantly change Equation 5.12. All it does is add $\mathcal{O}\big(\frac{\mathcal{E}_{\rm bump}}{\mathcal{E}_{\rm rot}}\big)^2$ terms that are small compared to the shift we focus on in Equation 5.13.

The upside of $\mathcal{B}_{2,0}$ for this systematic is that we will likely be able to tune the magnetic field along the Bucket Brigade quite easily. We envision applying $\mathcal{B}_{2,0}$ via a series of coils along the outside of the vacuum chamber around the Bucket Brigade, which will be discussed in Subsection 5.5. We can change the value of the $\tilde{B}$-even and $\tilde{B}$-odd bumps in $\mathcal{B}_{2,0}$ by adjusting the currents through these coils. Unfortunately, it will be challenging to measure the spatial profile of $\mathcal{B}_{2,0}$ with the ions. Our frequency measurements in this case will give us information about $\mathcal{B}_{2,0}r_{\rm rot} \propto \mathcal{B}_{2,0}\mathcal{E}_{\rm rot}$, so it will be difficult to disentangle the information about the two fields. Because these spatial gradients do not oscillate they could be measured by inserting a magnetometer into the apparatus.

In the case that we apply $\mathcal{B}_{2,0}$ we also require $\frac{\mathcal{E}_{\text{bump}}}{\mathcal{E}_{\text{rot}}}\frac{\mathcal{B}^B_{\text{bump}}}{\mathcal{B}_{2,0}} < 2\times10^{-6}$ where $\mathcal{B}_{\text{bump}}$ is now understood to be a bump in the magnetic field gradient.

5.2.4 Other Magnetic Systematics

There are more magnetic systematics to be concerned about for generation three. For example, we only limited the $\tilde{D}$-odd cloud size systematic discussed in Subsection 3.2.3 to 3.5 μHz in generation two. This is the desired size of the statistical error bar in generation three, so the systematic effect will need to be reduced by about an order of magnitude. For a summary of all the known requirements for the magnetic fields in generation three, see Table 5.3.

Table 5.3: Known Magnetic Field Requirements for Generation Three. These limits assume $f_{\text{rot}} = 375$ kHz and $f^0 = 100$ Hz.

Limit	Section in Thesis	Comments
$\mathcal{B}_{1,\pm1} < 0.25$ mG	5.2.1.2	$\mathcal{B}_{1,\pm1} = \mathcal{B}_{\text{x}}, \mathcal{B}_{\text{y}}$
$\mathcal{B}_{1,0} < 1$ mG	5.2.1.2	$\mathcal{B}_{1,0} = \mathcal{B}_{\text{z}}$
$\mathcal{B}_{\perp}\mathcal{B}^B_{\perp} < 20$ mG^2	5.2.1.2	$\mathcal{B}_{\perp}$ is perpendicular to $\vec{\mathcal{E}}_{\text{rot}}$
$f^{BR}\mathcal{B}_{\perp} < 0.6$ mG Hz	5.2.1.2	$\mathcal{B}_{\perp}$ is perpendicular to $\vec{\mathcal{E}}_{\text{rot}}$
$\mathcal{B}_{2,m} < 0.25$ mG/cm	5.2.1.3	Assumes gen two values of $\mathcal{E}_{\text{3hxy}}$ and $\mathcal{E}_{\epsilon}$
$\mathcal{B}_{3,m} < 25$ mG/cm^2	5.2.1.3	Assumes gen two values of $\mathcal{E}_{\text{3hxy}}$ and $\mathcal{E}_{\epsilon}$
$\left(\mathcal{B}_{x\partial z} - \mathcal{B}_{y\partial z}\right)z_0 < 0.04$ mG	5.2.2	Assumes gen two values of $\mathcal{E}_{\text{3hxy}}$ and $\mathcal{E}_{\epsilon}$
$\frac{\mathcal{E}_{\text{bump}}}{\mathcal{E}_{\text{rot}}}\frac{\mathcal{B}^B_{\text{bump}}}{\mathcal{B}_{\text{rot}}} < 2\times10^{-6}$	5.2.3	
$\tilde{D}$-odd Cloud Sizes	3.2.3	See Section VI D 2 of the Systematics paper

There will likely be new magnetic systematics we will discover when we take data with higher statistical precision. We did not fully appreciate the distinction between the $\tilde{D}$-even and $\tilde{D}$-odd Zeeman shifts until we saw evidence that Zeeman shifts could have different ratios of $\frac{f^D}{f^0}$ in January 2022, months before we took the generation two dataset. It will be exciting to see what details another order of magnitude or so in precision reveal about our experiment.

Of course there can always be systematic effects, magnetic or otherwise, that we do not predict or discover in our data. This is equally true of the JILA eEDM experiment and every other precision measurement, but that doesn't help me sleep at night.

5.3 Magnetic Shielding Overview

Our group is entirely new to magnetic shielding. Fortunately, there are groups here at CU and EDM experiments around the world that have extensive experience in the subject. In this section I will compile the useful resources I have found which will hopefully serve as a useful jumping off point for future JILA EDM students.

5.3.1 Diamagnetic, Paramagnetic and Ferromagnetic Materials

To this point we have discussed the magnetic field $\vec{\mathcal{B}}$ in a vacuum. An external magnetic field will induce a magnetic response in a solid that is parameterized by its dimensionless relative magnetic permeability μ_R. The convention is to distinguish between the external magnetic field intensity $\vec{\mathcal{H}}$, which has units of Amps/meter, and the induced magnetic field inside the material $\vec{\mathcal{B}}$. These quantities are related by:

$$\vec{\mathcal{B}} = \mu_R \mu_0 \vec{\mathcal{H}} \tag{5.14}$$

Here $\mu_0 = 4\pi \times 10^{-7}$ T·m/A is the magnetic permeability of free space.

I have always found notation a bit confusing. In order to understand magnetic shielding we need to know what magnetic field will be induced inside a material (in units of Gauss or Tesla) depending on the external field in our lab (also in units of Gauss or Tesla). It is easy to imagine how the definition of $\vec{\mathcal{H}}$ would be useful in the case where one material is enclosed in another, but for our purposes it would be easier to simply use the equation $\vec{\mathcal{B}}_{\text{int}} = \mu_R \vec{\mathcal{B}}_{\text{ext}}$. In the end it is less work to use the notation in Equation 5.14 as it is ubiquitous in the literature.

Materials are classified magnetically by their value of μ_R. Diamagnetic materials are those with μ_R slightly less than one. An example is silver which has $\mu_R = 0.99998$ [71]. That means inside an external magnetic field, silver generates its own magnetic field that is 2×10^{-5} times smaller and pointing in the opposite direction as $\vec{\mathcal{B}}_{\text{ext}}$. The net magnetic field inside silver still points in the same direction as the external field but it is slightly reduced. Paramagnetic materials have μ_R slightly greater than one such as aluminum with $\mu_R = 1.00002 = 1 + 2 \times 10^{-5}$. The magnetic field inside aluminum is therefore slightly greater than the external field. Ferromagnetic materials, those with $\mu_R \gg 1$, will be the ones we use for magnetic shielding. Two commonly used materials for shielding are steel ($\mu_R \sim 2,000$) and mumetal ($\mu_R \sim 80,000$). These materials significantly amplify the external magnetic field.

An important point to make is the relative permeability μ_R of ferromagnetic materials is only constant for small values of $\mathcal{B}_{\text{ext}}$. Figure 5.6 shows the $\mathcal{B}$ vs $\mathcal{H}$ and $\mathcal{B}_{\text{ext}}$ vs $\mathcal{B}_{\text{int}}$ curves of mumetal, and the slope of these curves gives the value of μ_R. For small values of $\mathcal{B}_{\text{ext}} \lesssim 0.2$ G mumetal has a constant $\mu_R \approx 80,000$. After this value mumetal begins to saturate – the the dipole moments of almost all of the atoms in the mumetal have already aligned in the external magnetic field – and the internal magnetic field no longer increases as quickly. Once $\mathcal{B}_{\text{ext}} \gtrsim 2$ G and all of the dipoles in the mumetal have been aligned, the field can no longer be further amplified and we say that the material has been saturated. Unless otherwise mentioned, the calculations in this section will assume that the ferromagnetic materials are unsaturated and μ_R can be treated as a constant.

5.3.2 Cylindrical Shield – Transverse Shielding Factor

We can now see how ferromagnetic materials like mumetal can be used to passively shield a volume of space from an external magnetic field. We are particularly interested in cylindrical shields as they will fit nicely around the Bucket Brigade and have conveniently calculable shielding factors. The transverse shielding factor S_T is defined as the magnitude of an external magnetic field perpendicular to the length of the shield divided by the field's magnitude inside the shield.

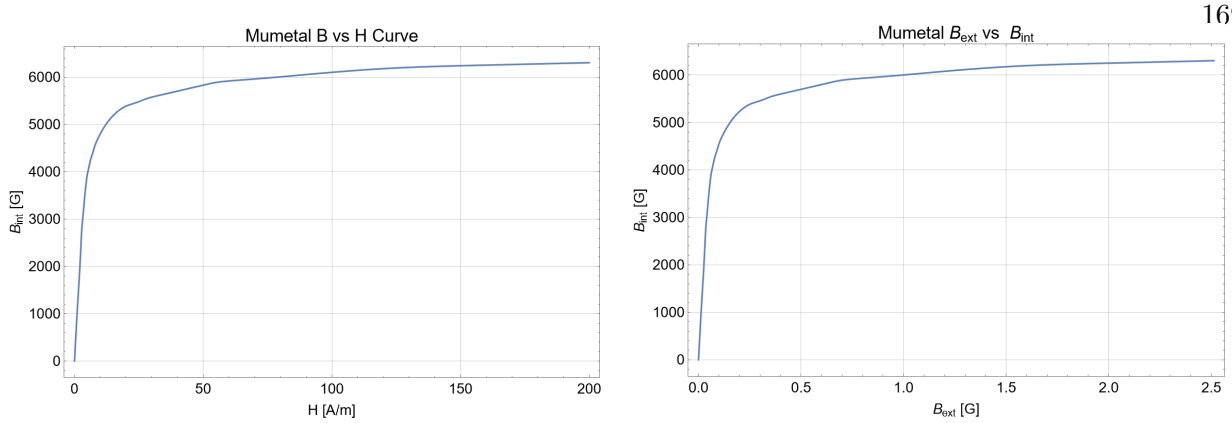

Figure 5.6: On the left is the $\mathcal{B}$ vs $\mathcal{H}$ curve for mumetal. The same information is shown, in my opinion more clearly, on the right in the $\mathcal{B}_{\text{ext}}$ vs $\mathcal{B}_{\text{int}}$ plot. The data shows that mumetal is responds linearly to an external field only up to about 0.2 Gauss. The data in these plots is from Comsol Multiphysics and is a set of discrete points connected by lines. This $\mathcal{B}$ vs $\mathcal{H}$ curve is what is used to simulate saturation effects later in this chapter.

The shield also has an axial shielding factor S_A defined the same way for magnetic fields along the shield's z-axis. In this subsection we analytically calculate S_T for an infinitely long cylindrical shield with mean radius R and thickness t, so the outer and inner radii are $R \pm \frac{t}{2}$. The situation is shown in Figure 5.7, and the derivation follows Timothy Sumner's 1979 dissertation on magnetic shielding for a neutron EDM experiment [72].[15]

We are interested in finding S_T at steady state without any currents moving around, so we can define the magnetic potential ϕ where $\vec{\mathcal{H}} = -\vec{\nabla}\phi$. Because there are no magnetic monopoles so $\vec{\nabla} \cdot \vec{\mathcal{B}} = 0$, and $\vec{\mathcal{B}} = \mu\vec{\mathcal{H}}$, we know that ϕ will satisfy Laplace's equation $\nabla^2\phi = 0$. At the boundary of two materials with different values of μ_R, there are two relevant boundary conditions to calculate the shielding factor. The component of $\vec{\mathcal{B}}$ that is normal to the boundary is continuous, and the tangential component of $\vec{\mathcal{H}}$ is continuous.[16] Because the external magnetic field is uniform, we can write the potential in all three regions of space as:

[15] While many such derivations assume that $R \gg t$, Timothy Sumner's derivation does not.

[16] $\vec{\mathcal{H}}$ is continuous as long as the surface current $\vec{K} = 0$, which we have already assumed. The general condition is $\hat{n} \times (\vec{\mathcal{H}}_2 - \vec{\mathcal{H}}_1) = \vec{K}$.

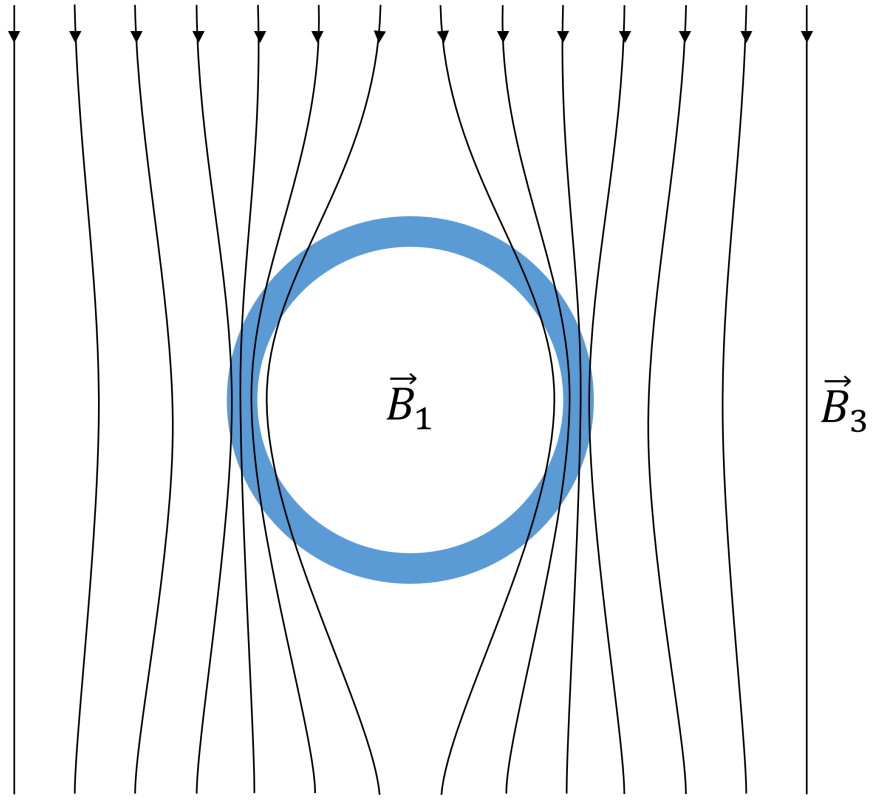

Figure 5.7: A two dimensional view of an infinitely long cylindrical magnetic shield. The space is split into regions one through three, inside the shield, the shield itself and outside the shield. There is a uniform external magnetic field $\vec{\mathcal{B}}_3$ that is transverse to the shield. The magnetic field lines bunch together inside the shield as its material has $\mu_R \gg 1$, and the internal magnetic field $\vec{\mathcal{B}}_1$ is small compared to $\vec{\mathcal{B}}_3$. The transverse shielding factor $S_T = \dfrac{\mathcal{B}_1}{\mathcal{B}_3}$ is calculated in the text.

$$\phi_k = (C_k \rho + \frac{D_k}{\rho}) \cos\theta \tag{5.15}$$

Here $k = 1, 2, 3$ for the inner, shield and outer regions respectively, and C_k and D_k are yet to be determined constants. The expression is written in cylindrical coordinates (ρ, θ, z). We can immediately determine that $D_1 = 0$ to prevent the potential from going to infinity at $\rho = 0$.

The boundary conditions set constraints on the potentials:

$$\mu_k \frac{d\phi_k}{d\rho}\bigg|_{r_{k,k+1}} = \mu_{k+1} \frac{d\phi_{k+1}}{d\rho}\bigg|_{r_{k,k+1}} \tag{5.16}$$

$$\frac{1}{r_{k,k+1}} \frac{d\phi_k}{d\theta}\bigg|_{r_{k,k+1}} = \frac{1}{r_{k,k+1}} \frac{d\phi_{k+1}}{d\theta}\bigg|_{r_{k,k+1}} \tag{5.17}$$

Here $r_{k,k+1}$ is the radius of the boundary between regions k and $k+1$. These two boundary conditions at each side of the shield provide four equations that relate C_1, C_2, C_3, D_2 and D_3. The system of equations can be solved to give the following expressions in terms of C_1:

$$C_2 = C_1 \frac{\mu_R + 1}{2\mu_R} \tag{5.18}$$

$$D_2 = C_1 \frac{(\mu_R - 1)(t - 2R)^2}{8\mu_R} \tag{5.19}$$

$$C_3 = C_1 \frac{(2R\mu_R + t)(2R + t\mu_R)}{\mu_R(2R + t)^2} \tag{5.20}$$

$$D_3 = C_1 \frac{Rt(\mu_R^2 - 1)}{2\mu_R} \tag{5.21}$$

Note that the magnetic field outside the shield goes like $C_3 - \frac{D_3}{\rho^2}$, so C_3 on its own defines the external magnetic field far away from the shield. Therefore the shielding factor is given by:

$$S_T = \frac{C_3}{C_1} = \frac{(2\mu_R R + t)(2R + \mu_R t)}{\mu_R(2R + t)^2} \tag{5.22}$$

In the limit where $R \gg t$ the transverse shielding factor simplifies to:

$$\lim_{R \gg t} S_T = 1 + \frac{(\mu_R - 1)^2 t}{2R\mu_R} \tag{5.23}$$

A good sanity check is that $S_T = 1$ when $t = 0$, as there will be no shielding if the magnetic shield is not there. This equation makes it clear why we want to make the magnetic shields out of ferromagnetic material like mumetal with $\mu_R \approx 80,000$. So long as the mumetal is not saturated, we can take the limit where $\mu_R \gg 1$ to further simplify the expression:

$$S_T \approx 1 + \frac{\mu_R t}{2R} \tag{5.24}$$

Now we have arrived at the formula for S_T that is most easily found online and in the literature. We can compare the general result in Equation 5.22 to Comsol Multiphysics simulations, as shown in Figure 5.8. The Comsol simulations were run in 2D with $\mu_R = 80,000$ and $t = 2$ mm for various values of R. The results were fit to a two parameter model $S_T = \frac{a}{R} + b$ and shows remarkable agreement with the analytically calculated shielding factor.

We can now consider how S_T changes when the cylinder has a finite length L that stretches from $z = -\frac{L}{2}$ to $\frac{L}{2}$, as shown in Figure 5.9. For $L \gg R$ we should expect that the shielding factor at $z = 0$ is unchanged, while the transverse magnetic field leaks some distance into the shield. Sumner shows this is the case by considering the general solution of the magnetic potential inside the shield [72]. The potential is given by Bessel functions of the first kind:

$$\phi = \sum_{k,n} J_n(k\rho)\left(A_k e^{kz} + B_k e^{-kz}\right)\cos(n\theta) \tag{5.25}$$

As the external magnetic field is transverse to the cylindrical shield its angular dependence is given by $\cos(\theta)$. We should expect that the solution to ϕ has the same angular dependence so we can restrict the sum to $n = 1$:

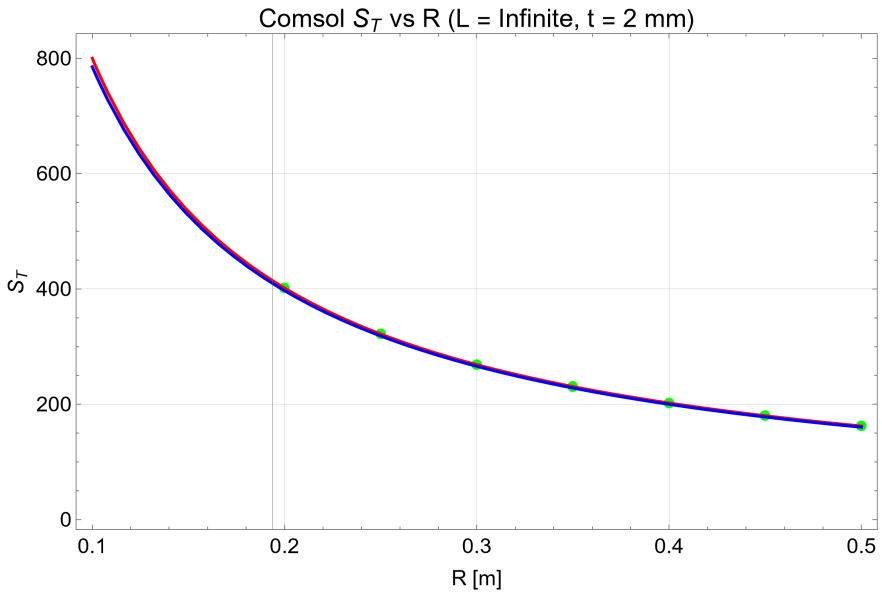

Figure 5.8: Comsol Multiphysics was used to calculate S_T for an infinitely long cylindrical shield with $\mu_R = 80,000$ and $t = 2$ mm for various values of R. The results are shown in green, which are then fit to a two parameter model $\frac{a}{R} + b$ shown in red. The prediction of Equation 5.22 is shown in blue which agrees quite nicely with the Comsol results.

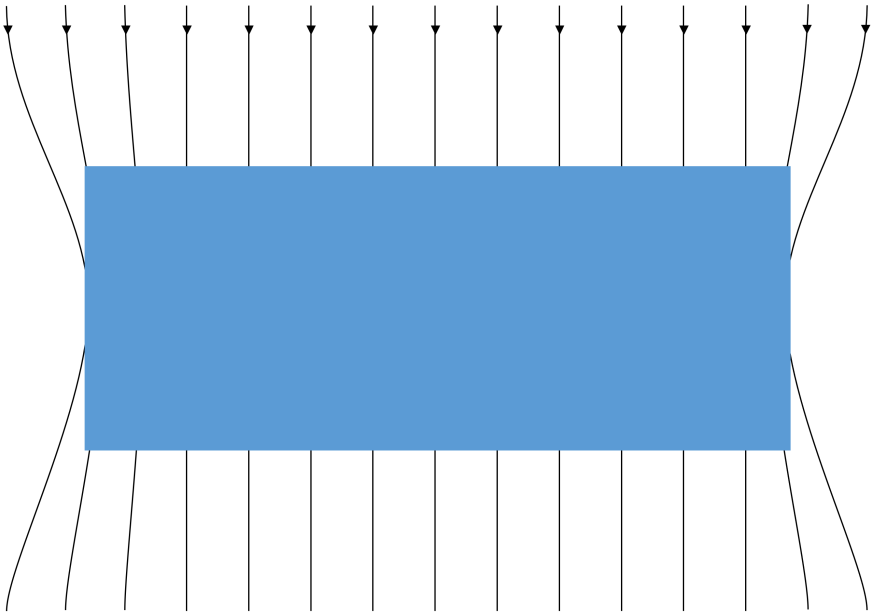

Figure 5.9: Transverse magnetic shielding with a cylinder of finite length. At the ends of the cylinder the magnetic shielding w.

$$\phi = \sum_k J_1(k\rho)\left(A_k e^{kz} + B_k e^{-kz}\right)\cos(\theta) \tag{5.26}$$

We can further restrict ϕ by noticing that the axial magnetic field at $z = 0$ must vanish by symmetry. That means that $\left.\frac{\partial \phi}{\partial z}\right|_{z=0} = 0$ which can only be achieved if $A_k = B_k$. We can therefore write ϕ as:

$$\phi = \sum_k J_1(k\rho) A_k \cosh(kz) \cos(\theta) \tag{5.27}$$

For high permeability shielding the axial and azimuthal magnetic field components must go to zero at $\rho = R$, meaning that $\left.\frac{\partial \phi}{\partial z}\right|_{\rho=R} = \left.\frac{1}{\rho}\frac{\partial \phi}{\partial \theta}\right|_{\rho=R} = 0$. This can only be true if $J_1(kR) = 0$, so we are restricted to $k = \frac{3.83}{R}, \frac{5.14}{R}, \frac{6.38}{R}$ etc. where the coefficients in the numerator are the zeros of J_1. With this restriction in place we can find what we were after originally, the transverse field within the shielded region:

$$\mathcal{B}_\rho = -\mu_0 \frac{\partial \phi}{\partial \rho} = -\mu_0 \sum_k k J_1'(k\rho) A_k \cosh(kz) \cos(\theta) \tag{5.28}$$

We are interested in how the transverse magnetic field behaves as we move from $z = \pm\frac{L}{2}$ toward $z = 0$. The argument $\cosh(kz)$ in the above equation tells us that the field will exponentially decay as we enter the shield. The smallest allowed value of k, $k = \frac{3.83}{R}$, will quickly be the largest term in the summation as we move into the magnetic shield. If we let x be the distance we move from the edge of the shield towards its center, the magnetic field decays as $e^{-3.83x/R}$. This result derived by Sumner agrees reasonably well with another source that approximates the decay as $e^{-3.5x/R}$ [73].

Note that the leaking transverse field $\mathcal{B}_\rho$ will not decay all the way to zero as we move further toward the center of the shield. Its value will asymptote toward the shielded value $\frac{\mathcal{B}_\rho(z \to \infty)}{S_T}$. In cases where L is not large enough for the field to decay below $\frac{\mathcal{B}_\rho(z \to \infty)}{S_T}$ at $z = 0$, the total transverse shielding factor at the center of the shield is given by:

$$\frac{1}{S_T^{\text{tot}}} = \frac{1}{S_T} + \frac{1}{\cosh\left(\frac{3.83L}{2R}\right)} \tag{5.29}$$

We can use this equation, as well as the analogous equation for the axial shielding factor in Subsection 5.3.3, to determine how far the shield should extend beyond the ends of the Bucket Brigade.

5.3.3 Cylindrical Shield – Axial Shielding Factor

The axial shielding factor S_A for an open cylindrical shield is, perhaps unsurprisingly, worse than its transverse shielding factor. Timothy Sumner derives this shielding factor as well, but I found it much less illuminating than his derivation of S_T. If we first ignore the effects of magnetic fields leaking into the ends of the cylinder, or take the limit $L \gg R$ and only worry about the shielding factor at the origin, we find that:

$$S_A = 1 + \frac{2K}{1 + \frac{L}{R} + \frac{\alpha L^2}{3R^2}} \frac{\mu_R t}{2R} \tag{5.30}$$

$$K = \beta - \frac{R}{L} + \frac{\beta R^3}{4L^3} + 2\alpha(I_1 - I_2) \tag{5.31}$$

$$I_1 = \ln\left(\frac{L}{R} + \sqrt{1 + \frac{L^2}{R^2}}\right) \tag{5.32}$$

$$I_2 = 2\sqrt{1 + \frac{R^2}{L^2}} - \frac{2R}{L} \tag{5.33}$$

$\alpha = 0.85$ and $\beta = 1.83$ are coefficients that Sumner determines in his thesis.

The contribution from the axial field that leaks into the ends of the shield can again be found by consider the magnetic potential ϕ written in terms of Bessel functions in Equation 5.25. This

time the external field has no angular dependence so we restrict the sum to $n = 0$. A similar argument means that the first zero of J_0 will determine the length scale for the exponential decay. We find that the axial magnetic field decays as $e^{-2.41x/R}$, which compares well to another source that approximates the decay as $e^{-2.25x/R}$. The total axial shielding factor at the center of the shield is therefore:

$$\frac{1}{S_A^{\text{tot}}} = \frac{1}{S_A} + \frac{1}{\cosh\left(\frac{2.41L}{2R}\right)} \tag{5.34}$$

We plot S_A^{tot}, the axial shielding factor at the origin, against the length of the shield in Figure 5.10. Here we use values of $R = 0.25$ m, $t = 2$ mm and $\mu_R = 80,000$. The figure also includes Comsol simulations of the axial shielding factor with the same parameters, which confirms the general behavior of Equations 5.30 and 5.34. It also verifies that for $L \gtrsim 8R$ the axial shielding scales like $\frac{1}{L}$.

This is a surprising result! It makes sense that the axial shielding is poor for $L \sim R$ because the shield is not long enough to attract the magnetic field lines away from the shielded region. But as L becomes large compared to R the axial shielding factor gets worse again. We do not have an intuitive explanation for this phenomenon but it is be important to remember when designing the shields. The axial shielding factor also gets worse with larger values of R, as shown in Figure 5.11, but that is less surprising.

5.3.4 Layers of Magnetic Shields

We can extend the transverse and axial shielding factors S_T and S_A to the case where we have multiple concentric magnetic shields with lengths L_i and radii R_i, where $i = 1$ denotes the innermost magnetic shield. To keep the expressions simple we assume they are made of the same material with magnetic permeability μ_R and thickness $t \ll R_1$, and that $L_i \gg R_i$ so we do not have to worry about field lines that enter through the ends of the shields.

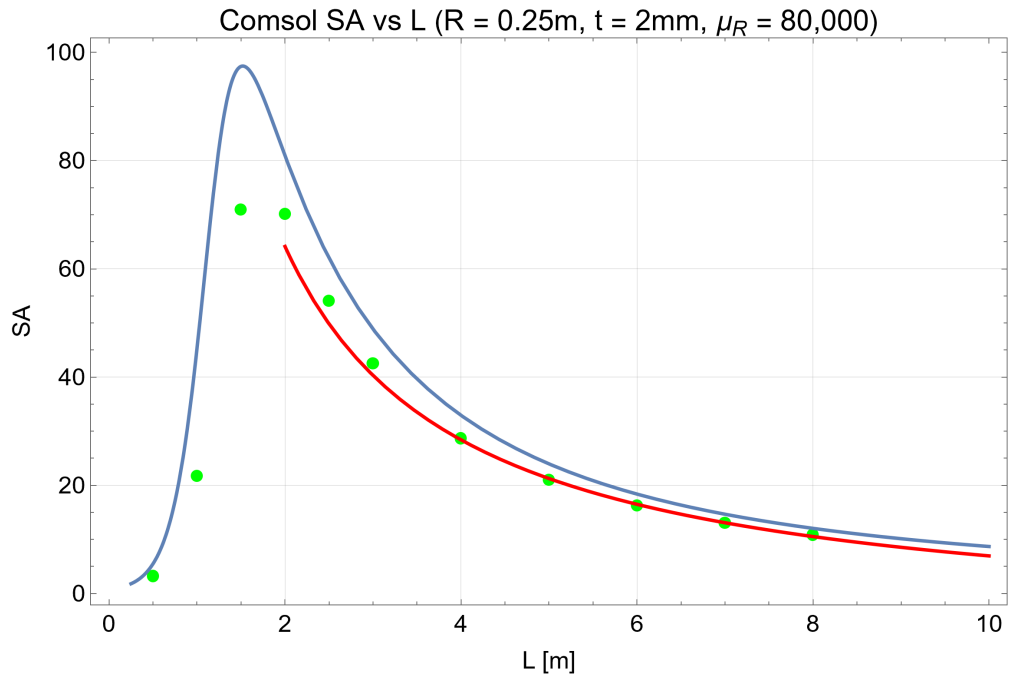

Figure 5.10: Comsol Multiphysics was used to calculate S_A for an cylindrical shield with $R = 0.25$ meters, $t = 2$ mm and $\mu_R = 80,000$ for various values of L. The results of the Comsol simulations shown in green. Comsol results with $L \geq 4$ meters are then fit to a two parameter model $\frac{a}{L} + b$. The prediction of Equation 5.30 is shown in blue, which slightly overestimates the Comsol results but has the same general behavior.

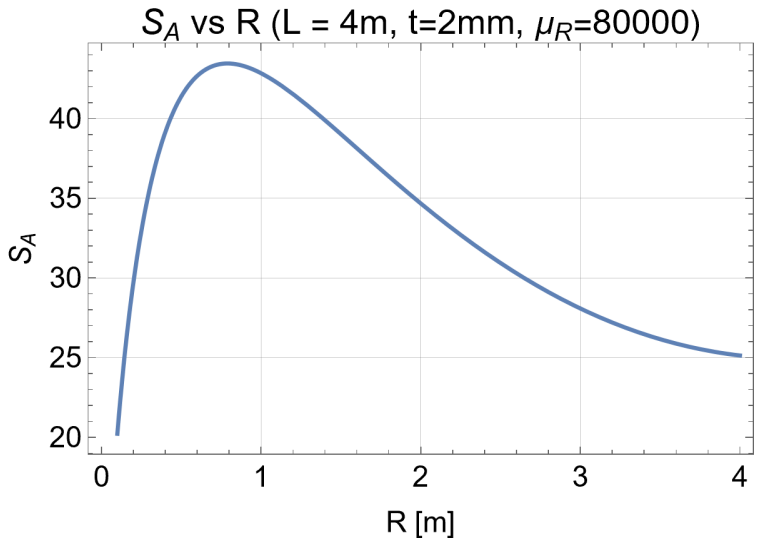

Figure 5.11: The prediction S_A vs R given by Equation 5.30. The calculation assumes $L = 4$ meters, $t = 2$ mm and $\mu_R = 80,000$.

The method in Subsection 5.3.2 where we calculated S_T via a system of equations derived from boundary conditions can be extended to the case where there are many cylindrical shields. We define $S_i^T = \dfrac{\mu_R t}{2R_i}$ to be the transverse shielding factor of a cylindrical shield, ignoring the addition of one that gives the correct answer in the limit $t \to 0$. Starting with the case of two nested shields we have:

$$\begin{aligned} S_{2\text{ nested}}^T &= 1 + S_1^T + S_2^T + S_1^T S_2^T \left(1 - \left(\frac{R_1}{R_2}\right)^2\right) \\ &= 1 + \frac{\mu_R t}{2R_1} + \frac{\mu_R t}{2R_2} + \frac{\mu_R^2 t^2}{4R_1 R_2}\left(1 - \left(\frac{R_1}{R_2}\right)^2\right) \end{aligned} \tag{5.35}$$

The total transverse magnetic shielding factor is equal to 1 plus sum of the individual shielding factors plus another term that is proportional to the product of the two shielding factors. As seen in Figure 5.8 the transverse shielding values for the individual shields with reasonable parameters will be on the order of 100, so the final term in Equation 5.35 will dominate. Importantly, this term tells us that by using two nested shields we get to multiply the individual shielding factors. If we had instead just doubled the thickness of one of our shields, by Equation 5.24 we would have only doubled the shielding factor.[17] Note that the shielding factor is maximized when $\dfrac{R_2}{R_1} = \sqrt{3}$ [73].

We can extend the expression further to a system of n cylindrically nested shields:

$$\begin{aligned} S_{n\text{ nested}}^T =& 1 + \sum_{i=1}^{n} S_i^T + \sum_{i=1}^{n-1}\sum_{j>i}^{n} S_i^T S_j^T \left(1 - \left(\frac{R_{j-1}}{R_j}\right)^2\right) \\ &+ \sum_{i=1}^{n-2}\sum_{j>i}^{n-1}\sum_{k>j}^{n} S_i^T S_j^T S_k^T \left(1 - \left(\frac{R_{j-1}}{R_j}\right)^2\right)\left(1 - \left(\frac{R_{k-1}}{R_k}\right)^2\right) + \ldots \end{aligned} \tag{5.36}$$

[17] See this article [74] for an interesting discussion of modeling magnetic shielding as an electrical circuit, which is interesting in its own right and explains why better shielding is achieved through multiple layers instead of thicker shielding.

The final term in this expression is equal to $\prod_{i=1}^{n-1} S_i^T S_n^T \left(1 - \left(\frac{R_i}{R_{i+1}}\right)^2\right)$. This term is typically the largest as it is proportional to the product of all the individual shielding factors.

We can also write down the axial shielding factor for 2 and n nested cylindrical shields. We define S_A^i to be equal to the right hand side of Equation 5.30 without the +1 and, following Sumner [72], we find:

$$S^A_{2\,\text{nested}} = 1 + S_1^A + S_2^A + S_1^A S_2^A \left(1 - \frac{L_1}{L_2}\right) \tag{5.37}$$

$$\begin{aligned} S^A_{n\,\text{nested}} =& 1 + \sum_{i=1}^{n} S_i^A + \sum_{i=1}^{n-1}\sum_{j>i}^{n} S_i^A S_j^A \left(1 - \frac{L_{j-1}}{L_j}\right) \\ &+ \sum_{i=1}^{n-2}\sum_{j>i}^{n-1}\sum_{k>j}^{n} S_i^T S_j^T S_k^T \left(1 - \frac{L_{j-1}}{L_j}\right)\left(1 - \frac{L_{k-1}}{L_k}\right) + ... \end{aligned} \tag{5.38}$$

For the transverse shielding factors we are guaranteed to get terms that are proportional to products of the individual shielding factors because $R_{i+1} > R_i$ by definition. On the other hand, if the cylindrical shields all have the same length the net axial shielding factor will only be the sum of the individual axial shielding factors, as can be seen in Figure 5.12. This tells us that we want our nested shields to grow in both radius and length as we move from the innermost shield outward.

5.3.5 Shielding Induced Gradients

Up to this point we have calculated shielding factors for axial and transverse magnetic fields. These are important because they will inform us what sort of shields allow us to reduce Earth's 500 mG field to $\lesssim 0.25$ mG which we require, as discussed in Subsection 5.2.1. It is equally important that we keep the magnetic field gradients to be $\lesssim 0.25$ mG/cm.

We can use Comsol to simulate the magnetic field gradients experienced by the ions due to shielded uniform transverse and axial magnetic fields. We define these "gradient shielding factors"

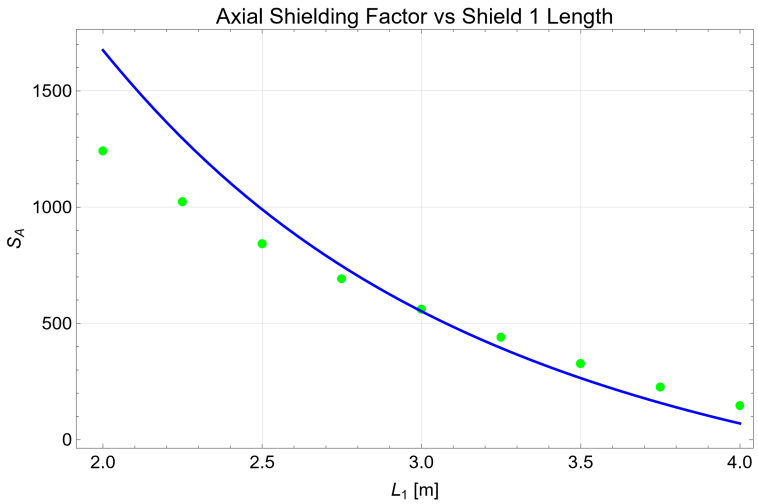

Figure 5.12: S_A when there are two layers of magnetic shielding. The inner shield has $R_1 = 0.25$ m, $t = 2$ mm, $\mu_R = 80,000$ and L_1 is varied. The outer shield has $R_2 = 0.25 \times \sqrt{3}$ m, $L_2 = 4$ m, $t = 2$ mm and $\mu_R = 80,000$. The plot shows the prediction of Equation 5.37 in blue and the results from Comsol simulations in green. Comsol verifies that the shielding factor grows as L_1 gets shorter than L_2.

to be equal to $S_A^{\text{grad}} = \dfrac{\mathcal{B}_z^{\text{ext}}}{\dfrac{\partial \mathcal{B}_z^{\text{int}}}{\partial z}}$ and $S_T^{\text{grad}} = \dfrac{\mathcal{B}_x^{\text{ext}}}{\dfrac{\partial \mathcal{B}_x^{\text{int}}}{\partial x}} = \dfrac{\mathcal{B}_y^{\text{ext}}}{\dfrac{\partial \mathcal{B}_y^{\text{int}}}{\partial y}}$, which have units of distance. We are interested in calculating these gradient shielding factors far away from the edges of the shields as we have already seen how transverse and axial fields decay as they enter the openings of the shields in Subsections 5.3.2 and 5.3.3 respectively.

A single layer of mumetal shielding with $R = 25$ cm, $L = 4$ m, $t = 2$ mm and $\mu_0 = 80,000$ has a axial shielding factor of ~ 30. Figure 5.13 shows the magnetic field as a function of z at $\rho = 0$. We can see that the magnetic field gradient is ~ 0.1 mG/cm over the central meter of the region with an external field of 100 mG, giving us $S_A^{\text{grad}} \sim 1000$ cm. Because the axial shielding function in Equation 5.30 is fairly complicated this relationship should be checked for different parameters R, L and t, but $S_A^{\text{grad}} \sim 1000$ cm should provide a reasonable order of magnitude estimate.

With the finest mesh and highest precision I was able to manage, Comsol was still unable to resolve the residual magnetic field gradients for transverse fields in an infinitely long magnetic shield. We could conclude that $S_T^{\text{grad}} \gg 1000$ cm, but in practice the dominant transverse gradients

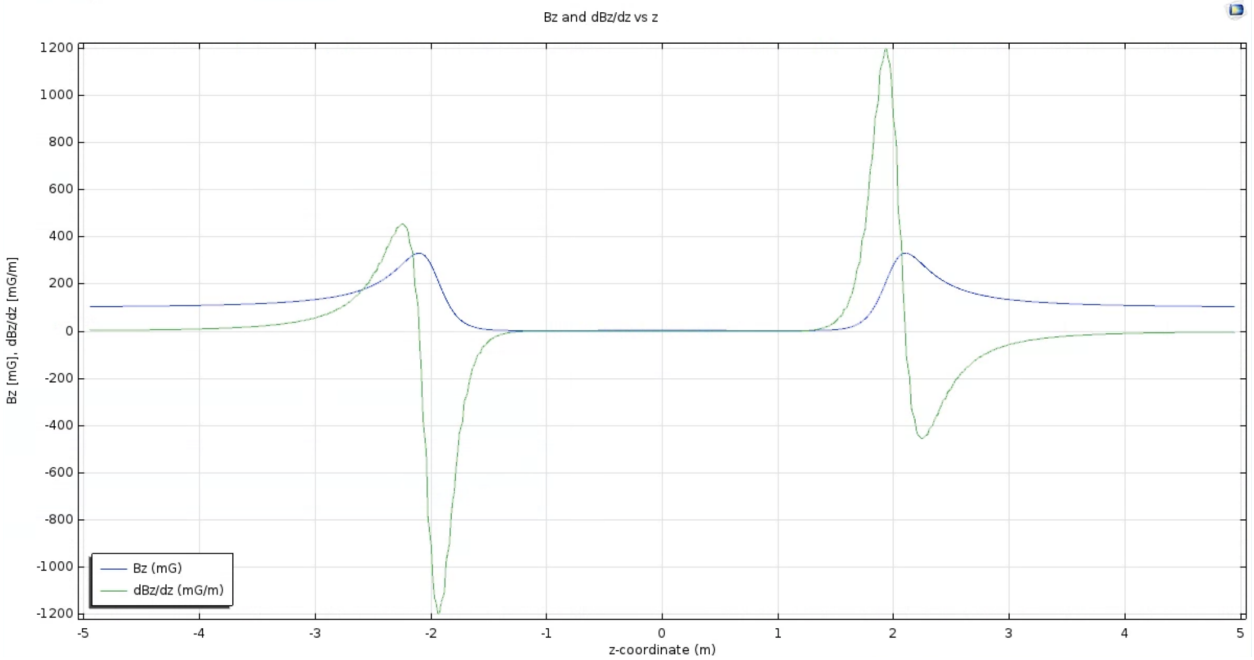

(a) Full Plot

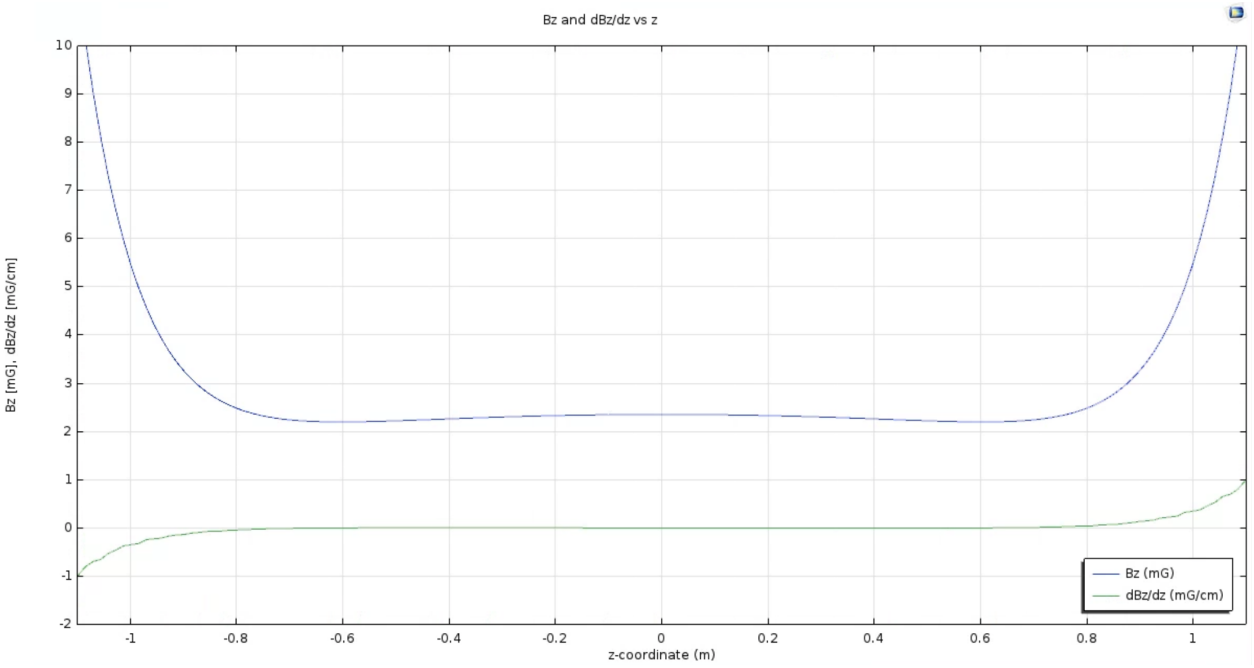

(b) Zoomed In

Figure 5.13: A Comsol simulation of the magnetic field vs z along the center ($\rho = 0$) of a single mumetal shield with $R = 25$ cm, $L = 4$ m, $t = 2$ mm and $\mu_0 = 80,000$. (a) The shield is centered at $z = 0$ and is in a background magnetic field of 100 mG along the z-axis. The blue trace shows how the magnetic field has a slight increase from 100 mG and then falls as it enters the magnetic shield at $z = \pm 2$. (b) The axial magnetic field has decayed to $\lesssim 5$ mG over the region between $z = \pm 1$ where the ions travel, and the gradient is $\lesssim 0.25$ mG/cm over this region as well.

will likely be caused by magnetized regions of the innermost magnetic shield. The consequences of these regions and how to minimize them are discussed in Subsection 5.3.7.

Fortunately, both external transverse and axial magnetic fields do not directly induce worryingly large magnetic field gradients inside the magnetic shielding. In the case where there is an external magnetic field gradient, the transverse and axial shielding factors are higher than those for uniform fields [75].

5.3.6 Seams and Holes

Up until now we have assumed that our magnetic shields will be perfect cylinders. This will not be the case for two reasons. The first is that our cylinders will need holes to let laser light and various other parts of the apparatus through. The second is that mumetal cylinders with a $R \sim 0.5$ meters and $L \sim 4$ meters are hard to make, ship and install around our apparatus. Instead each cylinder will be made of two half cylinders, or "clam-shells," that attach together at a seam. In this subsection I will address each of these imperfections.

We can approximate a hole in a magnetic shield as a magnetic dipole, so long as its diameter d is small compared to the shield's characteristic lengths L and R [73].[18] We can estimate the magnitude of the dipole to be $\mu_{\text{hole}} \approx \mathcal{B}_{\text{ext}} \frac{4\pi}{3\mu_0} d^3$. This will cause a magnetic field and magnetic field gradient at the center of the cylinder, where the ions live. From dimensional analysis, the magnitudes of the magnetic field and its gradient will approximately be $\frac{\mu_0}{4\pi}\frac{3\mu_{\text{hole}}}{R^3} \approx \frac{d^3}{R^3}\mathcal{B}_{\text{ext}}$ and $\frac{\mu_0}{4\pi}\frac{12\mu_{\text{hole}}}{R^4} \approx 4\frac{d^3}{R^4}\mathcal{B}_{\text{ext}}$ respectively.

If we just had one shield with $R = 25$ cm and did not reduce the background magnetic field from 500 mG, we would require any holes to have $d < 2.0$ cm and $d < 3.6$ in order to keep the magnetic field and its gradient less than 0.25 mG and 0.25 mG/cm, respectively. As discussed in

[18] We can think of the shield as a bunch of magnetic dipoles that conspire together to reduce the magnetic field in the shielded volume. A hole in the shield is equivalent to adding a magnetic dipoles pointing in the opposite direction in the same position as the hole.

Sections 5.4 and 5.5 we plan on using coils to reduce the background field to $\lesssim 100$ mG and will have multiple layers of shielding. With these precautions in place, holes in the shields will likely not be a problem. Even so, it would be good to check this via simulations before building a finalized design.[19]

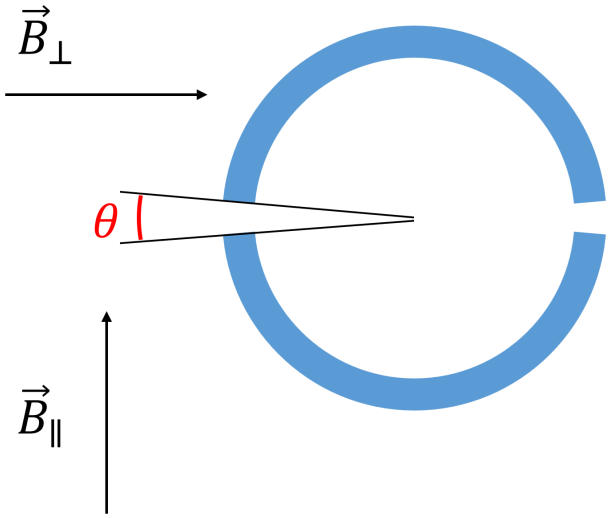

Figure 5.14: It is possible that there is an opening with angle θ between the two halves of our magnetic shields. This could reduce the parallel and perpendicular shielding factors for the two types of transverse magnetic fields shown in the image.

The other problem, that our cylinders will be made of two halves clamped together, could be more significant.[20] Suppose that the two halves of the shields do not quite meet each other so there is an opening with angle θ on both sides of the shield, as shown in Figure 5.14. This opening breaks the symmetry between magnetic fields along the x and y axes, which so far we have lumped together when calculating S_T. We now need to find both the parallel and perpendicular S_T values for the transverse magnetic field that are parallel and perpendicular to the opening.

We can see the calculated parallel and perpendicular transverse shielding factors as a function

[19] If holes prove to be a problem, the penetrating magnetic fields can be minimized with cylindrical ferromagnetic collars mounted over the holes [73]. See the cited article for more details.

[20] The Imperial College eEDM team ran into this issue when they first built their magnetic shields. They have since fixed the problem, and are good people to talk to if we have further questions.

of θ in Figure 5.15. Shields with an opening are still reasonably good at shielding transverse magnetic fields that are perpendicular to the gap for small values of θ, but are horrendous at shielding parallel transverse magnetic fields. We can mitigate this problem by 1) having the seam of subsequent layers of magnetic shielding be rotated and 2) ensuring the shield halves overlap one another instead of just meeting at the seems.

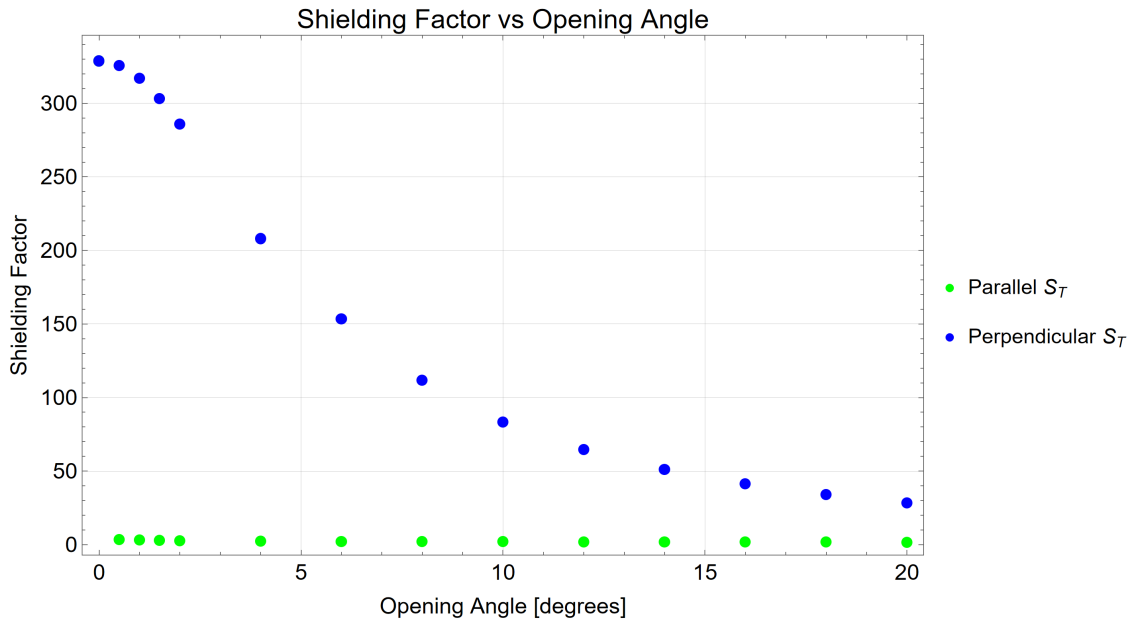

Figure 5.15: Transverse shielding factors calculated in Comsol for an infinitely long single shield with $R = 0.25$ m, $t = 2$ mm, and $\mu_R = 80,000$. The opening angle, defined in Figure 5.14, is varied between 0 and 20 degrees. Perpendicular magnetic fields are still shielded reasonably well with small opening angles, but S_T drops to about 3 for parallel magnetic fields at an opening angle of just 0.25°.

Say that the two halves of the shield overlap one another by 10 degrees but there is a small gap between the pieces of mumetal. How will the shielding factor change as a function of distance between the two shields? Figure 5.16 shows that, again, the parallel shielding factor falls rapidly according to simulations. While parallel S_T is over 300 for our expected parameters when the shield halves touch, it drops to about 40 if the distance is just 0.5 mm.

The discussion so far about gaps between the shields has avoided magnetic field gradients. As a general rule, when the parallel S_T is far below its intended value ~ 300 in Figures 5.15 and

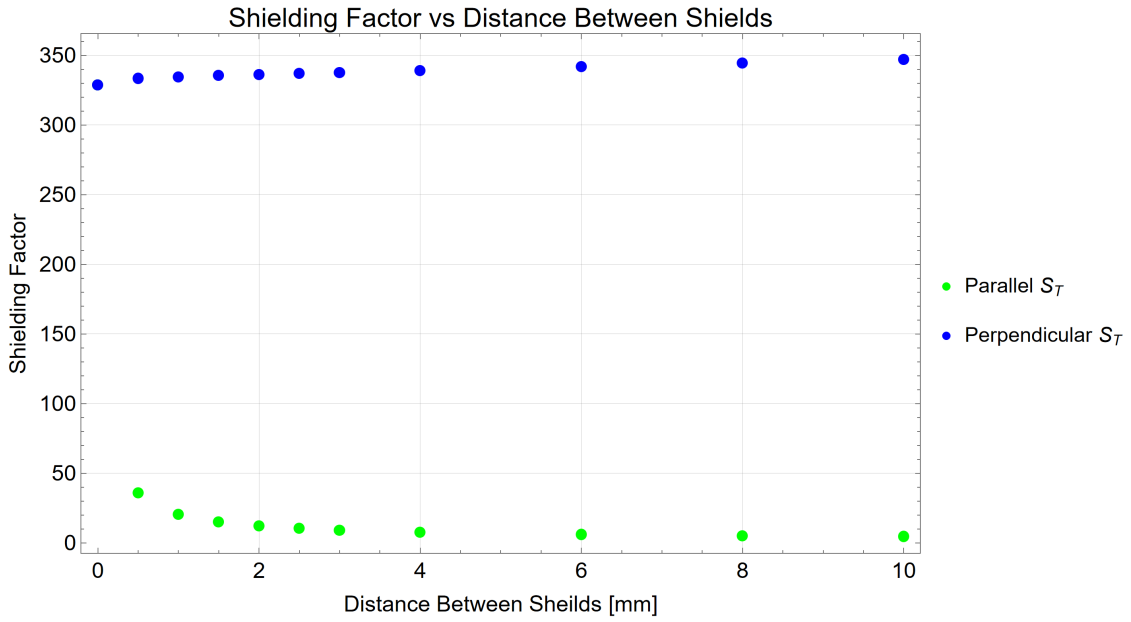

Figure 5.16: Transverse shielding factors calculated in Comsol for an infinitely long single shield with $R = 0.25$ m, $t = 2$ mm, and $\mu_R = 80,000$. The shields are overlapped by $\theta = 10°$. The gap between the shields is varied between 0 and 10 mm. Surprisingly, perpendicular magnetic fields are shielded better with a small gap between the shields. However, parallel magnetic fields can find their way through a small gap even if the shields are overlapped.

5.16, simulations show that the magnetic field gradients that leak into the center of the shield are unacceptably large as well. Because the gradients are linked to whether or not S_T is acceptably large along both the parallel and perpendicular axes, this does not need to be treated as a separate issue.

5.3.7 Degaussing

As mentioned in Subsection 5.3.5, improperly magnetized parts of the innermost shield can cause magnetic fields and gradients at the position of the ions. Highly ferromagnetic materials like mumetal are magnetically fragile, standard handling and assembly of the shields can result in magnetized regions. Fortunately, there is a standard procedure known as degaussing that can reduce the residual magnetic fields to well below our required sensitivity [73].

The idea of degaussing is to apply an AC magnetic field that is originally large enough to

saturate the shield (~ 1 G for mumetal) and then ramp the AC field to zero. If done properly, the magnetization of the shield will follow the applied magnetic field to zero, leaving the shield in its best state to have the theoretically predicted shielding factors.

The theory behind degaussing is explained well in the first two sections of [76],[21] and Zach Lasner gives a detailed explanation of how it was implemented in the ACME II experiment in section 5.2 his thesis [77]. ACME II required five(!) layers of mumetal magnetic shielding for their eEDM result. While we have not yet degaussed magnetic shields in the JILA EDM experiment, fortunately we do not need to reinvent the wheel.[22]

5.4 Magnetic Shield Design – Plan E

Now that I have introduced the generation three experiment (Section 5.1), covered its magnetic systematics (Section 5.2) and described magnetic shielding (Section 5.3), I will now outline our designs for the magnetic shields. The shielding requirements will depend on if we choose plan A or E. Shielding is more complicated if we choose plan A which requires $\mathcal{B}_{2,0} \sim 4$ G/m to generate the ~ 100 Hz f^0. This magnetic field would likely saturate the inner layer of magnetic shielding, complicating matters. Magnetic shielding with plan A will be discussed in Section 5.5.

Plan E, where we generate $f^0 \sim 100$ Hz by applying a 1.6 mG magnetic field that rotates at f_{rot}, poses no risk of saturating the shields. With this plan we only have to worry about the lab magnetic field saturating the shields. Using the $\mathcal{B}$ vs $\mathcal{H}$ curve in Figure 5.6, we can use Comsol to calculate the transverse and axial shielding factors for a single shield as a function of the external magnetic field. The results of these simulations are shown in Figure 5.17, which show that the S_A starts to drop at ~ 0.5 Gauss while S_T remains constant until almost 5 Gauss. The important conclusion to draw is that the calculated shielding factors are on the edge of being effected by

[21] The paper [76] explains that degaussing was invented out of necessity – magnetized submarines made easy targets in WWII.

[22] Future JILA EDM graduate students should be able to find all of the information they need in the three citations of this subsection.

saturation effects from Earth's magnetic field ~ 0.5 G.

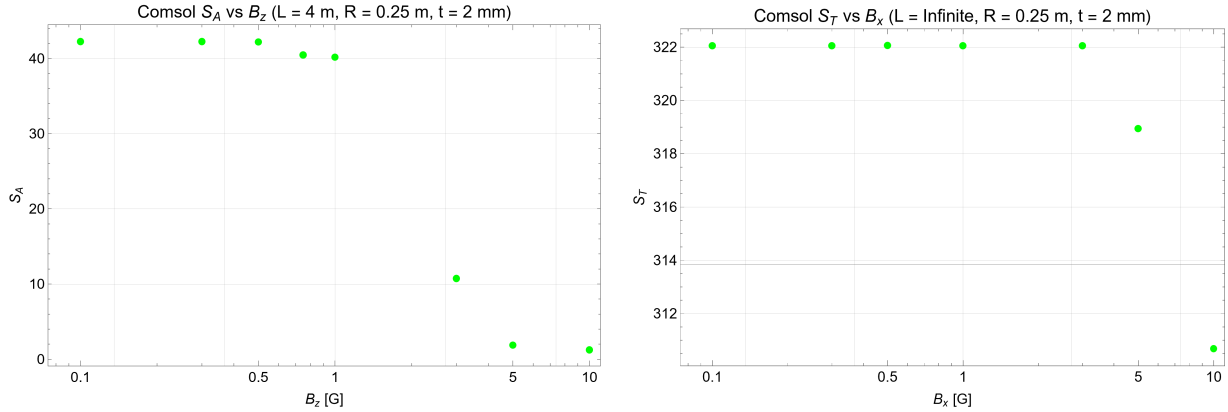

Figure 5.17: Comsol simulations of axial and transverse shielding factors vs applied external magnetic fields. The shield has $R = 0.25$ m, $t = 2$ mm and the $\mathcal{B}$ vs $\mathcal{H}$ curve defined in Figure 5.6. S_A is calculated with $L = 4$ m, while S_T is calculated assuming $L \gg R$.

In order to be confident that our outermost magnetic shield is not saturated we will build pairs of lab-scale x, y and z coils to reduce the magnetic field around our apparatus. This will be similar to the x, y and z coils that surrounded the generation two ion trap which brought the magnetic field to ~ 10 mG in all directions. In generation three these coils, and the volume of space they enclose, will be much larger. This sort of lab-scale shimming has been done at Nick Hutzler's lab at Caltech, where 6 ft x 7 ft x 8 ft coils reduce the ~ 420 mG background field to $\lesssim 10$ mG within ~ 15 cm from the center of the coils [78].

Our shields will a few meters long to enclose the ~ 2 meter long bucket brigade, so we want to reduce the magnetic field over length scales that are an order of magnitude larger. This would be more challenging, except that we only want the field to be $\lesssim 100$ mG. This is enough to prevent the mumetal from saturating and will relax our required shielding factors by a factor of ~ 5. With an ambient magnetic field is ~ 100 mG, we need $S_A > 100$ and $S_T > 400$ to meet the requirements spelled out in Table 5.3. To be conservative, and because magnetic shielding is notoriously finicky to implement properly, we will design the shields to have $S_A > 1000$ and $S_T > 4000$. This will also make imperfections from seams and holes in the shields discussed in Subsection 5.3.6 not as

worrisome.

There are a number of constraints on the parameters of our shields. First, the curtained off section of our lab that contains the apparatus and lasers is about 6.2 meters long. To leave room for students and postdocs to walk around the magnetic shields we would like the length of our outermost and longest shield to be no more than 5 meters. The radius of our outermost shield would ideally be smaller than one meter so there is room for the optics, electronics and everything else that needs to be around the apparatus. On the other hand, we cannot make our innermost magnetic shield too small. The innermost shield must be longer than the two or three meter long Bucket Brigade or else there will be large magnetic gradients where the ions are coherently evolving. Additionally, the innermost shield's radius must fit around the apparatus and must be large enough that holes and imperfectly degaussed regions of the shield are not problematic.

To satisfy all of these constraints, I propose that we have three layers of mumetal shielding with $t = 2$ mm.[23] They will have $R_1 = 0.25$ m, $R_2 = 0.25 \times \sqrt{3} = 0.433$ m, $R_3 = 0.75$ m, $L_1 = 3.5$ m, $L_2 = 4$ m and $L_3 = 4.5$ m. These magnetic shields meet our practical constraints and shielding requirements. Figure 5.18 shows the axial magnetic field along $\rho = 0$ in an external magnetic field $\mathcal{B}_z = 100$ mG. The magnetic field over the central two meters is ~ 0.1 mG meaning that $S_A \sim 1000$. Additionally, the magnetic field gradient $\frac{\partial \mathcal{B}_z}{\partial z} \lesssim 0.01$ mG/cm for the central 2 meters, comfortably below the required 0.25 mG/cm limit.

The same simulation that produced Figure 5.18 tells us that the magnitude of the gradient peaks at about 3 mG/cm at $z = \pm 2$ meters, at the openings of the intermediate shield. The magnitude of the magnetic field peaks close to 200 mG at $z = \pm 2.5$ meters, just outside the opening of the largest shield. While the axial magnetic field and its gradient are comfortably small at $z = \pm 1$ meter, they are both too large at $z = \pm 1.5$ meters. This means that if we want to

[23] This is a standard thickness for mumetal shields. Thicker shields will be more expensive and heavier, but will improve S_A and S_T which are proportional to t.

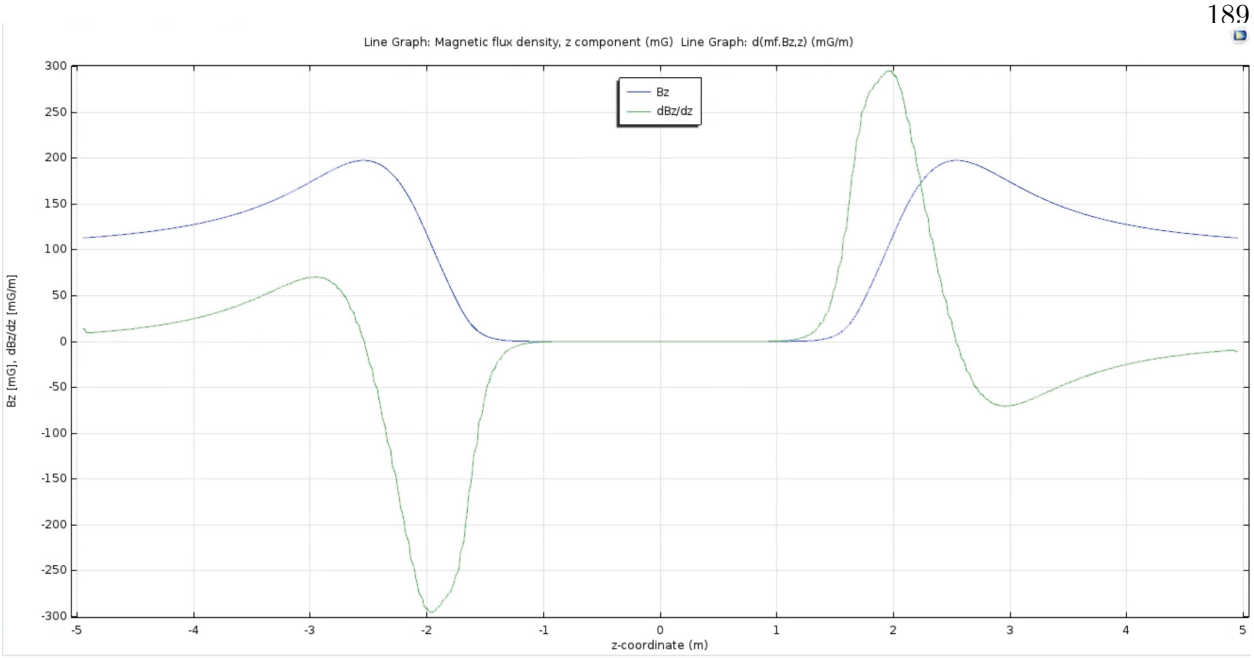

(a) Full Plot

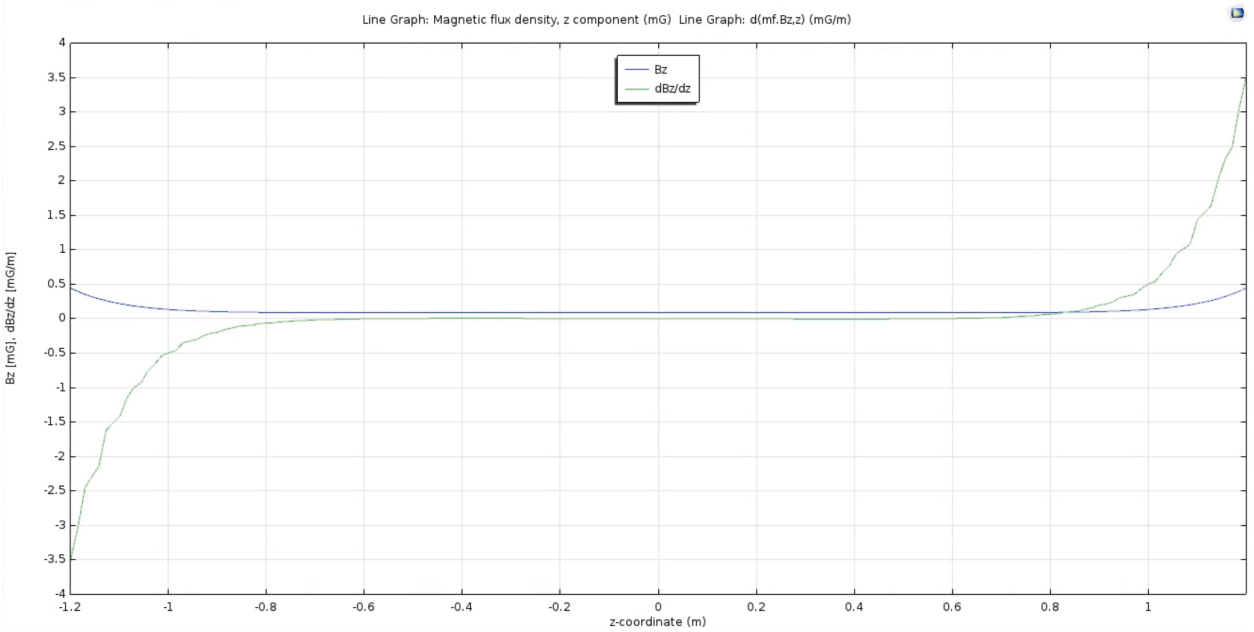

(b) Zoomed In

Figure 5.18: The axial magnetic field and its gradient in three layers of magnetic shielding designed for plan E as described in the text. The external magnetic field is $\mathcal{B}_z = 100$ mG, and we can see that $S_A > 1000$. The axial magnetic gradient is much smaller than the 0.25 mG/cm that we require.

lengthen the Bucket Brigade, we will need shields with lengths approaching the 6.2 meters of space we currently have.

This configuration of three shields works for the axial field, but what about the transverse field? According to Comsol, $S_T = 3.1 \times 10^6$, so a 100 mG external transverse magnetic field will result in a negligible ~ 33 nG magnetic field far from the openings of the shields. As discussed in Subsection 5.3.2, transverse magnetic fields decay faster than axial magnetic fields as a function of distance from the ends of the shield. If the shields work as advertised, transverse fields and gradients will not be a problem.

What if we cannot completely remove the issue of transverse magnetic fields leaking through the seams? We can combat this issue by rotating the seam locations in each shielding layer by 45 degrees, as shown in Figure 5.19. We assume that the layers of the shield are $\theta = 10$ degrees overlapped but have a 2 mm gap between layers. Note that Figure 5.16 tells us that the shielding factor for magnetic fields parallel to the seam is only 12 in this case instead of ~ 320 if there were no seam. The net S_T in this configuration depends on the orientation of the external transverse magnetic field, but $S_T \gtrsim 5,000$ in all cases. This strategy of rotating the seams for each layer of magnetic shielding should mitigate the issue.

We have not settled on the number or size of holes needed in the magnetic shields. When that has been decided, these simulations should be revisited to determine if the holes will cause an issue for the magnetic shielding. As long as the holes are not a problem, this geometry should give shielding factors that are 10 times larger than we need and stomp out the magnetic field gradients to a comfortable level.

5.5 Magnetic Shield Design – Plan A

Kia Boon Ng discusses two ways to implement plan A in his thesis [4]. The first option is to apply a magnetic field gradient $\mathcal{B}_{2,0} \sim 4$ G/m that has the opposite sign for every bucket of ions, as

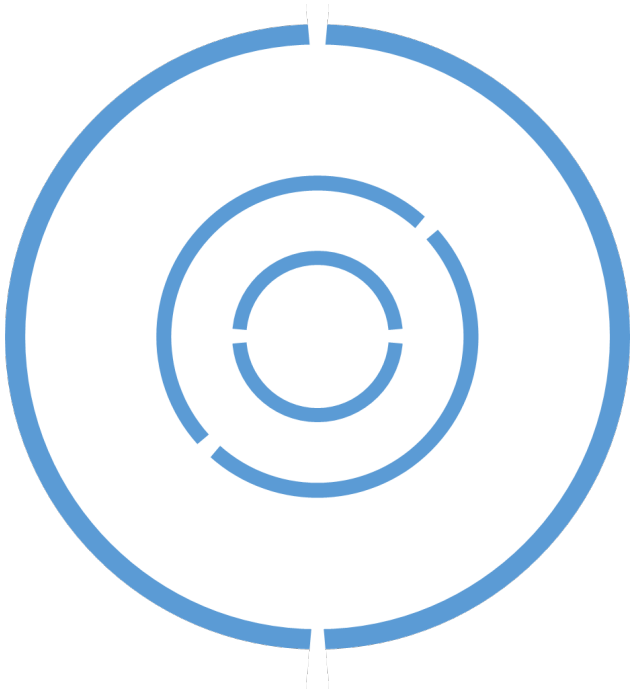

Figure 5.19: A schematic of the seams in three layers of concentric magnetic shielding. Each magnetic shield will be made of two half cylinders that are attached together. The gaps visible in the shields indicate the location of the seams, but the layers will have ~ 10 degree overlap at these spots. This diagram shows the optimal location of their seams to keep $S_T \gtrsim 5000$ for magnetic fields along x and y, given the shielding parameters proposed in Section 5.4, 10 degrees of layer overlap and 2 mm gaps between the layers. S_T will be larger if the gaps are smaller than 2mm.

shown in Figure 5.20. The main difficulty with this approach is that, in order to have a coherence time $\tau \gtrsim 20$ seconds, we have the magnetic uniformity requirement $|\frac{\partial^2 \vec{\mathcal{B}}_{2,0}}{\partial z^2}| \lesssim 12.5$ G/m^3.[24] The buckets of ions will likely be spaced ~ 30 cm apart from one another, and the magnetic field gradient needs to flip sign over that distance. Doing so while keeping $\frac{\partial^2 \vec{\mathcal{B}}_{2,0}}{\partial z^2} \lesssim 12.5$ G/m^3 at the bucket locations with a few coils seems challenging, which is discussed in Section 8.2.2.2 of Kia Boon Ng's thesis [4]. The magnetic shielding for this version of plan A is the same as plan E as discussed in the previous section.

[24] This requirement assumes that ions maintain their secular amplitude for their entire coherence time. If this were the case and $\frac{\partial^2 \vec{\mathcal{B}}_{2,0}}{\partial z^2} \neq 0$ G/m^3, molecules with large secular amplitude would have a larger frequency than molecules with a small secular amplitude. If the gradient is larger than 12.5 G/m^3, the two sets of molecules will dephase after 20 seconds. This assumption will not hold if ion-ion collisions change the secular amplitude of the ions involved. These collisions do take place but are difficult to characterize, so the 12.5 G/m^3 requirement is conservative.

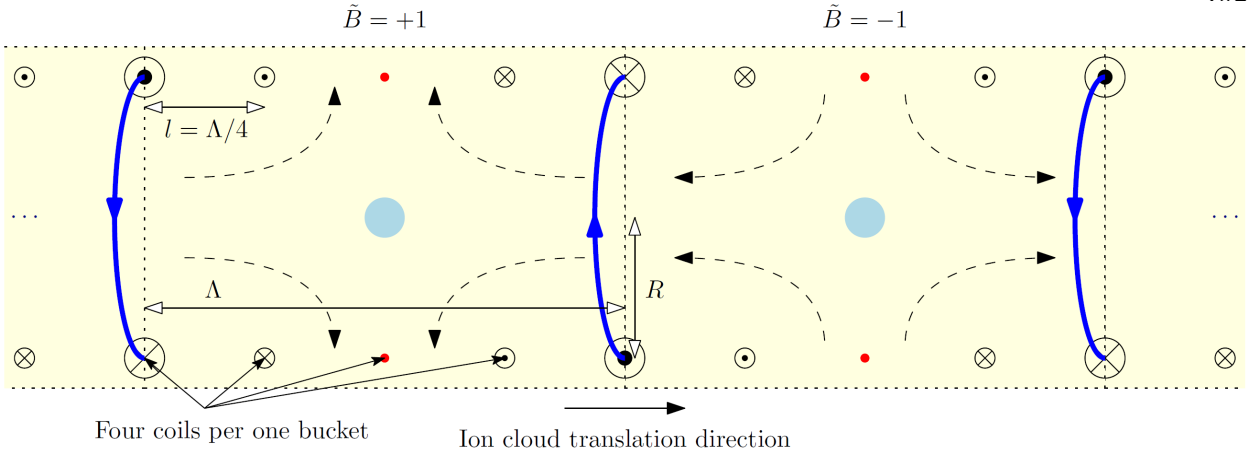

Figure 5.20: A schematic depicting how we can implement plan A so $\tilde{B}$ changes sign between every bucket. Clouds of ions are shown in blue, which are spaced by a distance Λ. The vertical dots lines are visual aids which indicate the boundary between buckets. There are four coils with radius R for every bucket with currents that drive the magnetic field gradients $\mathcal{B}_{2,0}$. The magnetic field is indicated by the dashed lines that end in arrows. As the ions move left to right, the currents through each coil change to keep the magnetic field gradient a constant magnitude at the bucket locations. This image is from Kia Boon Ng's thesis [4].

The simpler option to meet the magnetic field uniformity requirement is to apply $\mathcal{B}_{2,0} \sim 4$ G/m over the entire Bucket Brigade. The magnetic field gradient is defined as $\vec{\mathcal{B}}_{2,0} = \mathcal{B}_{2,0}\big(-\vec{x} - \vec{y} + 2\vec{z}\big)$, so this corresponds to a ~ 8 G/m magnetic field gradient along the 2 meter long z-axis. While it will be easier to make the magnetic gradient uniform, the challenge is that this field will saturate the innermost magnetic shield.

We can generate $\mathcal{B}_{2,0} \sim 4$ G/m with $\dfrac{\partial^2 \vec{\mathcal{B}}_{2,0}}{\partial z^2} \sim 8.3$ G/m^3 with 32 coil pairs of radius 5.25 inches, with locations and currents shown in Tables 5.4 and 5.5. These coil positions and currents were found numerically to minimize $\dfrac{\partial^2 \vec{\mathcal{B}}_{2,0}}{\partial z^2}$ and keep $\mathcal{B}_{2,0} \sim 4$ G/m over the two meter long bucket brigade, with the constraint that the coils must be evenly spaced.[25] The magnetic field created by these coils along $\rho = 0$, as well as its first and third order gradients, are plotted in Figure 5.21. We could generate a magnetic field that meets these requirements with fewer coil pairs if we increase the coils' radii. However, we want the coils to be as small as possible to minimize the magnetic

[25] Kia Boon Ng mentions in Section 8.2.2.3 of his thesis that the homogeneity of $\mathcal{B}_{2,0}$ can be controlled with "some numerical modeling" [4]. This result is one possible solution.

field at the innermost shield. The vacuum chamber containing the Bucket Brigade will have a 5 inch radius, so a radius of 5.25 inches is as small as the coils can be unless we put them in the vacuum chamber which is already crowded with electronics [3].

Table 5.4: Coil Positions and Currents to generate uniform $\mathcal{B}_{2,0} \sim 4$ G/m, Part 1

Coil Pair Number	Position (cm)	Current (Amp Turns)
1	±2.698	±0.937
2	±8.095	±2.810
3	±13.492	±4.683
4	±18.889	±6.557
5	±24.286	±8.431
6	±29.623	±10.306
7	±35.079	±12.181
8	±40.476	±14.057
9	±45.873	±15.933
10	±51.270	±17.813
11	±56.667	±19.690
12	±62.064	±21.575
13	±67.460	±23.453
14	±72.857	±25.347
15	±78.254	±27.223
16	±83.651	±29.136

The magnetic field generated by these coils along $\rho = 0$ is shown in Figure 5.22 with and without the three layers of magnetic shielding discussed in Section 5.4. We can see that the shields

Table 5.5: Coil Positions and Currents to generate uniform $\mathcal{B}_{2,0} \sim 4$ G/m, Part 2

Coil Pair Number	Position (cm)	Current (Amp Turns)
17	±89.048	±30.996
18	±94.444	±32.974
19	±99.841	±34.713
20	±105.238	±36.962
21	±110.635	±38.879
22	±116.032	±40.603
23	±121.429	±41.864
24	±126.825	±42.812
25	±132.222	±46.335
26	±137.619	±46.567
27	±143.016	±49.680
28	±148.413	±50.585
29	±153.810	±52.760
30	±159.206	±53.621
31	±164.603	±156.333
32	±170.000	±91.189

slightly increase the slope from 8.04 G/m to 8.11 G/m, a phenomenon explained in [75]. Since the precise values of $\mathcal{B}_{2,0}$ and f^0 are not particularly important for our experiment, this 0.9% change will not be a problem.

Figure 5.23 shows the magnetic field without magnetic shielding at $\rho = 0.25$ meters, the

radius of the innermost magnetic shield discussed in Section 5.4. This plot clearly shows that the innermost shield, which is 3.5 meters long and stretches between $z = \pm 1.75$ meters in the figure, will saturated towards its ends due to the magnetic field generated by the coils. This should make the shield less effective at reducing the background magnetic field and potentially allow large systematics.

The safest approach is to assume the innermost shield does not shield the external field at all. Its role would be to protect the remaining shields from the magnetic field generated by the coils. As we see in Table 5.5, the outermost coils have the largest number of amp turns and are $\sim \pm 1.65$ meters from the center of the Bucket Brigade. If we keep the radius of the inner shield the same at $R_1 = 0.25$ meters and increase its length slightly to $L_1 = 4$ meters to better enclose the coils, the magnetic field just outside this shield at $\rho = 0.3$ meters will peak at about 60 mG. This means that we could have similar total magnetic shielding to plan E with four layers. These layers would all have $t = 2$ mm, with $R_1 = 0.25$ meters, $R_2 = 0.3$ meters, $R_3 = 0.3 \times \sqrt{3} = 0.520$ meters, $R_4 = 0.9$ meters, $L_1 = 4$ meters, $L_2 = 4$ meters, $L_3 = 4.5$ meters and $L_4 = 5$ meters.

To see if another layer of shielding is necessary, we can look at the magnetic field along $\rho = 0$ with the coils and plan E's shielding, with and without an external axial magnetic field ~ 100 mG.[26] These two magnetic field profiles are shown in Figure 5.24a. The difference in these two simulations, displayed in Figure 5.24b, shows the axial shielding while the inner shield is partly saturated. We can compare this magnetic field profile with Figure 5.18, which shows the axial shielding without the magnetic coils. Remarkably, Comsol says that these magnetic field profiles agree to within 10^{-8} mG at all points along $\rho = 0$, indicating that the partial saturation of the magnetic shields due to the coils will not make the shields less effective.

The takeaway is that the magnetic shields described in Section 5.4 should work for both

[26] S_A is more important to check because $S_A < S_T$ generally and axial magnetic fields leak farther into the shields as we saw in Subsection 5.3.3. Conveniently, the coils, finite length shields and external axial fields can all be simulated in 2D axially-symmetric models that are much faster to simulate than 3D models.

plans A and E. According to Comsol, we should not need an additional layer of shielding to prevent $\vec{\mathcal{B}}_{2,0}$ from harming the magnetic shielding of the inner layer. It is important to note that these simulations do not include the effect of us reversing the sign of $\vec{\mathcal{B}}_{2,0}$ many times over when we flip $\tilde{B}$. To be safe with the magnetic shielding in plan A, an additional layer of shielding at $\rho = 0.3$ meters would be enough to keep the shielding factors large enough if the inner shield is not as effective as Comsol suggests.

To summarize, we saw that magnetic systematic effects and magnetic shielding would both be more manageable if we choose plan E. Applying a uniform magnetic field of ~ 1.6 mG that rotates at f_{rot} is not something we have done at JILA before, but we expect that we can overcome the new engineering challenge. If that fails we can still apply $f^0 \sim 100$ Hz with plan A which we have used in the previous two generations of the JILA eEDM experiment.

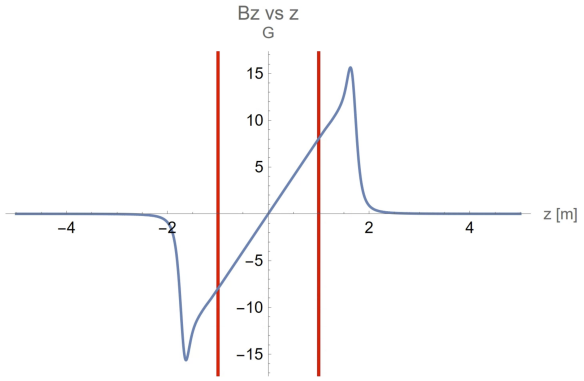

(a) $\mathcal{B}_z$

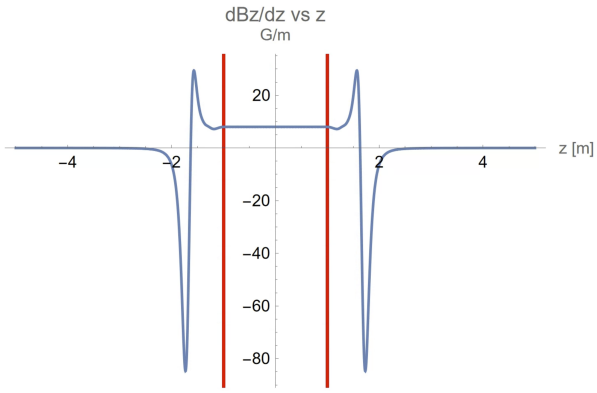

(b) $\dfrac{\partial \mathcal{B}_z}{\partial z}$

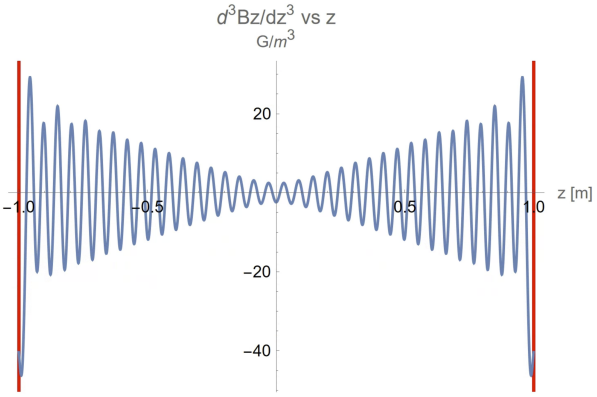

(c) $\dfrac{\partial^3 \mathcal{B}_z}{\partial z^3}$

Figure 5.21: The magnetic field and two of its gradients along $\rho = 0$ created by the coils with a radius of 5.25 inches and positions and currents given by Tables 5.4 and 5.5. The red vertical lines indicate the Bucket Brigade region between $z = \pm 1$. There are no magnetic shields around the coils in these calculations. The average first and third order gradients between $z = \pm 1$ are 8.04 G/m and 8.3 G/m^3. This will create $f^0 \sim 100$ Hz while keeping the coherence time above 20 seconds even in the absence of ion-ion collisions. The peak magnetic field along $\rho = 0$ is $\sim \pm 15$ Gauss and occurs at $z \sim \pm 1.7$ meters. Ideally the magnetic field would drop to zero outside of $z = \pm 1$, but it needs to continue increasing to keep the third order gradient in the Bucket Brigade region small. Further numerical optimization may be be able to decrease this peak field closer to $\sim \pm 10$ Gauss.

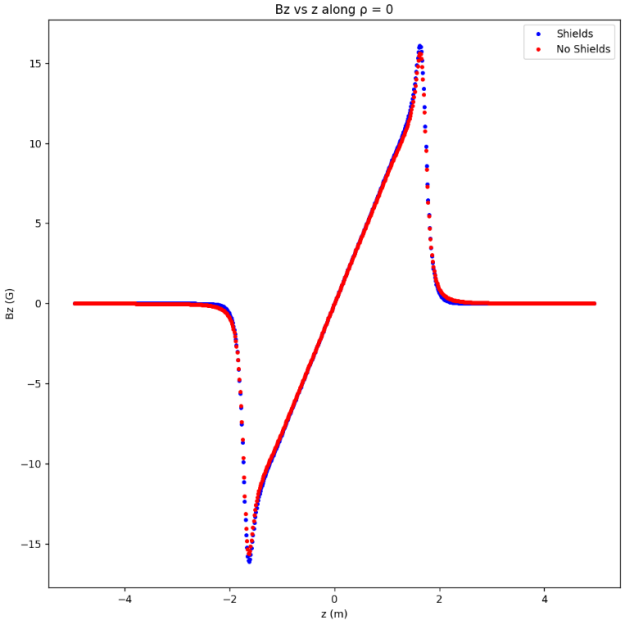

(a)

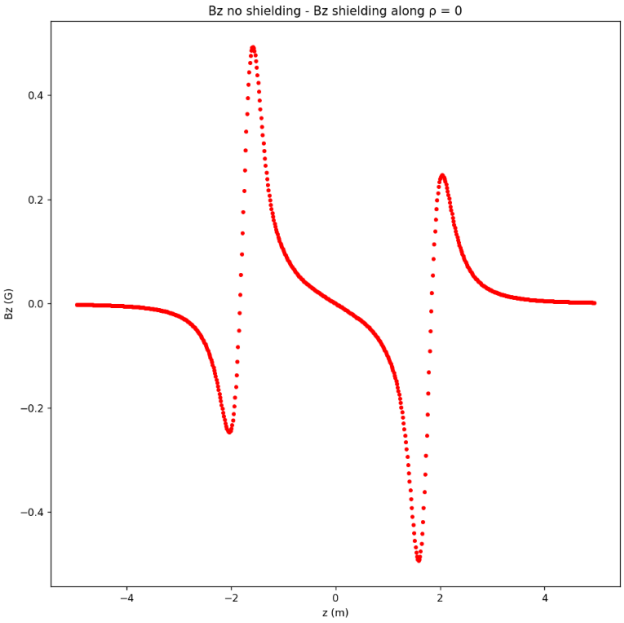

(b)

Figure 5.22: (a) Comsol simulations of $\mathcal{B}_z$ vs z along $\rho = 0$ from magnetic field created by the coils with parameters given in Tables 5.4 and 5.5. Blue and red dots are values of the field with and without magnetic shields. (b) The difference between the two magnetic fields in (a). The difference between the two fields is caused by the magnetic shields changing the field made by the coils.

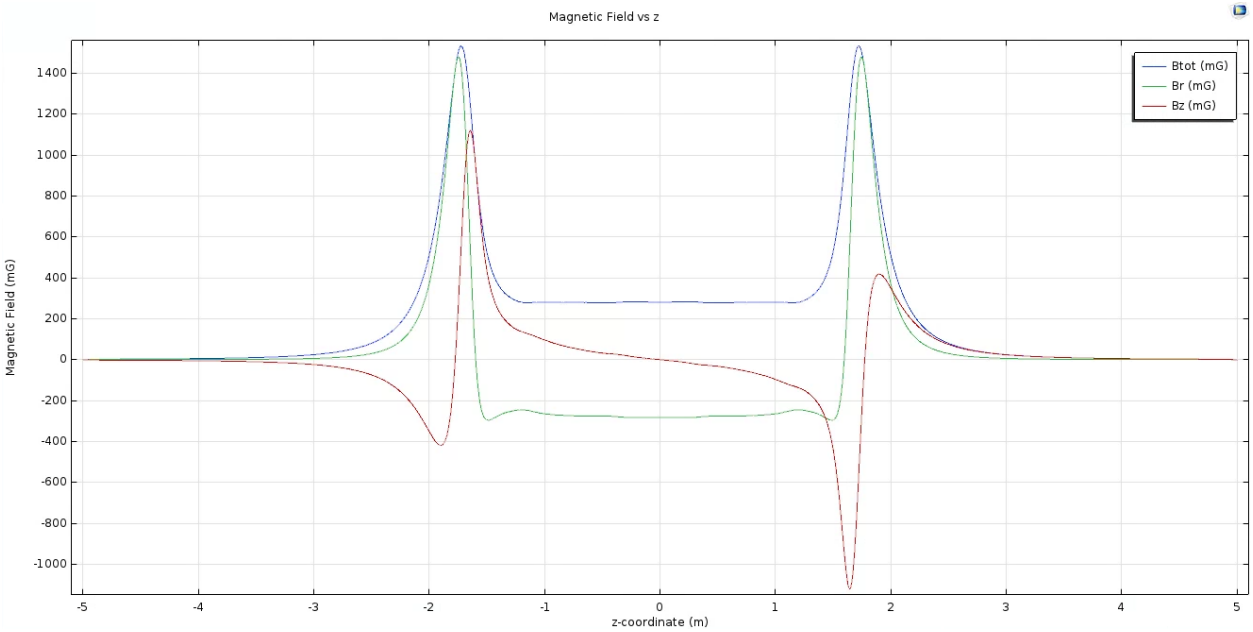

Figure 5.23: The magnetic field generated by the coils in Tables 5.4 and 5.5 along $\rho = 0.25$ meters without magnetic shields. There total magnetic field is shown in blue, its radial component in green and its axial component in red. The innermost mumetal shield is centered at zero and stretches between $z = \pm 1.75$ meters, and is saturated at the peak ~ 1.5 Gauss magnetic field (see Figure 5.6). This will decrease the shielding efficacy of the innermost shield.

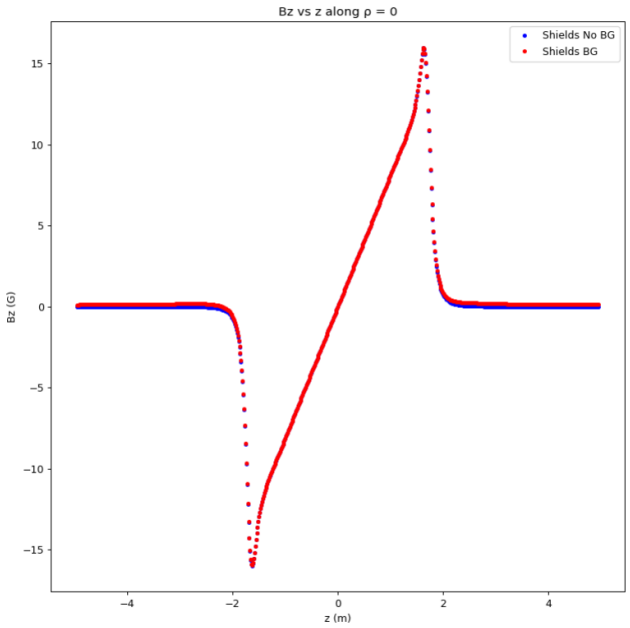

(a)

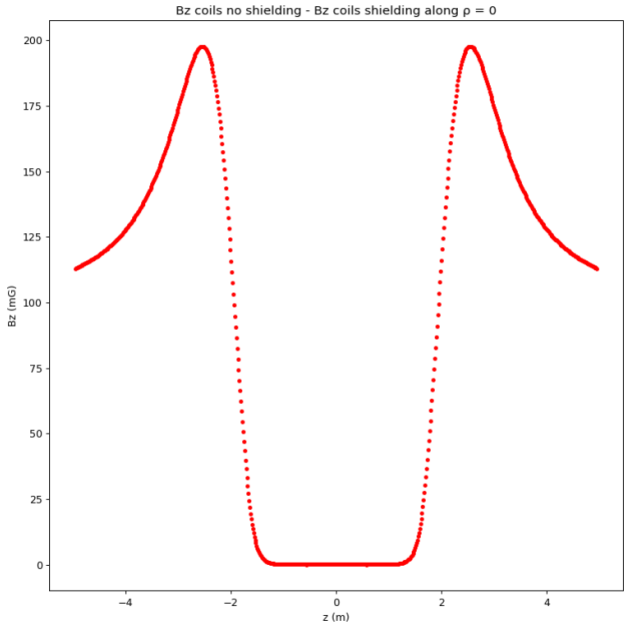

(b)

Figure 5.24: (a) The magnetic field $\mathcal{B}_z$ created by the coils in Tables 5.4 and 5.5 with the magnetic shielding for plan E described in Section 5.4. The red field also has a 100 mG external magnetic field along the z-axis. (b) The difference between the two magnetic fields in (a) which shows how well the external magnetic field is shielded with the innermost shield partly saturated.

Chapter 6

Conclusion

"I open at the close."

- J. K. Rowling, Harry Potter and the Deathly Hallows

This chapter is mostly an excuse to get in another Harry Potter quote, which I have already accomplished. I would like to wish everyone working on generation three of the JILA EDM experiment the best of luck. I think we don't get enough credit for how complicated this experiment is, especially given how few people work on it. Most AMO experiments are simpler, get results faster and publish more frequently. I think the experiment is incredibly cool and worth working on, but there really are a lot of steps between producing ions and making a particle physics measurement.

I'd like to conclude by presenting a plot that I've made, shown in Figure 6.1, which closely resembles a plot made by Dave DeMille. He was my advisor for my first two years in graduate school, so I think I can get away with it. It shows the relatively recent history of eEDM measurements and how their results compare to predictions made by beyond the Standard Model theories.

I have been incredibly lucky to work with/for many of the professors responsible for these experiments. The Amherst measurement was led by Larry Hunter, my undergraduate advisor, at a small liberal arts school with little funding and no graduate students to do all the work. Despite these constraints he reduced the limit on the eEDM by an astonishing factor of 21 [79]. Two of

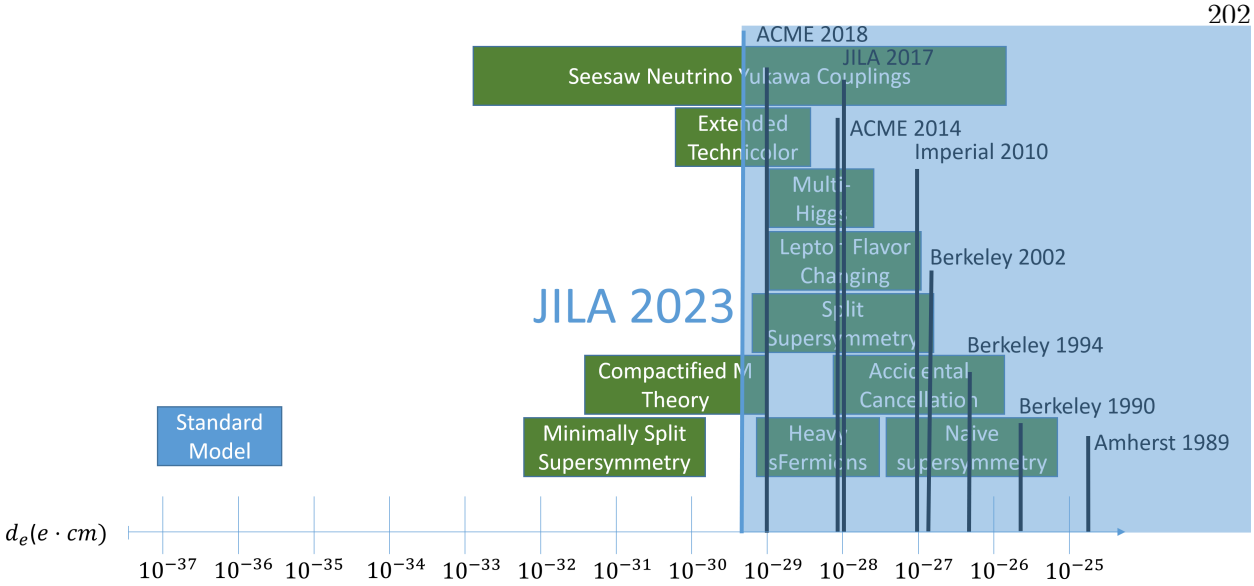

Figure 6.1: The black vertical lines are 90% confidence upper limits on the eEDM set by experiments dating back to 1989. That is to say, each experiment is 90% sure that the true value of the eEDM lies to the left of the black line. The experiments are labeled by the institution/collaboration which made the measurement and the year the result was published. The height of the line is proportional to the publication year, in some funny units. In the background are boxes which very roughly indicate the proposed value of the eEDM by different theories. The Standard Model prediction is in a blue box,[1]the beyond the Standard Model theories are in green boxes. The rough values of the eEDM predictions made by these theories were taken from Dave DeMille. The JILA generation two result is in blue and in a larger font because I was involved in that measurement and I made this plot.

the professors behind the Imperial College result, Ben Sauer and Mike Tarbutt, were kind enough to invite me to work in their lab in London for the summer of 2023 [47]. Dave DeMille is one of the three professors in charge of the ACME collaboration [28, 68]. I never met Eugene Commins, the professor who led of the experiment at Berkeley, but he advised both Larry Hunter and Dave DeMille who I learned much from [80, 81, 82]. And of course Eric Cornell and Jun Ye are my advisors at JILA, who have done their best to make me a qualified AMO physicist [27, 38].

I find it incredibly meaningful my work in graduate school resulted in a new measurement on this plot. Thank you to everyone who made my journey through graduate school possible.

[1]In Subsection 1.3.2 I state that the Standard Model prediction of the eEDM is 5.8×10^{-40} e cm, a value much smaller than is indicated in Figure 6.1. This larger value indicates the sensitivity required to measure the SM predicted value of the T-violating $\mathcal{C}_S$ term discussed briefly in Section 3.2, which will be measurable before the eEDM [83].

Bibliography

[1] W. B. Cairncross, Searching for time-reversal symmetry violation with molecular ions: Quantum state control and photofragment imaging. PhD thesis, University of Colorado Boulder and JILA, 2019.

[2] T. S. Roussy, A new limit on the electron's electric dipole moment. PhD thesis, University of Colorado Boulder and JILA, 2022.

[3] N. Schlossberger, An apparatus for measuring the electron's electric dipole moment in trapped ThF+. PhD thesis, University of Colorado Boulder and JILA, 2023.

[4] K. B. Ng, The ThF+ eEDM experiment: concept, design, and characterization. PhD thesis, University of Colorado Boulder and JILA, 2023.

[5] N. Craig, "The return of the LHC." `https://www.youtube.com/watch?v=sjHEI_ymkLo&ab_channel=PhysicsCUBoulder`. Accessed: 2023-12-05.

[6] M. E. Peskin and D. V. Schroeder, An Introduction to Quantum Field Theory. Westview Press, 1995. Reading, USA: Addison-Wesley (1995) 842 p.

[7] X. Fan, T. G. Myers, B. A. D. Sukra, and G. Gabrielse, "Measurement of the electron magnetic moment," Phys. Rev. Lett., vol. 130, p. 071801, Feb 2023.

[8] P. Agrawal, "(g-2) in qed and beyond," in Proceedings of the International Conference on Example, The Allure of Ultrasensitive Experiments, Fermilab, September 2013.

[9] S. Weinberg, "Models of lepton and quark masses," Physical Review D, vol. 101, no. 3, p. 035020, 2020.

[10] A. Tumasyan, W. Adam, J. W. Andrejkovic, T. Bergauer, S. Chatterjee, M. Dragicevic, A. E. Del Valle, R. Frühwirth, M. Jeitler, N. Krammer, et al., "Precision measurement of the w boson decay branching fractions in proton-proton collisions at s= 13 tev," Physical Review D, vol. 105, no. 7, p. 072008, 2022.

[11] A. Rasin, "Diagonalization of quark mass matrices and the cabibbo-kobayashi-maskawa matrix," arXiv preprint hep-ph/9708216, 1997.

[12] S. Descotes-Genon and P. Koppenburg, "The ckm parameters," Annual Review of Nuclear and Particle Science, vol. 67, pp. 97–127, 2017.

[13] R. Laymon and A. Franklin, Case Studies in Experimental Physics: Why Scientists Pursue Investigation. Springer Nature, 2022.

[14] C.-S. Wu, E. Ambler, R. W. Hayward, D. D. Hoppes, and R. P. Hudson, "Experimental test of parity conservation in beta decay," Physical review, vol. 105, no. 4, p. 1413, 1957.

[15] H. Greaves and T. Thomas, "On the cpt theorem," Studies in History and Philosophy of Science Part B: Studies in History and Philosophy of Modern Physics, vol. 45, pp. 46–65, 2014.

[16] M. Pospelov and A. Ritz, "Electric dipole moments as probes of new physics," Annals of physics, vol. 318, no. 1, pp. 119–169, 2005.

[17] T. Chupp, P. Fierlinger, M. Ramsey-Musolf, and J. Singh, "Electric dipole moments of atoms, molecules, nuclei, and particles," Rev. Mod. Phys., vol. 91, no. 1, p. 015001, 2019.

[18] W.-Y. Ai, J. S. Cruz, B. Garbrecht, and C. Tamarit, "Consequences of the order of the limit of infinite spacetime volume and the sum over topological sectors for cp violation in the strong interactions," Physics Letters B, vol. 822, p. 136616, 2021.

[19] N. Yamanaka, "Quantification of the electric dipole moment generated by hadronic cp violation: resolution of the strong cp problem," arXiv preprint arXiv:2310.10127, 2023.

[20] Y. Nakamura and G. Schierholz, "The strong cp problem solved by itself due to long-distance vacuum effects," Nuclear Physics B, vol. 986, p. 116063, 2023.

[21] J. Rafelski, J. Birrell, A. Steinmetz, and C. T. Yang, "A short survey of matter-antimatter evolution in the primordial universe," Universe, vol. 9, no. 7, p. 309, 2023.

[22] L. Canetti, M. Drewes, and M. Shaposhnikov, "Matter and Antimatter in the Universe," New J. Phys., vol. 14, no. 9, p. 095012, 2012.

[23] R. H. Cyburt, B. D. Fields, K. A. Olive, and T.-H. Yeh, "Big bang nucleosynthesis: Present status," Reviews of Modern Physics, vol. 88, no. 1, p. 015004, 2016.

[24] A. D. Sakharov, "Violation of CP Invariance, C asymmetry, and baryon asymmetry of the universe," Pisma Zh. Eksp. Teor. Fiz., vol. 5, pp. 32–35, 1967.

[25] J. F. Donoghue, E. Golowich, and B. R. Holstein, Dynamics of the standard model. Cambridge university press, 2014.

[26] Y. Yamaguchi and N. Yamanaka, "Large long-distance contributions to the electric dipole moments of charged leptons in the standard model," Physical Review Letters, vol. 125, no. 24, p. 241802, 2020.

[27] T. S. Roussy, L. Caldwell, T. Wright, W. B. Cairncross, Y. Shagam, K. B. Ng, N. Schlossberger, S. Y. Park, A. Wang, J. Ye, and E. A. Cornell, "An improved bound on the electron's electric dipole moment," Science, vol. 381, no. 6653, pp. 46–50, 2023.

[28] ACME Collaboration, "Improved limit on the electric dipole moment of the electron," Nature, vol. 562, no. 7727, pp. 355–360, 2018.

[29] J. Engel, M. J. Ramsey-Musolf, and U. Van Kolck, "Electric dipole moments of nucleons, nuclei, and atoms: The Standard Model and beyond," Prog. Part. Nucl. Phys., vol. 71, pp. 21–74, 2013.

[30] T. Bose, A. Boveia, C. Doglioni, S. P. Griso, J. Hirschauer, E. Lipeles, Z. Liu, N. R. Shah, L.-T. Wang, K. Agashe, et al., "Report of the Topical Group on Physics Beyond the Standard Model at Energy Frontier for Snowmass 2021," arXiv preprint arXiv:2209.13128, 2022.

[31] L. Caldwell, T. S. Roussy, T. Wright, W. B. Cairncross, Y. Shagam, K. B. Ng, N. Schlossberger, S. Y. Park, A. Wang, J. Ye, et al., "Systematic and statistical uncertainty evaluation of the hff+ electron electric dipole moment experiment," Physical Review A, vol. 108, no. 1, p. 012804, 2023.

[32] I. B. Khriplovich and S. K. Lamoreaux, CP Violation Without Strangeness: Electric Dipole Moments of Particles, Atoms, and Molecules. Texts and Monographs in Physics, Berlin, Heidelberg: Springer, 1997.

[33] R. A. Ready, G. Arrowsmith-Kron, K. G. Bailey, D. Battaglia, M. Bishof, D. Coulter, M. R. Dietrich, R. Fang, B. Hanley, J. Huneau, et al., "Surface processing and discharge-conditioning of high voltage electrodes for the ra edm experiment," Nuclear Instruments and Methods in Physics Research Section A: Accelerators, Spectrometers, Detectors and Associated Equipment, vol. 1014, p. 165738, 2021.

[34] A. C. Vutha, W. C. Campbell, Y. V. Gurevich, N. R. Hutzler, M. Parsons, D. Patterson, E. Petrik, B. Spaun, J. M. Doyle, G. Gabrielse, et al., "Search for the electric dipole moment of the electron with thorium monoxide," Journal of Physics B: Atomic, Molecular and Optical Physics, vol. 43, no. 7, p. 074007, 2010.

[35] E. R. Meyer and J. L. Bohn, "Prospects for an electron electric-dipole moment search in metastable tho and th f+," Physical Review A, vol. 78, no. 1, p. 010502, 2008.

[36] A. Petrov, N. Mosyagin, T. Isaev, and A. Titov, "Theoretical study of HfF^+ in search of the electron electric dipole moment," Phys. Rev. A, vol. 76, no. 3, p. 030501, 2007.

[37] K. C. Cossel, D. N. Gresh, L. C. Sinclair, T. Coffey, L. V. Skripnikov, A. N. Petrov, N. S. Mosyagin, A. V. Titov, R. W. Field, E. R. Meyer, E. A. Cornell, and J. Ye, "Broadband velocity modulation spectroscopy of HfF^+: Towards a measurement of the electron electric dipole moment," Chem. Phys. Lett., vol. 546, pp. 1–11, 2012.

[38] W. B. Cairncross, D. N. Gresh, M. Grau, K. C. Cossel, T. S. Roussy, Y. Ni, Y. Zhou, J. Ye, and E. A. Cornell, "Precision Measurement of the Electron's Electric Dipole Moment Using Trapped Molecular Ions," Phys. Rev. Lett., vol. 119, no. 15, pp. 1–5, 2017.

[39] H. Loh, Search for an electron electric dipole moment with trapped molecular ions. PhD thesis, University of Colorado Boulder and JILA, 2013.

[40] A. N. Petrov, L. V. Skripnikov, and A. V. Titov, "Revisiting the t, p-odd spin-rotational hamiltonian of hff+ for precise electron-electric-dipole-moment measurements," Physical Review A, vol. 107, no. 6, p. 062814, 2023.

[41] N. J. Stone, "Table of nuclear magnetic dipole and electric quadrupole moments," At. Data Nucl. Data Tables, vol. 90, no. 1, pp. 75–176, 2005.

[42] L. Skripnikov, "Communication: Theoretical study of hff+ cation to search for the t, p-odd interactions," The Journal of Chemical Physics, vol. 147, no. 2, 2017.

[43] T. Fleig, "$\mathcal{P},\mathcal{T}$-odd and magnetic hyperfine-interaction constants and excited-state lifetime for HfF^+," Phys. Rev. A, vol. 96, p. 040502, 2017.

[44] A. N. Petrov, L. V. Skripnikov, and A. V. Titov, "Zeeman interaction in the $^3\Delta_1$ state of HfF^+ to search for the electron electric dipole moment," Phys. Rev. A, vol. 96, p. 022508, 2017.

[45] T. Fleig and M. K. Nayak, "Electron electric-dipole-moment interaction constant for HfF^+ from relativistic correlated all-electron theory," Phys. Rev. A, vol. 88, no. 3, pp. 1–6, 2013.

[46] H. Loh, J. Wang, M. Grau, T. S. Yahn, R. W. Field, C. H. Greene, and E. A. Cornell, "Laser-induced fluorescence studies of HfF^+ produced by autoionization," J. Chem. Phys., vol. 135, no. 15, 2011.

[47] J. J. Hudson, D. M. Kara, I. J. Smallman, B. E. Sauer, M. R. Tarbutt, and E. A. Hinds, "Improved measurement of the shape of the electron," Nature, vol. 473, pp. 493–496, may 2011.

[48] K. Zhu, N. Solmeyer, C. Tang, and D. S. Weiss, "Absolute polarization measurement using a vector light shift," Phys. Rev. Lett., vol. 111, no. 24, p. 243006, 2013.

[49] Y. Zhou, Y. Shagam, W. B. Cairncross, K. B. Ng, T. S. Roussy, T. Grogan, K. Boyce, A. Vigil, M. Pettine, T. Zelevinsky, J. Ye, and E. A. Cornell, "Second-Scale Coherence Measured at the Quantum Projection Noise Limit with Hundreds of Molecular Ions," Phys. Rev. Lett., vol. 124, no. 5, p. 53201, 2020.

[50] K. K. Ni, H. Loh, M. Grau, K. C. Cossel, J. Ye, and E. A. Cornell, "State-specific detection of trapped HfF+ by photodissociation," J. Mol. Spec., vol. 300, pp. 12–15, 2014.

[51] Y. Shagam, W. B. Cairncross, T. S. Roussy, Y. Zhou, K. B. Ng, D. N. Gresh, T. Grogan, J. Ye, and E. A. Cornell, "Continuous temporal ion detection combined with time-gated imaging: Normalization over a large dynamic range," J. Mol. Spec., vol. 368, p. 111257, 2020.

[52] A. E. Leanhardt, J. L. Bohn, H. Loh, P. Maletinsky, E. R. Meyer, L. C. Sinclair, R. P. Stutz, and E. A. Cornell, "High-resolution spectroscopy on trapped molecular ions in rotating electric fields: A new approach for measuring the electron electric dipole moment," J. Mol. Spec., vol. 270, no. 1, pp. 1–25, 2011.

[53] E. R. Meyer, A. E. Leanhardt, E. A. Cornell, and J. L. Bohn, "Berry-like phases in structured atoms and molecules," Phys. Rev. A, vol. 80, no. 6, p. 062110, 2009.

[54] T. Chupp and M. Ramsey-Musolf, "Electric dipole moments: A global analysis," Phys. Rev. C, vol. 91, no. 3, pp. 1–11, 2015.

[55] M. Denis, M. S. Norby, H. J. A. Jensen, A. S. P. Gomes, M. K. Nayak, S. Knecht, and T. Fleig, "Theoretical study on ThF^+, a prospective system in search of time-reversal violation," New J. Phys., vol. 17, 2015.

[56] T. Fleig and M. Jung, "Model-independent determinations of the electron EDM and the role of diamagnetic atoms," J. High Energy Phys., vol. 2018, no. 7, p. 12, 2018.

[57] A. Petrov, "Numerical evaluation of systematics in the experiment for electron electric dipole moment measurement in hff+," Physical Review A, vol. 108, no. 6, p. 062804, 2023.

[58] M. B. Gavela, P. Hernández, J. Orloff, and O. Pène, "Standard model CP-violation and baryon asymmetry," Mod. Phys. Lett. A, vol. 09, p. 795, 1994.

[59] M. Pospelov and A. Ritz, "Electric dipole moments as probes of new physics," Ann. Phys., vol. 318, no. 1, pp. 119–169, 2005.

[60] Y. Nakai and M. Reece, "Electric dipole moments in natural supersymmetry," J. High Energy Phys., vol. 2017, no. 8, pp. 1–53, 2017.

[61] ACME Collaboration, "Methods, analysis, and the treatment of systematic errors for the electron electric dipole moment search in thorium monoxide," New J. Phys., vol. 19, no. 7, p. 073029, 2017.

[62] K. B. Ng, Y. Zhou, L. Cheng, N. Schlossberger, S. Y. Park, T. S. Roussy, L. Caldwell, Y. Shagam, A. J. Vigil, E. A. Cornell, and J. Ye, "Spectroscopy on the electron-electric-dipole-moment–sensitive states of thf^+," Phys. Rev. A, vol. 105, p. 022823, Feb 2022.

[63] E. R. Meyer, A. E. Leanhardt, E. A. Cornell, and J. L. Bohn, "Berry-like phases in structured atoms and molecules," Phys. Rev. A, vol. 80, no. 6, p. 062110, 2009.

[64] E. D. Commins, "Electric dipole moments of leptons," in Advances In Atomic, Molecular, and Optical Physics (B. Bederson and H. Walther, eds.), vol. 40, pp. 1–55, Academic Press, 1999.

[65] E. D. Commins, J. D. Jackson, and D. P. DeMille, "The electric dipole moment of the electron: An intuitive explanation for the evasion of schiff's theorem," American Journal of Physics, vol. 75, no. 6, pp. 532–536, 2007.

[66] E. R. Meyer, J. L. Bohn, and M. P. Deskevich, "Candidate molecular ions for an electron electric dipole moment experiment," Phys. Rev. A, vol. 73, no. 6, p. 062108, 2006.

[67] J. M. Brown and A. Carrington, Rotational spectroscopy of diatomic molecules. Cambridge university press, 2003.

[68] ACME Collaboration, "Order of magnitude smaller limit on the electric dipole moment of the electron," Science, vol. 343, no. 6168, pp. 269–272, 2014.

[69] L. Skripnikov and A. Titov, "Theoretical study of thf+ in the search for t, p-violation effects: Effective state of a th atom in thf+ and tho compounds," Physical Review A, vol. 91, no. 4, p. 042504, 2015.

[70] M. Denis, M. S. Nørby, H. J. A. Jensen, A. S. P. Gomes, M. K. Nayak, S. Knecht, and T. Fleig, "Theoretical study on thf+, a prospective system in search of time-reversal violation," New Journal of Physics, vol. 17, no. 4, p. 043005, 2015.

[71] S.-C. Su and T.-H. Chang, "Manipulating the permittivities and permeabilities of epoxy/silver nanocomposites over a wide bandwidth," Applied Physics Letters, vol. 116, no. 20, 2020.

[72] T. Sumner, "Progress Towards a New Experiment to Search for the Electric Dipole Moment of the Neutron Using Ultra-Cold Neutrons," 1979.

[73] V. Yashchuk, S. Lee, and E. Paperno, "Magnetic shielding," in Optical Magnetometry, pp. 225–248, Cambridge University Press, 2011.

[74] E. Paperno and I. Sasada, "Magnetic circuit approach to magnetic shielding," Journal of the Magnetics Society of Japan, vol. 24, no. 1, pp. 40–44, 2000.

[75] C. Bidinosti and J. Martin, "Passive magnetic shielding in static gradient fields," Aip Advances, vol. 4, no. 4, 2014.

[76] M. S. Fabus and S. Peggs, "Hysteresis and degaussing of h1 dipole magnets," CBETA Tech Note 045, 2019.

[77] Z. Lasner, Order-of-magnitude-tighter bound on the electron electric dipole moment. PhD thesis, Yale University, 2019.

[78] C. Conn. personal communication.

[79] S. Murthy, D. Krause Jr, Z. Li, and L. Hunter, "New limits on the electron electric dipole moment from cesium," Physical review letters, vol. 63, no. 9, p. 965, 1989.

[80] K. Abdullah, C. Carlberg, E. Commins, H. Gould, and S. B. Ross, "New experimental limit on the electron electric dipole moment," Physical review letters, vol. 65, no. 19, p. 2347, 1990.

[81] E. D. Commins, S. B. Ross, D. DeMille, and B. Regan, "Improved experimental limit on the electric dipole moment of the electron," Physical Review A, vol. 50, no. 4, p. 2960, 1994.

[82] B. Regan, E. D. Commins, C. J. Schmidt, and D. DeMille, "New limit on the electron electric dipole moment," Physical review letters, vol. 88, no. 7, p. 071805, 2002.

[83] Y. Ema, T. Gao, and M. Pospelov, "Standard Model Prediction for Paramagnetic Electric Dipole Moments," Phys. Rev. Lett., vol. 129, p. 231801, Nov 2022.

Appendix A

$\mathcal{B}_z$ and $\mathcal{B}_z^B$ Measurements

In Section 3.1 we saw that the off diagonal terms in our effective Hamiltonian gave us the following systematic errors:

$$\delta f^{DB} = \frac{\Delta^0\delta\Delta^{DB} + \Delta^D\delta\Delta^B + \delta\Delta^{DR}\delta\Delta^{BR} + \delta\Delta^R\delta\Delta^{DBR}}{|f_0^0|} + f^{BR}\frac{\Delta^0\delta\Delta^{DR} + \Delta^D\delta\Delta^R}{|f_0^0|^2} \tag{A.1}$$

Later in that section we estimated the size of the $\delta\Delta$ terms in this expression, which depend on $\mathcal{B}_z$ and $\mathcal{B}_z^B$. We were able to measure the magnetic field along the x and y axes by using the Zeeman shift described in Subsection 3.3.3, but we have no analogous effect that can easily probe the magnetic field along the z axis.

Instead we can find upper limits on $\mathcal{B}_z$ and $\mathcal{B}_z^B$ by carefully investigating some of our other frequency channels. We can write out the full expression for f^{DR} analogously to how we wrote Equation 3.2 for f^{DB}:

$$\begin{aligned} f^{DR} = \delta f_0^{DR} + \frac{\Delta^0\delta\Delta^{DR} + \Delta^D\delta\Delta^R}{|f_0^0|} - \delta f_0^{DR}\frac{(\Delta^0)^2 + (\Delta^D)^2}{2|f_0^0|^2} - \delta f_0^R\frac{\Delta^0\Delta^D}{|f_0^0|^2} \\ + \frac{1}{16}\sum_{\tilde{B},\tilde{R},\tilde{I},\tilde{D}=\pm1}\left[\tilde{D}\tilde{R}\frac{\delta\mathcal{D}^2}{2|f_0^0|} - \tilde{D}\tilde{B}\tilde{R}\delta\mathcal{F}_0\frac{2\tilde{R}(\Delta^0 + \tilde{D}\Delta^D)\delta\mathcal{D} + \delta\mathcal{D}^2}{2|f_0^0|^2} + ...\right] \end{aligned} \tag{A.2}$$

Keeping only the largest terms as discussed in Section 3.1 we find that:

$$f^{DR} = \delta f_0^{DR} + \frac{\Delta^0 \delta\Delta^{DR} + \Delta^D \delta\Delta^R + \delta\Delta^B \delta\Delta^{DBR} + \delta\Delta^{DB} \delta\Delta^{BR}}{|f_0^0|} + f^{BR} \frac{\Delta^0 \delta\Delta^{DB} + \Delta^D \delta\Delta^B + \delta\Delta^{BR} \delta\Delta^{DR} + \delta\Delta^{DBR} \delta\Delta^R}{|f_0^0|^2} \tag{A.3}$$

We now assume that the only frequency shifts included in δf_0^{DR} are Zeeman effects with $\frac{\langle \vec{\mathcal{E}} \cdot \vec{\mathcal{B}} \rangle / |\mathcal{E}|}{\langle \hat{\mathcal{E}} \cdot \vec{\mathcal{B}} \rangle} = 1$ so they show up ~ 460 times larger in δf_0^R.[1] In that case we can write:

$$f^{DR} - \frac{\delta g_F}{g_F} f^R = \frac{\Delta^0 \delta\Delta^{DR} + \Delta^D \delta\Delta^R + \delta\Delta^B \delta\Delta^{DBR} + \delta\Delta^{DB} \delta\Delta^{BR}}{|f_0^0|} + f^{BR} \frac{\Delta^0 \delta\Delta^{DB} + \Delta^D \delta\Delta^B + \delta\Delta^{BR} \delta\Delta^{DR} + \delta\Delta^{DBR} \delta\Delta^R}{|f_0^0|^2} \tag{A.4}$$

Note that we are ignoring the Δ contributions to f^R. While these shifts have similar magnitude to the ones on the right hand side of the above equation, they are suppressed by a factor of $\frac{\delta g_F}{g_F}$ and can be ignored.

Plugging in the values of $\delta\Delta^R$, $\delta\Delta^B$, $\delta\Delta^{BR}$, $\delta\Delta^{DR}$, $\delta\Delta^{DB}$ and $\delta\Delta^{DBR}$ found in Section 3.1 into Equation A.4 we find that:

$$f^{DR} - \frac{\delta g_F}{g_F} f^R = \frac{6\mathcal{B}_z g_F \mu_B \Delta^0 \Delta^D}{h|f_0^0| f_{\text{rot}}} + \frac{36\mathcal{B}_z (\mathcal{B}_z^B)^2 g_F^3 \mu_B^3 \Delta^0 \Delta^D}{h^3 |f_0^0| f_{\text{rot}}^3} + f^{BR} \frac{30\mathcal{B}_z \mathcal{B}_z^B g_F^2 \mu_B^2 \Delta^0 \Delta^D}{h^2 |f_0^0|^2 f_{\text{rot}}^2} \tag{A.5}$$

[1] While there are Zeeman effects with $\frac{\langle \vec{\mathcal{E}} \cdot \vec{\mathcal{B}} \rangle / |\mathcal{E}|}{\langle \hat{\mathcal{E}} \cdot \vec{\mathcal{B}} \rangle} = 1$ and Berry's phase shifts that are entirely $\tilde{D}$-even, the largest shift by far in our experiment is a Zeeman shift with $\frac{\langle \vec{\mathcal{E}} \cdot \vec{\mathcal{B}} \rangle / |\mathcal{E}|}{\langle \hat{\mathcal{E}} \cdot \vec{\mathcal{B}} \rangle} = 1$. This shift ideally does not show up in f^R but it can due to the digitization of how we apply V_{rot}, see Appendix B 3 of our Systematics paper. We expect this shift to overwhelm other Zeeman shifts with $\frac{\langle \vec{\mathcal{E}} \cdot \vec{\mathcal{B}} \rangle / |\mathcal{E}|}{\langle \hat{\mathcal{E}} \cdot \vec{\mathcal{B}} \rangle} \neq 1$ and Berry's phase shifts which naturally show up in our $\tilde{B}$-odd frequency channels.

The second and third terms in this equation are much smaller than the first for reasonable values of $\mathcal{B}_z$ and $\mathcal{B}_z^B \lesssim 1$ Gauss. We can therefore drop the latter two terms and use our measured values of $f^{DR} = 0.07(2)$ mHz and $f^R = -4.23(9)$ mHz to find that $\mathcal{B}_z = 80$ mG in our generation two experiment. We expect that this is an overestimate of the magnetic field as we measure $\mathcal{B}_x \sim \mathcal{B}_y \sim 10$ mG before using our ions to further reduce this field, but we use $\mathcal{B}_z = 80$ mG to calculate the systematic shifts in Section 3.1.

We can go through a similar procedure for f^{DBR} and f^{BR}, in which case we find:

$$f^{DBR} - \frac{\delta g_F}{g_F} f^{BR} = \frac{6\mathcal{B}_z^B g_F \mu_B \Delta^0 \Delta^D}{h|f_0^0|f_{\text{rot}}} + \frac{36\mathcal{B}_z^2 \mathcal{B}_z^B g_F^3 \mu_B^3 \Delta^0 \Delta^D}{h^3 |f_0^0| f_{\text{rot}}^3} + f^{BR}\frac{\Delta^0 \Delta^D}{|f_0^0|^2} \tag{A.6}$$

Unsurprisingly, the $\tilde{B}$-odd version of Equation A.5 allows us to set a limit on the magnetic field with the opposite $\tilde{B}$ dependence, $\mathcal{B}_z^B$. In this equation the term proportional to f^{BR} is not negligible. This is because the product of f^{BR}, Δ^0 and Δ^D, the largest frequency channel other than f^0 and largest Δs, happens to have the correct switch state dependence to show up in f^{DBR}. While we cannot neglect this term we do know its value, so it can be included when finding $\mathcal{B}_z^B$. In this case we also allow for a 5 mHz contribution to f^{BR} from Berry's phase[2] that is not otherwise accounted for which inflates the maximum possible value of $\mathcal{B}_z^B$. Even with this all taken into account we find that $\mathcal{B}_z^B < 88$ mG.

[2] As discussed in Section 3.5, Berry's phase shifts can naturally show up in f^B or f^{BR}. While analyzing systematics we found that we expect that a 5 mHz shift is split between these two frequency channels which we assumed showed up entirely in f^B as that would cause the largest systematic. Here we assume the effect is entirely in f^{BR}.

Appendix B

The Harmonics of $\mathcal{E}_{\text{rot}}$

"Is it over now?"

- Taylor Swift, Is It Over Now? (Taylor's Version)

In order to apply $\mathcal{E}_{\text{rot}}$ we have eight op-amps each amplify a 375 kHz sine wave. The output voltage V_{rot} of each op-amp is sent to the top or bottom of one of our eight radial electrodes as described in Subsection 3.4.2. These voltages result in our rotating electric field $\vec{\mathcal{E}}_{\text{rot}}$ that we need to perform our EDM measurement. Our op-amps are imperfect and in addition to outputting V_{rot} the op-amps also produce harmonics that oscillate at $n \times 375$ kHz where n is a positive integer. These harmonic voltages produce electric fields that contribute to Zeeman and Berry's phase shifts which cause systematic shifts as explained in Chapter 3.

In order to quantify these systematic shifts we measured the magnitude of the harmonic voltages on each of our radial electrodes. The challenge of this measurement is that there is a ~ 350 Volt fundamental signal at 375 kHz on each of the radial electrodes that is, by design, much larger than the harmonics we want to measure. If our measurement device is nonlinear and causes any harmonic distortion itself it will be difficult to tell if the measured harmonics are really on the fins or artifacts of our measurement.

To that end I built a very linear custom filter designed to notch the fundamental voltage at

375 kHz, as well as the smaller RF voltage $\sim$ 23.5 V at 50 kHz. This filter was also designed to have a relative maximum of transmission at 750 kHz, the frequency of the second harmonic. This is because the second harmonic was a particularly worrying source of systematics – it interacts with magnetic fields in the xy-plane to create a Zeeman shift or ellipticity in $\mathcal{E}_{\text{rot}}$ to induce a Berry's phase shift, both of which are relatively large systematics in our experiment.

The circuit diagram of the home built filter, attached to a radial electrode and our fancy oscilloscope, can be seen in Figure B.1. The input voltage comes from one of our eight op-amps that creates V_{rot}. This voltage is connected directly to the radial electrode, denoted in this circuit diagram by the fin capacitor. The input voltage also goes to a system of four resistors which, if unattached from the rest of the circuit, act like a voltage divider. The voltage division is either a factor of 7 or 14 depending on if the switch is attached high or low in Figure B.1. We made eight small identical boxes that contain the voltage divider and switch, one for each of the fins. They were electrically connected to their op-amp and fin during the data collection.

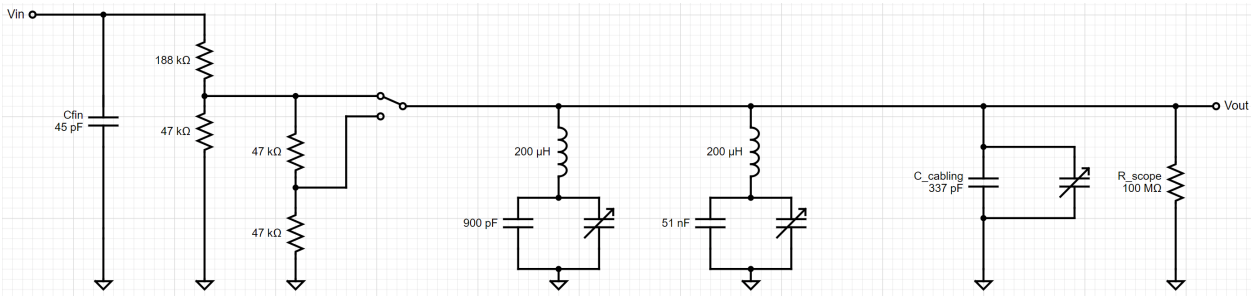

Figure B.1: Circuit diagram of the electronics used to measure harmonics. The components are described in the text.

We made one circuit containing the two notch filters in Figure B.1. These inductors are made using hand wound coils with an air core to prevent harmonic distortion, each with an inductance of about 200 μH. The inductors were connected to capacitors which were chosen such that $\frac{1}{\sqrt{LC}} = \omega_{\text{rot}}, \omega_{\text{RF}}$. These components together have very low impedance at their resonant frequencies, causing V_{rot} and V_{rf} to be grounded and not reach the output port of our circuit. In order to make sure the resonance of the filters was very close to ω_{rot} and ω_{RF}, the main capacitors were connected

to variable capacitors that could vary from $\sim$ 0 to 50 pF. These two notch filters were held in a separate grounded box that had an input (connected to a voltage divider box) and an output (connected to the scope).

The two boxes and scope were connected by standard BNC cables which had a total capacitance of about 337 pF. The cabling connected the notch filter box to our oscilloscope which had an input impedance of 100 MΩ. The complete circuit had one additional resonance that allowed a relatively large amount of the signal to pass through. This was engineered to appear near $2\omega_{\mathrm{rot}}$, the frequency of the second harmonic. We added a third variable capacitor in parallel with the cabling (which we put in the same box as the notch filters) that tuned this final resonance. The measured throughput of the entire circuit is shown in Figure B.2.

Figure B.2 only shows the throughput of the first and second harmonics of $\mathcal{E}_{\mathrm{rot}}$. We measured the throughput all the way out to the 17th harmonic for the "High V" or "switch up" setting of our circuit, shown in Figure B.3.

This allowed us to measure the voltages on each of our radial electrodes and two endcaps (electrodes at the top and bottom of our ion trap we used to apply the DC trapping potential) up to the 17th harmonic, as shown in Table B.1. Because we were particularly worried about the second harmonic, we used our initial measurements of its amplitude to apply a "feedforward" signal, also at $2\omega_{\mathrm{rot}}$ to minimize the second harmonic as much as possible. The data shown in Table B.1 is with the feedforward signal applied. Note that we saw a signal that stood out from the noise floor for all 17 harmonics on the radial electrodes. This was only the case up to the third harmonic on the axial endcaps; for the higher harmonics on the endcaps we conservatively report the noise floor of our reading modulo the frequency dependent conversion factor in Figure B.3 as the magnitude.

Table B.1 also includes the magnitude of the electric fields generated by the harmonic voltages we measured. There are two pages of fairly dry math in Section VI B 5 of the Systematics paper that explain how we perform this conversion.

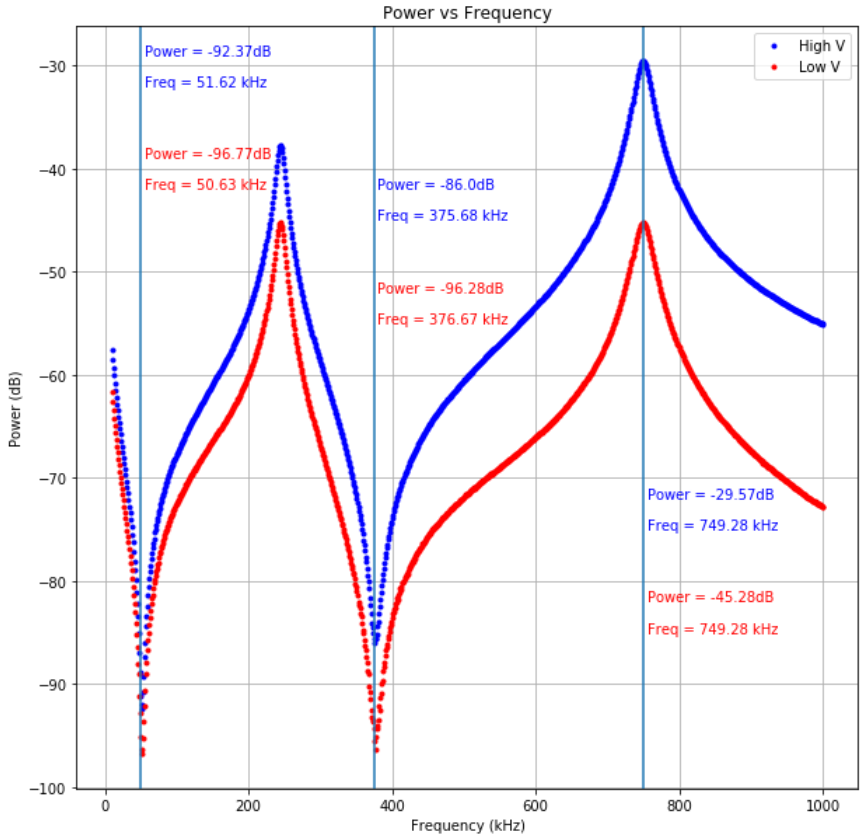

Figure B.2: Throughput data from home built circuit in Figure B.1. It was collected by the JILA electronics shop's signal analyzer which also had a 100 MΩ input impedance. The blue "High V" data was taken with the switch in Figure B.1 "up", and the red data was taken with the switch "down". The thin blue vertical lines indicate the three desired resonance frequencies ω_{RF}, ω_{rot} and $2\omega_{\mathrm{rot}}$. The power and frequencies are given at the local maxima/minima recorded by the signal analyzer, which reports the throughput power at discrete frequencies.

All I will say here is to comment on why the electric fields in the xy plane for the 7th, 9th, 15th and 17th harmonics are particularly large given the radial voltages. This is because when n differs from a multiple of 8 by ± 1 is a special case. Suppose that the nth harmonic on all eight electrodes has the same phase difference ϕ_n from V_{rot}. In this case the voltages for when n differs from a multiple of 8 by ± 1 constructively interfere to create the electric field $\mathcal{E}_{x,ynh}$. For these harmonics we assume this worst case which results in comparatively large electric field magnitudes. This effect explains why we measured all the way out to the 17th harmonic.

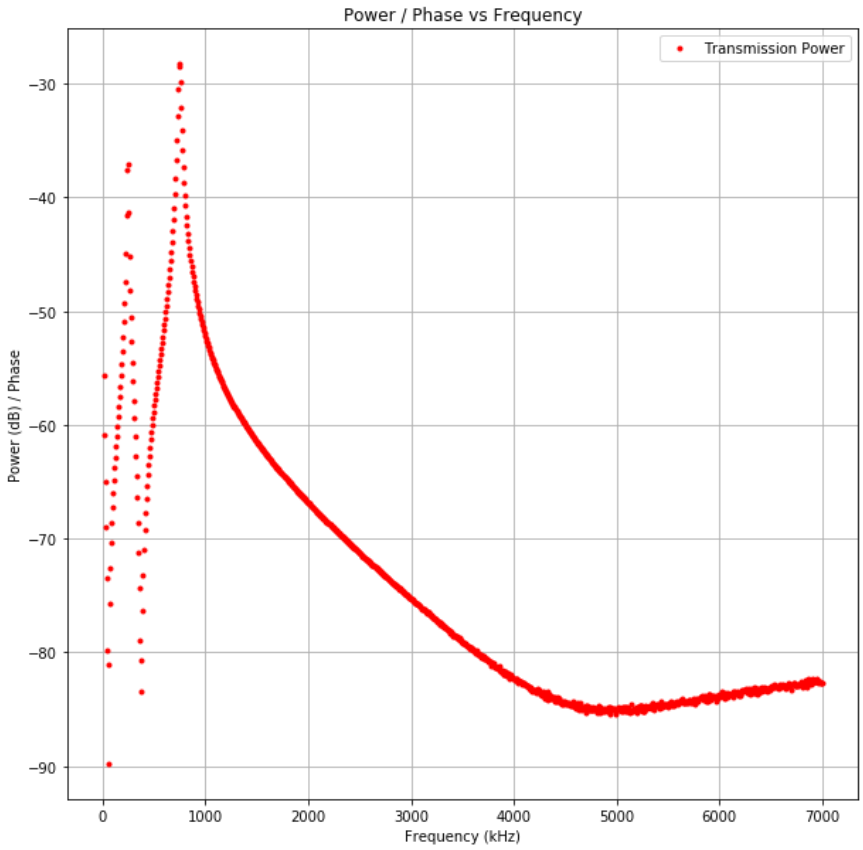

Figure B.3: This is the recorded power throughput of our circuit immediately before measuring the voltages on our ten electrodes, as reported in Table B.1.

Table B.1: Constraints on electric fields from higher-harmonic voltages on radial electrodes and endcaps. For reference, the amplitude of the fundamental on the radial electrodes is $\sim 350\,\mathrm{V}$. This table is an extension of Table V in the Systematics paper.

	Amplitudes (mV)		Fields ($\mathrm{mV\,m^{-1}}$)	
n	Radial	Axial	$\lvert\delta\mathcal{E}_{x,ynh}\rvert$	$\lvert\delta\mathcal{E}_{znh}\rvert$
2	11	0.5	250	1.0
3	310	0.3	1296	2.1
4	190	0.1	649	1.8
5	410	0.2	1715	2.7
6	100	0.4	341	0.8
7	230	0.5	4000	1.7
8	45	0.7	154	3.1
9	170	1.0	2957	1.8
10	37	1.4	126	2.0
11	140	1.8	586	2.7
12	42	2.1	143	3.1
13	120	2.2	501	1.8
14	60	2.2	206	1.7
15	45	2.1	777	1.5
16	16	1.9	53	1.4
17	34	1.9	596	1.4